GRADUATE SCHOOL OF SCIENCE,
NAGOYA UNIVERSITY

DOCTORAL THESIS

Probing Primordial Perturbations on Small Scales through Dark Matter Halos

(ダークマターハローを用いた小スケール原始ゆらぎの観測的検証)

Author:
Katsuya ABE

Supervisor:
Kiyotomo ICHIKI

A thesis submitted in fulfillment of the requirements
for the degree of Doctor of Science

in the

Cosmology Group
Department of Physics

February 16, 2023

Abstract

Our Universe has rich hierarchical structures spanning many orders of magnitude. The seeds of such hierarchical structures are called primordial perturbations. Precise measurements such as Cosmic microwave background (CMB) and large-scale structure (LSS) surveys have been achieved to measure the amplitude of primordial perturbations on larger scales than 1 Mpc. They have also allowed us to reveal their several statistical features on large scales, which are surprisingly consistent with the prediction from the simple inflation scenario. On the other hand, measurements of the smaller-scale perturbations have not succeeded well due to, e.g., their nonlinear effects associated with the structure formation. Several indirect probes have been provided for evaluating the amplitude of the perturbations on small scales. So far, we have obtained the robust upper limit through the CMB spectral distortion measurement by the COBE/FIRAS. However, other methods are highly demanded to measure the amplitude.

This thesis proposes a new method to probe the primordial small-scale perturbations focusing on the small-mass dark matter (DM) halos. As the LSS surveys give information on large scales, measuring small-mass DM halos would lead us to investigate small-scale perturbations. We show that a measurement of free-free emission signals is a good probe to the small-mass DM halos and, subsequently, primordial small-scale perturbation in terms of the spectral index and the running parameters. Although the signal from DM halos is smaller than the 10% level of the observed signals mainly composed of the galactic origin, we find that the free-free emission signal from DM halos is modified by $\sim$ 20% even in the two-parameter sets, which is consistent with the recent Planck result. The measurement of the cosmological free-free signals has the potential to provide more stringent constraints on the primordial small-scale perturbations while carefully removing the Galactic free-free emission is required through the multifrequency radio observation or the cross-correlation study with, e.g., the galaxy surveys or 21-cm intensity map.

This thesis also focuses on the small-mass DM halos formed at higher redshift from excess power of primordial perturbations, which are called ultracompact minihalos (UCMHs). Several previous works already suggested the constraint tighter than one of COBE/FIRAS through the non-detection of energetic signals from DM annihilation inside UCMHs, which, however, depends on the nature of DM. Then this thesis discusses the 21-cm signal and the astrophysical effects associated with UCMHs as DM model-independent methods. Our study of the 21-cm signal indicates that the upcoming 21-cm observation of the Square Kilometre Array provides the constraint on the amplitude of primordial small-scale perturbation tighter than of the COBE/FIRAS through non-detection of the UCMH signals. In the other study, we test the effect of first-generation stars formed in UCMHs on the cosmic reionization history using the Planck CMB observation data. As a result, we find that the Planck observation data of CMB E-mode polarization is unfavorable to the ionizing effect in the high-redshift epoch. Therefore, we obtain the constraint on the amplitude of the primordial small-scale perturbations tighter than the existing ones.

Among the several observational missions in the future, the precise study of primordial small-scale perturbations will be one of the main topics. The theoretical work to predict observables regarding small-scale perturbation will attract more attention.

Acknowledgements

I want to thank all the people who have been involved with my Ph.D. research. The work for this thesis is publicly supported by a Research Fellow of the Japan Society for the Promotion of Science, KAKENHI Grants No. JP20J22260. First, I am profoundly grateful to my supervisor, Kiyotomo Ichiki, for his scientific advice and daily support for my campus life. I am also extremely appreciative to Dr. Hiroyuki Tashiro, who has patiently taught me since I was a fourth-year undergraduate student. He gave me a lot of fruitful comments and opportunities to develop my Ph.D. work. I deeply thank my collaborators, Kenji Hasegawa, Toshiyuki Tanaka, Daiki Hashimoto, and Kunihiko Furugori, for their practical discussions and valuable comments about theoretical and numerical studies. My thesis studies are made up of precious discussions with them.

I thank all staff members and the students of the Cosmology group at Nagoya University for scientific discussions. Especially, I greatly thank Shuichiro Yokoyama, Yuichiro Tada, Teppei Minoda, Ikumi Ueda, and Ryoto Inui for giving me a new direction for my research through innumerable discussions with them. I also strongly thank the secretaries of the Cosmology group, Hitomi Tanaka and Mio Kato, for countless support for my office work. Thanks to their great kindness, I can devote my Ph.D. life to my thesis studies. Finally, I appreciate my family and my girlfriend for their continuous encouragement in my life.

Contents

Abstract **iii**

Acknowledgements **v**

1 Introduction **1**
- 1.1 Inflationary cosmology on global scales 1
- 1.2 Cosmological perturbations on local scales 1
- 1.3 Primordial perturbations from inflation era 2
  - 1.3.1 Primordial small-scale perturbations 2
- 1.4 Probes to explore primordial small-scale perturbations 3
  - 1.4.1 CMB spectral distortion 3
  - 1.4.2 Primordial black hole 3
  - 1.4.3 Galaxies and small-mass halos 5
  - 1.4.4 Ultracompact minihalos 5
- 1.5 Aim of this thesis 6
- 1.6 Structure of this thesis 7

2 Cosmological Perturbations and Structure Formation **9**
- 2.1 Cosmological perturbations 9
- 2.2 Background level 10
  - 2.2.1 Background level - Geometric side - 10
  - 2.2.2 Background level - Matter side - 11
  - 2.2.3 Consequences at background level 11
- 2.3 Time evolution of $\bar{\phi}$ and slow-roll condition 12
- 2.4 Linear level 13
  - 2.4.1 Gauge choice 13
  - 2.4.2 Scalar, Vector and Tensor perturbations 13
  - 2.4.3 Inhomogeneous Universe 14
  - 2.4.4 Gauge transformation - Metric perturbations - 14
  - 2.4.5 Gauge transformation - Matter perturbations - 16
  - 2.4.6 Gauge invariant quantities 16
  - 2.4.7 Consequences at linear order 18
- 2.5 Initial condition of perturbations 19
  - 2.5.1 Mukhanov-Sasaki variable 20
  - 2.5.2 Quantum fluctuation of the inflation scalar field 21
- 2.6 Primordial power spectrum of scalar perturbations 24
- 2.7 Observational implications from the Planck 2018 data 25
- 2.8 Evolution of cosmological perturbations 26
- 2.9 CMB anisotropy 28
  - 2.9.1 CMB Temperature 28
- 2.10 Large-scale structures 29
  - 2.10.1 The linear evolution of Dark Matter perturbations 29
  - 2.10.2 Galaxy Bias and DM Halo Bias 30

2.10.3 Press-Schechter Halo Formalism 31
2.10.4 Peak-Theory Halo Formalism 32

3 Primordial Small-Scale Perturbations **37**
3.1 CMB spectral distortion 37
3.1.1 Physics underlying the CMB distortion 37
3.1.2 Relation with Primordial Power Spectrum 40
3.1.3 Limits from the COBE/FIRAS observation 41
3.2 Primordial black hole 42
3.2.1 Abundance of PBHs 42
3.3 Galaxies and small-mass DM halo 45
3.3.1 UV Luminosity function of high redshift galaxies 45
3.3.2 Free-free emission from DM halos 47
3.4 Ultracompact minihalos 47
3.4.1 Abundance of UCMHs 48
3.4.2 The observational limit 50
3.4.3 Baryonic effects from UCMHs 51
21-cm line emission/absorption background 51
Astrophysical effects 52

4 Free-free emission from DM halos **53**
4.1 Introduction 53
4.2 Free-free emission rate from an individual halo 55
4.3 Free-free background emission from DM halos 57
4.3.1 Mass and redshift distribution 59
4.4 Statistical Anisotropy of the free-free emission from DM halos 60
4.4.1 Mass and redshift distribution 63
4.5 Cosmological application: n_s and r_{n_s} 64
4.6 Conclusion 70

5 The 21-cm signals from UCMHs **73**
5.1 Introduction 73
5.2 UCMHs with the spiked matter spectrum 75
5.3 21-cm signal from a single UCMH 76
5.3.1 Baryon gas mass in UCMHs 76
5.3.2 Baryon gas density and temperature in UCMHs 77
5.3.3 Brightness temperature 79
5.4 21-cm fluctuations due to the UCMH clustering 82
5.4.1 Detectability with SKA 84
5.5 Conclusion 86

6 Population III stars in UCMHs **89**
6.1 Introduction 89
6.2 The properties of UCMHs 91
6.3 Pop. III stars formation in UCMHs 92
6.4 Reionization model including UCMH Pop. III stars 96
6.5 MCMC analysis with Planck 2018 97
6.5.1 Setup 97
6.5.2 MCMC results and discussion 101
6.6 Conclusion 102

7 Summary of this thesis **107**

A Stress-Energy Tensor **111**

B Relation between ζ and $\mathcal{R}$ on superhorizon scales **113**

C Jeans mass **115**

D 21-cm signals from IGM and Minihalos **119**
D.1 IGM fluctuations . . . 119
D.2 Minihalo fluctuations . . . 119
D.3 Noise level of SKA . . . 120

List of Figures

1.1 Constraint on the primordial power spectrum on wide scales. 4
1.2 Constraints on the PBH fraction concerning DM as a function of the PBH mass. 5

2.1 Current constraints on the the tensor-to scalar ration r and the spectral index. 27
2.2 The anisotropies of the CMB temperature as observed by Planck. . . . 28
2.3 Comparison between the fitting functions for the matter transfer function. 31

3.1 Limits on the total amplitude of the primordial power spectrum with a step-like excess in $k > k_{\rm s}$. 42
3.2 Limits on the amplitude of the primordial power spectrum from exploring PBHs in several ways. 44
3.3 Measurements of the matter power spectrum at $z = 0$. 46
3.4 Present mass variance parameter produced by the almost scale-invariant spectrum. 50
3.5 Limits on the amplitude of primordial density and curvature perturbations. 51

4.1 The intensity of the global free-free emission from DM halos. 58
4.2 The redshift dependence of the clumping factor. 59
4.3 Mass distribution of the global free-free emission from DM halos. . . . 60
4.4 Redshift distribution of the global free-free emission from DM halos. . 61
4.5 Angular power spectrum of the cosmological free-free emission induced by DM halos. 63
4.6 Mass distribution of the one-halo term of the free-free emission anisotropy induced by the distribution of DM halos. 65
4.7 Redshift distribution of the one-halo term of the free-free emission anisotropy induced by the distribution of DM halos. 65
4.8 Redshift distribution of the two-halo term of the free-free emission anisotropy induced by the distribution of DM halos. 66
4.9 The global signals of halos' free-free emission with the six parameter sets. 67
4.10 The anisotropies of halos' free-free emission signal with the six parameter sets. 68
4.11 The difference of anisotropies of free-free emission by halos with the six parameter sets. 68
4.12 The difference of CMB temperature anisotropies with the six parameter sets. 69
4.13 The difference of anisotropies of CMB temperature induced by Compton scattering with the six parameter sets. 70

5.1 Baryon gas mass ratio to the DM mass at the redshift $z = 20$. 78
5.2 The 21-cm signal from a single UCMH. 81
5.3 Dependence of the 21-cm signal from a single UCMH on the spike scale. 82
5.4 (*Top*) Redshift dependence of the 21-cm fluctuations from UCMHs. (*Bottom*) Dependence of the 21-cm fluctuations on the spike wave number at $z = 20$. 85
5.5 Detectability of the signal from UCMHs with observation by SKA. . . 86

6.1 The minimum mass of UCMHs to host Pop. III stars. 95
6.2 The cosmological evolution of the global ionization fraction estimated. 98
6.3 (*Top*): Angular power spectrum of the CMB temperature. (*Bottom*): Ratio between the standard CMB temperature anisotropy and one of each UCMH initial mass model. 99
6.4 (*Top*): Angular power spectrum of the CMB E-mode polarization. (*Bottom*): Ratio between the standard CMB E-mode polarization anisotropy and one of each UCMH initial mass model. 100
6.5 MCMC results for several models of the UCMH initial mass, $M = 10^8 M_\odot$ (top left), $M = 10^{8.2} M_\odot$ (top right), $M = 10^{8.4} M_\odot$ (bottom left), $M = 10^9 M_\odot$ (bottom right). $z_{\rm reio}$ and $\mathcal{A}_{\rm mat,0}$ are free paramters, and τ is the derived paramter. The thick shaded region shows the 1σ region, and the thin shaded region shows the 2σ region. 103
6.6 Upper limit on the amplitude of the additional spike-type power spectrum. 104

7.1 Constraint on the primordial power spectrum on wide scales with this works. 109

Physical Constants and Notations

Speed of Light in vacuum	$c = 2.997\,924\,58 \times 10^{8}\,\mathrm{m\,s^{-1}}$
Newton constant	$G = 6.672\,598\,5 \times 10^{-11}\,\mathrm{m^3kg^{-1}s^{-2}}$
Planck constant	$h_{\mathrm{pl}} = 6.626\,075\,54 \times 10^{-34}\,\mathrm{J\,s}$
Planck constant in eV	$h_{\mathrm{pl}} = 4.135\,669\,212 \times 10^{-15}\,\mathrm{eVs}$
Electron-volt	$\mathrm{eV} = 1.602\,176\,487 \times 10^{-19}\,\mathrm{J}$
h-bar	$\hbar = 1.054\,572\,666\,3 \times 10^{-34}\,\mathrm{J\,s}$
h-bar in eV	$\hbar = 6.582\,122\,02 \times 10^{-16}\,\mathrm{eVs}$
Electron mass	$m_{\mathrm{e}} = 9.109\,389\,754 \times 10^{-31}\,\mathrm{kg}$
Electron mass in eV	$m_{\mathrm{e}} = 510\,999.0615\,\mathrm{eV}$
Proton mass	$m_{\mathrm{e}} = 1.672\,623\,11 \times 10^{-27}\,\mathrm{kg}$
Proton mass in eV	$m_{\mathrm{e}} = 938\,272\,312.8\,\mathrm{eV}$
Boltzmann constant	$k_{\mathrm{B}} = 1.380\,658\,12 \times 10^{-23}\,\mathrm{JK^{-1}}$
Boltzmann constant	$k_{\mathrm{B}} = 8.617\,385\,73 \times 10^{-5}\,\mathrm{eVK^{-1}}$
Stefan-Boltzmann constant	$\sigma_{\mathrm{SB}} = 5.670\,511\,9 \times 10^{-8}\,\mathrm{Wm^{-2}K^{-4}}$
Hyperfine structure constant	$\alpha = 1/137.035999679$
Thomson scattering cross-section	$\sigma_{\mathrm{T}} = 0.665\,245\,855\,8\,\mathrm{m^2}$

Units

Throughout we basically take the God-given natural units where the speed of light and the reduced Planck constant are set to be unity, $c = \hbar = 1$.

Metric

Also, we will use the God-given natural units Our metric signature is $(-,+,+,+)$, i.e. $diag(-1,1,1,1)$ for the Minkowski spacetime. The indices of Greek alphabets like μ,ν,ρ,λ,... will take the values from 0 to 3 and of Latin alphabets like i, j, k, l,... stand for the values from 1 to 3.

Fourier convention

We take the following Fourier convention,

$$\mathcal{R}_{\mathbf{k}} = \int \mathrm{d}^3\mathbf{x}\mathcal{R}(\mathbf{x})e^{-i\mathbf{k}\cdot\mathbf{x}}. \tag{1}$$

In line with this convention, the inverse Fourier transform is given by

$$\mathcal{R}(\mathbf{x}) = \int \frac{\mathrm{d}^3\mathbf{k}}{(2\pi)^3}\mathcal{R}_{\mathbf{k}}e^{i\mathbf{k}\cdot\mathbf{x}}. \tag{2}$$

Astronomical Units/Constants and Cosmological Parameters

Astronomical unit	$1AU = 1.495\,978\,707\,00 \times 10^{11}\,\mathrm{m}$
Jansky	$1\mathrm{Jy} = 1 \times 10^{-26}\,\mathrm{Wm^{-2}Hz^{-1}}$
parsec	$1\mathrm{pc} = 3.085\,677\,580\,7 \times 10^{16}\,\mathrm{m}$
Solar mass	$M_\odot = 1.9884 \times 10^{30}\,\mathrm{kg}$
Equatorial Solar radius	$R_\odot = 6.9551 \times 10^{8}\,\mathrm{m}$
Solar luminosity	$L_\odot = 3.8427 \times 10^{26}\,\mathrm{W}$
Earth mass	$M_\oplus = 5.9722 \times 10^{24}\,\mathrm{kg}$
Equatorial Earth radius	$R_\oplus = 6.378\,137 \times 10^{6}\,\mathrm{m}$
Hubble constant	$H_0 = 100h\ \mathrm{kms^{-1}Mpc^{-1}}$
Dimensionless hubble constant	$h = 0.6736$
Present critical density	$\rho_{\mathrm{c},0} = 2.77536627 \times 10^{11} h^2 M_\odot \mathrm{Mpc}^{-3}$
Baryon denisty param.	$\Omega_{\mathrm{b}} h^2 = 0.02237$
CDM density param.	$\Omega_{\mathrm{c}} h^2 = 0.1200$
Matter density param.	$\Omega_{\mathrm{m}} h^2 = 0.1430$
Radiation density param.	$\Omega_{\mathrm{r}} h^2 = 4.155 \times 10^{-5}$
Λ density param.	$\Omega_\Lambda = 0.6847$
Amp. of (Fiducial) Primorial power spectrum	$A_\zeta^{\mathrm{CMB}} = 2.100 \times 10^{-9}$
Amp. of Matter density perturbation	$\sigma_8 = 0.8111$
Spectral index	$n_{\mathrm{s}} = 0.9649$
CMB Optical depth	$\tau = 0.0544$
Reionization redshift (mid-point)	$z_{\mathrm{re}} = 7.67$
Age of Universe	$t_0 = 13.797\mathrm{Gyr}$

Notes

Here we adopt the best-fit values from the Planck 2018 observation data (TT, TE, EE + lowE+lensing) for cosmological parameters [1]. It should be noted that this value depends on the cosmology model, and the ΛCDM model is assumed here. Since the two types of primordial power spectrum will be introduced in this thesis, we call the fiducial one as $\mathcal{P}_\zeta^{\mathrm{CMB}}$ and the amplitude as $\mathcal{A}_\zeta^{\mathrm{CMB}}$ because this value is derived by the CMB observation by Planck.

Chapter 1

Introduction

Our universe has rich hierarchical structures that span more than 15 orders of magnitude, from Earth-like planets ($\sim 10^7$m) to galaxy clusters ($\sim 10^{22}$m). The seeds of such hierarchical structures are called primordial scalar perturbations. Thanks to the advancement of cosmological observations, the understanding of the seeds has greatly improved. In particular, the precise measurement of Cosmic microwave background (CMB) by the Planck mission has been achieved to measure the primordial curvature perturbations with surprising accuracy through the observation of the CMB anisotropies. The observation result tells us several statistical features of the perturbation, such as the variance and the scale invariance. Besides, combining the detailed galaxy surveys, it is confirmed that these statistical features appear on larger scales than 1 Mpc. Also, the surprising agreement of the prediction from the simple inflation mechanism with these observed features strongly supports the inflationary scenario. Then what is going on on smaller scales?

In this chapter, we begin with a brief introduction to inflationary cosmology. After that, we introduce the primordial perturbations on large and small scales. We also introduce their current limit. Lastly, we clarify their standpoint in this thesis.

1.1 Inflationary cosmology on global scales

First of all, in cosmology, there is an underlying assumption, so-called *cosmological principle* indicating the homogeneity and isotropy of the Universe on quite large scales, ($\gtrsim$ 1Gpc). Combining this principle and general relativity, one can describe the evolution of the Universe with only one time-dependent parameter, the scale factor. Actually, in 1929, the expansion of the Universe, i.e., Hubble law, is confirmed through observations of Cepheid variables [2]. The principle was also confirmed in 1965 through the accidental discovery of the CMB by A. Penzias and R. Wilson [3]. Such expanding Universe can be expressed so-called Friedmann-Robertson-Walker (FRW) metric, which describes the evolution of the Universe only through the time evolution of the scale factor. Then the evolution of the Universe is controlled by the Einstein equations.

1.2 Cosmological perturbations on local scales

Let us move on to the cosmology on local scales($\lesssim$ 1Gpc). Although the *cosmological principle* is quite potent on larger scales, one can easily verify that the Universe is not isotropic locally through, e.g., numerous galaxies surrounding us. Furthermore, in 1989 the *COsmic Background Explorer (COBE)* discovered the CMB temperature anisotropy on small scales [4]. To explain these anisotropies and inhomogeneities, one needs to study perturbations in the Universe. Then the cosmological perturbation theory is quite advantageous, allowing us to solve the time evolution of perturbations. Many studies have developed the theory and the application to the structure formation and CMB fluctuations. Especially the advance of the theory for CMB temperature fluctuations is remarkable in qualitative and quantitative aspects. In 1967, R.K. Sachs and A.M. Wolfe estimated CMB temperature fluctuations induced by gravitational potentials through the gravitational redshift effect, which is called Sachs-Wolfe effects [5]. In 1968, J. Silk succeeded in finding that the CMB fluctuation is exponentially suppressed on small scales ($\lesssim$ 1Mpc) due to the diffusion of photons gradually decoupling with baryons, which is called Silk damping [6]. In 1995, W. Hu and N. Sugiyama provided an analytic approach to estimate CMB fluctuations quite accurately [7]. Thanks to these pioneering works, the community of CMB measurements became able to predict CMB temperature fluctuations precisely from primordial perturbations. Inversely, by comparing this prediction with the observed data, one can research the amplitude or features of the primordial perturbation. The latest CMB observational data by the *Planck* satellite reveals that the amplitude of the primordial power spectrum is about 10^{-9}, and the shape is almost scale-invariant [1]. Then where do such primordial perturbations come from?

1.3 Primordial perturbations from inflation era

In standard cosmology, it is believed that primordial scalar perturbations originate from quantum fluctuations of the scalar field, which drives inflation, an accelerated expansion that occurred in the very early stage of the Universe. The benefits of introducing an inflationary scenario are not only resolving the problems of the conventional big bang cosmology, e.g., the Horizon problem, the flatness problem, and the monopole problem but also generating initial seeds of the “design" of the late-time Universe.

There are countless amounts of models to derive inflation. Among them, the most simple inflationary scenario must be based on the slow-roll inflation by a single scalar field called inflaton [8]. This scenario anticipates the statistical features for the primordial scalar perturbations, which are almost scale-invariant, adiabatic, and Gaussian. The high sensitivity of the *Planck* satellite made it possible to observe CMB anisotropies precisely and investigate the statistical features of the primordial power spectrum. Surprisingly, the observed features in the Planck measurement correspond to the theoretical prediction by the single field slow-roll inflation [9]. Combining the large-scale structures (LSS) surveys and the Lyman-α observations by, e.g., the Sloan Digital Sky Survey (SDSS) with the Planck result, it is confirmed that primordial power spectrum has the statistical features on large scales, $k \lesssim$ 1Mpc. Then, how about the features on scales smaller than 1Mpc?

1.3.1 Primordial small-scale perturbations

The small-scale perturbations would also originate from the quantum fluctuation of inflaton. Primordial perturbations in different scales would be created at different periods during inflation. Therefore, exploring the smaller-scale perturbations is also crucial for understanding the detailed inflationary mechanism. The statistical features verified on large scales may not be valid on small scales. The slow-roll approximation could break at some moment, like ultra slow-roll inflation. Investigations of primordial small-scale perturbations are one of the primary topics among the several observational missions in cosmology.

1.4 Probes to explore primordial small-scale perturbations

It would be challenging to investigate small-scale primordial perturbations because they are strongly affected by dissipation through the Silk damping mechanism or nonlinear effects associated with the evolution of the Universe. Therefore, it is hard to observe these perturbations directly. However, several ways to indirectly probe the primordial small-scale perturbation have been provided so far. We give a brief review of the indirect probes below. We discuss the detail in Chapter 3.

1.4.1 CMB spectral distortion

In this context, CMB spectral distortion would be the most robust probes [10]–[12]. Although the small-scale perturbations are smoothed out due to the Silk damping, as mentioned before, the energy dissipated in the process of the Silk damping flows into CMB and creates the distortions from the blackbody spectrum in the CMB energy spectrum [13]–[15]. Hence, measurements of the CMB distortion allow us to understand the small-scale perturbations more [14], [16]–[19]. In fact, from the measurements of CMB distortion by COBE/FIRAS [20], the constraint on the amplitude of the primordial power spectrum, $\mathcal{A}_\zeta \lesssim 10^{-5}$ for the wave number range, $k \approx 1 - 10^4$ Mpc^{-1} was suggested in Ref. [16]. Furthermore, they also mention that in the next-generation CMB measurements like *Primordial Inflation Explorer (PIXIE)*[1] [29], [30], which will allow us to know the CMB distortion very precisely, e.g., at levels of $\mu \sim 10^{-8}$. If no distortion with $\mu > 2 \times 10^{-8}$ is discovered, the constraint would improve in order of $P_\zeta \lesssim 10^{-8}$, which immediately rule out many inflationary models enhancing small-scale perturbations at $k \simeq 10 - 10^4$Mpc^{-1}. On the other hand, it must be more interesting if μ-distortion is detected. That would suggest that the inflation mechanism diverges from the slow-rolling at some moment. The green-shaded region and green dashed line in Fig. 1.1 show the constraints through the measurements of CMB spectral distortion.

1.4.2 Primordial black hole

A primordial black hole (PBH) is a black hole that could have been formed in the early Universe. Although several formation scenarios have been proposed, the original and most extensively discussed is the formation through a gravitational collapse of an over-dense region in the radiation-dominated (RD) Universe after inflation [33], [34].

When an overdense region with somehow highly enhanced primordial scalar perturbations enters the horizon scale, the gravitational collapse of this region will happen to form a PBH. The resultant mass of the formed PBH corresponds to the horizon mass at the horizon-crossing epoch of the overdense region. As a result, the PBH mass range can span very widely. Therefore, studies of the abundance of PBHs in the broad mass range lead us to explore the primordial scalar perturbations in various small scales. The current status for the investigation of the PBH abundance is as follows.

For small-mass PBHs, the abundance can be constrained by the effects of their evaporation. As first pointed out by Hawking [35], a black hole emits many kinds

---

[1] The *PIXIE* project was not selected and stopped now. There are other plans of ground-, balloon-, and space-based CMB distortion detectors such as e.g., APSERa [21], COSMO,OLIMPO [22], [23], BISOU [24], PRISM [25], PRISTINE [26], SuperPIXIE [27] and Voyage2050 [28]. However, all of these projects has not been funded yet.

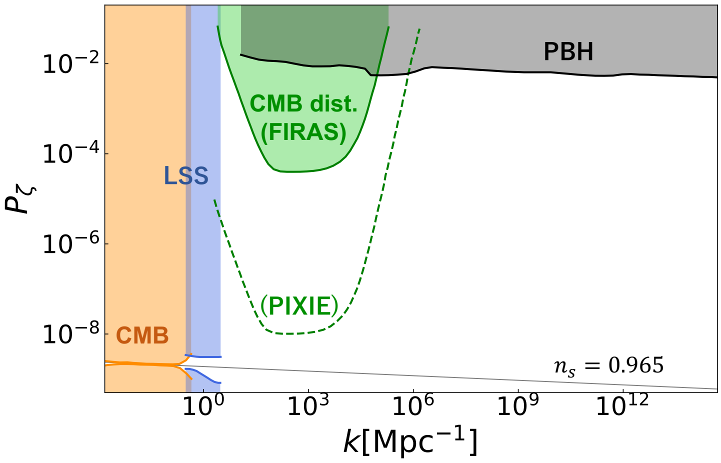

FIGURE 1.1: Constraint on the primordial power spectrum on wide scales. The orange-shaded region represents current constraints on the primordial power spectrum through measurements of the CMB anisotropy [1], and the blue-shaded region shows the one through measurements of the LSS, especially the Lyman-α forests [148]. The green-shaded region and green dashed line represent the constraints through measurements of the CMB distortion especially, μ-distortion by COBE/FIRAS and PIXIE respectively (see Ref. [31] for more detail). The black-shaded region shows the constraints through the investigation of primordial black holes (PBHs). The grey line shows the one of primordial power spectrum allowed through current measurements with the spectral index, $n_s = 0.965$.

of particles with the thermal spectrum. As a result, PBHs with a mass smaller than 10^{15} g have evaporated by the present epoch. The abundance constraint on evaporated PBHs is obtained by investigating the effect of their evaporation on big bang nucleosynthesis [36], the CMB spectrum distortion [37], the recombination and reionization processes [38], [39], and the diffuse gamma-ray background [40]–[42].

For nonevaporated PBHs, the robust constraint is provided by gravitational lensing observations [43]–[45]. The black hole merger rate evaluated from the recent detection of gravitational wave (GW) events also limits their abundance [46], [47]. Recently several works focused on the gas accreting on massive PBHs. Because of the release of the gravitational energy during accretion, the gas becomes hot and emits x-ray and UV photons [48]–[50]. Resultantly the surrounding gas around a PBH is heated and ionized. Studying the cosmological effects of such heating and reionization provides the constraint on stellar mass PBHs with the recent CMB measurement [48]–[51]. Also, several works suggest that future 21-cm observations can probe these PBH heating and ionizing processes and strongly constrain the massive PBH abundance [52], [53].

These constraints are summarized in Fig. 1.2 and can be converted to the limit on the primordial power spectrum as shown in the black-shaded region in Fig. 1.1. Note that since the PBH must be a rare object due to its nature as dark matter (DM), measurements of the PBH abundance are not powerful for getting information on primordial perturbations. We will discuss the detail in Sec. 3.2.

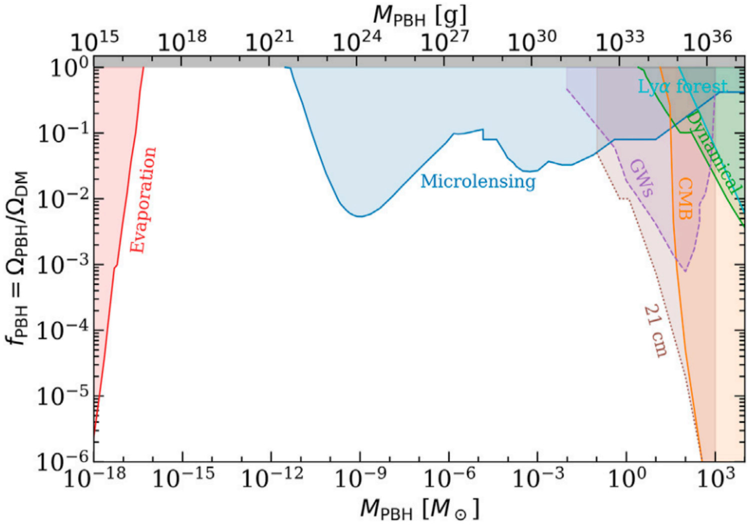

FIGURE 1.2: Compilation of constraints on the PBH fraction concerning DM as a function of the PBH mass, with a monochromatic mass function. The plotted constraints come from: the effects of PBH evaporation [36], [38] (red); nondetection of microlensing events by several projects [43], [54]–[58] (blue); PBH accretion signatures on the CMB [59] (orange); dynamical constraints [60], [61](green); power spectrum from the Lyα forest [62] (cyan); PBH merger rates from gravitational waves [63]–[65] (purple). The dotted brown line corresponds to predictions from the 21-cm power spectrum and 21-cm forest with SKA sensitivities [66], [67]. This figure is taken from Ref. [68].

1.4.3 Galaxies and small-mass halos

So far, we have greatly archived to obtain the primordial power spectrum on large scales from the measurements of large-scale structures. In the same way, one could obtain information about the smaller-scale perturbations through measurements for smaller objects like galaxies or small-mass halos.

One of the potent observables would be the UV Luminosity Function (LF) of high redshift galaxies. The UV galaxy LF contains a wealth of information on the physics of cosmological structure formation at small scales. Recently Ref. [69] proposed a unique approach using high-redshift UV galaxy LF data to probe small-scale perturbations. As another clue for exploring primordial small-scale perturbations, small-mass DM halos would be also important. In Ref. [70], we studied the free-free emission from DM halos in the standard ΛCDM cosmology. We explain the detail in Chapter 4.

1.4.4 Ultracompact minihalos

Ultracompact minihalos (UCMHs) are gravitational objects formed by denser regions induced by the excess power of primordial small-scale perturbations [71]. The formation mechanism seems similar to the one of PBHs. However, in the UCMH case, the density perturbation does not collapse immediately after the horizon entry. From the perturbative Boltzmann equations, it is known that perturbations of DM fluid would evolve gravitationally in the matter-dominated (MD) epoch and also the radiation-dominated (RD) epoch. Therefore, with an enhanced power in primordial perturbations at some scales, the perturbations would reach the threshold to collapse earlier than the ones on other scales through gravitational evolution. The resultant early-formed DM halos are so-called UCMHs. Although there is no smoking gun observed events to confirm the existence of UCMHs[2], they can be a significant cosmological probe of primordial perturbation, especially in smaller scales, $k \gtrsim 1\mathrm{Mpc}^{-1}$.

For example, through the gravitational growth in the RD epoch, it would be possible to form UCMHs at an early era like $z \sim 1000$ as long as the initial density contrast is large enough. That is an original idea of the UCMH formation process. Ref. [71] theoretically points out that UCMHs have a more compact profile with a larger central density than typical DM halos through the radial infalling in high redshift. After that, Refs. [72], [73] performed the cosmological simulation of the UCMH formation for the spike-type power spectrum on small scales. They revealed that the excess power of small-scale primordial scalar perturbation actually leads to the form of UCMHs, which have a DM density profile steeper than standard DM halos.

Through the steepness of their density profile, the energetic emission from DM self-annihilation inside UCMHs has been studied well. With the present gamma-ray and CMB observations, the abundance of UCMHs is significantly constrained [72]–[78]. Accordingly, primordial perturbations as the seed of UCMHs are also constrainted [74]–[76].

1.5 Aim of this thesis

Under the history mentioned above, we deeply study the primordial small-scale perturbation in this thesis. There are mainly two aims of this thesis,

1. To summarize the present status of observational constraint on the primordial small-scale perturbations in detail,
2. To show our new directions to approach the small-scale perturbations.

Although we briefly review their several probes and the references which would most gather attention in each context, we revisit these probes more qualitatively through the observational aspect of the present constraint in Chapter. 3. For example, although measuring CMB distortion would be the most robust way to explore them, there are no funded projects for CMB distortion right now. Investigations of PBHs have proceeded well, which gives the weak constraint for the amplitude of primordial small-scale perturbations from their no-detection. Also, UCMHs have been studied well through their energetic emission from DM annihilation inside UCMHs. However, these works highly depend on the nature of DM. Then we focus on small-mass DM halos and UCMHs and propose three ideas to approach the primordial small-scale perturbations.

First, we suggest that measurements of free-free emission from the DM halos could be a powerful probe for the perturbations. As the LSS distribution indicates the large-scale matter density perturbations, measurements for smaller objects would provide information about the smaller-scale matter density perturbations. The matter density perturbations can be converted to primordial ones by considering their relation and evolution, i.e., the transfer function. Although our predicting signal for the free-free emission is smaller than the observed signal, we find that the free-free emission signal is significantly sensitive to the primordial small-scale perturbations.

---

[2] The James Webb Telescope (JWST) launched in 2022 by NASA, has reported that they detected candidates of high-redshift galaxies more than expected in the standard theory. That might suggest the existence of UCMHs.

Second, we present that measurements of 21-cm line emission/absorption background induced by UCMHs can give information on the perturbations. Depending on the mass of UCMH, it can host abundant neutral hydrogen gas regardless of the nature of DM. We show that the upcoming 21-cm observation can provide a stringent limit on the abundance of UCMHs and the amplitude of the primordial perturbations.

Third, we suggest that measurements of astrophysical effects that occurred in UCMHs, e.g., the formation of first-generation stars, would be powerful probes for the perturbations. UCMHs could host first-generation stars like the halos formed in the standard structure formation scenario. Such stars would emit abundant ionizing photons during their main sequence, which boosts the cosmic reionization process in higher redshifts. We discuss their effects on the global cosmic reionization history with Planck’ s CMB anisotropy observation data.

1.6 Structure of this thesis

The rest parts of this thesis are organized as follows. In Chapter 2, we explain the primordial perturbations, how the perturbations evolve, and how the perturbations relate to the observables in the Universe through the cosmological linear perturbation theory and the formation formalism of the gravitationally collapsed objects. In Chapter 3, we revisit the probes to explore primordial small-scale perturbations while adding qualitative and quantitative discussion. In the second half of this thesis, we propose three new directions to probe primordial small-scale perturbations. In Chapter 4, we show that measurements of the free-free emission from the DM halos are potent to investigate primordial small-scale perturbations. In Chapter 5, we explain our second direction related to the 21cm-line emission anisotropy induced by the UCMHs. In Chapter 6, we discuss the potential of measuring the astrophysical effect in UCMHs for exploring primordial small-scale perturbations. Lastly, in Chapter 7, we conclude this thesis.

Chapter 2

Cosmological Perturbations and Structure Formation

Although the Universe is globally homogeneous and isotropic, it is trivially known that there locally exists inhomogeneous structures consisting of countless gravitational collapsed objects through the observation of, e.g., local environment such as the solar system, Milky Galaxy, and so on. Recent cosmological observations like CMB show that these inhomogeneities are in order of 10^{-5}. Thus linear perturbations theory around a homogeneous background is effective for their analysis.

It is also noted that the observed inhomogeneities have specific features compatible with the simple inflation mechanism. In the inflationary scenario, the quantum fluctuations of inflaton can produce primordial fluctuations.

This chapter presents the famous calculation of the primordial fluctuation spectra generated by quantum fluctuations during inflation, especially slow-roll single-field inflation. We first briefly review the fundamental aspects of cosmological perturbation theory. After that, we give a qualitative summary of the basic mechanism by which inflation converts microscopic quantum fluctuations into macroscopic seeds for cosmological structure formation.

2.1 Cosmological perturbations

In this section, we present the calculation in cosmological linear perturbation theory with the primordial fluctuations originating from quantum fluctuations during inflation. Firstly, we introduce the cosmological linear perturbation theory and inflaton scalar field as the matter sector. Secondly, we derive the feature of the seeds with the belief that the quantum fluctuations of inflaton create the seeds. Lastly, we demonstrate the feature corresponds to the observed one.

Here, the perturbation of X is defined as

$$\delta X(t, \mathbf{x}) \equiv X(t, \mathbf{x}) - \bar{X}(t). \tag{2.1}$$

Note that the background value depends only on time (not on spatial coordinates) as the background metric, FRW metric, indicates,

$$\mathrm{d}s^2 = -\mathrm{d}t^2 + a^2(t)\left[\frac{\mathrm{d}r^2}{1-Kr^2} + r^2(d\theta + \sin^2\theta d\phi)\right], \tag{2.2}$$

where $a(t)$ is the scale factor as a function of cosmic time t, and K represents the spatial curvature.

In the cosmological linear perturbation theory, one of the main topics considered here is to solve the Einstein equation,

$$G^{\mu}_{\ \nu} + \Lambda \delta^{\mu}_{\ \nu} = 8\pi G T^{\mu}_{\ \nu}, \tag{2.3}$$

expanding at the linear order and to understand these consequences. Since we know that the perturbations are tiny, $\delta X \ll \bar{X}$, this expanding Einstein Equations at linear order in perturbations approximates the full non-linear solution with very high accuracy.

Before moving to the linear order calculation of the Einstein equation, let me briefly introduce and calculate the Einstein equation at the background level.

2.2 Background level

The Einstein equation at the background level can be written by

$$\bar{G}^{\mu}_{\ \nu} + \Lambda \delta^{\mu}_{\ \nu} = 8\pi G \bar{T}^{\mu}_{\ \nu}. \tag{2.4}$$

Let me separate Eq. (2.4) into the left-hand side (Geometric side) and the right-hand side (Matter side) and consider them in order.

2.2.1 Background level - Geometric side -

The metric of the Universe at the background level is the so-called FRW metric, as mentioned in Eq. (2.2). Even if the spatial curvature exists initially in the inflation epoch, it will disappear due to the exponential expansion. Therefore, we will neglect the curvature parameter K hereafter.

With the use of conformal time instead of cosmic time and Cartesian coordinates for the space, the FRW metric $\bar{g}_{\mu\nu}$ can be written by

$$\bar{g}_{00} = -a^2, \quad \bar{g}_{0i} = \bar{g}_{i0} = 0, \quad \bar{g}_{ij} = a^2 \gamma_{ij}. \tag{2.5}$$

Then the connection coefficients, so-called Christoffel symbols, are given by

$$\begin{aligned} &\bar{\Gamma}^0_{00} = \mathcal{H}, \quad \bar{\Gamma}^0_{0i} = \bar{\Gamma}^0_{i0} = \bar{\Gamma}^i_{00} = 0, \quad \bar{\Gamma}^0_{ij} = \gamma_{ij}\mathcal{H}, \\ &\bar{\Gamma}^i_{0j} = \bar{\Gamma}^i_{j0} = \delta^i_{\ j}\mathcal{H}, \quad \bar{\Gamma}^i_{jk} = \frac{1}{2}\gamma^{il}(\gamma_{lk,j} + \gamma_{jl,k} - \gamma_{jk,l}). \end{aligned} \tag{2.6}$$

From the above Christoffel coefficients, the Ricci tensor at the background level is given by

$$a^2 \bar{R}^0_{\ 0} = -3\mathcal{H}', \tag{2.7}$$

$$a^2 \bar{R}^0_{\ i} = 0, \tag{2.8}$$

$$a^2 \bar{R}^i_{\ j} = \delta^i_{\ j} \left(2\mathcal{H}^2 + \mathcal{H}'\right), \tag{2.9}$$

and subsequently the background Ricci scalar is written by

$$\bar{R} = \frac{6}{a^2}\left(\mathcal{H}^2 + \mathcal{H}'\right). \tag{2.10}$$

Therefore, the background Einstein tensor is written by

$$a^2\bar{G}^0_{\ 0} = -3\mathcal{H}^2, \tag{2.11}$$

$$a^2\bar{G}^i_{\ 0} = a^2\bar{G}^0_{\ i} = 0, \tag{2.12}$$

$$a^2\bar{G}^i_{\ j} = \delta^i_{\ j}\left(\mathcal{H}^2 + 2\mathcal{H}'\right). \tag{2.13}$$

2.2.2 Background level - Matter side -

Let me move on to the matter side. Since our interesting epoch is inflation, inflaton ϕ would play the role of the dominant component as "matter." In that case, the action is given by

$$S = \int \mathrm{d}^4x\sqrt{-g}\left[\frac{1}{2}R - \frac{1}{2}g^{\mu\nu}\partial_\mu\phi\partial_\nu\phi - V(\phi)\right] \equiv S_{\mathrm{EH}} + S_\phi. \tag{2.14}$$

The action of Eq. (2.14) is the sum of S_{EH} which is the Einstein-Hilbert action and S_ϕ which is action of the scalar field, ϕ with a canonical kinetic term.

The stress-energy tensor at the background level for ϕ is estimated by $\bar{\phi}$ like

$$\bar{T}^{(\phi)}_{\mu\nu} \equiv -\frac{2}{\sqrt{-g}}\frac{\delta\bar{S}_\phi}{\delta\bar{g}^{\mu\nu}} = \partial_\mu\bar{\phi}\partial_\nu\bar{\phi} - \bar{g}_{\mu\nu}\left(\frac{1}{2}\partial^\lambda\bar{\phi}\partial_\lambda\bar{\phi} + V(\bar{\phi})\right), \tag{2.15}$$

where $\delta X/\delta Y$ denotes the functional derivative of X by Y.

Let us decompose the scalar field ϕ into the background and perturbative component,

$$\phi(t, \mathbf{x}) = \bar{\phi}(t) + \delta\phi(t, \mathbf{x}). \tag{2.16}$$

Then the background component of Eq. (2.15) reads,

$$\bar{T}^{0(\phi)}_{\ 0} = -\frac{1}{2a^2}\bar{\phi}'^2 - V(\bar{\phi}) = -\bar{\rho}_\phi, \tag{2.17}$$

$$\bar{T}^{i(\phi)}_{\ 0} = \bar{T}^0_{\ i} = 0, \tag{2.18}$$

$$\bar{T}^{i(\phi)}_{\ j} = \delta^{i(\phi)}_{\ j}\left[\frac{1}{2a^2}\bar{\phi}'^2 - V(\bar{\phi})\right] = \delta^i_{\ j}\bar{p}_\phi. \tag{2.19}$$

Here we link each components of $T^{\mu\ (\phi)}_{\nu}$ to the energy and pressure density of $\bar{\phi}$. We explain the general discussion of the stress-energy tensor in the Appendix A.

2.2.3 Consequences at background level

Combining Eqs. (2.11) to (2.13) and Eqs. (2.17) to (2.19), one can obtain following two equations,

$$\mathcal{H}^2 = \frac{8\pi G}{3}\left(\frac{\bar{\phi}'^2}{2} + a^2V_{,\phi}\right) + \frac{\Lambda a^2}{3} = \frac{\bar{\rho}_\phi}{3M_{\mathrm{pl}}} + \frac{\Lambda a^2}{3}, \tag{2.20}$$

$$\mathcal{H}^2 + 2\mathcal{H}' - \Lambda a^2 = \frac{\bar{\phi}'^2}{2} - a^2V(\bar{\phi}). \tag{2.21}$$

The first equation is often called *Hubble equation* in the inflationary epoch. The second equation can be rewritten by

$$\mathcal{H}' = \frac{1}{6M_{\mathrm{pl}}}\left(\bar{\rho}_\phi + 3\bar{p}_\phi\right) + \frac{\Lambda a^2}{3}, \tag{2.22}$$

with a pressure density of ϕ, $\bar{p}_\phi = \bar{\phi}'^{\,2}/2 - a^2 V(\phi)$. This is the equation describing the evolution of the Hubble parameter.

2.3 Time evolution of $\bar{\phi}$ and slow-roll condition

Let us here also show the time evolution of ϕ here. With the inflaton's action S_ϕ, the equation of motion for ϕ is given by

$$\frac{\delta S_\phi}{\delta \phi} = \frac{1}{\sqrt{-g}}\partial_\mu\left(\sqrt{-g}\partial^\mu \phi\right) + V_\phi = 0, \tag{2.23}$$

where V_ϕ denotes $dV/d\phi$. In the background spacetime, Eq. (2.23) reads

$$\bar{\phi}'' + 2\mathcal{H}\bar{\phi}' + a^2 V_\phi = 0, \tag{2.24}$$

thus with respect to cosmic time t, one can obtain

$$\ddot{\phi} + 3H\dot{\phi} + V_{,\phi} = 0. \tag{2.25}$$

This equation equals the one of point mass which one-dimensionally moves in some potential while receiving friction proportional to the velocity. Thus if V_ϕ is too small, the value of the inflaton's scalar field would change very slowly during the exponential expansion of the Universe. Then the friction term represented in the second term of Eq. (2.25) would be larger than the acceleration term in the first term, which reads,

$$\dot{\bar{\phi}} \simeq -\frac{1}{3H}V_\phi. \tag{2.26}$$

The requirements for this approximation in Eq. (2.26) are following two conditions,

$$\dot{\bar{\phi}}^2 \ll 2V(\phi), \quad |\ddot{\bar{\phi}}| \ll 3H|\dot{\bar{\phi}}|, \tag{2.27}$$

which are often called *slow-roll conditions*. Adopting this slow-roll condition to Eqs. (2.20) and (2.22), one can approximately obtain,

$$H^2 \simeq \frac{8\pi G}{3}V, \tag{2.28}$$

and

$$\dot{H} = -4\pi G\dot{\phi}^2. \tag{2.29}$$

Here we neglect the cosmological constant term. Combining Eqs. (2.28) and (2.29) read

$$\frac{\dot{H}}{H^2} \simeq -\frac{3\dot{\phi}^2}{2V} \ll 1. \tag{2.30}$$

The second time derivative of ϕ in the slow-roll approximation is given by

$$\ddot{\phi} \simeq -\frac{\dot{\phi}}{3H} V_{\phi\phi} - \frac{\dot{\phi}^2}{2V} V_{\phi}, \tag{2.31}$$

from the time derivative of Eq. (2.25). Through Eqs. (2.30) and (2.31), one can rewritten the slow-roll condition as

$$\epsilon \ll 1 \qquad \eta \ll 1, \tag{2.32}$$

introducing two *slow-roll parameters*,

$$\epsilon = \frac{1}{16\pi G}\left(\frac{V_{\phi}}{V}\right)^2, \quad \eta = \frac{1}{8\pi G}\frac{V_{\phi\phi}}{V}. \tag{2.33}$$

2.4 Linear level

Then let us turn next to the discussion of the Einstein equation at the linear perturbation level. In the linear perturbation theory, some difficulties will be accompanied by the fact that the split into background and perturbations defined by Eq. (2.1) is not unique but depends on the choice of coordinates, which is so-called the gauge choice. We begin with the introduction of the gauge problem.

2.4.1 Gauge choice

When one considers the perturbation theory, there is one problem that one needs to take into account properly, which is *Gauge choice*. That is because the definition of perturbations represented in Eq. (2.1) is not unique, but depends on the choice of the coordinates of perturbed spacetime.

There are mainly two routes to avoid this problem. The first is to choose some gauge and drop two non-physical degrees of freedom. The second one is to discuss with only use of variables which do not depend on the gauge choice.

We want to discuss the gauge invariant physical quantities while we would like to drop the degrees for easier calculations. To do that, we first begin with calculations without the gauge fix and find the gauge invariant quantities. After that, we set the conformal Newtonian gauge to make the calculation more painless.

2.4.2 Scalar, Vector and Tensor perturbations

Thanks to a great deal of symmetry possessed by the homogeneous and isotropic background spacetime, one can decompose the metric and the stress-energy perturbations into a scalar, vector, and tensor components independently. That is called the SVT decomposition and is easily described in Fourier space. In Fourier space, the variable $X(t, \boldsymbol{x})$ is expressed by

$$X_{\mathbf{k}}(t) = \int \mathrm{d}^3\mathbf{x} X(t, \mathbf{x}) e^{-i\mathbf{k}\cdot\mathbf{x}}. \tag{2.34}$$

Here the variable X shows for instance, $\delta\phi$, $\delta g_{\mu\nu}$, and so on. Note that perturbations of the different Fourier modes do not mix due to translation invariance. We see this proof in Appendix **??**. Then we consider rotations around a Fourier mode. Under rotation of the coordinate system around the wavevector by an angle ψ, the amplitude of perturbations would change in different ways corresponding to their helicity

m as

$$X_{\mathbf{k}} \to e^{im\phi} X_{\mathbf{k}}. \tag{2.35}$$

The helicity values for scalar, vector, and tensor perturbations are different, like 0, ±1, and ±2, respectively, which indicates that one can independently calculate each type of perturbation's evolution. This SVT decomposition makes the study of cosmological perturbations extremely simplified. Note that this decomposition holds only in the linear order, not the higher-order perturbation theory. The scalar-induced GW is one example of the mixing of different types of perturbations. In this case, the gauge issue would be more problematic (see Refs. [79], [80] for the detail).

Upon understanding these general remarks, let us now move on to the linear perturbation theory around the homogeneous and isotropic FRW Universe.

2.4.3 Inhomogeneous Universe

The Einstein equation expanding in linear order is written by

$$\delta G^{\mu}_{\ \nu} = 8\pi G \delta T^{\mu}_{\ \nu}. \tag{2.36}$$

With the above general statements, we find gauge invariant variables on the left-hand side and right-hand side of Eq. (2.36).

2.4.4 Gauge transformation - Metric perturbations -

Let us consider the left-hand side of Eq. (2.36), which is about the metric side in linear order. In general, the spacetime metric can be written by

$$g_{\mu\nu} = \bar{g}_{\mu\nu} + h_{\mu\nu}, \tag{2.37}$$

where $\bar{g}_{\mu\nu}$ represents the homogeneous and isotropic background component(called background spacetime), and $h_{\mu\nu}$ shows the other inhomogeneous but still an isotropic component, called perturbed spacetime. In the cosmological literature, the spatially-flat FRLW metric is often adopted for the back ground spacetime,

$$\bar{g}_{\mu\nu} = a(\tau)^2 \begin{pmatrix} -1 & 0 & 0 & 0 \\ 0 & 1 & 0 & 0 \\ 0 & 0 & 1 & 0 \\ 0 & 0 & 0 & 1 \end{pmatrix}, \tag{2.38}$$

and whose line element can be written by

$$ds^2 = a^2(\tau)\left(-d\tau^2 + \delta_{ij} dx^i dx^j\right). \tag{2.39}$$

On the other hand, the metric of the perturbed spacetime, $h_{\mu\nu}$ is given by

$$h_{\mu\nu} = 2a(\tau)^2 \left(\begin{array}{c|ccc} -A & B_1 & B_2 & B_3 \\ \hline B_1 & & & \\ B_2 & & C_{ij} & \\ B_3 & & & \end{array}\right), \tag{2.40}$$

in the most general form. Then the line element of the Universe can be written by

$$ds^2 = a^2(\tau)\left[-(1+2A)d\tau^2 - 2B_i d\tau dx^i + \left(\delta_{ij} + 2C_{ij}\right)dx^i dx^j\right]. \tag{2.41}$$

In real space, thanks to the SVT decomposition, the $h_{\mu\nu}$ metric perturbations are decomposed like

$$B_i \equiv \partial_i B^{(S)} - B_i^{(V)}, \quad \text{where} \quad \partial^i S_i = 0, \tag{2.42}$$

and

$$C_{ij} \equiv \delta_{ij} D + \partial_{ij} E^{(S)} + 2\partial_{(i} E_{j)}^{(V)} + E_{ij}^{(T)}, \quad \text{where} \quad \partial^i E_i^{(V)} = 0, \quad \left(E^{(T)}\right)^i_i = \partial^i E_{ij}^{(T)} = 0. \tag{2.43}$$

Here we define that

$$B^i \equiv \gamma^{ij} B_j, \quad C^i{}_j \equiv \gamma^{ik} C_{kj}, \quad C_i{}^j \equiv \gamma^{jk} C_{ik}, \quad C^{ij} \equiv \gamma^{ik}\gamma^{jl} C_{kl}. \tag{2.44}$$

Since we are interested in scalar perturbations in this thesis, the component of scalar type in metric would be given by

$$g_{\mu\nu}^{(S)} = a(\tau)^2 \begin{pmatrix} -(1+2A) & \partial_j B^{(S)} \\ \partial_i B^{(S)} & (1+2D)\delta_{ij} + 2\partial_i\partial_j E^{(S)} c \end{pmatrix}, \tag{2.45}$$

and

$$(g^{\mu\nu})^{(S)} \simeq \frac{1}{a(\tau)^2} \begin{pmatrix} -1+2A & \partial^j B^{(S)} \\ \partial^i B^{(S)} & (1-2D)\delta^{ij} - 2\partial^i\partial^j E^{(S)} \end{pmatrix}. \tag{2.46}$$

Here the determinant of this metric is given by

$$\sqrt{-g} \simeq -a^8 - 2a^8\left(A + 3D + \nabla^2 E^{(S)}\right). \tag{2.47}$$

Scalar fluctuations will change under a change in the coordinate choice. Let us consider the gauge transformation like

$$x^\mu \to \tilde{x}^\mu = x^\mu + \xi^\mu \qquad \textit{where} \;\; \xi^\mu = (\alpha, +\partial^i\beta). \tag{2.48}$$

Now we assume $|\xi^\mu| \ll 1$. Under this transformation, the metric would be transformed as

$$g_{\mu\nu}(x) \to \tilde{g}_{\mu\nu}(\tilde{x}) = \frac{\partial x^\alpha}{\partial \tilde{x}^\mu}\frac{\partial x^\beta}{\partial \tilde{x}^\nu} g_{\alpha\beta}(x). \tag{2.49}$$

Note that this transformation corresponds to the invariance of the line elements ds^2 under the coordinates transformation. Using Eq. (2.49), one can derive the functional derivative of the metric $g_{\mu\nu}$ at the same spacetime x. In linear approximation, it is given by

$$\begin{aligned} \tilde{g}_{\mu\upsilon}(x) - g_{\mu\nu}(x) &= \tilde{g}_{\mu\nu}(\tilde{x}) - g_{\mu\nu}(x) - \partial_\alpha g_{\mu\nu}(x)\xi^\alpha \\ &= -g_{\mu\alpha}(x)\partial_\nu\xi^\alpha - g_{\nu\alpha}(x)\partial_\nu\xi^\alpha - \partial_\alpha g_{\mu\nu}(x)\xi^\alpha \end{aligned} \tag{2.50}$$

The R.H.S of Eq. (2.50) represents the Lie derivative of $g_{\mu\nu}$ along the $-\xi^{\mu}$. Beneath this coordinate transformation, the scalar metric perturbations alter as

$$\begin{aligned} A &\to A - \mathcal{H}\alpha - \alpha', \\ B^{(S)} &\to B^{(S)} - \alpha + \beta', \\ D &\to D - \mathcal{H}\alpha, \\ E^{(S)} &\to E^{(S)} - \beta. \end{aligned} \tag{2.51}$$

2.4.5 Gauge transformation - Matter perturbations -

Then let us turn next to the right-hand side of Eq. (2.36), which is about the matter side in linear order. The stress-energy tensor for the scalar field, ϕ, is given by (2.15). Following the decomposition of the scalar field, ϕ of Eq. (2.16), the perturbative component in linear order with the metric represented by Eq. (2.41) reads,

$$\begin{aligned} \delta T^{0(\phi)}_{\ \ 0} &= -\frac{\bar{\phi}'}{a^2}\left(\delta\phi' - \bar{\phi}'A\right) - \frac{dV}{d\phi}\delta\phi \\ \delta T^{0(\phi)}_{\ \ i} &= -\frac{\bar{\phi}'}{a^2}\partial_i\delta\phi \\ \delta T^{i(\phi)}_{\ \ 0} &= \frac{\bar{\phi}'}{a^2}\gamma^{ij}\left(\partial_j\delta\phi - \bar{\phi}'\partial_j B^{(S)}\right) \\ \delta T^{i(\phi)}_{\ \ j} &= \delta^i_{\ j}\left[\frac{\bar{\phi}'}{a^2}\left(\delta\phi' - \bar{\phi}'A\right) - \frac{dV}{d\phi}\delta\phi\right] \end{aligned} \tag{2.52}$$

In the same way as Eqs. (2.17) to (2.19), one can find linear perturbative components of the energy density $\bar{\rho}_{\phi}$, the pressure density $\bar{p}_{\phi}$, the velocity $v_{\phi i}$, and the anisotropic stress σ_{ij} of ϕ as

$$\begin{aligned} \delta\rho_{\phi} &= \frac{\bar{\phi}'}{a^2}\left(\delta\phi' - \bar{\phi}'A\right) + \frac{dV}{d\phi}\delta\phi. \\ v_{\phi i} \equiv \partial_i v_{\phi} &= -\frac{\partial_i\delta\phi}{\bar{\phi}'} + \partial_i B^{(S)}, \\ \delta p_{\phi} &= \frac{\vec{\phi}'}{a^2}\left(\delta\phi' - \bar{\phi}'A\right) - \frac{dV}{d\phi}\delta\phi, \\ (\sigma_{\phi})^i_{\ j} &= 0. \end{aligned} \tag{2.53}$$

We explain these correspondence in Appendix A.

Also these matter perturbations are gauge dependent except for $(\sigma_{\phi})^i_{\ j}$. Then these perturbations would be transformed as

$$\begin{aligned} \delta\phi &\to \delta\phi - \bar{\phi}'\alpha, \\ \delta\rho &\to \delta\rho - \bar{\rho}'\alpha, \\ v_{\phi} &\to v_{\phi} + \beta', \\ \delta p &\to \delta p - \bar{p}'\alpha. \end{aligned} \tag{2.54}$$

2.4.6 Gauge invariant quantities

Using the gauge transformations represented in Eqs. Eqs. (2.51) and (2.54), one can readily find the combination to cancel out the gauge dependence, which is called gauge invariant quantities. The examples are as follows:

$$\Phi \equiv A - (B^{(S)} + E^{(S)\prime})' - \mathcal{H}(B^{(S)} + E^{(S)\prime}), \tag{2.55}$$

$$\Psi \equiv D - \mathcal{H}(B^{(S)} + E^{(S)\prime}), \tag{2.56}$$

$$\delta\phi^{(\mathrm{GI})} \equiv \delta\phi - \bar{\phi}' \left(B^{(\mathrm{S})} + E^{(\mathrm{S})'}\right), \tag{2.57}$$

$$\delta^{(\mathrm{GI})} \equiv \delta - \frac{\bar{\rho}'}{\bar{\rho}} \left(B^{(\mathrm{S})} + E^{(\mathrm{S})'}\right) = \delta + 3\mathscr{H}(1+w) \left(B^{(\mathrm{S})} + E^{(\mathrm{S})'}\right), \tag{2.58}$$

$$v_{\phi}^{(\mathrm{GI})} \equiv v_{\phi}^{(\mathrm{S})} + E^{(\mathrm{S})'}, \tag{2.59}$$

and

$$\delta p^{(\mathrm{GI})} \equiv \delta p - \bar{p}' \left(B^{(\mathrm{S})} + E^{(\mathrm{S})'}\right) = \delta p + 3\mathscr{H}\bar{\rho}c_{\mathrm{s}}^2(1+w) \left(B^{(\mathrm{S})} + E^{(\mathrm{S})'}\right), \tag{2.60}$$

where $w \equiv p/w$ is so-called equation of state parameter, and $c_{\mathrm{s}} \equiv \partial p/\partial\rho$ denotes the sound speed.

Among them, one of the most commonly used gauge-invariant quantities is the curvature perturbation on uniform-density hypersurfaces,

$$\zeta \equiv D - \frac{\mathcal{H}}{\bar{\rho}'}\delta\rho. \tag{2.61}$$

In a gauge defined by spatially flat hypersurfaces, $D = 0$, the perturbations ζ is the dimensionless density perturbation $\delta\rho/3(\bar{\rho} + \bar{p})$. Employing suitable transfer functions to describe the evolution of the fluctuations in sub-horizon scales, CMB, and large-scale structure (LSS) observations can be related to the primordial value of ζ. During the slow-roll inflationary epoch, we have approximately

$$\delta\rho_{\phi} \approx \frac{dV}{d\phi}\delta\phi \approx -3\mathcal{H}\phi'\delta\phi. \tag{2.62}$$

Considering $\bar{\rho}' = 3\mathcal{H}\bar{\phi}'^{\,2}$, one would approximately have

$$\zeta \approx D - \frac{\mathcal{H}}{\bar{\phi}'}\delta\phi. \tag{2.63}$$

Also, the comoving curvature perturbation and entropy perturbation are the significant gauge-invariant quantities defined by

$$\mathcal{R} \equiv D - \frac{H}{\bar{\rho} + \bar{p}}\delta q, \tag{2.64}$$

and

$$\Gamma \equiv \frac{\delta p^{(\mathrm{GI})} - c_{\mathrm{s}}^2\bar{\rho}\delta^{(\mathrm{GI})}}{\bar{p}}, \tag{2.65}$$

respectively, where δq is the scalar part of the 3-momentum density defined by $T_i^0 \equiv \partial_i\delta q$. During inflation, δq is expressed as Eq. (2.52). Then the comoving curvature perturbation is given by

$$\mathcal{R} = D - \frac{\mathcal{H}}{\bar{\phi}'}\delta\phi. \tag{2.66}$$

Geometrically, $\mathcal{R}$ is helpful to measure the spatial curvature on comoving surfaces. Note that ζ and $\mathcal{R}$ are equal during slow-roll inflation as seen in Eqs. (2.63) and (2.66). Furthermore, ζ and $\mathcal{R}$ would match on superhorizon scales, which we explain in Appendix B. The correlation functions of ζ and $\mathcal{R}$ are therefore equal at horizon crossing.

2.4.7 Consequences at linear order

As mentioned before, we employ the conformal Newtonian gauge from here, and thus we set to $A = \Phi$, $D = \Psi$, and $B^{(S)} = E^{(S)} = 0$ hereafter. Under the conformal Newtonian gauge, the scalar components of the metric represented in Eqs. (2.45) and (2.46) would be written by

$$g_{\mu\nu}^{(S)} = a(\tau)^2 \begin{pmatrix} -(1+2\Phi) & 0 \\ 0 & (1+2\Psi)\delta_{ij} \end{pmatrix}, \tag{2.67}$$

and

$$(g^{\mu\nu})^{(S)} \simeq \frac{1}{a(\tau)^2} \begin{pmatrix} -1+2\Phi & 0 \\ 0 & (1-2\Psi)\delta^{ij} \end{pmatrix}. \tag{2.68}$$

Then the scalar components of the Ricci tensor in linear order would be given by

$$\begin{aligned} a^2(\delta R^0{}_0)^{(S)} &= -6\mathscr{H}'\Phi - \Delta\Phi - 3\mathscr{H}\Phi' + 3\Psi'' + 3\mathscr{H}\Psi', \\ a^2(\delta R^0{}_i)^{(S)} &= -2\mathscr{H}\nabla_i\Phi + 2\nabla_i\Psi', \\ a^2(\delta R^i{}_0)^{(S)} &= 2\mathscr{H}\gamma^{ij}\nabla_j\Phi - 2\gamma^{ij}\nabla_j\Psi', \\ a^2(\delta R^i{}_j)^{(S)} &= \left[-2\left(2\mathscr{H}^2 + \mathscr{H}'\right)\Phi - \mathscr{H}\Phi' + 3\mathscr{H}\Psi'\right]\delta^i_j \\ &\quad - \nabla^i\nabla_j\Phi + \gamma^i{}_j\Psi'' + 2\mathscr{H}\gamma^i{}_j\Psi' - \nabla^i\nabla_j\Psi - \gamma^i{}_j\Delta\Psi. \end{aligned} \tag{2.69}$$

The linear-order Ricci scalar δR would be given by

$$\delta R = -(6\mathcal{H}^2\Phi + 6\Phi\mathcal{H}' + 3\mathcal{H}(\Phi' - 3\Psi') - 3\Psi'' + \nabla^2\Phi + 2\nabla^2\Psi). \tag{2.70}$$

Combining these calculations for the metric side and matter side represented in Eqs. (2.15), (2.69) and (2.70) gives us the consequence of the Einstein equation expanding in linear order, that is

$$(00): \nabla^2\Psi - 3\mathcal{H}\Psi' - (\mathcal{H}' + 2\mathcal{H}^2)\Phi = 4\pi G\left(\bar{\phi}'\delta\phi' + a^2\frac{dV}{d\phi}\delta\phi\right), \tag{2.71}$$

$$(0i): \Psi' - \mathcal{H}\Phi = -4\pi G\bar{\phi}'\delta\phi, \tag{2.72}$$

$$(ii): \Psi'' - \frac{1}{3}\nabla^2(\Phi + \Psi) + \mathcal{H}(2\Psi' - \Phi') = -4\pi G\left(\bar{\phi}'\delta\phi' - a^2\frac{dV}{d\phi}\delta\phi\right), \tag{2.73}$$

$$(ij): \Phi + \Psi = 0. \tag{2.74}$$

Here the head number like $(\mu\nu)$ in Eqs. (2.71) to (2.74) represents the corresponding component of the Einstein equation. Integrating Eqs. (2.71) to (2.74), one can obtain gauge invariant equations for Φ as follows:

$$\begin{aligned}\Delta\Phi - 3\mathscr{H}\Phi' - \left(\mathscr{H}' + 2\mathscr{H}^2\right)\Phi &= 4\pi G\left[\vec{\phi}'\delta\phi^{(\mathrm{GI})'} + a^2\frac{dV}{d\phi}\delta\phi^{(\mathrm{GI})}\right],\\ \Phi' + \mathscr{H}\Phi &= 4\pi G\bar{\phi}'\delta\phi^{(\mathrm{GI})},\\ \Phi'' + 3\mathscr{H}\Phi' + \left(\mathscr{H}' + 2\mathscr{H}^2\right)\Phi &= 4\pi G\left[\vec{\phi}'\delta\phi^{(\mathrm{GI})'} - a^2\frac{dV}{d\phi}\delta\phi^{(\mathrm{GI})}\right].\end{aligned} \tag{2.75}$$

Furthermore, combining these equations in Eq. (2.75) reads the so-called Bardeen equation,

$$\Phi'' + 2\left(\mathscr{H} - \frac{\bar{\phi}''}{\bar{\phi}'}\right)\Phi' - \Delta\Phi + 2\left(\mathscr{H}' - \mathscr{H}\frac{\bar{\phi}''}{\bar{\phi}'}\right)\Phi = 0. \tag{2.76}$$

Eq. (2.76) is one of the main consequences of the Einstein equation expanding in linear order.

2.5 Initial condition of perturbations

As we mentioned in Chapter 1, it is believed that these perturbations discussed above originate from the quantum fluctuations of inflaton. Let us investigate the perturbation of the inflaton in more detail. Then we discuss the comoving curvature perturbation $\mathcal{R}$ defined in Eq. (2.64) instead of $\delta\phi$ for their quantization explained in the next section. In the conformal Newtonian gauge without the anisotropic stress tensor, one can obtain

$$\mathcal{R} = \Phi + \frac{\mathcal{H}}{\bar{\phi}'}\delta\phi. \tag{2.77}$$

Substituting Eq. (2.77) to Eq. (2.76) and utilizing the Einstein equations in **??** lead us the equation of motion of $\mathcal{R}$,

$$\mathcal{R}'' + 2\frac{z'}{z}\mathcal{R}' - \Delta\mathcal{R} = 0, \tag{2.78}$$

where $z \equiv \frac{a\bar{\phi}'}{\mathcal{H}}$. Eq. (2.78) can be rewritten by

$$\frac{\partial}{\partial\tau}\left(z^2\mathcal{R}'\right) - z^2\Delta\mathcal{R} = 0. \tag{2.79}$$

In the Fourier mode, Eq. (2.79) reads

$$\frac{\partial}{\partial\tau}\left(z^2\mathcal{R}_k'\right) + z^2k^2\mathcal{R}_k = 0, \tag{2.80}$$

and the solution of the superhorizon mode ($k \to 0$) would be

$$\mathcal{R}_k \to C_1 + C_2\int d\tau\,\frac{1}{z^2}, \tag{2.81}$$

with the integration constant C_1 and C_2. The second term in Eq. (2.81) represents the decaying mode because z would increase exponentially in the inflation epoch.

Therefore, the first term in Eq. (2.81) is the effective solution, which indicates that the value of $\mathcal{R}$ would be conserved on superhorizon scales. This behavior of $\mathcal{R}$ is favorable for cosmologists. We do not need to follow the entire evolution of $\mathcal{R}$ from the beginning (e.g., inflation) to some redshift in which we are interested. Instead, we only need to follow the evolution from when the perturbation enters the horizon to the redshift. However, for one condition, the information fo the amplitude of $\mathcal{R}$ at the horizon entry, that is C_1 in Eq. (2.81) is required.

Then where does the "primordial" perturbation come from? The inflation scenario would provide an answer to the question. The key point is quantum fluctuations. In order to consider the "quantum" fluctuation, one needs to quantize the field considered here. From the equation of motion represented in Eq. (2.79), the quadratic action form of $\mathcal{R}$ can be inferred as

$$S_2 = \frac{1}{2}\int d\tau dx^3 \left(z^2 \mathcal{R}'^2 - z^2 \partial_i \partial^i \mathcal{R} \right). \tag{2.82}$$

Since $\mathcal{R}$ is not a canonical field as seen in Eq. (2.82), it is difficult to quantize $\mathcal{R}$ itself.

2.5.1 Mukhanov-Sasaki variable

In order to quantize the classical scalar field represented in Eq. (2.82), we need to change of the variable $\mathcal{R}$ to make the scalar field canonicalize. Let us get straight to the point. We introduce a new variable $\mathcal{U} \equiv z\mathcal{R}$, so-called *Mukhanov-Sasaki variable*. Then the quadratic action of Eq. (2.82) becomes

$$S_2 = \frac{1}{2}\int d\tau dx^3 \left(\mathcal{U}'^2 - \partial_i \partial^i \mathcal{U} - 2\frac{z'}{z}\mathcal{U}\mathcal{U}' + \frac{z'^2}{z^2}\mathcal{U}^2 \right). \tag{2.83}$$

Employing the following relation,

$$-\frac{\partial}{\partial \tau}\left(\frac{z'\mathcal{U}^2}{z} \right) = -2\frac{z'}{z}\mathcal{U}\mathcal{U}' + \frac{z'^2}{z^2}\mathcal{U}^2 - \frac{z''}{z}\mathcal{U}^2, \tag{2.84}$$

and integrating by parts while dropping the surface term read the new canonicalized expression for quadratic action with respect to $\mathcal{U}$ as

$$S_2 = \frac{1}{2}\int d\tau dx^3 \left(\mathcal{U}'^2 - \partial_i \partial^i \mathcal{U} + \frac{z''}{z}\mathcal{U}^2 \right). \tag{2.85}$$

As seen in Eq. (2.85), the quadratic action for $\mathcal{U}$ has canonical kinetic term rather than the one of $\mathcal{R}$ represented in Eq. (2.82), which means that the variable $\mathcal{U}$ is appropriate field to be quantized.

From Eq. (2.78) and the relation of $\mathcal{U} = z\mathcal{R}$, the equation of motion of $\mathcal{U}$ is given by

$$\mathcal{U}'' - \Delta\mathcal{U} - \frac{z''}{z}\mathcal{U} = 0, \tag{2.86}$$

which is often called the *Mukhanov-Sasaki equation*. Considering the last term in Eq. (2.86) as the mass term like $z''/z \sim m^2$, Eq. (2.86) becomes the equation of motion for a single scalar field.

2.5.2 Quantum fluctuation of the inflation scalar field

Now we are ready to quantize the action. Quantizing the classical scalar field represented in Eq. (2.85) would lead us to obtain the primordial perturbations so that C_1 represented in Eq. (2.81). Before calculating, we should note that the action in Eq. (2.85) seems the same as the action for the single scalar field with the Minkowski spacetime except for the time-dependent mass term, $m^2 = -z''/z$. First, let us define the momentum conjugate of $\mathcal{U}$ as

$$\Pi \equiv \frac{\partial \mathcal{L}}{\partial \mathcal{U}'} = \mathcal{U}'. \tag{2.87}$$

Here we introduce the quantum operators from the classical fields $\mathcal{U}$ and Π. The canonical commutation relations are as follows.

$$[\hat{\mathcal{U}}(\tau,\boldsymbol{x}),\hat{\Pi}(\tau,\boldsymbol{y})] = i\delta^3(\boldsymbol{x}-\boldsymbol{y}), \quad [\hat{\mathcal{U}}(\tau,\boldsymbol{x}),\hat{\mathcal{U}}(\tau,\boldsymbol{y})] = 0, \quad [\hat{\Pi}(\tau,\boldsymbol{x}),\hat{\Pi}(\tau,\boldsymbol{y})] = 0 \tag{2.88}$$

Let us expand the operator $\hat{\mathcal{U}}$ by the plane wave as

$$\hat{\mathcal{U}}(\tau,\boldsymbol{x}) = \int \frac{\mathrm{d}^3k}{(2\pi)^3}\left[u_k(\tau)\hat{a}_{\boldsymbol{k}}\mathrm{e}^{i\boldsymbol{k}\cdot\boldsymbol{x}} + u_k^*(\tau)\hat{a}_{\boldsymbol{k}}^\dagger\mathrm{e}^{-i\boldsymbol{k}\cdot\boldsymbol{x}}\right], \tag{2.89}$$

where $k = |\boldsymbol{k}|$, $u_k(\tau)$ is the mode function, and $\hat{a}_{\boldsymbol{k}}^\dagger$ and $\hat{a}_{\boldsymbol{k}}$ represent the creation and annihilation operators respectively. The field of $\mathcal{U}$ breaks the time-translational symmetry by the time-dependent mass term. Therefore, $u_k(\tau)$ has the time-dependence, and the integral element, $\mathrm{d}^3k/(2\pi)^3$, has only the spatial parity symmetry rather than the Lorentz-invariance.

The mode function obeys the classical equation of motion for u_k,

$$u_k'' + \left(k^2 - \frac{z''}{z}\right)u_k = 0. \tag{2.90}$$

Equation (2.90) does not include the first derivative term for u_k. Then the wronskian of u_k and u_k^* is constant timewise, and we can normalize the mode function alternatively through the value of the wronskian. Here we define the commutation relations for the annihilation operator $\hat{a}_{\boldsymbol{k}}$ and the creation operator $\hat{a}_{\boldsymbol{k}}^\dagger$ in the Fourier space as

$$\left[\hat{a}_{\boldsymbol{k}_1},\hat{a}_{\boldsymbol{k}_2}^\dagger\right] = (2\pi)^3\delta\left(\boldsymbol{k}_1-\boldsymbol{k}_2\right), \quad [\hat{a}_{\boldsymbol{k}_1},\hat{a}_{\boldsymbol{k}_2}] = \left[\hat{a}_{\boldsymbol{k}_1}^\dagger,\hat{a}_{\boldsymbol{k}_2}^\dagger\right] = 0. \tag{2.91}$$

To make u_k and u_k^* being compatible with this definition, we set the normalization condition for the wronskian as

$$u_k u_k^{*\prime} - u_k^* u_k' = i. \tag{2.92}$$

After that, with the definition of the vacuum state,

$$\hat{a}_k|0\rangle = \langle 0|\hat{a}_k^\dagger = 0, \tag{2.93}$$

One can proceed with the quantization in the standard way. During the inflation epoch, even if there exist classical perturbations before the inflation, they would decay due to the exponential expansion. Therefore, it is believed that observable fluctuations in our Universe originate from quantum vacuum fluctuations.

Next, let us derive the solution of Eq. (2.90) in the slow-roll inflation approximation as mentioned in Sec. 2.3. Remind that in the approximation, the equation of motion of $\bar{\phi}$ becomes

$$\bar{\phi}' \simeq -\frac{a^2}{3\mathcal{H}}\frac{dV}{d\phi}, \tag{2.94}$$

and this condition is expressed by

$$\bar{\phi}'^2 \ll 2a^2 V(\phi), \qquad |\bar{\phi}'' - \mathcal{H}\bar{\phi}'| \ll 3\mathcal{H}|\bar{\phi}'|. \tag{2.95}$$

Hubble parameter and the relevant parameters also become easier forms as

$$\mathcal{H}^2 \simeq \frac{8\pi G a^2}{3}V, \tag{2.96}$$

$$\bar{\phi}'^2 \simeq \frac{2a^2 V}{3}\epsilon, \quad \mathscr{H}' \simeq \mathscr{H}^2(1-\epsilon), \quad \bar{\phi}'' \simeq \mathscr{H}\bar{\phi}'(1+\epsilon-\eta). \tag{2.97}$$

Thus the derivative of slow-roll parameters in linear order can be written by

$$\epsilon' \simeq 2\mathscr{H}\epsilon(2\epsilon-\eta), \quad \eta' \simeq \mathscr{H}\left(2\epsilon\eta - \xi^2\right). \tag{2.98}$$

Using Eqs. (2.96) to (2.98), the derivative of $z = a\bar{\phi}'/\mathcal{H}$ and the second derivative in the slow-roll approximation can be obtained as

$$z' \simeq \mathscr{H}(1+2\epsilon-\eta)z, \quad z'' \simeq \mathscr{H}^2(2+5\epsilon-3\eta)z. \tag{2.99}$$

Here the second equation in Eq. (2.97) can be integrated because ϵ is constant in liner order as

$$(1-\epsilon)\tau \simeq -\frac{1}{\mathcal{H}}, \tag{2.100}$$

where we assume that the inflation last forever and set $\tau = 0$ to $t \to \infty$. Then the term of z''/z can be written by

$$\frac{z''}{z} \simeq \frac{2+5\epsilon-3\eta}{(1-\epsilon)^2\tau^2} \simeq \frac{2+9\epsilon-3\eta}{\tau^2}. \tag{2.101}$$

Here let us define a variable v satisfying

$$\frac{z''}{z} = \frac{v^2 - 1/4}{\tau^2}. \tag{2.102}$$

Concerning the slow-roll parameters with the use of Eq. (2.101), v is written by

$$v \simeq \frac{3}{2} + 3\epsilon - \eta, \tag{2.103}$$

in linear order. Using the expression of v in Eq. (2.103), Eq. (2.90) can be rewritten by

$$\frac{d^2 u_k}{d\tau^2} + \left[k^2 - \left(v^2 - \frac{1}{4}\right)\frac{1}{\tau^2}\right]u_k = 0. \tag{2.104}$$

Changing the variable as $u_k = \sqrt{-\tau} F_k$ in Eq. (2.104) reads the Bessel derivative function, and the solution is given by

$$u_k(\tau) = \sqrt{\frac{\pi}{4k}}\sqrt{-k\tau}\left[\alpha_k H_v^{(1)}(-k\tau) + \beta_k H_v^{(2)}(-k\tau)\right], \tag{2.105}$$

where α_k and β_k are integration constants, and $H_v^{(1)}$ and $H_v^{(1)}$ are the Hankel functions. Considering the feature of Hankel function, the normalization related to the wronskian in Eq. (2.92) can be given by

$$|\alpha_k|^2 - |\beta_k|^2 = 1. \tag{2.106}$$

In order to determine the dynamics considered here, α_k and β_k must be specified. It is known that the general curved spacetime has the ambiguity of the choice of a vacuum state. In the standard inflation scenario, one can elude this ambiguity by requiring that the vacuum state $|0$ is an eigenstate of the Hamiltonian in the far past, called *Bunch-Davies vacuum*.

In the limit of $k \to \infty$ $(\tau < 0)$, the Hankel functions represented in Eq. (2.105) are approximately expressed by

$$\begin{aligned} H_v^{(1)}(-k\tau) &\to \sqrt{-\frac{2}{\pi k\tau}}\exp\left[-i\left(k\tau + \frac{\pi}{4} + \frac{\pi v}{2}\right)\right] \\ H_v^{(2)}(-k\tau) &\to \sqrt{-\frac{2}{\pi k\tau}}\exp\left[i\left(k\tau + \frac{\pi}{4} + \frac{\pi v}{2}\right)\right]. \end{aligned} \tag{2.107}$$

In this limit, the equation of motion of u_k in Eq. (2.90) would be

$$u_k'' + k^2 u_k = 0, \tag{2.108}$$

and one might get the solution as

$$u_k(\tau) = \frac{e^{-ik\tau}}{\sqrt{2k}}. \tag{2.109}$$

This choice characterizes the *Bunch-Davis vacuum*. In order to satisfy that the solution in Eq. (2.105) approximates to the solution represented in Eq. (2.109) in the limit $-k\tau \to \infty$, the integration coefficients, α_k and β_k should be chosen as

$$\alpha_k = \exp\left[\frac{i\pi}{2}\left(v + \frac{1}{2}\right)\right], \quad \beta_k = 0. \tag{2.110}$$

Then the solution of the mode function u_k with *Bunch-Davis vacuum* is given by

$$u_k(\tau) = \sqrt{\frac{\pi}{4k}} e^{i\pi(v+1/2)/2}\sqrt{-k\tau} H_v^{(1)}(-k\tau). \tag{2.111}$$

On the other hand, for long-wave modes, $-k\tau \to 0$, the equation of motion of u_k in Eq. (2.90) would be given by

$$u_k'' - \frac{z''}{z} u_k = 0, \tag{2.112}$$

and the solution becomes

$$u_k = C(k)z(\tau), \tag{2.113}$$

where $C(k)$ is the integration constant. Here we neglected the decaying mode of $u_k \propto z(\tau)\int^\tau \frac{d\tau'}{z^2(\tau')}$. In the long-wave mode, the Hankel function is approximated by

$$H_v^{(1)}(x) \to \sqrt{\frac{2}{\pi}}e^{-i\pi/2}2^{v-3/2}\frac{\Gamma(v)}{\Gamma(3/2)}x^{-v}. \tag{2.114}$$

Then the solution of Eq. (2.113) is approximately given by

$$u_k \to \frac{1}{\sqrt{2k}}e^{i\pi(v-1/2)/2}2^{v-3/2}\frac{\Gamma(v)}{\Gamma(3/2)}(-k\tau)^{1/2-v}. \tag{2.115}$$

One can obtain the expression of

$$u_k \simeq \frac{1}{\sqrt{2k}}e^{i\pi(1+3\epsilon-\eta)/2}[1-(3\gamma+3\ln 2-5)\epsilon+(\gamma+\ln 2-2)\eta]\left(\frac{k}{\mathscr{H}}\right)^{-1-3\epsilon+\eta}, \tag{2.116}$$

as the linear order solution through the expansion of Eq. (2.115) in terms of slow-roll parameters.

2.6 Primordial power spectrum of scalar perturbations

In order to link to the observables, we need the statistics for quantum perturbations. The two-point functions of the scalar perturbations in the vacuum state are defined by

$$\langle 0\,|\hat{\mathcal{U}}_{\boldsymbol{k}}\hat{\mathcal{U}}_{\boldsymbol{k}'}|\,0\rangle := (2\pi)^3\delta^3\left(\boldsymbol{k}+\boldsymbol{k}'\right)\frac{2\pi^2}{k^3}\mathcal{P}_{\mathcal{U}}(k), \tag{2.117}$$

where $\mathcal{P}_{\mathcal{U}}$ is the dimensionless power spectrum of the $\mathcal{U}$, and $\hat{\mathcal{U}}_{\boldsymbol{k}}$ is the Fourier mode of $\hat{\mathcal{U}}$ as

$$\hat{\mathcal{U}}_{\boldsymbol{k}}(\tau) = \int d^3xe^{-ik\cdot x}\hat{\mathcal{U}}(\boldsymbol{x},\tau) = u_k(\tau)\hat{a}_{\boldsymbol{k}} + u_k^*(\tau)\hat{a}^\dagger_{-\boldsymbol{k}}. \tag{2.118}$$

Considering the relation between $\mathcal{U}$ and the curvature perturbation ζ like $\mathcal{U} = -z\zeta$, the power spectrum of ζ would be given by

$$\mathcal{P}_\zeta(k,\tau) = \mathcal{P}_{\mathcal{U}}(k,\tau)/z^2, \tag{2.119}$$

where $\mathcal{P}_\zeta$is defined by

$$\langle 0\,|\hat{\zeta}_{\boldsymbol{k}}\hat{\zeta}_{\boldsymbol{k}'}|\,0\rangle := (2\pi)^3\delta^3\left(\boldsymbol{k}+\boldsymbol{k}'\right)\frac{2\pi^2}{k^3}\mathcal{P}_\zeta(k), \tag{2.120}$$

and often called primordial power spectrum.

For the long-wave modes, the primordial power spectrum would be

$$\mathcal{P}_\zeta(k,\tau) = \frac{4\pi}{m_{\rm Pl}^2\epsilon}\left(\frac{H}{2\pi}\right)^2\left(\frac{k}{\mathscr{H}}\right)^{2\eta-6\epsilon} \tag{2.121}$$

through the mode function u_k represented in Eq. (2.116). Here we assume that the expression of the power spectrum of the classical curvature perturbations is given by the quantum one represented in Eq. (2.121). Also, remind that ζ and $\mathcal{R}$ would match on superhorizon scales. Therefore, the expression of $\mathcal{P}_\zeta$ represented in Eq. (2.121) equals the power spectrum for $\mathcal{R}$ until the modes' horizon reentry. We explain more in detail in Appendix B.

Although the power spectrum of the scalar mode is scale-invariant in the de Sitter limit and called the Harrison-Zeĺdovich spectrum, the derived power spectrum, including a small change of the Hubble parameter, slightly depends on scales. We introduce the spectral index and the running for primordial power spectrum as

$$n_\mathrm{s} - 1 := \frac{\mathrm{d}\ln \mathcal{P}_\zeta}{\mathrm{d}\ln k}, \quad \text{and} \quad r_s := \frac{dn_\mathrm{s}}{d\ln k}. \tag{2.122}$$

At the horizon crossing, we approximately get

$$\mathrm{d}\ln k \simeq H\, \mathrm{d}t. \tag{2.123}$$

Therefore in this slow-roll inflation case, the spectral index and the running at the leading order are given by

$$n_\mathrm{s} = 1 - 6\epsilon + 2\eta, \quad \text{and} \quad r_{n_\mathrm{s}} = 16\epsilon\eta - 24\epsilon^2 - 2\xi^2. \tag{2.124}$$

So far, we have discussed the primordial perturbations only aiming at the scalar type, which is the target of this thesis. We here skip the discussion for the vector- and tensor-type perturbations because they are beyond our scope.

2.7 Observational implications from the Planck 2018 data

Finally, let us briefly summarize the observational implications for primordial perturbations, especially by the Planck satellite [1]. The primary observables related to primordial perturbations are the amplitude of the power spectrum of the curvature perturbation $\mathcal{A}_\zeta$, the spectral index of the power spectrum n_s, and the tensor-to-scalar ratio r. From the Planck measurements, especially combining Planck TT,TE,EE+lowE +lensing data, these parameters are known to be

$$\begin{aligned} n_\mathrm{s} &= 0.9649 \pm 0.0042 \ (68\%CL), \\ 10^9 \mathcal{A}_\zeta^\mathrm{CMB} &= 2.100 \pm 0.030 \ (68\%CL), \\ r &< 0.11, \end{aligned} \tag{2.125}$$

where they are quoted 68% confidence limits on n_s and $\mathcal{A}_\zeta^\mathrm{CMB}$, and 95% upper bounds on r. It is noted that the scale of $k = 0.05\mathrm{Mpc}^{-1}$ is adopted as a pivot scale in the Planck data analysis, and this result is obtained assuming the ΛCDM model without the running of the spectral index n_s. When the analysis is extended to include the running, defined by

$$r_{n_\mathrm{s}} \equiv dn_\mathrm{s}/d\ln k, \tag{2.126}$$

as a free parameter, the result for n_s and r would slightly change like

$$\begin{aligned} n_\mathrm{s} &= 0.9647 \pm 0.0044 \ (68\% CL), \\ r_{n_\mathrm{s}} &= -0.0085 \pm 0.0073 \ (68\% CL), \\ r &< 0.16. \end{aligned} \tag{2.127}$$

We should also note the recent result by the BICEP/Keck [81]. The authors have reported that if we add the observational data of the Baryon Acoustic Oscillation (BAO) and the BICEP/Keck data for the Planck data, the constraint on the tensor-to-ratio is tightened to

$$r < 0.036, \tag{2.128}$$

by setting the pivot scale as $k = 0.05\mathrm{Mpc}^{-1}$.

The blue-shaded region in Fig. 2.1 shows the constraints in the r vs. n_s plane for the Planck 2018 baseline analysis adding BAO data and the BICEP/Keck data through the end of the 2018 season (thick:1σ-, thin:2σ-region). The green contour represents the allowed parameter region obtained from the Planck baseline analysis. The chaotic inflation models expressed by the power-law type potential of ϕ are known to predict a relatively large tensor-to-scalar ratio when assuming that the e-fold number $N \equiv \int_t^{t_\mathrm{f}} H dt$ is in the range of $[50, 60]$, where t_f is the cosmic time at the end of inflation. That conflicts with the contour from the Planck+BICEP/Keck+BAO analysis, as seen in Fig. 2.1. The purple contour represents the prediction of the natural inflation [82], [83]. Also, the concave potential means the potential satisfying $V''(\phi) < 0$, and the convex potential means the one of $V''(\phi) > 0$.

2.8 Evolution of cosmological perturbations

So far, we have discussed the creation and evolution of cosmological perturbations during inflation. To summarize, we have gotten the following gist as the consequences:

1. Cosmological perturbations would originate from the quantum fluctuations of inflaton.
2. Although there are several kinds of perturbations coming from the quantum fluctuations, the curvature perturbations ζ and $\mathcal{R}$ are beneficial to express the subsequent evolution of the Universe due to that they are conserved on super-horizon scales.

On local scales, $k \gtrsim 1\mathrm{Gpc}^{-1}$, we know that the Universe is not isotropic through measurements of CMB and LSS. One of the support for inflation is that such anisotropy and inhomogeneity are explainable from the quantum fluctuations of inflaton. In this section, we link the primordial perturbations and the observations of CMB and LSS. Especially the connection between primordial perturbations and LSS relates to our works as we introduce in Chapter 3. We should stress that observables are CMB and LSS rather than the amplitude of primordial power spectrum $\mathcal{A}_\zeta$, the spectral index n_s, and the tensor-to-scalar ratio r. It is essential to make this relation clear as as to approach the inflationary mechanism.

To connect them, we have following two things to do:

(1) Relate ζ to $\mathcal{Q}$ which is the quantity actually measured by experiments

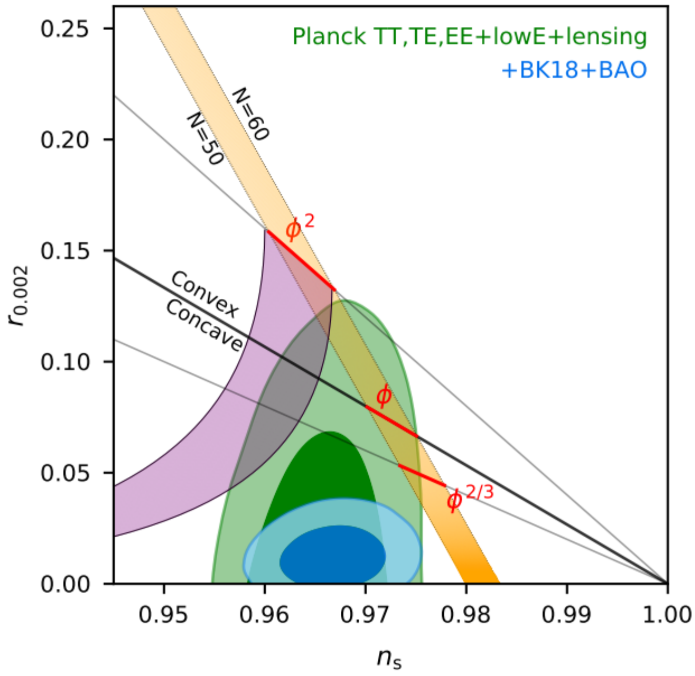

FIGURE 2.1: Current constraints on the the tensor-to scalar ration r and the spectral index of the power spectrum of the curvature perturbation n_s at the the pivot scale $k = 0.002\text{Mpc}^{-1}$ from CMB measurements of Planck, BAO and BICEP/Keck. Figure is adapted from Ref. [81].

(2) Consider the time evolution of $\mathcal{Q}$ after the horizon entry.

2.9 CMB anisotropy

In the CMB anisotropy case, the quantity $\mathcal{Q}$ corresponds to CMB temperature fluctuation ΔT_γ, or the CMB E-mode/B-mode polarization. Here we give a brief review of the physics of CMB temperature fluctuations. See Ref. [84] for more details.

2.9.1 CMB Temperature

Figure 2.2 represents an all-sky map of the CMB temperature fluctuation ΔT_γ measured by the Planck mission. Concretely, they plot the difference from the average CMB temperature $\bar{T}_\gamma = 2.725\mathrm{K}$.

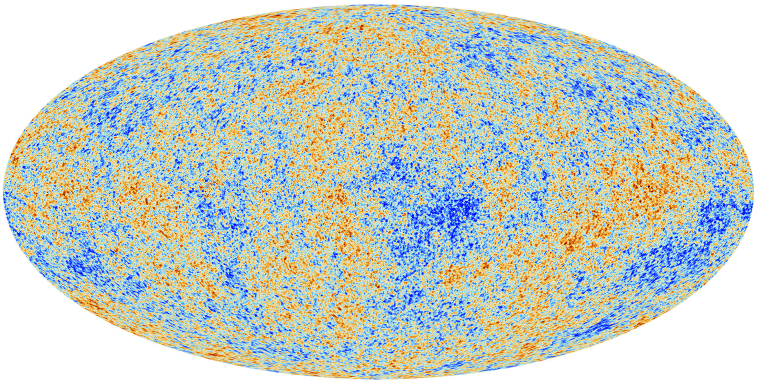

FIGURE 2.2: The anisotropies of the CMB temperature as observed by Planck.

This map is expressed through the harmonic expansion like

$$\Theta(\hat{n}) \equiv \frac{\Delta T_\gamma(\hat{n})}{\bar{T}_\gamma} = \sum_{\ell m} a_{\ell m} Y_{\ell m}(\hat{n}), \tag{2.129}$$

where $\hat{n}$ is the unit vector for the direction in sky, $Y_{\ell m}$ is the standard spherical harmonics on a $2-D$ sphere, and $a_{\ell m}$ is the coefficient which represents the multipole moments of the CMB temperature fluctuations and can be written by

$$a_{\ell m} = \int \mathrm{d}\Omega Y^*_{\ell m}(\hat{n})\Theta(\hat{n}). \tag{2.130}$$

The angular power spectrum is calculated by this multipole moments $a_{\ell m}$ like

$$C_\ell^{TT} = \frac{1}{2\ell+1}\sum_m \langle a^*_{\ell m} a_{\ell m}\rangle, \quad \text{or} \quad \langle a^*_{\ell m} a_{\ell' m'}\rangle = C_\ell^{TT}\delta_{\ell\ell'}\delta_{mm'}, \tag{2.131}$$

where the subscription of T means the CMB temperature. The angular power spectrum is a statistically vital quantity describing key features of the Universe on behalf of millions of pixels in the CMB map.

CMB temperature fluctuations are mostly created by ζ as the observed tensor-to-scalar ratio limit indicates, while vector- and tensor-perturbations can theoretically create the fluctuations. The relation between ζ and ΔT_γ and their linear evolution are expressed by the transfer function $\Delta T_\ell(k)$. Then the coefficient $a_{\ell m}$ can be written by

$$a_{\ell m} = 4\pi(-i)^{\ell} \int \frac{\mathrm{d}^3 k}{(2\pi)^3} \Delta T_{\ell}(k) \zeta_{\mathbf{k}} Y_{\ell m}(\hat{\mathbf{k}}). \tag{2.132}$$

From Eqs. (2.131) and (2.132), one can obtain

$$C_{\ell}^{TT} = 4\pi \int \mathrm{d}\log k \underbrace{\mathcal{P}_{\zeta}(k)}_{\text{Inflation}} \underbrace{\Delta T_{\ell}(k) \Delta T_{\ell}(k)}_{\text{Anisotropies}}, \tag{2.133}$$

where we have used the identity for the standard spherical harmonics as

$$\sum_{m=-\ell}^{\ell} Y_{\ell m}(\hat{\mathbf{k}}) Y_{\ell m}\left(\hat{\mathbf{k}}'\right) = \frac{2\ell+1}{4\pi} P_{\ell}\left(\hat{\mathbf{k}} \cdot \hat{\mathbf{k}}'\right). \tag{2.134}$$

Generally, the transfer functions $\Delta T_{\ell}(k)$ have to be computed numerically using Boltzmann-codes such as *CMBFAST* [85] or *CAMB* [86].

2.10 Large-scale structures

In the LSS case, the quantity $\mathcal{Q}$ corresponds to the number fluctuation Δn of DM halos or galaxies. Here we briefly review the physics and the statistical interpretation of LSS. The big difference between this case and the CMB anisotropy case is focusing on non-linear objects formed by a gravitational collapse rather than perturbations. Therefore, we must carefully consider the effects of subhorizon evolution.

2.10.1 The linear evolution of Dark Matter perturbations

Density fluctuations of cosmic fluid would evolve under the competition between influences of gravity and pressure, and the growth rate is often expressed by $D(a)$. For example, during the RD epoch, the immense pressure from radiation prevents the growth of fluctuations. Then DM density fluctuations only grow logarithmically, $D(a) \propto \ln a$. During the MD epoch, the background pressure would be negligible if one neglects the baryonic pressure. Then DM density contrasts evolve more rapidly, $D(a) \propto a$. Under the simplifying assumption to neglect the evolution in the RD epoch, one may derive the following transfer function approximately,

$$T_{\delta}(k) \approx \begin{cases} 1 & k < k_{\mathrm{eq}} \\ \left(k_{\mathrm{eq}}/k\right)^2 & k > k_{\mathrm{eq}} \end{cases}, \tag{2.135}$$

where k_{eq} is the wavenumber corresponding to the horizon scale at the matter-radiation equality epoch. It is noted that this transfer function expresses the linear evolution of matter density perturbation so that

$$T_{\delta}(k) \equiv \frac{\delta_{\mathrm{k}}(z=0)}{\delta_{\mathrm{k}}(z) D(z)}. \tag{2.136}$$

This approximate transfer function in Eq. (2.135) is beneficial for an intuitive understanding of the matter power spectrum, which would be a kind of double power law function. However, it is not accurate enough for most calculations. Several pioneering works provided the fitting functions for the matter transfer function. For example, Bardeen, Bond, Kaiser, *et al.* [87] provided the famous fitting function,

$$T_\delta(q) = \frac{\ln(1+2.34q)}{2.34q}\left[1 + 3.89q + (1.61q)^2 + (5.46q)^3 + (6.71q)^4\right]^{-1/4}, \tag{2.137}$$

where $q = k/\Gamma h\mathrm{Mpc}^{-1}$, and Γ is the apparent shape parameter generalized by Ref. [88] for applying to the general cosmological model with $\Omega_{\mathrm{m},0} \neq 0$,

$$\Gamma \equiv \Omega_{\mathrm{m},0} h \exp\left(-\Omega_{\mathrm{b},0} - \sqrt{2h}\,\Omega_{\mathrm{b},0}/\Omega_{\mathrm{m},0}\right). \tag{2.138}$$

Weinberg [89] also provided the well-known fitting function as

$$T_\delta(k) = \frac{45}{2}\frac{\Omega_{\mathrm{m},0}^2 H_0^2}{\Omega_{\mathrm{r},0} k^2}\left(-\frac{7}{2} + \gamma_{\mathrm{E}} + \ln\left(\frac{4\sqrt{\Omega_{\mathrm{r},0}}k}{\sqrt{3}\Omega_{\mathrm{m},0}H_0}\right)\right), \tag{2.139}$$

where $\gamma_{\mathrm{E}} \simeq 0.577$ is the Euler-Mascheroni constant. It must be noted that this function is valid at $\sqrt{\Omega_{\mathrm{r},0}}k/\Omega_{\mathrm{m},0}H_0 \gg 1$ so that $k \gg 10^{-2}\mathrm{Mpc}^{-1}$ in the realistic case ($\Omega_{\mathrm{m},0} \sim 0.3$). Figure 2.3 shows the comparison of these fitting functions in the Einstein – de Sitter Universe ($\Omega_{\mathrm{m},0} = 1$) and the realistic Universe ($\Omega_{\mathrm{m},0} = 0.31$). One may obtain a more accurate fitting function in, e.g., Ref. [90] and the exact transfer functions would be computed numerically with *CMBFAST* [85] or *CAMB* [86]. We stress that the above fitting functions are only for the evolution of matter density fluctuations δ. The complete transformation between ζ and δ at some redshift would be given by

$$\delta_{\mathrm{k}}(a) = \frac{2}{5}\frac{k^2}{\Omega_{\mathrm{m},0}H_0^2}\zeta_{\mathrm{k}}\mathcal{T}_\delta\left(\frac{\sqrt{\Omega_{\mathrm{r},0}}k}{H_0\Omega_{\mathrm{m},0}}\right)a. \tag{2.140}$$

Also, we remind that our purpose here is to obtain the inflationary spectrum $\mathcal{P}_\zeta$ from the power spectrum of the DM halo/galaxy number fluctuations rather than the matter density perturbation.

2.10.2 Galaxy Bias and DM Halo Bias

Except for the gravitational lensing method, one cannot observe the DM directly. What we actually observe would be luminous baryonic matter. In the context of LSS, the following relation between the DM distribution and the galaxy distribution has proven helpful,

$$\delta_{\mathrm{gal}} = b_{\mathrm{gal}}\delta, \qquad \text{so that,} \qquad P_{\delta_{\mathrm{gal}}} = b_{\mathrm{gal}}^2 P_\delta, \tag{2.141}$$

where δ_{gal} is the fluctuation of the galaxy number density, b_{gal} is called the linear galaxy bias parameter, and $P_{\delta_{\mathrm{gal}}}$ is the galaxy power spectrum defined by

$$\langle\delta_{\mathrm{gal}}(\mathbf{k})\delta_{\mathrm{gal}}(\mathbf{k}')\rangle = (2\pi)^3\delta^3(\mathbf{k}+\mathbf{k}')P_{\delta_{\mathrm{gal}}}(k). \tag{2.142}$$

The linear galaxy bias b_{gal} can be obtained by measuring the galaxy power spectrum and the bispectrum. From the above discussion, one can relate the P_{δ_g} as observables and the inflationary spectrum $\mathcal{P}_\zeta$. As it can probe small scales, it would complement the CMB observations.

In the same way, the DM halo bias can be introduced, which is helpful in connecting the DM halo distribution with the DM distribution. Introducing the number

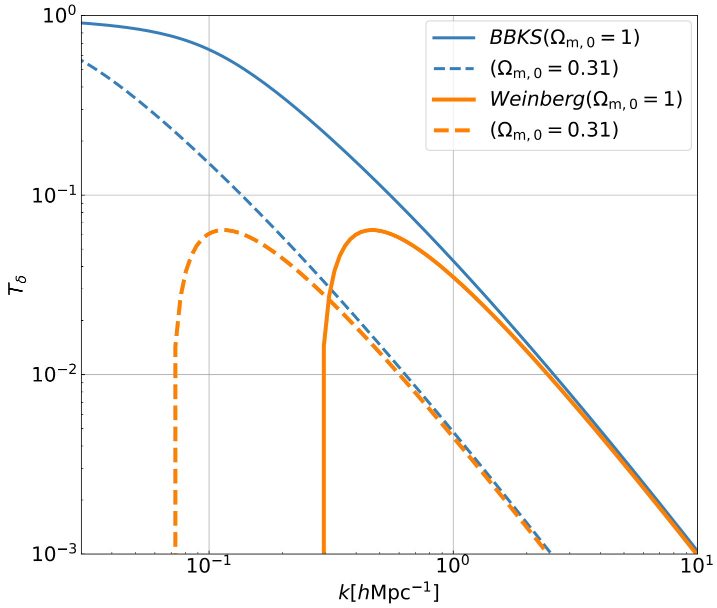

FIGURE 2.3: Comparison between the fitting functions for the matter transfer function provided by Ref. [87] and by Ref. [89]. The solid lines show the functions in the case of Einstein – de Sitter Universe. The dashed lines show the functions in the realistic case ($\Omega_{\mathrm{m},0} = 0.31$).

density fluctuation of DM halos δ_{halo}, one might obtain the following relation,

$$\delta_{\mathrm{halo}} = b_{\mathrm{halo}}\delta, \qquad \text{so that,} \qquad P_{\delta_{\mathrm{halo}}} = b_{\mathrm{halo}}^2 P_\delta, \tag{2.143}$$

where b_{halo} is called the linear halo bias parameter, and $P_{\delta_{\mathrm{halo}}}$ is the halo power spectrum defined by

$$\langle \delta_{\mathrm{halo}}(\mathbf{k})\delta_{\mathrm{halo}}(\mathbf{k}')\rangle = (2\pi)^3\delta^3(\mathbf{k}+\mathbf{k}')P_{\delta_{\mathrm{halo}}}(k). \tag{2.144}$$

Theoretically, the value of the halo bias can be predicted for each halo formation model. Before finishing this chapter, we briefly review two famous halo formation models; the Press-Schechter model and the Peak theory model.

2.10.3 Press-Schechter Halo Formalism

In 1974, William H. Press and Paul Schechter published a paper describing a mathematical model to predict the number of gravitationally collapsed objects such as galaxies and DM halos [91]. Press and Schechter focused on the fact that the fraction of mass in collapsed objects heavier than some mass M is related to the fraction of volume in which the smoothed density fluctuations are larger than some critical density fluctuation δ_{crit}.

According to this formalism, the probability of forming a collapsed object heavier than M is expressed by

$$P_{>\delta_{\mathrm{crit}}}(M) = 2\int_{\delta_{\mathrm{crit}}}^{\infty} d\delta_{\mathrm{M}} P(\delta_{\mathrm{M}}), \tag{2.145}$$

where $P(\delta_{\rm M})$ is not the matter power spectrum but the probability function of the amplitude of the perturbation $\delta_{\rm M}$ in the Lagrangian coordinate,

$$P(\delta_{\rm M}) = \frac{1}{\sqrt{2\pi \mathcal{S}(M)}} \exp\left(-\frac{\delta_{\rm M}^2}{2\mathcal{S}(M)}\right), \tag{2.146}$$

with the variance $\mathcal{S}(M)$ of $\delta_{\rm M}$. Therefore, the probability of forming a collapsed object with a mass ranging from M to $M + dM$ is estimated by

$$\beta(M) = P_{>\delta_{\rm crit}}(M) - P_{>\delta_{\rm crit}}(M + dM). \tag{2.147}$$

Since the matter distributes homogeneously in the Lagrangian coordinates, the number density of the collapsed objects with a mass ranging from M to $M + dM$ is given by

$$n^{\rm PS}(M) M dM = \bar{\rho}_{\rm m} \beta(M), \tag{2.148}$$

where $n^{\rm PS}(M)$ is the Press-Schechter mass function and $\bar{\rho}_{\rm m}$ is the mean energy density of matter. Taking the factor 2 which is naturally derived from the extended Press-Schechter theory (often called *excursion set formalism*) into account [92], [93], the Press-Schechter mass function is given by

$$n^{\rm PS}(M) = \sqrt{\frac{2}{\pi}} \frac{\bar{\rho}_{\rm m}}{M^2} \left|\frac{d \ln \mathcal{S}^{1/2}(M)}{d \ln M}\right| \frac{\delta_{\rm crit}}{\mathcal{S}^{1/2}(M)} \exp\left(-\frac{{\delta_{\rm crit}}^2}{2\mathcal{S}(M)}\right). \tag{2.149}$$

Applying the critical density contrast for the linear threshold for collapse, $\delta_{\rm c} = 1.686$, to the $\delta_{\rm crit}$ in Eq. (2.149), the Press-Schechter halo mass function is given by

$$n_{\rm halo}(M) = \sqrt{\frac{2}{\pi}} \frac{\bar{\rho}_{\rm m}}{M^2} \left|\frac{d \ln \mathcal{S}^{1/2}(M)}{d \ln M}\right| \frac{\delta_{\rm c}}{\mathcal{S}^{1/2}(M)} \exp\left(-\frac{{\delta_{\rm c}}^2}{2\mathcal{S}(M)}\right). \tag{2.150}$$

The linear halo bias in the Press-Schechter formalism has been well studied. The famous and basic expression is given by [94],

$$b_{\rm halo} = 1 + \frac{\nu^2 - 1}{\delta_{\rm c}}, \tag{2.151}$$

where $\nu \equiv \delta_{\rm c}/\mathcal{S}^{1/2}(M)$.

2.10.4 Peak-Theory Halo Formalism

Another famous halo formalism would be of the peak theory [87]. According to the peak theory, the high peak in some random Gaussian field $g(x)$ would typically take the spherically symmetric profile like

$$\hat{g}(r) = \mu_0 \left[\frac{1}{1-\gamma_1^2}\left(\psi_0(r) + \frac{1}{3}R_1^2 \Delta\psi_0(r)\right) - k_1^2 \frac{1}{\gamma_1\left(1-\gamma_1^2\right)} \frac{\sigma_0}{\sigma_2}\left(\gamma_1^2 \psi_0(r) + \frac{1}{3}R_1^2 \Delta\psi_0(r)\right)\right], \tag{2.152}$$

with two random variables, μ_0 and k_1^2, representing the peak height and width, respectively, and four statistical parameters, σ_n, ψ_n, γ_n, and R_n. The definitions of these two random variables are

$$\mu_0 = \left. g \right|_{r=0}, \tag{2.153}$$

and

$$k_1^2 = -\left. \Delta g \right|_{r=0} / \mu_0. \tag{2.154}$$

Also the four statistical parameters are defined as

$$\sigma_n^2 = \int \frac{\mathrm{d}k}{k} k^{2n} \mathcal{P}_g(k), \tag{2.155}$$

$$\psi_n(r) = \frac{1}{\sigma_n^2} \int \frac{\mathrm{d}k}{k} k^{2n} \frac{\sin(kr)}{kr} \mathcal{P}_g(k), \tag{2.156}$$

$$\gamma_n = \frac{\sigma_n^2}{\sigma_{n-1}\sigma_{n+1}}, \tag{2.157}$$

$$R_n = \frac{\sqrt{3}\sigma_n}{\sigma_{n+1}}, \qquad \text{for odd } n, \tag{2.158}$$

and determined by the power spectrum of the Gaussian field g,

$$\mathcal{P}_g(k) = \frac{k^3}{2\pi^2} \int \mathrm{d}^3\mathbf{x} \mathrm{e}^{-i\mathbf{k}\cdot\mathbf{x}} \left\langle g\left(\frac{\mathbf{x}}{2}\right) g\left(-\frac{\mathbf{x}}{2}\right) \right\rangle. \tag{2.159}$$

Here hat denotes typical-profile-related quantities, and Δ means the Laplacian. The radius center is the point where satisfying $\nabla g = \left. \mathbf{0} \right|_{r=0}$. The comoving number density of such peaks is also statistically expected as

$$n_{\mathrm{pk}}^{(\mu_0,k_1)} \mathrm{d}\mu_0 \, \mathrm{d}k_1 = \frac{2 \cdot 3^{3/2}}{(2\pi)^{3/2}} \mu_0 k_1 \frac{\sigma_2^2}{\sigma_0 \sigma_1^3} f\left(\frac{\mu_0 k_1^2}{\sigma_2}\right) P_1^{(1)}\left(\frac{\mu_0}{\sigma_0}, \frac{\mu_0 k_1^2}{\sigma_2}\right) \mathrm{d}\mu_0 \, \mathrm{d}k_1, \tag{2.160}$$

with

$$\begin{aligned} f(\xi) = {} & \frac{1}{2}\xi\left(\xi^2 - 3\right)\left(\mathrm{erf}\left[\frac{1}{2}\sqrt{\frac{5}{2}}\xi\right] + \mathrm{erf}\left[\sqrt{\frac{5}{2}}\xi\right]\right) \\ & + \sqrt{\frac{2}{5\pi}}\left\{\left(\frac{8}{5} + \frac{31}{4}\xi^2\right)\exp\left[-\frac{5}{8}\xi^2\right] + \left(-\frac{8}{5} + \frac{1}{2}\xi^2\right)\exp\left[-\frac{5}{2}\xi^2\right]\right\}, \end{aligned} \tag{2.161}$$

and

$$P_1^{(n)}(\nu, \xi) = \frac{1}{2\pi\sqrt{1-\gamma_n^2}} \exp\left[-\frac{1}{2}\left(\nu^2 + \frac{(\xi - \gamma_1\nu)^2}{1-\gamma_n^2}\right)\right], \tag{2.162}$$

where $\mathrm{erf}(x)$ is the error function defined by $\mathrm{erf}(z) = \frac{2}{\sqrt{\pi}} \int_0^z \mathrm{e}^{-t^2} \, \mathrm{d}t$. Hence when focusing on the collapsed objects formed by the high-peak perturbations, e.g., sourced by the excess power of primordial perturbations, one can precisely predict the number density using peak theory. Note that this theory is based on the assumption that the perturbation follows the Gaussian distribution.

The linear halo bias in the peak-theory formalism is given by [95]

$$b_\mathrm{halo} = 1 + \frac{\nu^2 + g_1}{\delta_\mathrm{c}}, \tag{2.163}$$

where

$$g_k = \frac{(-1)^k}{k!} \frac{(\gamma_1 \nu)^k}{G_1(\gamma_1 \nu)} \frac{\partial^k G_1(y)}{\partial y^k}\bigg|_{y=\gamma_1\nu}. \tag{2.164}$$

$G_1(y)$ is the function related to the functions of $f(\xi)$ and $P_1^{(1)}(\nu,\xi)$ in Eq. (2.160),

$$G_1(y) = \int_0^\infty \mathrm{d}x \frac{f(x)}{2\pi\sqrt{1-\gamma_1^2}} \exp\left[-\frac{(x-y)^2}{2(1-\gamma_1^2)}\right] \tag{2.165}$$

.

Lastly, let us show an example applying to monochromatic perturbations for some Gaussian random field δ_X so that

$$\mathcal{P}_\mathrm{X}(k) = \mathcal{A}_\mathrm{X} k_\mathrm{s} \delta\left(k - k_\mathrm{s}\right), \tag{2.166}$$

where $\mathcal{A}_\mathrm{X}$ is the amplitude of the power spectrum, k_s represents the monochromatic mode, and $\delta(x)$ is the Delta function. In this monochromatic case, the peak theory would be significantly simplified. For instance, the variances are calculated as $\sigma_n^2 \to A_X k_\mathrm{s}^{2n}$, and all γ parameters becomes unity, $\gamma_{1,2,3,\ldots} \to 1$. In this case, taking $\nu = \mu_0/\sqrt{\mathcal{A}_\mathrm{X}}$ into account, one might get

$$P_1^{(1)}\left(\nu, \nu\frac{k_1^2}{k_\mathrm{s}^2}\right) \to \frac{k_\mathrm{s}}{2\nu} \mathrm{e}^{-\frac{1}{2}\nu^2} \delta\left(k_1 - k_\mathrm{s}\right). \tag{2.167}$$

Note that the independent parameter becomes effectively only μ_0 (or ν).

Then the number density of high peaks can be obtained by

$$n_\mathrm{pk}^{(\mu_0)} \mathrm{d}\mu_0 = \int n_\mathrm{pk}^{(\mu_0,k_1)} \mathrm{d}k_1 \mathrm{d}\mu_0 \to \left(\frac{3}{2\pi}\right)^{3/2} k_\mathrm{s}^3 f(\nu) \frac{1}{\sqrt{2\pi\mathcal{A}_X}} \mathrm{e}^{-\frac{1}{2}\nu^2} \mathrm{d}\mu_0. \tag{2.168}$$

Subsequently, let us apply this estimation to collapsed objects such as halos coming from the density contrast peaks higher than the linear collapse threshold δ_c. Then the halo number density would be given through $\delta_X \to \delta_\mathrm{mat}$ as

$$n_\mathrm{halo}^\mathrm{mono}(a) = \frac{3^{3/2} k_s^3}{(2\pi)^2} \int_{\delta_c/\mathcal{S}_\mathrm{mat}^{1/2}(a)}^\infty f(\nu) e^{-\nu^2/2} \mathrm{d}\nu, \tag{2.169}$$

where δ_mat shows the matter density constrast, and $\mathcal{S}_\mathrm{mat}(a)$ is the variance of δ_mat. We also exhibit the differential number density for the coming discussion in Chapter 5,

$$\frac{\mathrm{d}n_\mathrm{halo}^\mathrm{mono}}{\mathrm{d}a} = \frac{k_s^3}{a} h\left(\frac{\delta_c}{\mathcal{S}_\mathrm{mat}^{1/2}(a)}\right), \tag{2.170}$$

where

$$h(\nu) \equiv \frac{3^{3/2}\nu}{(2\pi)^2} e^{-\nu^2/2} f(\nu). \tag{2.171}$$

In the end, the linear halo bias in the monochromatic case is given by

$$b_{\mathrm{halo}}^{\mathrm{mono}} = 1 + \frac{\nu^2}{\delta_{\mathrm{c}}} \tag{2.172}$$

due to $g_1 \to 0$.

Chapter 3

Primordial Small-Scale Perturbations

The precise measurements of small-scale perturbations will be one of the main topics among the several observational missions in the future. It would be challenging to investigate primordial perturbations on small scales because they are strongly affected by dissipation, called Silk damping, and nonlinear effects associated with the gravitational evolution of our Universe. Considering and predicting observables related to small-scale perturbations are essential from the theoretical aspect. In this chapter, we give a review of the current status of exploring small-scale perturbations, especially focusing on four topics: CMB spectral distortion, PBHs, galaxies, and small-mass DM halos, and UCMHs, although we already mentioned briefly in Chapter 1.

3.1 CMB spectral distortion

Among methods to explore primordial small-scale perturbations, measuring CMB distortion would be most robust [10]–[12]. That is because the physics underlying the production of CMB distortions is well understood compared to other methods. Creations of the distortion can be derived analytically using secondary (or higher) perturbation theory. Additionally, measurements of CMB distortion have unique merit when connecting with primordial small-scale perturbations. The first one is that the CMB distortion is less sensitive to unknown Non-Gaussianity because the extent of the distortion is determined by the total energy stored in density perturbations. The second is that the CMB distortion produced by the dissipation of acoustic modes induced by the primordial power spectrum over a wide range of scales, for example, $50\mathrm{Mpc}^{-1} \lesssim k \lesssim 10^4\mathrm{Mpc}^{-1}$ for μ-distortion. Therefore, one could obtain deeper insight into the overall shape of the primordial power spectrum through CMB distortion measurements rather than PBH and UCMH measurements. Here we show the physics related to the CMB spectral distortion induced by primordial perturbation and the current limits obtained by the COBE/FIRAS mission. We refer Ref. [16] for this review. We also mention the future experiment to measure the CMB distortion.

3.1.1 Physics underlying the CMB distortion

The effective energy release rate caused by the damping of acoustic modes is determined by

$$\frac{1}{\rho_\gamma}\frac{\mathrm{d}Q_{\mathrm{ac}}}{\mathrm{d}z} = \frac{4\dot{\tau}\,\langle \mathcal{S}_{\mathrm{ac}}\rangle}{H(1+z)}, \tag{3.1}$$

where $\langle \mathcal{S}_{\rm ac} \rangle$ shows the source function, $\dot{\tau} = \sigma_{\rm T} n_{\rm e} c \approx 4.4 \times 10^{-21} (1+z)^3 {\rm sec}^{-1}$ is the Thomson scattering rate, and H is the Hubble expansion rate. Defining the visibility function for the spectral distortion by

$$\mathcal{J}_{\rm bb}(z) = \exp\left(- \left[z/z_\mu \right]^{5/2} \right), \tag{3.2}$$

with $z_\mu \approx 1.98 \times 10^6$, the weighted total energy released in the μ- and y-era would be written by

$$\begin{aligned} \left. \frac{\Delta\rho_\gamma}{\rho_\gamma} \right|_\mu &= \int_{z_{\mu,y}}^{\infty} \frac{\mathcal{J}_{\rm bb}(z)}{\rho_\gamma} \frac{{\rm d}Q_{\rm ac}}{{\rm d}z}\, {\rm d}z, \\ \left. \frac{\Delta\rho_\gamma}{\rho_\gamma} \right|_y &= \int_{0}^{z_{\mu,y}} \frac{1}{\rho_\gamma} \frac{{\rm d}Q_{\rm ac}}{{\rm d}z}\, {\rm d}z, \end{aligned} \tag{3.3}$$

where $z_{\mu,y} \approx 5 \times 10^4$ [96]. During the very early epoch, such as $z \gg z_\mu$, the thermalization process is very efficient, so all the released energy will be used to increment the entropy in the Universe. In this case, only the average temperature of the CMB would rise, and CMB spectral distortions would not occur. On the other hand, in the epoch at $z < z_\mu$, the thermalization process becomes less efficient, and released energy leads to CMB spectral distortions. Sunyaev and Zeldovich [97] provided the simple expressions,

$$\mu \approx 1.4 \left. \frac{\Delta\rho_\gamma}{\rho_\gamma} \right|_\mu, \tag{3.4}$$

$$y \approx \frac{1}{4} \left. \frac{\Delta\rho_\gamma}{\rho_\gamma} \right|_y. \tag{3.5}$$

These expressions can be used practically to predict residual distortion at high frequencies. However, the numerical calculation would be needed on the other frequency ranges. In Refs, the authors developed the cosmological thermalization code, named *COSMOTHERM*, which can solve the coupled photon – electron Boltzmann equation for a small CMB spectral distortion. This code allows us to compute the shape of the spectral distortions caused by energy release from several sources: dissipation of acoustic waves, decaying relic particles, and quasi-instantaneous heating.

Therefore, once the source function, $\langle \mathcal{S}_{\rm ac} \rangle$, for the dissipation of the primordial small-scale perturbations is known, the resulting spectral distortion can be obtained by calculating the weighted energy release in the μ- and y-era.

Since we are mainly interested in CMB distortions caused by the dissipation of acoustic waves much earlier than the cosmological recombination epoch, one can adopt the tight coupling approximation when computing the source term as [15]

$$\langle \mathcal{S}_{\rm ac} \rangle \approx \frac{\alpha_\nu}{\tau'} \partial_\eta k_{\rm D}^{-2} \int {\rm d}\log k\, k^2 \mathcal{P}_\zeta(k) 2 \sin^2 (k r_{\rm s})\, e^{-2k^2/k_{\rm D}^2}, \tag{3.6}$$

where

$$\alpha_\nu = \left(1 + \frac{4R_\nu}{15} \right)^{-2} \approx 0.81, \tag{3.7}$$

with the contribution of the energy density of massless neutrinos ρ_ν to the one of radiation ρ_γ,

$$R_\nu = \frac{\rho_\nu}{(\rho_\gamma + \rho_\nu)} \approx 0.41. \tag{3.8}$$

r_s denotes the sound horizon with the conformal time η calculated by

$$r_\mathrm{s} \approx c_\mathrm{s}\eta \approx 2.7 \times 10^5 (1+z)^{-1}\mathrm{Mpc}, \tag{3.9}$$

with the sound speed of the tightly-coupled baryon photon fluid,

$$c_\mathrm{s} = \frac{1}{\sqrt{3(1+R)}}, \tag{3.10}$$

and the baryon ratio,

$$R = \frac{3\rho_\mathrm{b}}{4\rho_\gamma} \approx 673(1+z)^{-1}, \tag{3.11}$$

where ρ_b is the baryon energy density. In Eq. (3.6), $\tau' = a\sigma_\mathrm{T} n_\mathrm{e} \approx 4.5 \times 10^{-7}(1+z)^2\mathrm{Mpc}^{-1}$ is the derivative Thomson scattering rate with respect to η, and k_D is the damping scale estimated by

$$k_\mathrm{D} \approx 4.0 \times 10^{-6}(1+z)^{3/2}\mathrm{Mpc}^{-1}, \tag{3.12}$$

with

$$\partial_\eta k_\mathrm{D}^{-2} = \frac{c_\mathrm{s}^2}{2\tau'}\left[\frac{R^2}{1+R} + \frac{16}{15}\right] \approx \frac{8}{45\tau'} \approx 3.9 \times 10^5 (1+z)^{-2}\mathrm{Mpc}. \tag{3.13}$$

In the limit of $R \ll 1$, the effective energy release rate in Eq. (3.3) is therefore given by

$$\begin{aligned}\frac{1}{\rho_\gamma}\frac{\mathrm{d}Q_\mathrm{ac}}{\mathrm{d}z} &\approx \frac{32\alpha_v c}{45\tau' H}\int \mathrm{dlog}k\, k^2 \mathcal{P}_\zeta(k) 2\sin^2(kr_\mathrm{s})\, e^{-2k^2/k_\mathrm{D}^2} \\ &\approx 9.4a \int \frac{k^2\,\mathrm{dlog}k}{k_\mathrm{D}^2}\mathcal{P}_\zeta(k) 2\sin^2(kr_\mathrm{s})\, e^{-2k^2/k_\mathrm{D}^2},\end{aligned} \tag{3.14}$$

which indicates that energy release happens when $k \sim k_\mathrm{D}$. Considering the ratio between the damping scale and the horizon scale as

$$\left.\frac{k_\mathrm{D}}{k_\mathrm{h}}\right|_{k_\mathrm{h}=aH} \approx 2(1+z)^{1/2}, \tag{3.15}$$

the dissipation of the acoustic mode induced by the primordial perturbations would occur well inside the horizon, for instance $50\mathrm{Mpc}^{-1} \lesssim k \lesssim 10^4\mathrm{Mpc}^{-1}$ for μ-distortion and $k \lesssim 50\mathrm{Mpc}^{-1}$ for y-distortion.

3.1.2 Relation with Primordial Power Spectrum

Of course, the released energy depends on the primordial power spectrum, $\mathcal{P}_\zeta$. In this context, the shape of $\mathcal{P}_\zeta$ is often parameterized by

$$\mathcal{P}_\zeta(k) = \mathcal{P}_\zeta^{\mathrm{CMB}}(k) + \Delta\mathcal{P}_\zeta(k), \tag{3.16}$$

where $\Delta\mathcal{P}_\zeta$ represents the deviation of the primordial power spectrum from the fiducial form [98],

$$\mathcal{P}_\zeta^{\mathrm{CMB}}(k) = \mathcal{A}_\zeta^{\mathrm{CMB}} \left(k/k_0\right)^{n_{\mathrm{s}}-1+\frac{1}{2}r_{n_{\mathrm{s}}}\ln(k/k_0)}, \tag{3.17}$$

with the adopted/derived parameters, $k_0 = 0.05$, $\mathcal{A}_\zeta^{\mathrm{CMB}} = 2.1 \times 10^{-9}$, $n_{\mathrm{s}} = 0.9641$, and $r_{n_{\mathrm{s}}} = -0.0045$ from the Planck CMB observation, which are summarized in Eq. (2.127).

With the simplifying assumption that we can neglect r_{s}, Ref. [15] provided the useful expressions for the total μ- and y-distortion from the fiducial power spectrum,

$$\begin{aligned} \mu_{\mathrm{ac}}^{\mathrm{CMB}} &\approx 5.54 \times 10^{-4} \mathcal{A}_\zeta^{\mathrm{CMB}} \exp\left(9.92 n_{\mathrm{s}}^{1.23}\right), \\ y_{\mathrm{ac}}^{\mathrm{CMB}} &\approx 2.85 \times 10^{-2} \mathcal{A}_\zeta^{\mathrm{CMB}} \exp\left(4.32 n_{\mathrm{s}}^{1.53}\right), \end{aligned} \tag{3.18}$$

with numerical perturbative calculations by *COSMOTHERM*.

Similarly, one can predict the CMB spectral distortion induced by the excess of the primordial power spectrum $\Delta\mathcal{P}_\zeta$ in Eq. (3.16) utilizing above equations and the *COSMOTHERM*. As one example, let us estimate them for the monochromatic power spectrum case,

$$\Delta\mathcal{P}_\zeta = \mathcal{A}_\zeta \delta\left(\log k - \log k_*\right). \tag{3.19}$$

Inserting Eq. (3.19) to Eq. (3.14), one can obtain the effective energy release rate for this monochromatic excess as

$$\frac{1}{\rho_\gamma}\frac{\mathrm{d}Q_{\mathrm{ac}}(z)}{\mathrm{d}z} \approx 18.8 a \mathcal{A}_\zeta \left(\frac{k_*}{k_{\mathrm{D}}}\right)^2 \sin^2\left(k_* r_{\mathrm{s}}\right) e^{-2k_*^2/k_{\mathrm{D}}^2}. \tag{3.20}$$

This expression suggests that a single k-mode's power will be released, taking the cosmological time at the redshift. The redshift where the energy is most released is

$$z_{\mathrm{peak}} \approx 4.5 \times 10^5 \left(\frac{k_*}{10^3 \mathrm{Mpc}^{-1}}\right)^{2/3}, \tag{3.21}$$

but while rapidly oscillating due to the sine part of the transfer function. Since the oscillation period is much shorter than the energy release time scale, one can take the time averaging for the sine term, which yields

$$\frac{1}{\rho_\gamma}\frac{\mathrm{d}Q_{\mathrm{ac}}}{\mathrm{d}z} \approx 9.4 a \mathcal{A}_\zeta \left(\frac{k_*}{k_{\mathrm{D}}}\right)^2 e^{-2k_*^2/k_{\mathrm{D}}^2}. \tag{3.22}$$

Then using Eqs. (3.4) and (3.5), one can analytically obtain the approximated expressions of μ- and y-distortion at high frequencies as

$$\mu_{\rm mono} \approx 2.2\mathcal{A}_\zeta \left[\exp\left(-\frac{k_*}{5400{\rm Mpc}^{-1}}\right) - \exp\left(-\left(\frac{k_*}{31.6{\rm Mpc}^{-1}}\right)^2\right)\right], \tag{3.23}$$

and

$$y_{\rm mono} \approx 0.4\mathcal{A}_\zeta \exp\left(-\left(\frac{k_*}{31.6{\rm Mpc}^{-1}}\right)^2\right). \tag{3.24}$$

It should be noted that these expressions are valid only for $k_* \gtrsim 5{\rm Mpc}^{-1}$. On larger scales, the numerical calculations implemented by *COSMOTHERM* might be powerful.

3.1.3 Limits from the COBE/FIRAS observation

Among the existing observational limits of the CMB distortion, the COBE/FIRAS limit would be the most powerful [20],

$$\mu \lesssim 9 \times 10^{-5}, \tag{3.25}$$

$$y \lesssim 1.5 \times 10^{-5}, \tag{3.26}$$

which are 2σ upper limits. These constraints can impose a strong upper bound on the amplitude of the primordial power spectrum. Figure 3.1 shows the resulting limits with the assumption of the step-like primordial power spectrum as

$$\mathcal{P}_\zeta = \begin{cases} \mathcal{A}_\zeta^{\rm CMB}\left(\frac{k}{k_0}\right)^{n_{\rm s}-1} & k \leq k_{\rm s}, \\ (\mathcal{A}_\zeta^{\rm CMB} + \mathcal{A}_\zeta^{\delta})\left(\frac{k}{k_0}\right)^{n_{\rm s}-1} & k > k_{\rm s}. \end{cases} \tag{3.27}$$

The blue-shaded region shows the limit from the y-distortion measurement, and the yellow-shaded region represents the one from the μ-distortion measurement by COBE/FIRAS. The limits from the μ-distortion measurement are most stringent in the range of $k < 10^3{\rm Mpc}^{-1}$. That is because the thermalization process becomes very efficient at smaller scales. As seen in Fig. 3.1, the limits obtained by the y-distortion measurement by COBE/FIRAS are weaker than the one of μ-distortion.

Figure 3.1 also displays the constraint foreseeing by the PIXIE-like measurements. In the PIXIE-like measurement, the following 2σ detection limits are expected [29],

$$\mu^{\rm PIXIE} \simeq 2 \times 10^{-8}, \tag{3.28}$$

$$y^{\rm PIXIE} \simeq 4 \times 10^{-9}. \tag{3.29}$$

Then the limit on the total amplitude of the power spectrum would be much improved, like the light blue region in Fig. 3.1. The difference of line styles in Fig. 3.1 represents the difference in the value of the spectral index $n_{\rm s}$. The bending feature in the PIXIE limit curve of $n_{\rm s} = 1, 1.05, 1.1$ comes from the fact that the value of $\mu(k > k_{\rm s})$ itself already exceeds $\mu^{\rm PIXIE}$ in Eq. (3.28).

However, unfortunately, the PIXIE project was not selected(funded) and is stopping now. Therefore, the current most robust limit from the CMB distortion is the one of the μ-distortion measurement by COBE/FIRAS represented by a yellow region surrounded by the dash-dot line ($n_s \sim 0.95$) in Fig. 3.1. Although there are other future projects proposed to measure the μ- and y-distortion in the CMB spectrum such as PRISM [25], PRISTINE [26], SuperPIXIE [27] and Voyage2050 [28], they have not been selected yet.

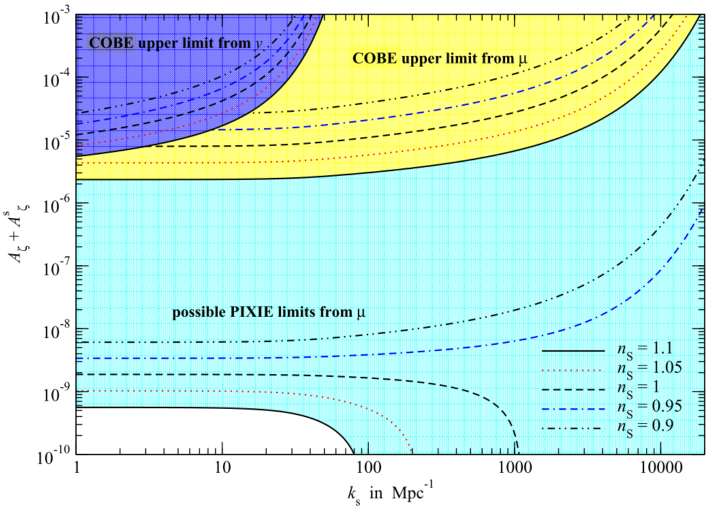

FIGURE 3.1: Limits on the total amplitude of the primordial power spectrum with a step-like excess in $k > k_s$. This figure is adapted from Chluba *et al.* [32].

3.2 Primordial black hole

PBHs are theoretically suggested as produced due to strongly amplified primordial perturbations. An overdense region with largely enhanced primordial perturbations would gravitationally collapse after entering the horizon, forming PBH [99], [100]. Since the 2010s, PBH has been gathering attention for two main reasons. One reason is that the first direct detection of GWs by the LIGO/Virgo collaboration sheds light on the possibility that the observed massive black holes might be of primordial origin [101]. The other one originates from their possibility as a main component of DM which has been still opened in a light mass region $\sim 10^{-10}\mathrm{M}_\odot$. Therefore, studying the PBH abundance gives us insights into not only the primordial density fluctuations on small scales but also DM. We do not explain the details of PBHs as DM, which is beyond our scope in this thesis. However, Carr, Kohri, Sendouda, *et al.* [102] might be useful for studying them. Here we discuss the PBH abundance concerning the primordial perturbation on small scales. We refer to Ref. [103] for this discussion.

3.2.1 Abundance of PBHs

So far, the abundance of PBHs has been investigated in various ways. The Press – Schechter formalism, as explained in Sec. 2.10.3, would supply the simplest way. This formalism allows us to estimate the abundance of collapsed objects (PBHs in this case) by the probability that the locally averaged value of the random density contrast field exceeds a given critical value. Carr [34] firstly evaluated the critical value to form PBH in terms of the density contrast as $\delta_{\mathrm{c,PBH}} \sim w = 1/3$ in the RD epoch, where $w = p/\rho$ denotes an equation of state parameter with the pressure p and the energy density ρ of the cosmic fluid. Subsequently, Refs. [104]–[106] estimated this value more accurately in various analytic or numerical approaches. However, these results do not match well, suggesting the difficulty of predicting PBH abundance with the Press – Schechter formalism and the necessity to take into account the detailed local profile of overdensities.

Recently, several works proposed the *compaction function* with the peak theory as a better indicator for the PBH formation [107], [108]. In a spherically symmetric case, the compaction function $\mathcal{C}$ is defined by the difference between the Misner – Sharp mass M_{MS},

$$M_{\mathrm{MS}} = 4\pi \int_0^R \rho R'^{\,2}\, \mathrm{d}R', \tag{3.30}$$

and the mass M_{bg} enclosed in the background Universe within the areal radius R,

$$M_{\mathrm{F}} = \frac{4\pi}{3} \bar{\rho} R^3, \tag{3.31}$$

as

$$\mathcal{C} = \frac{M_{\mathrm{MS}} - M_{\mathrm{F}}}{4\pi M_{\mathrm{Pl}}^2 R}, \tag{3.32}$$

on a comoving slice, where $\bar{\rho}$ is the background energy density, and M_{Pl} denotes the reduced Planck mass. It should be noted that this compaction function represents the average value of the density contrast $\delta\rho = (\rho - \bar{\rho})/\bar{\rho}$ when the mode reentries the horizon $RH = 1$ as

$$\mathcal{C} = (RH)^2 \times \left(4\pi \int_0^R \delta R'^{\,2}\, \mathrm{d}R' \right) \Big/ \left(\frac{4\pi}{3} R^3 \right). \tag{3.33}$$

Let us define the curvature perturbation ζ via the spatial metric as

$$\mathrm{d}s_3^2 = a^2(t) \mathrm{e}^{2\zeta(t,\mathbf{x})} \tilde{\gamma}_{ij}\, \mathrm{d}x^i\, \mathrm{d}x^j, \tag{3.34}$$

where $\det \tilde{\gamma} = 1$. The comoving density contrast relates to ζ as

$$\delta = -\frac{4(1+w)}{5+3w} \frac{1}{a^2 H^2} \mathrm{e}^{-5\zeta/2} \Delta \mathrm{e}^{\zeta/2} \overset{RD}{=} -\frac{8}{9} \frac{1}{a^2 H^2} \mathrm{e}^{-5\zeta/2} \Delta \mathrm{e}^{\zeta/2}, \tag{3.35}$$

where we put $w = 1/3$ in the second equality. Considering the expression of the areal radius, $R(r) = a\mathrm{e}^{\zeta} r$, one can obtain the simple form of the compaction function,

$$\mathcal{C}(r) = \frac{2}{3} \left[1 - \left(1 + r\zeta'\right)^2 \right]. \tag{3.36}$$

This expression would be conserved on superhorizon scales due to the feature of ζ as mentioned in Chapter 2. One of the criteria regarding $\mathcal{C}$ for the PBH formation would be whether the innermost maximum value of $\mathcal{C}$ at some radius r_{m} exceeds some threshold or not. However Refs. [106], [109] suggested that the threshold value in terms of $\mathcal{C}(r_{\mathrm{m}})$ slightly changes depending on the peak profile. The more universal and profile-independent indicator would be the averaged compaction function which is defined by

$$\overline{\mathcal{C}}_{\mathrm{m}}=\left(4\pi\int_{0}^{R(r_{\mathrm{m}})}\mathcal{C}(r)\tilde{R}^{2}(r)\mathrm{d}\tilde{R}(r)\right)\Big/\left(\frac{4\pi}{3}R^{3}\left(r_{\mathrm{m}}\right)\right). \tag{3.37}$$

Refs. [106], [109] suggested the universal threshold value as $\overline{\mathcal{C}}_{\mathrm{m}}^{\mathrm{th}}=2/5$, in this case.

Figure 3.2 shows the limit on the primordial power spectrum by the nondetection of PBHs through several ways. We take this figure from Ref. [110]. In Fig. 3.2, the green dashed line shows the limit from measurements of FRB lensing [111]. The green dash-dot line shows the one from caustic-crossing stars [112], and the yellow solid and dashed lines represent limits obtained by measurements of known pulsars and SKA pulsars respectively [113]. The pink dot and dashed line show the constraint from the measurement of the merger rate by LIGO [101] and the stochastic GW background [114] respectively. The current observational constraints are merged, and the most stringent bound is shown in solid blue. The solid grey line comes from the limitation that the density of PBHs cannot exceed that of DM.

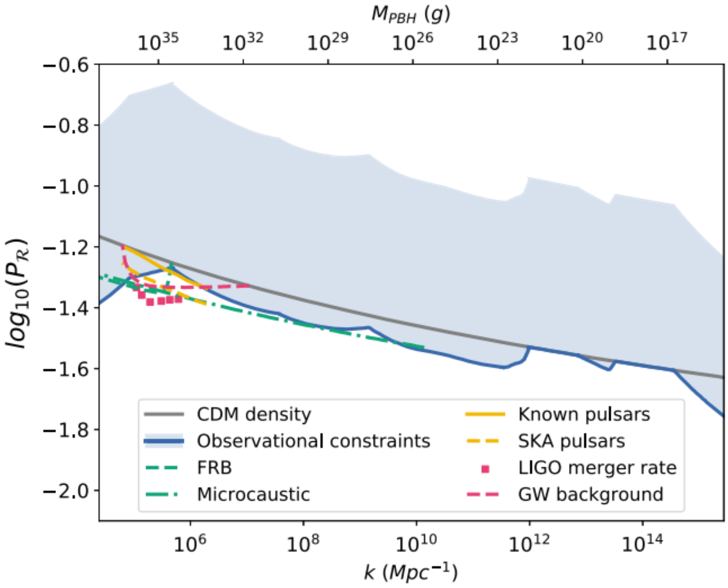

FIGURE 3.2: Limits on the amplitude of the primordial power spectrum from exploring PBHs in several ways: measurements of FRB lensing (FRB) [111], caustic-crossing stars (microcaustic) [112], pulsar timing (known pulsars and SKA pulsars) [113], the merger rate from LIGO [101], and the stochastic GW background [114]. The current observational constraints are merged, and the most stringent bound is shown in solid blue. The solid grey line comes from the limitation that the density of PBHs cannot exceed that of DM. This figure is taken from Ref. [110].

Before finishing the discussion of PBHs, we should stress that the limit on primordial power spectrum obtained by the nondetection of PBHs is much weaker than other constraints like the CMB distortion measurements, as seen in Fig. 3.2. That is because PBH must be a rare object formed by a large-amplitude perturbation by chance from the request that the PBH energy density cannot exceed that of DM.

3.3 Galaxies and small-mass DM halo

As the galaxy clusters distribution indicates the large-scale matter density perturbations, measurements for smaller objects like galaxies or small-mass halos would provide information about the smaller-scale perturbations.

3.3.1 UV Luminosity function of high redshift galaxies

One of the powerful observables would be the UV Luminosity Function (LF) of high redshift galaxies. Recently Ref. [69] presented new measurements of the matter power spectrum on small scales, $0.5\text{Mpc}^{-1} < k < 10\text{Mpc}^{-1}$, at $\sim 30\%$ precision level, using high-redshift UV galaxy LF data from the Hubble Space Telescope. The UV galaxy LF captures the abundance of galaxies as a function of their luminosity at different epochs. Therefore it contains a wealth of information on the physics of cosmological structure formation at small scales.

Let us briefly give a review of the connection between the UV galaxy LF and the small-scale perturbation (see Ref. [69] for detail). The UV galaxy LF is defined as the comoving number density of galaxies per unit magnitude of luminosity,

$$\Phi_{\rm UV} = {\rm d}n_{\rm gal}\,/{\rm d}M_{\rm UV}, \tag{3.38}$$

where $M_{\rm UV}$ denotes the absolute UV magnitude of the galaxies. For simplicity, let us assume that one halo hosts one central galaxy. In that case, UV galaxy LF can be written by

$$\Phi_{\rm UV} = \frac{{\rm d}n_{\rm halo}}{{\rm d}M_{\rm halo}} \times \frac{{\rm d}M_{\rm halo}}{{\rm d}M_{\rm UV}}, \tag{3.39}$$

where $dn_{\rm halo}/dM_{\rm halo}$ represents the halo mass function like the one of Press-Schechter formalism represented in Eq. (2.150), and $dM_{\rm halo}/dM_{\rm UV}$ is the relation between halo mass and the UV magnitude of the galaxies residing inside the halo. Here we adopt a double-power law,

$$f_* = \frac{\dot{M}_*}{\dot{M}_{\rm halo}} = \frac{\epsilon_*}{\left(\frac{M_{\rm halo}}{M_c}\right)^{\alpha_*} + \left(\frac{M_{\rm halo}}{M_c}\right)^{\beta_*}}, \tag{3.40}$$

to relate mass accretion rates of star and halo, where $\alpha_* \leq 0$ and $\beta_* \geq 0$ control the slope of the faint and bright end of the UV galaxy LF respectively, $\epsilon_* \geq 0$ regulates the star-formation efficiency, and $M_c \geq 0$ denotes the peak mass of the star-formation rate. These four are free parameters to be fitted by observational data. The relation between the star mass accretion rate $\dot{M}_*$ and the UV luminosity $L_{\rm UV}$ is given by [115], [116]

$$\dot{M}_* = \kappa_{\rm UV} L_{\rm UV}, \tag{3.41}$$

where $\kappa_{\rm UV} = 1.15 \times 10^{-28} M_\odot {\rm s\,erg}^{-1}{\rm yr}^{-1}$ [117]. The luminosity can be converted to $M_{\rm UV}$ via their relation [118],

$$\log_{10}\left(\frac{L_{\rm UV}}{\rm erg\ s^{-1}}\right) = 0.4\,(51.63 - M_{\rm UV})\,. \tag{3.42}$$

For the halo mass accretion rate $\dot{M}_{\mathrm{h}}$, we adopt the extended Press-Schechter formalism. Then one can obtain $\dot{M}_{\mathrm{h}}$ by determining cosmological parameters.

Combining the above ingredients, one can obtain the UV galaxy LF as a function of cosmological and astrophysical parameters. Therefore, one can explore such parameters regarding the small-scale physics through a statistical analysis like Markov chain Monte Carlo (MCMC) with cosmological observations like CMB and the measurements of UV LF of high redshift galaxies by, e.g., Hubble Space Telescope (HST) [119], [120].

Figure 3.3 shows the result for measurements of the matter power spectrum at $z = 0$. The two black data points are the joint analysis results between the Planck observation and the UV galaxy LF data from HST [121]. The blue, green, and purple data points represent the results obtained by Planck 2018 TT, EE, and $\phi\phi$ data, respectively [1]. The pink data point represents the result from observation data of Dark Energy Survey (DES) cosmic shear [122]. The orange and yellow data points show the ones of SDSS galaxy clustering [123] and SDSS Lyman-α [124] data, respectively. The black line is the prediction within ΛCDM, using the best-fit values from Planck 2018 [1].

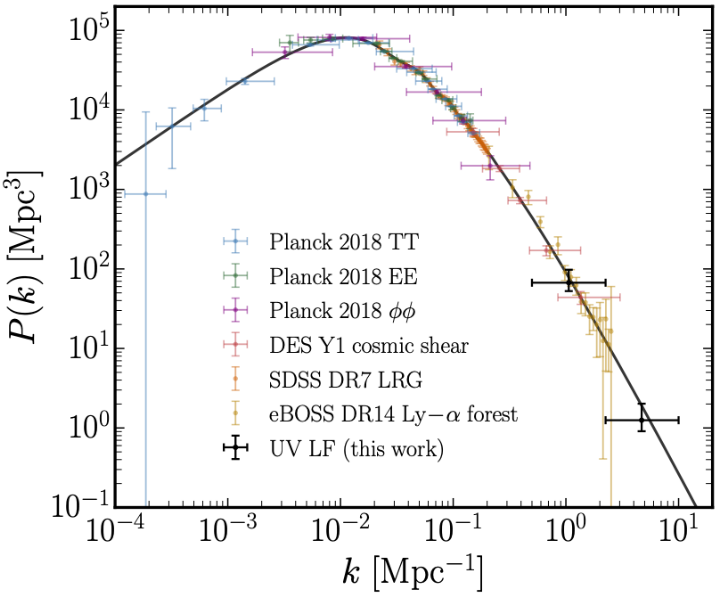

FIGURE 3.3: Measurements of the matter power spectrum at $z = 0$. The two black data points are the results obtained by the joint analysis between the Planck observation and the UV galaxy LF data from HST [121]. The blue, green, and purple data points represent the results obtained by Planck 2018 TT, EE, and $\phi\phi$ data, respectively [1]. The pink data point represents the result from observation data of Dark Energy Survey (DES) cosmic shear [122]. The orange and yellow data points show the ones of SDSS galaxy clustering [123] and SDSS Lyman-α [124] data, respectively. The black line is the prediction within ΛCDM, using the best-fit values from Planck 2018 [1]. All uncertainties in this figure are at 68% CL. This figure is adapted from Ref. [121].

In Fig. 3.3, one can find that the matter power spectrum is consistent with the theoretical spectrum predicted in a standard ΛCDM cosmology up to $k \sim 10\mathrm{Mpc}^{-1}$, where other large-scale observation have not reached yet.

3.3.2 Free-free emission from DM halos

The measurements of free-free emission signals from DM halos also provide information about the smaller-scale perturbations.

When a charged particle is deflected by another charged particle, especially an electron by a proton in an ionized gas hosted by DM halos in this thesis, electromagnetic radiation would be produced due to the deceleration. In this process, the moving charged particle loses kinetic energy, which is converted into photons following the energy conservation law. This radiation is often created by the transition of electrons from one free state to another free state. Here the word “free" means that another particle, like protons, does not bind the electron. Therefore, this emission is called free-free emission[1]. One feature of free-free emission is that the spectrum is continuous and flat.

As we will see the detail in Chapter 4, the dominant contribution to free-free emission from DM halos comes from relatively small-mass halos. Therefore, if we measure it accurately, we can know the abundance of small-mass halos and thus get an insight into the primordial small-scale perturbations through, e.g., investigations of $n_{\rm s}$ on small scales like UV galaxy LF measurements.

3.4 Ultracompact minihalos

UCMHs are beyond standard structures, which might be formed earlier than the standard DM halos by the excess power of primordial perturbations on small scales. In general, the primordial perturbations induce density fluctuations which grow gravitationally even in the RD epoch. Through the growth, the overdense region on small scales finally collapses into the nonlinear structures called UCMHs in higher redshifts than the standard hierarchical structure formation due to the scale-invariant primordial perturbations [71]. For instance, the overdensity regions with the large density contrast, $\delta > 10^{-3}$, at the horizon entry can form UCMHs around $z \sim 1000$, which is much before the standard structure formation history.

In order to consider the linear growth of DM density fluctuations, the Meśzáros equation [125] is useful,

$$\frac{d^2\delta}{dy^2} + \frac{2+3y}{2y(y+1)}\frac{d\delta}{dy} - \frac{3}{2y(y+1)}\delta = 0. \tag{3.43}$$

Here $y \equiv a/a_{\rm eq}$, and $a_{\rm eq}$ shows the scale factor at the matter-radiation equality. This equation describes the linear growth of DM density perturbations on subhorizon scales, assuming that we can neglect the baryon and photon density perturbation. One can obtain the physical solution for the Meśzáros equation in Eq. (3.43) by matching the linear growth rate in RD, $\delta \propto \log(0.44a/a_{\rm H})$, with the scale factor at the horizon entry of a given mode. This physical solution would be [126]

$$\delta \propto \left[\log\left(\frac{k}{0.12h{\rm Mpc}^{-1}}\right) - \log\left(\frac{\sqrt{1+y}+1}{\sqrt{1+y}-1}\right)\right]\left(y+\frac{2}{3}\right) + 2\sqrt{1+y}, \tag{3.44}$$

---

[1] More broadly speaking, radiation created by a deceleration of a charged particle is called bremsstrahlung. Bremsstrahlung includes not only free-free emission but also synchrotron radiation, cyclotron radiation, and the emission of electrons and positrons during beta decay. Also, free-free emission is produced by the thermal motion of electrons; thus, this is one kind of thermal emission.

which can be a convenient prescription for the linear growth rate of the DM density perturbation during the MD and RD epochs. The criteria for forming UCMHs are given by whether the linearly evolved density field has a peak larger than the linear density threshold for collapse, $\delta_{\rm c} = 1.686$, in the same way as the standard DM halo formation.

Since UCMHs could be formed by the radial infalling in high redshifts, UCMHs are assumed to have a more compact profile with a larger central density than typical DM halos in the standard hierarchical structure formation. Ricotti and Gould [71] firstly suggested that UCMHs has a strongly steep profile, $\rho \propto r^{-9/4}$ by the analytical work of Ref. [127]. This compactness greatly boosts the observational signals, and UCMHs had therefore attracted attention in the astrophysical and cosmological context. However, this unusual compactness, $\rho \propto r^{-9/4}$, is theoretically derived in an idealized picture including spherical symmetry, radial motion, and self-similarity. In fact, it had not been reproduced in N-body simulations from realistic conditions [128]–[130], although it can be reproduced from carefully tuned self-similar initial conditions[2] [131], [132].

The first cosmological simulation of the UCMH formation has been done by Ref. [133]. They revealed that a large amplitude on small scales actually leads to early structure formation, and the resultant DM halos are compact. Recent numerical simulations by Delos, Erickcek, Bailey, *et al.* [72], [73] showed that UCMHs originating from the spike-type spectrum on small scales have the Moore profile, $\rho \propto r^{-3/2}$, rather than the conventional profile, $\rho \propto r^{-4/9}$, at the inner cusp region [134]. This profile is still steeper than the Navarro-Frenk-White (NFW) profile which represents the density profile of the standard DM halo expected in the N-body simulation [135],

$$\rho(r) = \frac{\rho_s}{(r/r_s)\,(1 + r/r_s)^2}, \tag{3.45}$$

where $\rho_{\rm s}$ is the scale density, and $r_{\rm s}$ shows the scale radius. Hereafter in this thesis, we define UCMH as a collapsed object originating from the spike-type spectrum on small scales and having the Moore-type density profile inside.

3.4.1 Abundance of UCMHs

In our assumption, we posit the presence of a spike-type power spectrum on a specific small scale in addition to the almost scale-invariant spectrum with an amplitude of $\mathcal{A}_\zeta^{\rm CMB} \sim 2.1 \times 10^{-9}$ as measured by Planck CMB observations. For the sake of simplicity, we employ the Dirac delta function to represent this additional spike-type power spectrum as,

$$\mathcal{P}_\zeta^{\rm add}(k) = \mathcal{A}_\zeta^{\rm add} k_{\rm s} \delta(k - k_{\rm s}), \tag{3.46}$$

where $\mathcal{A}_\zeta^{\rm add}$ is the amplitude of the additional power spectrum, and $k_{\rm s}$ is the wave number corresponding to the spike center.

In the spike-type power spectrum case, the initial mass of UCMHs $M_{\rm i}$ are related to the spike-wave number $k_{\rm s}$ as

$$M_{\rm i} \sim 4 \times 10^4 \, M_\odot \times \left(\frac{k_{\rm s}}{10^3\ {\rm Mpc}^{-1}} \right)^{-3}. \tag{3.47}$$

---

[2] In reality, a Gaussian random field spreads in the Universe. The self-similarity would be ruled out by its appearance in the field.

The number density of UCMHs can be calculated by utilizing the peak theory as outlined in Sec. 2.10.4, which is formulated for the case of a monochromatic power spectrum. This is because UCMHs are expected to form at the locations of density fluctuation peaks, as dictated by the peak-type power spectrum outlined in Eq. (3.46) in this scenario. Following the peak theory, the UCMH number density can be obtained by

$$n(M_{\rm i}, z) = \frac{3^{3/2} k_s^3}{(2\pi)^2} \int_{\delta_c / S_{\rm mat,0}^{1/2}(M_{\rm i}) D(z)}^{\infty} e^{-\nu^2/2} f(\nu) \mathrm{d}\nu, \tag{3.48}$$

where $S_{\rm mat,0}$ is the present mass variance of the matter density fluctuation, and $f(\nu)$ is the function represented in Eq. (2.161). It is worth noting that the expression for the number density in Eq. (3.48) does not take into account any merger effects of UCMHs, which have been neglected in this thesis.

With regards to the relation between the additional spike-type power spectrum, as outlined in Eq. (3.46), and the present mass variance, $S_{\rm mat,0}$, it is important to understand that $S_{\rm mat,0}$ is calculated from the power spectrum of the primordial curvature perturbations, $\mathcal{P}_\zeta(k)$, via

$$\begin{aligned} & S_{\rm mat,0}(M) \\ & = \int d\log k \, \frac{4}{25} \frac{k^4}{\Omega_{\rm m,0}^2 H_0^4} \mathcal{P}_\zeta(k) C_\Lambda^2 T_\delta^2(k) \tilde{W}_k^2(kR(M)) \\ & \equiv C_\Lambda^2 \, \mathcal{A}_{\rm mat,0}(M), \end{aligned} \tag{3.49}$$

where $\tilde{W}_k(x)$ is the Fourier function of the window function, $R(M)$ is the comoving scale enclosing the mass M in the background matter density $\rho_{\rm m,0}$, $T_\delta(k)$ is the transfer function for the matter density fluctuations during the MD epoch as shown in Sec. 2.10.1, and $C_\Lambda \approx 0.79$ is the correction factor for the growth rate during the late-time Λ dominated epoch, which is estimated by the growth factor in the epoch [136]. In the second line of Eq. (3.49), we have introduced the new mass variance parameter, $\mathcal{A}_{\rm mat,0}$. By utilizing this parameter, it is possible to estimate the mass variance at an alternative redshift in the MD epoch by $\mathcal{A}mat, 0/(1+z)^2$.

Given our interest in the mass variance $\mathcal{A}_{\rm mat,0}(M_{\rm i})$, the dominant contribution to the mass variance in Eq. (3.49) is expected to come from the additional power spectrum, $P_\zeta^{\rm add}(k_{\rm s})$. By utilizing the pointwise window function for the $\tilde{W}_k$, as originally proposed in the peak theory [87], $\mathcal{P}_\zeta(k)\tilde{W}k^2(kR)$ in Eq. (3.49) attains its maximum value at ks. Therefore, Eq. (3.49) can be approximately written as

$$\mathcal{A}_{\rm mat,0}(M_{\rm i}) \approx \frac{4}{25} \frac{k^4}{\Omega_{\rm m,0}^2 H_0^4} \mathcal{P}_\zeta^{\rm add}(k) T^2(k) \bigg|_{k=k_{\rm s}} . \tag{3.50}$$

It can be inferred from Eq. (3.50) that the abundance of UCMHs is linked to the properties of the additional spike-type power spectrum, specifically $\mathcal{A}_\zeta^{\rm add}$ and $k_{\rm s}$. However, it is important to note that this approximation is only valid when the mass variance contributed by the additional spike-type spectrum is significantly greater than the one stemming from the almost scale-invariant spectrum, with an amplitude of $\mathcal{A}_\zeta^{\rm CMB} \simeq 2 \times 10^{-9}$. Figure 3.4 illustrates the present mass variance parameter estimated by the almost scale-invariant spectrum. To satisfy the aforementioned condition, the value of the mass variance parameter from the additional spike-type spectrum must be larger than $\mathcal{A}_{\rm mat,0}^{\rm CMB}$, as depicted in Fig. 3.4, for each initial UCMH mass.

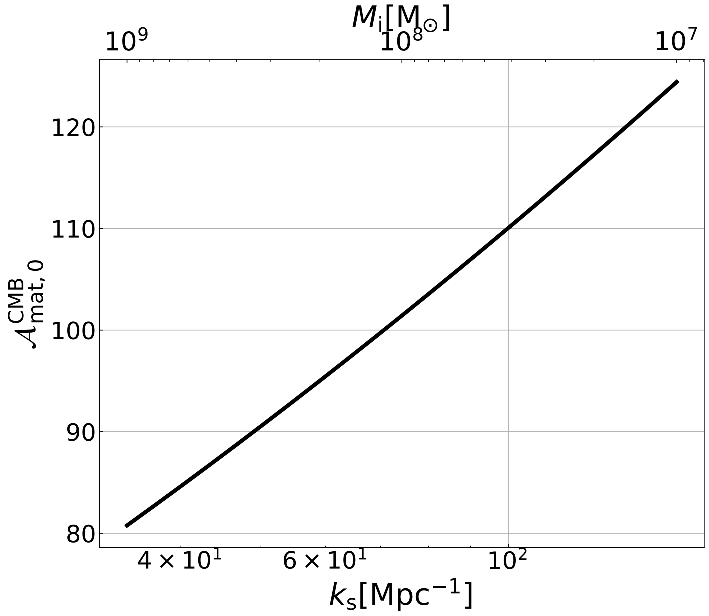

FIGURE 3.4: Mass variance parameter at present which originates from the almost scale-invariant spectrum with the amplitude $\mathcal{A}_\zeta^{\rm CMB} \simeq 2.1 \times 10^{-9}$ in the scale of $k_{\rm s}$ corresponding to the initial mass of UCMHs of $M_{\rm i}$. In order to validate the approximation in Eq. (3.50), the value of the mass variance coming from $\mathcal{P}_\zeta^{\rm add}$ at $k_{\rm s}$ should be larger than $\mathcal{A}^{\rm CMB}_{\rm mat,0}(k_{\rm s})$.

3.4.2 The observational limit

One can obtain a strong insight into primordial small-scale perturbation from measurements of the UCMH abundance through their relation represented by Eq. (3.48). Here we briefly review the current observational limit on the UCMH abundance.

If DM is of the particle type, particularly the weakly interacting massive particle (WIMP) [137]–[139], UCMHs would emit energetic emissions through the enhancement of WIMP annihilation due to their dense profiles. To date, various studies [72]–[78] have investigated the gamma-ray emission signal and imposed constraints on the abundance of UCMHs. Furthermore, these studies have also provided constraints on small-scale primordial scalar perturbations, with $\mathcal{A}_\zeta < 10^{-7}$ for $10\ {\rm Mpc}^{-1} < k < 10^8\ {\rm Mpc}^{-1}$, through the non-detection of such energetic signals in gamma-ray observations such as Fermi-LAT [140]. Additionally, UCMHs have been investigated through their gravitational lensing effect [77], [141] and their contribution to cosmic reionization [142]–[145].

Figure 3.5 shows the main constraint on the UCMH abundance. This figure is adapted from Ref. [76]. In this figure, the purple line represents the limit on large scales from the CMB, LSS, Lyman-α observations[146]–[148]. The black dashed line shows the limit from PBHs as shown in Fig. 3.2. The blue dashed line represents the limit from the contribution of UCMHs on the cosmic reionization through their WIMP annihilation. The solid red line shows the limit obtained by the nondetection of gamma-ray emission from UCMHs through the Fermi-LAT mission [140].

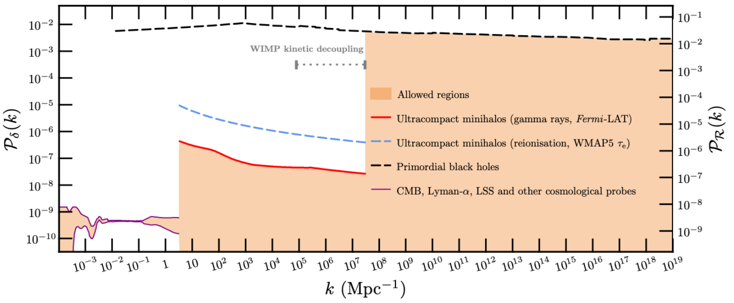

FIGURE 3.5: Limits on the amplitude of primordial density and curvature perturbations, $\mathcal{P}_\delta$ and $\mathcal{P}_\zeta$ respectively, at wide scales. The purple line shows the limit on large scales from the CMB, large scale structure, Lyman-α observations[146]–[148]. The black dashed line shows the limit from PBHs as shown in Fig. 3.2. The blue dashed line shows the limit coming from the measurements of the UCMH contribution to the cosmic reionization through their WIMP annihilation. The solid red line represents the limit obtained by the nondetection of gamma-ray emission from UCMHs through the Fermi-LAT mission. For ease of reference, the range of possible DM kinetic decoupling scales for some indicative WIMPs is plotted by the grey dotted line [149]. This figure is adapted from Ref. [76].

In the current status where there are no funded projects to measure the CMB distortion and with the fact that the measurements of UCMHs can limit on primordial power spectrum stronger than ones of PBHs, the studies of UCMHs would be attracting the attention more and more. For example, the constraint from the nondetection of the energetic signals from UCMH in gamma-ray observations is very powerful, even compared to the COBE/FIRAS limit. However, it should be stressed that this constraint highly depends on the parameters of WIMP. Furthermore, ground experiments like *Xenon1T* have been putting a tighter constraint on the WIMP parameter year after year [150]. Then it might happen that the commonly used value of the parameter, $m_\chi \sim 1$TeV, would be excluded by the future coming experiment. Based on the above, new measurements which can more deeply explore the primordial power spectrum have been demanded.

3.4.3 Baryonic effects from UCMHs

We have been establishing a DM-model independent approach to UCMHs, focusing on the signals from baryon gas in UCMHs. If the mass of UCMHs is heavier than the Jeans mass, UCMHs will host baryon gas in the same way as the standard DM halos. Then the baryon gas emits several cosmological signals like 21-cm line emission/absorption. This doctoral dissertation represents our study to investigate these signals from UCMHs.

21-cm line emission/absorption background

In Chapter 5, we study the 21-cm line emission/absorption background induced by UCMHs. Depending on their mass, UCMHs can host abundant neutral hydrogen gas. Therefore, redshifted 21-cm observations can probe the abundance of UCMHs [151]. We show that SKA can provide a stringent limit on the abundance of UCMHs and the amplitude of the primordial perturbations.

Astrophysical effects

Astrophysical effects that occurred in UCMHs, e.g., the formation of first-generation stars, would be powerful probes for UCMHs. In Chapter 6, we discuss the formation of the first stars and investigate their effects on the global cosmic ionization history in the method of MCMC analysis with Planck CMB anisotropy observation data.

Chapter 4

Free-free emission from DM halos

Investigation of diffuse background-free-free emission from dark matter (DM) halos is the focus of our study. Given that DM halos are known to contain ionized thermal plasma, they could be a substantial source of cosmological free-free emission. We assess the intensity of the global background and the anisotropy of this emission and deduce that the major contribution arises from DM halos with a mass comparable to the Jeans mass, i.e., $M_{\rm halo} \sim 10^{10} M_{\odot}$, at a redshift of approximately $z \sim 3$. This implies that the intensity of the free-free emission is dependent on primordial small-scale perturbations that produce such small-mass DM halos. We determine that the intensity of the global and anisotropic free-free emission is less than 10% of the free-free emission observed in high galactic-latitude regions. We also find that the free-free emission signal is subject to $\sim 20\%$ modification, even in cases where the spectral index and the running are consistent with recent Planck results. As such, measuring cosmological free-free signals could provide more stringent constraints on the abundance of small-mass DM halos and curvature perturbations, including the spectral index and running. However, to achieve this, the Galactic free-free emission must be carefully removed through multifrequency radio observations, cross-correlation studies with galaxy surveys or 21-cm intensity maps.

4.1 Introduction

The Planck space mission was designed to measure cosmic microwave background (CMB) anisotropies with unprecedented accuracy. The observation results obtained by Planck are consistent with the hypothesis of primordial curvature perturbations that are almost scale-invariant, adiabatic, and Gaussian [1]. Furthermore, when combined with galaxy surveys [152], [153], it is possible to confirm that these statistical features extend from the present horizon scale to the 1 Mpc scale [154]. Probing the statistical nature of the primordial curvature perturbations can provide insight into the early Universe, particularly the inflation model. Notably, the observed statistical features are consistent with the predictions of a simple inflation model, specifically the slow roll inflation model with a single scalar field [9] (for a review, see e.g. Ref. [8]).

One of the next goals in modern cosmology is to reveal the primordial curvature perturbations on a smaller scale than the Mpc scale. In this context, CMB distortion can serve as a powerful probe [10]–[12]. Although small-scale perturbations are smoothed out by the Silk damping effect, the energy flows dissipated during this process create distortions in the blackbody spectrum of the CMB energy spectrum [13]–[15]. Thus, measurements of CMB distortion can provide a deeper understanding of small-scale perturbations [14], [16]–[19].

In fact, from the measurements of CMB distortion by the COBE/FIRAS instrument, a constraint on the primordial power spectrum was suggested, specifically that $P_\zeta \lesssim 10^{-5}$ for the wave number range $k \approx 1 - 10^4\ \mathrm{Mpc}^{-1}$ [16]. Additionally, it is anticipated that with next-generation CMB measurements such as PIXIE [28], this constraint will be improved to the order of $P_\zeta \lesssim 10^{-8}$.

In the future, measurements of the redshifted 21-cm signal are also expected to be beneficial in determining small-scale perturbations. As the 21-cm signal is emitted through the transition of neutral hydrogen, in which the electron flips its spin, measurements of the spatial fluctuations in the redshifted 21-cm signal can trace the evolutionary history of matter density fluctuations prior to the epoch of reionization (for a comprehensive review, see Ref. [155]). Redshifted 21-cm measurements have the potential to explore density perturbations on smaller scales than the Silk scale [156]. To accomplish these measurements, the Square Kilometre Array project, which aims to construct the largest radio telescope with over a square kilometer of collecting area, is currently in progress.

This work centers on diffuse background free-free emission as a means of investigating small-scale perturbations. The study of diffuse background free-free emission has been conducted in relation to foreground components such as the CMB in the microwave and radio frequency range. While the majority of observed free-free emission is believed to have a Galactic origin, free-free emission with cosmological origins also exists, such as in the intergalactic medium (IGM) [157], galaxy groups and clusters after reionization [158], and during the formation of structures during reionization [159]. Among these sources, the contribution from DM halos may be the most significant [160].

In this study, we re-examine the free-free emission from DM halos in the standard ΛCDM cosmology by considering the impact of small-scale primordial curvature perturbations. Specifically, we investigate the dependency on the spectral index n_s of the primordial power spectrum and the running r_{n_s} of the free-free emission, which has not been examined. To do this, we first analyze the distribution of redshift and DM halo mass for both the global signal and the anisotropy of the free-free emission. Afterwards, we establish various parameter sets, $(n_\mathrm{s}, r_{n_\mathrm{s}})$, which can alter the number density evolution, particularly for low-mass DM halos, and evaluate how the emission signal and the anisotropy vary with different parameter sets. Additionally, we also evaluate the dependence on the gas profile model within DM halos.

In this chapter, we will outline the methodology for our analysis of free-free emission from dark matter halos in the standard ΛCDM cosmology. In Section 4.2, we will describe the halo model that characterizes the density and temperature profiles of the gas within halos, and calculate the intensity of free-free emission from individual halos of varying masses. In Section 4.3, we will consider the historical formation of halos and formulate the diffuse background intensity, which comprises the sum of free-free emission from individual halos. We will also examine the mass and redshift distribution of this diffuse background intensity. In Section 4.4, we will formulate the anisotropies of the free-free emission and evaluate the mass and redshift distribution of these anisotropies in the same way as the diffuse background intensity. Finally, in Section 4.5, we will explore the implications of our findings for constraining primordial curvature perturbations and present our conclusions in Section 4.6.

In this chapter, we adopt a flat ΛCDM cosmology and use the best-fit cosmological parameters from the latest Planck result [1]. We also use the calculation package named HMFcalc [161] to estimate the halo mass function, the matter power spectrum, and so on.

4.2 Free-free emission rate from an individual halo

The emission of free-free radiation from thermal plasma can be quantified through the number density $n_{\rm gas}$, temperature $T_{\rm gas}$, and ionization fraction $x_{\rm e}$ of free electrons in the plasma. The emission coefficient at a frequency ν can then be determined by [162]

$$\begin{aligned}\epsilon_\nu^{\rm ff} =& \frac{2^3 e^6}{3 m_{\rm e} c^3}\left(\frac{2\pi}{3 m_{\rm e} k_{\rm B} T_{\rm gas}}\right)^{1/2} \\ & \times x_{\rm e}^2 n_{\rm gas}^2 \exp\left(-h_{\rm p}\nu / k_{\rm B} T_{\rm gas}\right) \bar{g}_{\rm ff}\,, \end{aligned} \tag{4.1}$$

where e is the electric charge, m_e is the mass of electrons, and $h_{\rm p}$ and $k_{\rm B}$ are the Planck constant and the Boltzmann constant. In Eq. (4.1), $\bar{g}_{\rm ff}$ is a velocity-averaged Gaunt factor. We utilize the fitting formula for $\bar{g}_{\rm ff}$ as presented in Ref. [163],

$$\bar{g}_{\rm ff} = \log\{\exp\left[5.960 - \sqrt{3}/\pi \log\left(\nu_9 T_4^{-3/2}\right)\right] + {\rm e}\}, \tag{4.2}$$

where $\nu_9 \equiv \nu/(1\ {\rm GHz})$, $T_4 \equiv T_{\rm gas}/(10^4\ {\rm K})$, and e is Napier's constant. The free-free emission at frequencies exceeding the critical frequency, $\nu_{\rm c} = \frac{k_{\rm B} T_{\rm gas}}{h_{\rm p}}$, is subject to exponential damping as depicted in Eq. (4.1). However, in the context of the CMB or radio frequency range, this damping effect is virtually insignificant.

To assess the free-free emission from DM halos, it is imperative to formulate a model for the energy density and temperature of the gas within these halos. In this study, we utilize the gas profile model, referred to as the KS model, presented in previous works [164], [165].

In the KS model, the gas density and temperature profiles are written by

$$\rho_{\rm gas}(x) = \rho_{\rm gas}(0) y_{\rm gas}(x), \tag{4.3}$$

$$T_{\rm gas}(x) = T_{\rm gas}(0) y_{\rm gas}^{\gamma-1}(x), \tag{4.4}$$

where x is given by $x = r/R_{\rm vir}$ with the virial radius $R_{\rm vir}$, $\rho_{\rm gas}(0)$, and $T_{\rm gas}(0)$ are the number density and temperature at $x = 0$, γ is the polytropic index, and $y_{\rm gas}$ is the shape function of the profile which satisfies $y_{\rm gas}(0) = 1$. In order to determine the shape function, $y_{\rm gas}$, of the gas profile, the equation of hydrostatic equilibrium must be solved. In this study, we utilize the NFW density profile of DM as outlined in Ref. [166] and adopted in Ref. [164]. While this profile is widely used, it should be noted that actual halos hosted by galaxies may exhibit shallower profiles, as reviewed in Ref. [167]. Then one can obtain

$$y_{\rm gas} \equiv \left\{1 - B\left[1 - \frac{\ln(1+x)}{x}\right]\right\}^{1/(\gamma-1)}, \tag{4.5}$$

with

$$B \equiv 3\eta_0^{-1}\frac{\gamma-1}{\gamma}\left[\frac{\ln(1+c_s)}{c_s} - \frac{1}{1+c_s}\right]^{-1}, \tag{4.6}$$

where η_0 is the mass-temperature normalization factor which is defined by

$$\eta_0 \equiv \frac{3 k_{\rm B} R_{\rm vir} T_{\rm gas}(0)}{G \mu m_{\rm p} M_{\rm halo}}, \tag{4.7}$$

and c_s is the concentration parameter. In Eq. (4.7), G is the gravitational constant, μ represents the mean molecular weight (we set $\mu = 0.6$), and $m_{\rm p}$ is the proton mass. For the values of η_0 and γ, Ref. [165] provides the useful fitting formula as functions of c_s,

$$\eta_0 \approx 2.235 + 0.202(c_s - 5) - 1.16 \times 10^{-3}(c_s - 5)^2, \tag{4.8}$$

and

$$\gamma = 1.137 + 8.94 \times 10^{-2} \ln(c_s/5) - 3.68 \times 10^{-3}(c_s - 5). \tag{4.9}$$

These functions are valid in range of $0 < c_s < 25$.

The study in reference [168] has investigated the concentration parameter c_s through the implementation of N-body simulations, spanning from high redshifts to the present. Based on the findings of these simulations, the authors provide analytic fitting formulae for the concentration parameter c_s for DM halos with a mass of $M_{\rm halo} \gtrsim 10^9 M_\odot$ in the redshift range of $0 < z < 14$. We here utilize their results for the concentration parameter c_s. Our investigation confirms that the value of c_s is less than 25 for the range of DM halo masses and redshifts examined in this paper. As such, the fitting formulae presented in Eqs. (4.8) and (4.9) are deemed valid throughout the remainder of the paper.

With η_0 in Eq. (4.7), we can estimate $T_{\rm gas}(0)$ as

$$T_{\rm gas}(0) = 2\eta_0 \left(\frac{\mu}{0.6}\right) \left(\frac{M_{\rm halo}}{10^{10} h^{-1} M_\odot}\right) \left(\frac{R_{\rm vir}}{67 h^{-1}{\rm kpc}}\right)^{-1} [{\rm eV}]. \tag{4.10}$$

It is noted that the Eq. (4.10) with $\eta_0 = 1$ shows a value of the virial temperature of the halo with a mass $M_{\rm halo}$, $T_{\rm vir}(M_{\rm halo})$. The integration of the density profile provides $\rho_{\rm gas}(0)$ as

$$\begin{aligned}\rho_{\rm gas}(0) &= M_{\rm gas}\left[4\pi r_{\rm s}^3 \int_0^{u_{\rm v}} y_{\rm gas}(u) u^2 du\right]^{-1} \\ &= 2.63 \times 10^{12} {\rm M_\odot Mpc^{-3}} \\ &\times \left(\frac{\Omega_{\rm b,0} h^2}{\Omega_{\rm m}, 0}\right) \left(\frac{M_{\rm halo}}{10^{10} h^{-1} M_\odot}\right) \left(\frac{R_{\rm vir}}{67 h^{-1}{\rm kpc}}\right)^{-3} \\ &\times c_s^3 \left[\frac{y_{\rm gas}^{-1}(c_s)}{c_s^2 (1 + c_s)^2}\right] \left[\ln(1 + c_s) - \frac{c_s}{1 + c_s}\right]^{-1},\end{aligned} \tag{4.11}$$

where $M_{\rm gas}$ is the total baryonic mass contained in the halo with a mass, $M_{\rm halo}$. Here we assume that the DM halos can host the baryon gas whose mass is given by

$$M_{\rm gas} = \frac{\Omega_{\rm b,0}}{\Omega_{\rm m,0}} M_{\rm halo}. \tag{4.12}$$

The ionization fraction is determined by the equilibrium between the processes of recombination and ionization via thermal collisions or ultraviolet photons emitted by galaxies and stars. It is postulated that a majority of DM halos contribute to free-free radiation after the Epoch of Reionization. Consequently, in this study, we assume that the ultraviolet radiation from galaxies and stars is sufficient to maintain ionization within DM halos. Thus we set the ionization fraction, x_e, equal to one.

4.3 Free-free background emission from DM halos

The free-free emission from a DM halo can be computed utilizing the gas profile described in the previous section, through the use of Eq. (4.1). We then proceed to evaluate the aggregate intensity of the diffuse free-free background emission, which is achieved by summing the emission from all DM halos in the universe. In order to determine this global intensity, it is beneficial to compute the average intensity of free-free emission from an individual halo with mass $M_{\rm halo}$ at a redshift z,

$$I_\nu^{\rm ind}(z, M_{\rm halo}) = \frac{\int_{V_{\rm halo}} \epsilon_\nu^{\rm ff} dV}{4\pi S_{\rm halo}}, \tag{4.13}$$

where $V_{\rm halo}$ and $S_{\rm halo}$ is the physical volume and cross section on the sky for the DM halo, $V_{\rm halo} = 4\pi R_{\rm vir}^3/3$ and $S_{\rm halo} = \pi R_{\rm vir}^2$, respectively. It is noteworthy that the optically thin approximation is adopted to derive Eq. (4.13), owing to the negligible nature of free-free absorption in our scenario.

We now consider a redshift shell located at redshift z, with a width of dz. The free-free emission contribution from the DM halos within this redshift shell is represented by

$$dI_\nu^{\rm ff}(z) = dz \frac{dV_{\rm com}}{dz} \int_{M_{\rm min}} dM_{\rm halo} \frac{\Omega_{\rm halo}}{4\pi} I_\nu^{\rm ind} \frac{dn_{\rm halo}^{\rm com}}{dM_{\rm halo}}, \tag{4.14}$$

where $dn_{\rm halo}^{\rm com}/dM_{\rm halo}$ is the comoving mass function of DM halos, $V_{\rm com}$ is the comoving volume, and $\Omega_{\rm halo}(z, z_{\rm f}, M_{\rm halo})$ is the solid angle of a DM halo given by $\Omega_{\rm halo} = \pi((1+z)R_{\rm vir})^2/\chi^2$ with the comoving distance χ to a redshift z. In Eq. (4.14), we set the DM minimum mass $M_{\rm min}$ to the Jeans mass with the background baryon temperature $T_{\rm b,bg}$. Since we are interested in the redshifts after the epoch of reionization, we take $T_{\rm b,bg} \sim 10^4$ K [169]–[173]. For DM halos with masses below $M_{\rm min}$, the baryonic gas is unable to collapse during their formation, and these halos can only retain a relatively small amount of baryonic gas through accretion. As such, we disregard the contribution of these low-mass DM halos. Finally, the result of the redshift integration yields the total global intensity at an observed frequency $\nu_{\rm obs}$ from DM halos,

$$I_{\rm obs}(\nu_{\rm obs}) = \int_0^\infty dz \frac{1}{(1+z)^3} \frac{dI_{\nu_{\rm em}}^{\rm ff}(z, M_{\rm halo})}{dz}, \tag{4.15}$$

where $\nu_{\rm em}$ is $\nu_{\rm em} = (1+z)\nu_{\rm obs}$ and the factor $(1+z)^{-3}$ is the redshift effect for the intensity.

The result of Eq.(4.15) is depicted in Fig.4.1. In order to obtain this result, we adopt the Press-Schechter mass function, as examined in Sec. 2.10.3, utilizing the cosmological parameter set derived from the Planck best-fit. It may be informative to express the intensity in terms of the brightness temperature, $T_{{\rm b},\nu}$. In the Rayleigh-Jeans limit, the brightness temperature is related to the intensity through

$$T_{{\rm b},\nu} = \frac{c^2}{2\nu_{\rm obs}^2} I_{\rm obs} \simeq 0.32 \left(\frac{I_{\rm obs}}{1\ {\rm Jy/str}}\right) \left(\frac{\nu_{\rm obs}}{10\ {\rm GHz}}\right)^{-2} [\mu{\rm K}]. \tag{4.16}$$

Consequently, while the intensity of free-free signals remains relatively constant across frequency, the brightness temperature of the free-free signal is inversely proportional to ν^{-2}. The strength of the intensity is highly dependent on the gas profile

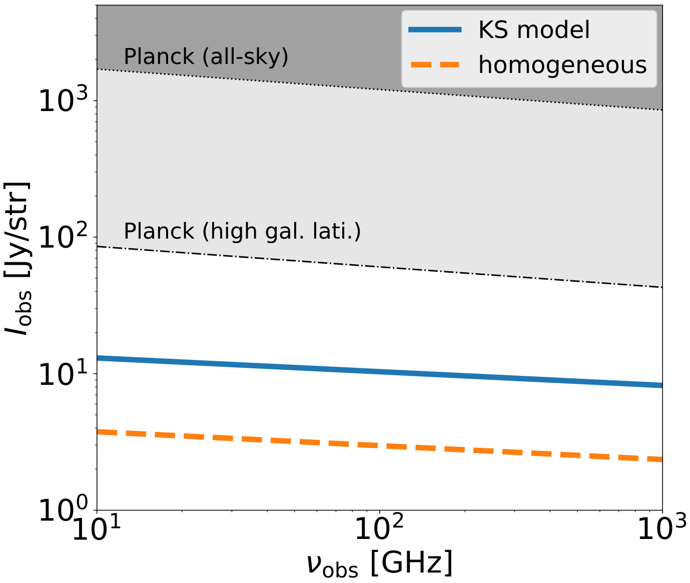

FIGURE 4.1: The figure depicts the intensity of the global free-free emission from DM halos as a function of frequency, measured in GHz. The solid blue line represents the global intensity for the KS model, while the orange dashed line corresponds to the intensity for the homogeneous gas model, as estimated by Eq. (4.15). The dark gray-shaded region represents the frequencies excluded by the all-sky mean intensity observed by Planck, and the light gray-shaded region represents the frequencies excluded by the high galactic latitude mean intensity observed by the Planck satellite.

model adopted for DM halos, in this study we use the KS model discussed in Sec.4.2. To showcase the effect of the gas profile, we also calculate the intensity using a homogeneous gas model, where $n_{\rm gas} = 200 n_{\rm gas,IGM}$ with the background IGM gas number density $n_{\rm gas,IGM}$ and $T_{\rm halo} = T_{\rm vir}(M_{\rm halo})$, and plot the intensity as an orange dashed line in Fig. 4.1.

The clumpiness serves as a useful metric to demonstrate the influence of the gas profile model on the free-free emission and is quantified as

$$C(z) \equiv \frac{\int dM_{\rm halo} \int_{V_{\rm halo}} dV n_{\rm e}^2(r, M_{\rm halo}) \frac{dn_{\rm halo}^{\rm com}}{dM_{\rm halo}}}{\bar{n}_{\rm e,bg}^2}, \tag{4.17}$$

where the radial electron number density in an individual halo, $n_{\rm e}(r, M_{\rm halo})$, is proportional to the gas density, so that $n_{\rm e}(r, M_{\rm halo}) = x_{\rm e} n_{\rm gas}$, and the mean value of the free electron number density in the IGM is denoted by $\bar{n}_{\rm e,bg}^2$. The clumpiness of both models are depicted in Fig. 4.2, revealing that the clumpiness in the KS model is roughly ten times greater than in the homogeneous model. However, this increase in clumpiness does not result in a corresponding amplification of the free-free intensity in the KS model, as the gas temperature in DM halos also follows a profile, which dilutes the enhancement from clumpiness, as indicated in Eq. (4.1). It is important to note that the homogeneous model represents the minimum possible intensity of free-free emission from DM halos, and as such, Fig. 4.1 illustrates that differences in the gas profile can modify the intensity by a factor of a few.

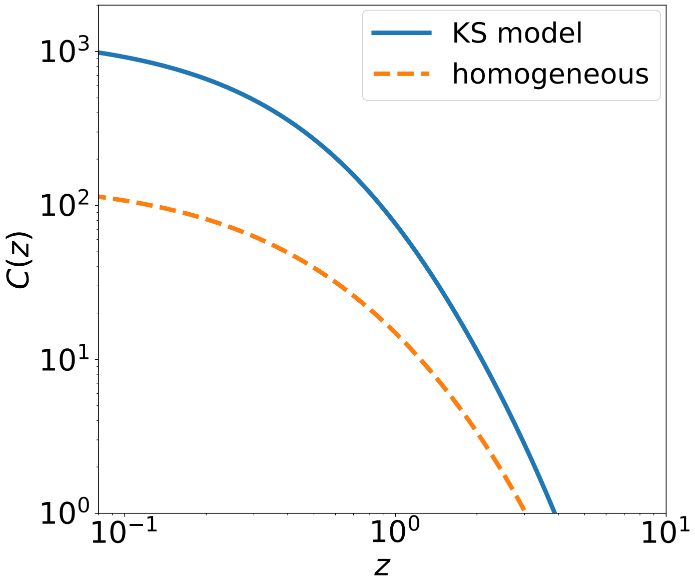

FIGURE 4.2: The redshift dependence of the clumping factor in Eq. (4.17). The blue solid and orange dashed lines are for the KS model and the homogeneous gas model, respectively.

The free-free emission at CMB frequencies has been extensively studied as a foreground of the CMB. In Fig. 4.1, we plot the all-sky mean free-free intensity provided by the Planck collaboration and the one at high galactic latitudes reported in Ref. [174]. The current observed signal, even at high galactic latitudes, is ten times larger than our prediction based on the Planck best-fit parameters. In the observed free-free signals, the cosmological contribution has yet to be identified, although it is generally believed that the majority of the observed free-free signals have a Galactic origin. As predicted in this study, further investigations to identify the cosmological contributions are necessary, such as the removal of Galactic signals, the analysis of statistical anisotropy in the signal, and cross-correlation with other cosmological observations.

4.3.1 Mass and redshift distribution

The free-free signals calculated above are the sum of the contribution from all DM halos distributed across a wide range of masses and redshifts. It is of interest to investigate the mass and redshift contributions to the global intensity. The halo mass distribution of $I_{\rm obs}$ at $\nu_{\rm obs} = 70$ GHz is illustrated in Fig. 4.3. The figure clearly demonstrates that the dominant contribution comes from relatively low-mass halos around $M_{\rm halo} \sim 10^{10} M_{\odot}$. The monotonic decrease at large masses is due to the shape of the halo mass function; as the DM mass increases, the number density of DM halos decreases, resulting in a decrease in the intensity contribution. The cutoff on the lower mass side is due to the Jeans mass. Therefore, the majority of the free-free emission signals originate from DM halos around the Jeans mass scale. The concentration parameter also varies with mass, with lower mass halos having higher concentration parameters and a resultant enhanced signal. However, we found that the mass distributions of the signals for both the KS and the homogeneous gas models are almost identical. This is because the contribution from the halo mass function

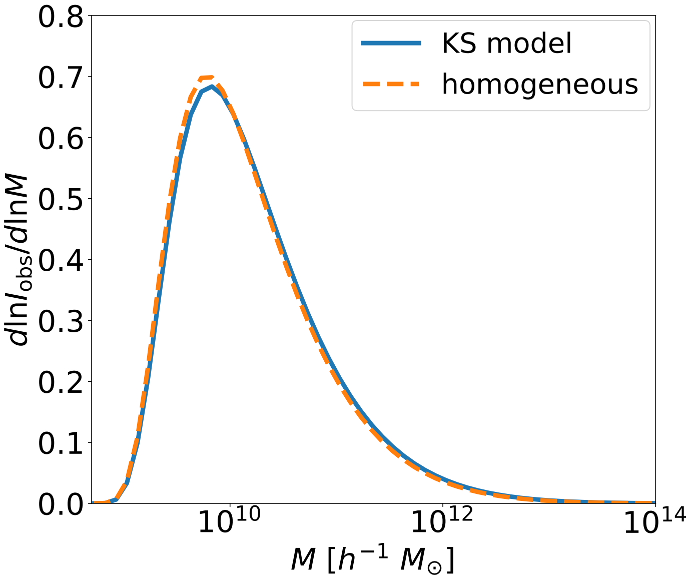

FIGURE 4.3: Mass distribution of the global free-free emission from DM halos. The blue solid and orange dashed lines are for the KS model and the homogeneous gas model, respectively.

is much greater than that from the concentration parameters.

In the same manner, as Fig.4.3, we also plot the redshift distribution for these two models. The redshift distribution reflects the history of the formation efficiency of DM halos, particularly for halos with $M_{\rm peak} \sim 10^{10} M_\odot$, which corresponds to the peak in Fig.4.3. Specifically, the peak feature occurs at redshift $z_{\rm peak} \sim 3$ when $\sigma(M_{\rm peak}, z_{\rm peak})/\delta_c \sim 1$. The redshift distribution of DM halos differs from the mass distribution, as the evolution of the concentration parameter has a significant impact. Figure 10 in Ref. [168] demonstrates that for halos with masses near $M_{\rm halo} \sim M_{\rm peak}$, the concentration parameter increases with decreasing redshift. Consequently, the redshift distribution for the KS model is shifted towards lower redshifts compared to the homogeneous model.

Given the redshift dependence, it is proposed that redshift tomographic information on the global signals of free-free emission could be obtained through techniques such as cross-correlation analysis with 21-cm line intensity. This information could provide insights into the formation of small-scale structure in the Universe and the gas profile in low-mass halos.

4.4 Statistical Anisotropy of the free-free emission from DM halos

In this section, we examine the anisotropy in the free-free emission caused by DM halos. The anisotropy of the cosmic free-free signals is generated by the clustering of DM halos and the Poisson contribution to their number density. The degree of anisotropy is quantified through the evaluation of the angular power spectrum. To calculate the angular power spectrum, we utilize the halo formalism outlined in

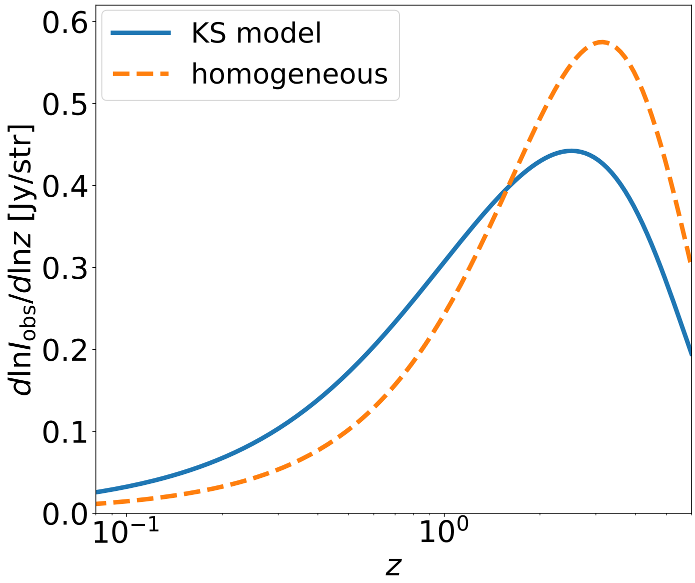

FIGURE 4.4: Redshift distribution of the global free-free emission from DM halos. The blue solid line is for the KS model, and the orange dashed line is for the homogeneous gas model.

Ref. [175]. The resulting power spectrum is comprised of two distinct components,

$$C_\ell^{\rm ff} = C_\ell^{\rm 1h} + C_\ell^{\rm 2h}. \tag{4.18}$$

Here $C_\ell^{\rm 1h}$ is the "one-halo" term describing the Poisson contribution, and $C_\ell^{\rm 2h}$ is the "two-halo" term describing the clustering contribution. With the limber approximation, they can be written by [176], [177]

$$C_\ell^{\rm 1h} = \int_0^\infty dz \, \frac{d^2V}{dzd\Omega} \int dM_{\rm halo} \, \frac{dn_{\rm halo}^{\rm com}}{dM_{\rm halo}} \left| \tilde{I}_\ell(z) \right|^2, \tag{4.19}$$

and

$$C_\ell^{\rm 2h} \approx \int_0^\infty dz \frac{d^2V}{dzd\Omega} P\left(\frac{\ell}{\chi(z)}, z\right) \left| \int dM_{\rm halo} \, \tilde{\Psi}(M_{\rm halo}, z) \right|^2, \tag{4.20}$$

where $P(k,z)$ is the conventional matter power spectrum at the redshift z. In Eq. (4.20), $\tilde{\Psi}$ is defined as

$$\tilde{\Psi} \equiv \frac{dn_{\rm halo}^{\rm com}}{dM_{\rm halo}} \tilde{I}_\ell(M_{\rm halo}, z) b(M_{\rm halo}, z), \tag{4.21}$$

where $\tilde{I}_\ell$ is the 2D Fourier modes of the intensity, and b is the halo bias which we employ in Ref. [94].

Since our gas model is spherically symmetric, the 2D Fourier modes of the intensity are calculated by

$$\tilde{I}_\ell = \frac{1}{d_{\rm A}^2} \int dR R^2 \epsilon_\nu^{\rm ff}(R) \frac{\sin(\ell R/d_{\rm A})}{\ell R/d_{\rm A}}, \tag{4.22}$$

where R is the proper radial distance from the center of the halo, and $d_\mathrm{A} = d_\mathrm{A}(z)$ is the proper angular diameter distance.

We computed the angular power spectrum of the free-free emission in the KS model, $D_\ell \approx \ell^2/2\pi C_\ell^{\mathrm{ff}}$, as illustrated in Figure 4.5. The frequency was set to $\nu_{\mathrm{obs}} = 10[\mathrm{GHz}]$ for the calculation of the angular power spectrum. The blue dotted line in the figure represents the one-halo term contribution, as outlined in Eq.(4.19), and the red dashed-dotted line represents the two-halo term, as outlined in Eq.(4.20). The total angular spectrum is represented by the solid black line. As seen in the figure, on large scales, the one- and two-halo terms contribute equally to the anisotropy. However, on small scales ($\ell \gtrsim 10^3$), the dominant contribution of the anisotropy comes from the one-halo term rather than the two-halo term. It is worth noting that the CMB and radio frequency range of $\mathcal{O}(1-100)$GHz is ideal for observing not only CMB but also free-free emissions. Therefore, to detect the free-free emission anisotropy from standard DM halos, it is necessary to be able to observe fluctuations at a level of at least 1Jy/str on angular scales of 0.1 deg to 0.01 deg in this frequency range. Although the Planck satellite and also future observations for CMB at a frequency level of $\mathcal{O}(100)$GHz, e.g., CMB-S4 do not have the sensitivity, it would be achieved by future radio observations at a frequency level of $\mathcal{O}(10)$GHz such as SKA-mid project.

Let us here briefly mention the sensitivity of the SKA observation, especially SKA1-mid project. According to the Ref. [155], the interferometer's noise level is expressed in terms of the brightness temperature as

$$\delta T_\mathrm{N}(\lambda) = \frac{\lambda^2/\theta^2}{A_\mathrm{e}} \frac{T_{\mathrm{sys}}}{\sqrt{\Delta\nu_{\mathrm{obs}} t_{\mathrm{obs}}}}, \tag{4.23}$$

where θ is the beam width, $\Delta\nu_{\mathrm{obs}}$ is the width of frequency bands, T_{sys} is the system temperature, A_e is the effective collecting area, and t_{obs} is the total observation time. The system temperature can be expressed as a sum of two components, namely the instrumental noise temperature T_{ins} and the sky temperature T_{sky}, as

$$T_{\mathrm{sys}} = T_{\mathrm{ins}} + T_{\mathrm{sky}}. \tag{4.24}$$

In the SKA1-mid project, the performance is expected to be $A_\mathrm{e} \approx 5 \times 10^4 \mathrm{m}^2$, $min(\Delta\nu_{\mathrm{obs}}) = 3\mathrm{MHz}$, and $T_{\mathrm{ins}} = 30\mathrm{K}$. Then we set $A_\mathrm{e} \approx 5 \times 10^4 \mathrm{m}^2$ and $T_{\mathrm{ins}} = 30\mathrm{K}$ [178]. As we are now focused on the continuous-spectrum emission, there is no need to establish a narrow frequency bandwidth. Here we are interested in e.g. 10GHz as the observation frequency. Thus we set $\Delta\nu_{\mathrm{obs}}) = 1\mathrm{GHz}$. For the system temperature, we choose to use the temperature of the sky at high Galactic latitude, where the foreground emission exhibits its minimum. This sky temperature in the region is approximately computed to be

$$T_{\mathrm{sky}} \sim 180 \left(\frac{180\mathrm{MHz}}{\nu}\right)^{2.6} \mathrm{K}. \tag{4.25}$$

There exists a difference in the frequency dependence between the instrumental noise temperature and the sky temperature. At frequencies lower than 150MHz, the noise is dominated by the sky temperature, and the resultant noise brightness temperature can be approximately expressed as

$$\delta T_\mathrm{N}(\nu) \simeq 7.36 \left(\frac{10^5\,\mathrm{m}^2}{A_\mathrm{e}}\right) \left(\frac{1'}{\theta}\right)^2 \left(\frac{1\mathrm{MHz}}{\Delta\nu_{\mathrm{obs}}} \frac{100\mathrm{hr}}{t_{\mathrm{obs}}}\right)^{1/2} \left(\frac{1420\mathrm{MHz}}{\nu_{\mathrm{obs}}}\right)^{4.6} \mu\mathrm{K}. \tag{4.26}$$

On the other hand, at higher frequencies where we are interested in, the instrumental noise becomes the primary contributor. Thus the resultant noise brightness temperature can be approximately written as

$$\delta T_{\rm N}(\nu) \simeq 0.03 \left(\frac{T_{\rm ins}}{30\,{\rm K}}\right)\left(\frac{10^5\,{\rm m}^2}{A_{\rm e}}\right)\left(\frac{1'}{\theta}\right)^2\left(\frac{1{\rm GHz}}{\Delta\nu_{\rm obs}}\frac{1000{\rm hr}}{t_{\rm obs}}\right)^{1/2}\left(\frac{10{\rm GHz}}{\nu_{\rm obs}}\right)^{2.0}\mu{\rm K}. \tag{4.27}$$

To make a comparison between the noise level and the results depicted in Fig. 4.5, it is necessary to convert the energy unit of the noise brightness temperature from ¯K to Jy/str. By utilizing Eq.(4.16) and assuming an observation time of $t_{\rm obs} = 1000$hr and an angular resolution of $\theta = 0.1$deg, the estimated noise brightness temperature of the SKA1-mid at 10GHz can be approximated as

$$\delta T_{\rm N}(10{\rm GHz}) \approx 0.01{\rm Jy/str}, \tag{4.28}$$

which meets the minimum sensitivity of 1Jy/str on angular scales of 0.1 deg required to detect the anisotropy of free-free emission from standard DM halos.

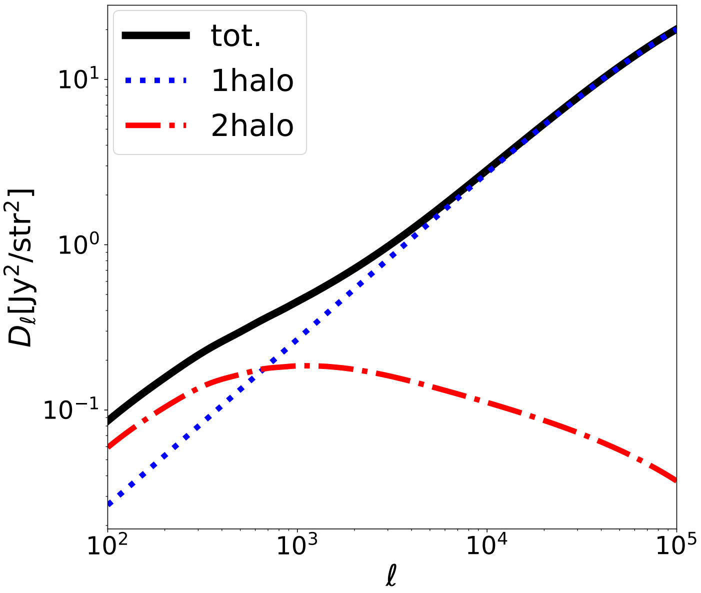

FIGURE 4.5: Angular power spectrum of the cosmological free-free emission induced by DM halos. The blue dotted line shows the one-halo term in Eq. (4.19), the red dash-dot line represents the two-halo term in Eq. (4.20), and the black solid line is the total.

4.4.1 Mass and redshift distribution

In this section, we investigate the mass and redshift distribution in the anisotropy of the cosmological free-free emission. We begin by considering the mass distribution of the one-halo term. This distribution can be evaluated by

$$\frac{d\ln C_\ell^{\rm 1h}}{d\ln M_{\rm halo}} \equiv \frac{M_{\rm halo}\int dz\frac{dV}{dz}\frac{dn_{\rm halo}^{\rm com}(M_{\rm halo},z)}{dM_{\rm halo}}\left|\tilde{I}_\ell(M_{\rm halo},z)\right|^2}{\int dz\frac{dV}{dz}\int dM_{\rm halo}\frac{dn_{\rm halo}^{\rm com}(M_{\rm halo},z)}{dM_{\rm halo}}\left|\tilde{I}_\ell(M_{\rm halo},z)\right|^2}. \tag{4.29}$$

Figure 4.6 illustrates the mass distribution for different angular scales. As the ℓ mode becomes small, the peak location of the contribution shifts to larger-mass halos. As previously discussed, small-mass halos produce the dominant contribution to the overall intensity. However, in the anisotropy mass distribution, the contribution of small-mass halos to small ℓ values is proportionally suppressed by ℓ^2 due to the Poisson contribution. As a result, the large-mass halo profile structure cannot be relatively neglected on large scales when compared to the small-mass halo contributions.

Subsequently, we examine the redshift contribution. The redshift distributions are obtained through

$$\frac{d\ln C_\ell^{1\mathrm{h}}}{d\ln z} \equiv \frac{z\frac{dV}{dz}\int dM_{\mathrm{halo}}\frac{dn_{\mathrm{halo}}^{\mathrm{com}}(M_{\mathrm{halo}},z)}{dM_{\mathrm{halo}}}\left|\tilde{I}_\ell(M_{\mathrm{halo}},z)\right|^2}{\int dz\frac{dV}{dz}\int dM_{\mathrm{halo}}\frac{dn_{\mathrm{halo}}^{\mathrm{com}}(M_{\mathrm{halo}},z)}{dM_{\mathrm{halo}}}\left|\tilde{I}_\ell(M_{\mathrm{halo}},z)\right|^2}, \tag{4.30}$$

and

$$\frac{d\ln C_\ell^{2\mathrm{h}}}{d\ln z} \equiv \frac{z\frac{dV}{dz}P\left(\frac{\ell}{\chi(z)}\right)\left|\int dM_{\mathrm{halo}}\tilde{\Psi}(M_{\mathrm{halo}},z)\right|^2}{\int dz\frac{dV}{dz}P\left(\frac{\ell}{\chi(z)}\right)\left|\int dM_{\mathrm{halo}}\tilde{\Psi}(M_{\mathrm{halo}},z)\right|^2}. \tag{4.31}$$

Figures 4.7 and 4.8 depict the redshift distribution for the one- and two-halo terms, respectively. The peak location of the one-halo term exhibits a dependence on ℓ modes, shifting towards lower redshifts as ℓ decreases. This is due to the significant role of the apparent size of DM halos, as conveyed through I_ℓ. As demonstrated in the mass contribution of the one-halo term in Fig.4.6, the majority of contributions stem from small-mass halos in the form of Poisson contributions. On small ℓ modes, the larger apparent angle size of the DM halos results in a weaker suppression of Poisson noise, as the suppression is proportional to $\ell/\ell_{\mathrm{halo}}^3$, where ℓ_{halo} corresponds to the apparent angular size of halos. Thus, as the ℓ mode decreases, the peak location shifts towards lower redshifts due to the presence of more substantial DM halos at lower redshifts. Conversely, the two-halo term displays a sharp peak at a constant redshift, $z \sim 3$, for all ℓ modes. This is a result of the strong dependence of the two-halo term on the abundance of DM halos with $M_{\mathrm{halo}} \sim 10^{10}M\odot$, as expressed through $C\ell^{2\mathrm{h}} \propto (dn_{\mathrm{halo}}/dM_{\mathrm{halo}})^2$. These halos actively form at $z \sim 3$ and thus contribute significantly to the two-halo term at this redshift.

4.5 Cosmological application: n_{s} and $r_{n_{\mathrm{s}}}$

As previously discussed in sections accompanied by Figs 4.3 and 4.6, the majority of the global signal and anisotropy of free-free emission arises from small-mass DM halos whose mass corresponds to the Jeans scale. This implies that the observation of the cosmological free-free signal may serve as an effective tool for probing the abundance of such DM halos. The examination of the abundance of small-mass DM halos is crucial for studying the statistics of primordial curvature perturbations, particularly on small scales. In this section, we investigate the dependence of free-free signals on the statistics of primordial curvature perturbations.

The statistical nature of primordial curvature perturbations can be described through the dimensionless primordial curvature power spectrum, $\mathcal{P}\zeta$. To characterize the k-dependence, the spectral index, n_{s}, and the running, rn_{s}, are often utilized

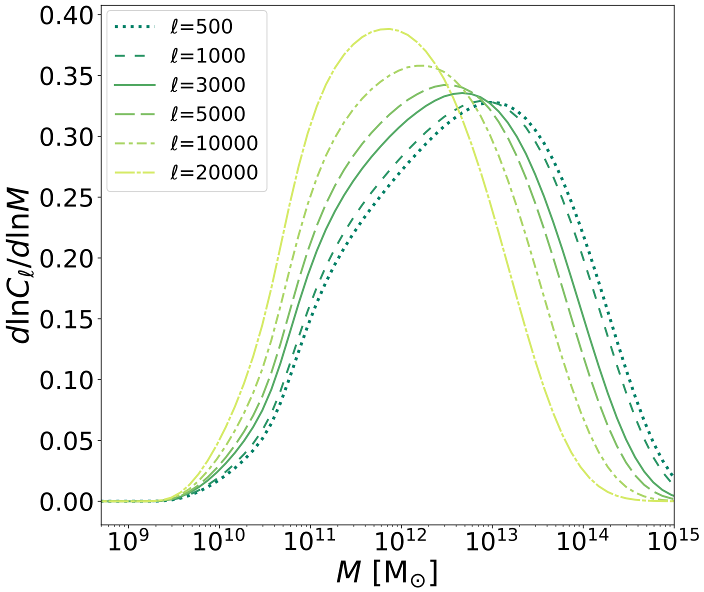

FIGURE 4.6: The mass distribution of the one-halo term of the free-free emission anisotropy that is induced the distribution of DM halos, as presented in Eq. (4.29). The coloration represents the magnitude of the anisotropy on smaller and larger angular scales, respectively.

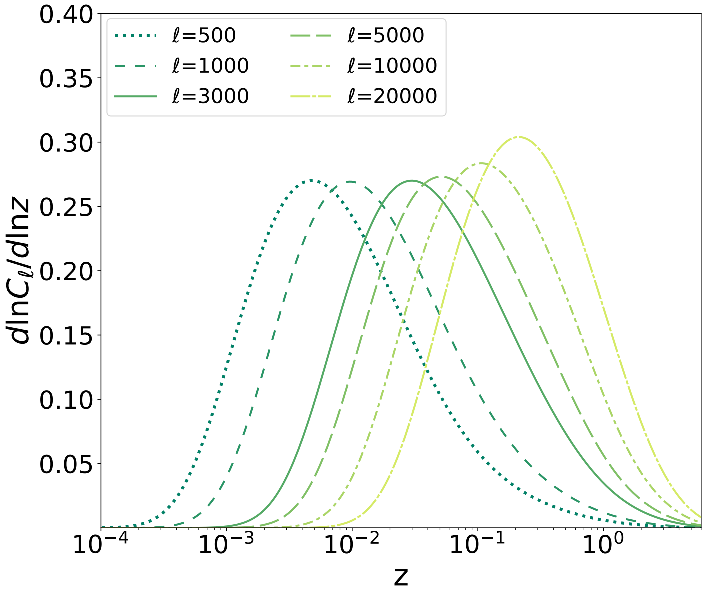

FIGURE 4.7: The redshift distribution of the one-halo term of the free-free emission anisotropy that is induced the distribution of DM halos, as presented in Eq. (4.30). The coloration represents the magnitude of the anisotropy on smaller and larger angular scales, respectively.

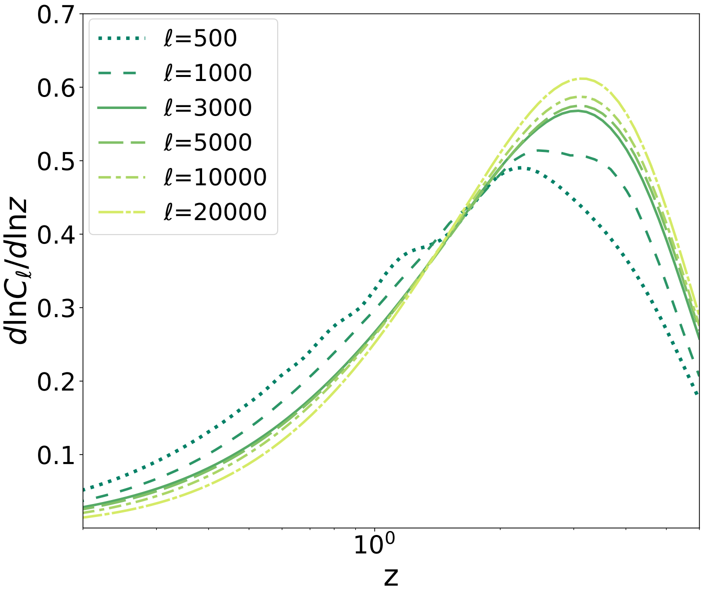

FIGURE 4.8: The redshift distribution of the one-halo term of the free-free emission anisotropy that is induced the distribution of DM halos, as presented in Eq. (4.31). The coloration represents the magnitude of the anisotropy on smaller and larger angular scales, respectively.

as

$$
\begin{aligned}
\mathcal{P}_\zeta &= \left(\frac{k}{k_{\rm pivot}}\right)^{n(k)}, \\
n(k) &\equiv n_{\rm s} - 1 + \frac{1}{2} r_{n_{\rm s}} \ln\left(\frac{k}{k_{\rm pivot}}\right),
\end{aligned}
\tag{4.32}
$$

where $k_{\rm pivot}$ is the pivot scale given in $k_{\rm pivot} = 0.05 {\rm Mpc}^{-1}$.

According to the latest Planck paper, the spectral index and the running are evaluated as

$$
\begin{aligned}
n_{\rm s} &= 0.9659 \pm 0.0040 \quad (69\%{\rm CL}), \\
r_{n_{\rm s}} &= -0.0041 \pm 0.0067 \quad (69\%{\rm CL}).
\end{aligned}
\tag{4.33}
$$

In this study, we establish six distinct parameter combinations, $(n_{\rm s}, r_{n_{\rm s}})$, as outlined in Table 4.1, based on Eq. (4.33), to investigate the dependency of the cosmological free-free signal on the spectral index. The first three models (columns I-III) are non-running models, yet they feature the best-fit value of the spectral index, as well as the maximum values within the 1σ- and 2σ-regions. The latter three models (columns IV-VI), in addition to the tilts, also comprise the running of the best-fit value and the 1σ- and 2σ-maximum values for the running, respectively.[1]

Figure 4.9 illustrates the global signals with six distinct parameter sets. Although the frequency dependences among the six parameter sets are consistent, the amplitudes differ. As the spectrum approaches a blue tilt, the signal amplitude increases,

---

[1] It is noteworthy that in the Planck analysis, the estimated value from the cosmological model with running and the one without running should be distinguished. However, in this study, we refer to the value estimated by the cosmological model incorporating the running index as the best-fit value, even in our model without running.

	I	II	III	IV	V	VI
n_s	0.9659	0.9699	0.9739	0.9659	0.9699	0.9739
r_{n_s}	0	0	0	-0.0041	0.0026	0.0093

TABLE 4.1: Parameter sets

owing to the enhancement of the abundance of small-mass DM halos, which primarily contribute to the free-free signals. The impact of the running parameter r_{n_s} is particularly pronounced. Even within the parameter set that is consistent with the Planck data, the amplitude of the free-free signal would increase by approximately 12%. This implies that a minimum sensitivity of $\sim 0.1 \mathrm{Jy/str}$ is required to detect the impact of the spectral index and running on the free-free emission anisotropy from standard DM halos. This requirement can be verified by examining Eq. (4.28) and assuming $t_{\mathrm{obs}} = 1000\mathrm{hr}$ and $\theta = 0.1\mathrm{deg}$.

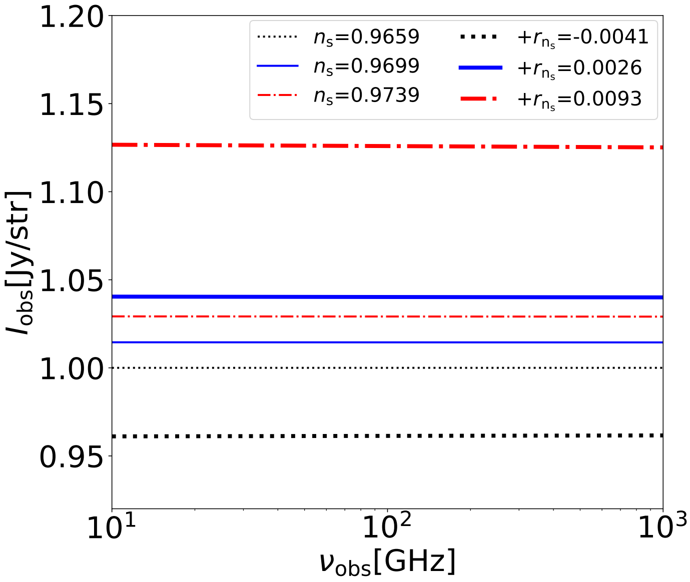

FIGURE 4.9: The global signals of halos' free-free emission with the six parameter sets are summarized in Table. 4.1.

The anisotropies of the free-free emission for the six distinct parameter sets are depicted in Fig.4.10. For comparative purposes, we present the ratio of the anisotropy of free-free emission to the parameter set (I) for the other parameter sets in Fig.4.11. Consistent with the global signal, the anisotropy signal is augmented in the models that possess a substantial amplitude of the primordial curvature perturbations on large k scales. In particular, the enhancement becomes substantial on small scales, reaching approximately 20% amplification for the parameter set (VI).

It is of value to compare the dependence of this anisotropy on the parameter set with one of the CMB signals; the primordial temperature anisotropy of the CMB and the thermal Sunyaev-Zel'dovich effect.

The primordial temperature anisotropy of the CMB is a powerful probe of the primordial curvature perturbations. This has been demonstrated by the Planck analysis of the cosmological parameter sets mentioned above. Similarly to Fig. 4.11, we plot the ratio of the CMB temperature anisotropy for the six parameter sets in

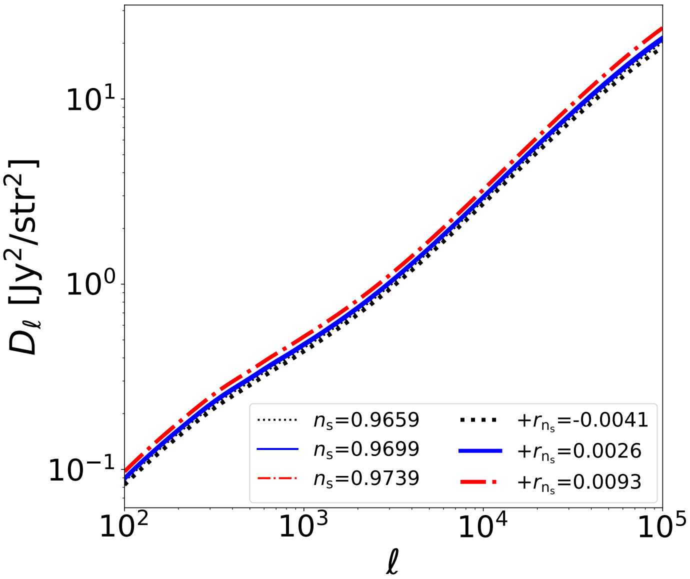

FIGURE 4.10: The anisotropies of halos' free-free emission signal with the six parameter sets are summarized in Table. 4.1.

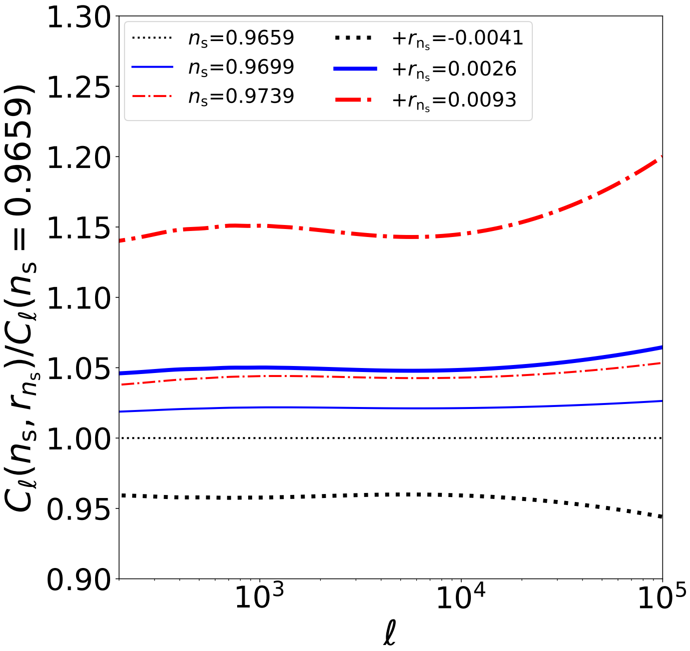

FIGURE 4.11: The difference of anisotropies of free-free emission by halos with the six parameter sets summarized in Table. 4.1. We normalized them by the parameter set (I), $(n_s, r_{n_s}) = (0.9659, 0)$.

Fig. 4.12. As the scale deviates from the pivot scale of $\ell \sim 1000$, the deviation of the ratio from unity increases. For instance, the signal enhancement reaches a maximum of $\sim 1\%$ among the six sets of parameters on small scales, $\ell \sim 3000$. It is anticipated that the deviation will become substantial on even smaller scales. However, these smaller scales are subject to substantial damping of the primordial temperature anisotropies due to the Silk effect, making them challenging to measure. As a result, it is difficult to explore small-scale primordial curvature perturbations through the examination of primordial temperature perturbations.

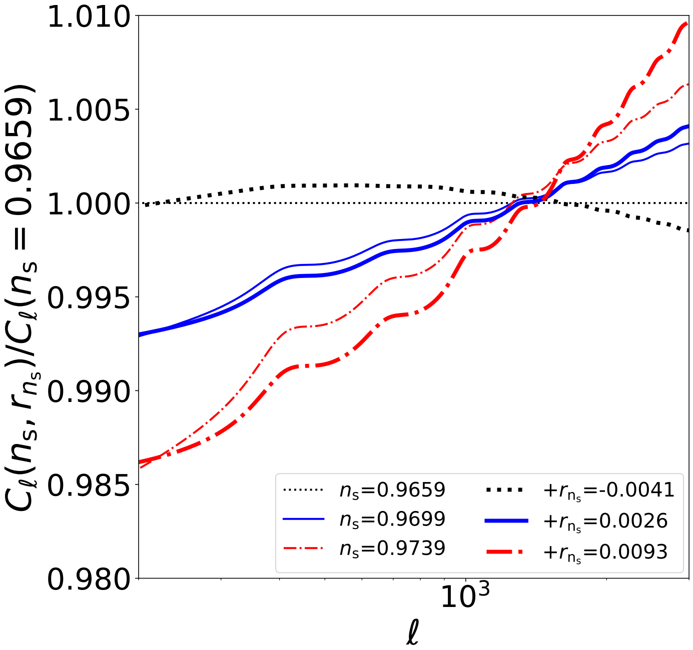

FIGURE 4.12: The difference of CMB temperature anisotropies with the six parameter sets summarized in Table. 4.1. We normalized them by the parameter set (I), $(n_\mathrm{s}, r_{n_\mathrm{s}}) = (0.9659, 0)$.

Next, we examine the thermal Sunyaev-Zel'dovich (SZ) effect. The thermal SZ effect is the inverse Compton scattering of CMB photons caused by hot electrons inside DM halos. This leads to an increase in the brightness temperature of the CMB photons. As a result, CMB temperature anisotropy is produced, following the distribution of DM halos in the sky. Therefore, the SZ effect temperature anisotropy is sensitive to the abundance of DM halos. Using the same gas model as explained in Sec.4.3, we calculate the thermal SZ effect temperature anisotropy and investigate the signal dependence on the six parameter sets. In Fig. 4.13, we plot them as the ratio of the thermal SZ signals, similar to Fig. 4.11.

In reference to the thermal SZ effect, the abundance of DM halos with masses greater than $10^{13} M_\odot$ as described in Ref. [165] influences the angular power spectrum. The variance of these halos is not highly sensitive to the spectral index and running because the scale in question is close to the pivot scale defined in Eq. (4.32). Thus, the signal's dependence on the parameter set is limited. Nonetheless, on smaller scales ($\ell \gtrsim 10^3$), the internal structure of such massive DM halos impacts the thermal SZ anisotropy. The concentration parameter, which influences the internal structure, depends on the spectral index and running in our model, thus increasing the dependence on the parameter set. Despite this increase, the maximum difference remains at $\sim$ 15% at the smallest scale ($\ell \sim 10^5$) in Fig. 4.13.

Compared to these CMB observations that are sensitive to the primordial curvature perturbations, the free-free signals exhibit a stronger dependence on the spectral index and the running. This is because the majority of the free-free signals stem from DM halos with smaller masses, to which other observations are not as sensitive. As a result, these findings suggest that observations of free-free emission have the potential to be a valuable tool for probing the small-scale primordial perturbations, particularly the spectral index and the running.

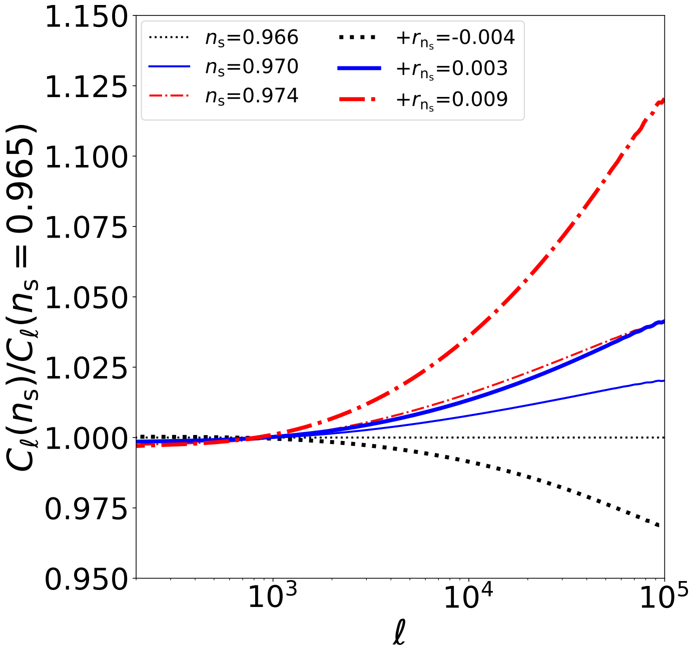

FIGURE 4.13: The difference of anisotropies of CMB temperature induced by Compton scattering with the six parameter sets summarized in Table. 4.1. We normalized them by the parameter set (I), $(n_s, r_{n_s}) = (0.9659, 0)$.

4.6 Conclusion

In this study, we have explored the cosmological free-free emission produced by DM halos in the ΛCDM paradigm. Utilizing an analytic gas model that is compatible with the hydrostatic equilibrium within a DM NFW profile, we have estimated the free-free emission from individual halos. The global signal and anisotropy have been then calculated, taking into account the effects of cosmological structure formation as described in Sec. 2.10.3.

The obtained amplitude of the global free-free emission spectrum is approximately 10 Jy/str and is largely uniform across the CMB and radio frequency domains. As for anisotropy, the Poisson contribution dominates, resulting in an angular power spectrum proportional to the square of the multipole. However, on large scales, $\ell < 1000$, the clustering contribution becomes comparable or greater than the Poisson contribution. Consequently, the anisotropy of cosmological free-free emission on large scales reflects matter density fluctuations. We have also calculated the above quantities for the constant gas profile model for checking the gas-model dependency. We have found that the amplitude of the free-free signal becomes 5 Jy/str which would be the lowest signal.

In addition, we have investigated the mass distribution of the free-free signals. We have demonstrated that the majority of the contribution arises from DM halos with a mass of approximately $10^{11} M_\odot$ for both the global signal and the anisotropy. This implies that the measurement of cosmological free-free signals has the potential to probe the abundance of such small-mass DM halos or the primordial curvature perturbations on small scales, which are the origin of these halos.

As an application of probing small-scale perturbations in the cosmological context, we assess the sensitivity of the cosmological free-free signal to the spectral index and the running. The difference in these parameters modifies the amplitude of the global signal and results in a deviation from the scale dependence with $\propto \ell^2$ in the angular power spectrum. Our results indicate that the free-free signals are altered by 20 % even in the parameter set consistent with the Planck results. This modification is larger than that of the CMB temperature anisotropy induced by the halo thermal SZ effect, which changes the signal by 15 % for the same parameter set. Consequently, the measurement of the cosmological free-free signals could provide a more stringent constraint on the spectral index and the running.

However, the measurement of the cosmological free-free signal poses a significant challenge. Although the free-free emission in the sky has been investigated in the CMB and radio frequency range, the observed free-free emission sky is dominated by signals from the Milky Way Galaxy, which are roughly 100 times larger in the all-sky average and ten times larger in high galactic latitudes than the cosmological free-free emission obtained in this paper. As a result, the cosmological free-free signal cannot be accurately measured without effectively removing the Milky Way contribution. The future radio observatory, Square Kilometre Array, has sufficient sensitivity to measure cosmological free-free signals. The utilization of cross-correlation studies can aid in reducing foreground contamination. The clustering effect of DM halos, due to underlying matter density fluctuations, can make a non-negligible contribution to the cosmological free-free emission anisotropy on large scales. Therefore, cross-correlating with other cosmological probes of matter density fluctuations, including ongoing and upcoming deep galaxy surveys such as the Prime Focus Spectrograph or future 21-cm intensity maps around $z \sim 1$, could be useful in revealing cosmological free-free anisotropy on large scales.

The theoretical uncertainty of the gas profile within DM halos also poses a significant challenge in probing the abundance of these halos and the primordial curvature perturbations. Calibration using other cosmological observations, such as X-ray and SZ cluster observations, may prove useful, despite the fact that the free-free emission signals originate from smaller DM halos than those observed in other contexts. In this study, we demonstrate that differences in gas profile models primarily affect the overall amplitude of anisotropy, rather than its scale dependence, which remains proportional to ℓ^2. Conversely, variations in the scale dependence of primordial curvature perturbations, including the spectral index and running, do affect the scale dependence. Thus, a detailed measurement of the scale dependence in anisotropy can aid in resolving the degeneracy between uncertainties in the gas profile model and the scale dependence of primordial curvature perturbations.

Chapter 5

The 21-cm signals from UCMHs

Through this chapter, we demonstrate that by measuring fluctuations in the 21-cm signal prior to the epoch of reionization, we can impose constraints on the abundance of ultracompact minihaloes (UCMHs). We calculate the 21-cm signal emitted by UCMHs and show that UCMHs enhance the 21-cm fluctuations. Furthermore, we examine the constraints on UCMH abundance and small-scale curvature perturbations. Our findings indicate that the upcoming 21-cm observation, the Square Kilometre Array (SKA), will impose constraints on the amplitude of the primordial curvature power spectrum, $\mathcal{A}_\zeta \lesssim 10^{-6}$, on the range 100 $\mathrm{Mpc}^{-1} \lesssim k \lesssim$ 1000 Mpc^{-1}. Although this constraint is not as strong as the one derived from the non-detection of gamma rays caused by dark matter (DM) annihilation in UCMHs, it is significant because it is independent of the DM particle model.

5.1 Introduction

Recent advancements in cosmological observations have allowed us to gain a deeper understanding of the origins of galaxies, galaxy clusters, and large-scale structures. The highly precise measurement of anisotropies in the CMB has revealed that the statistical properties of these seeds can be expressed in the form of an almost scale-invariant power spectrum of curvature perturbations with an amplitude $\mathcal{A}_\zeta \sim 10^{-9}$ [179], which is in agreement with predictions made by the inflationary paradigm [180], [181]. The observations of the Lyman-alpha forest have further supported this, showing that this trend holds true up to a wave number of $k \sim 1\mathrm{Mpc}^{-1}$ [148], [182]. However, understanding perturbations on scales smaller than 1 Mpc remains a significant challenge. Currently, the upper limits on the amplitude of small-scale perturbations have been obtained through constraints on CMB distortions [16], [18], the abundance of primordial black holes [183], and gravitational waves. However, these constraints are weaker than those on larger scales [184].

Ultracompact minihalos (UCMHs) have gained attention as a potential probe of small-scale perturbations in the universe. The formation of UCMHs is thought to be linked to the presence of excess power on small scales in the primordial power spectrum [71]. These halos can collapse and form well before the standard structure formation history, as early as $z \sim 1000$. UCMHs are characterized by their compact, high-density profiles and may be formed via radial infalling in high redshifts [71]. Simulations [133] have shown that a large amplitude on small scales leads to the formation of early, high-density halos. Recent studies [72], [73] have also shown that these halos have a Moore profile, with a steep inner cusp ($\rho \propto r^{-3/2}$) that is steeper than the NFW profile [135].

The absence of gamma-ray emissions resulting from the annihilation of weakly interacting massive particles (WIMPs) [137]–[139] in UCMHs has provided constraints on the abundance of these structures, as well as on the small-scale curvature power spectrum, with $A_\zeta < 10^{-7}$ for 10 $\mathrm{Mpc}^{-1} < k < 10^8$ Mpc^{-1} [72]–[74], [76]–[78], [185]. Similarly, the lack of detection of neutrinos from WIMP annihilations has also yielded similar constraints [78], [186]. Additionally, measurements of the Thomson scattering optical depth of CMB photons can be used to infer the abundance of UCMHs, as the gamma-rays emitted by these structures can contribute to the photon budget required for cosmic reionization [142]–[145]. Furthermore, observations of gravitational lensing by UCMHs can also be utilized to constrain their abundance [77], [141].

The objective of this study is to demonstrate that upcoming 21-cm observations can provide constraints on the ultracompact minihalo (UCMH) abundance and small-scale curvature power spectrum, without the need for a specific dark matter (DM) particle model. The measurement of the 21-cm line emitted by the hyperfine transition of neutral hydrogen in the high-redshift universe is expected to be an invaluable tool for investigating the formation of structures during the dark ages to the epoch of reionization (EoR) [155]. The amplitude of the signal is closely linked to the spatial distribution of neutral hydrogen in the intergalactic medium (IGM) and collapsed objects. 21-cm observations can probe IGM matter fluctuations on much smaller scales than the Silk scales[156]. Minihalos, which formed during the early stages of the hierarchical structure formation history, can also be a potential source of 21-cm signals in high redshifts [151], [187]. Recent research has demonstrated that future measurements of 21-cm signals from minihalos can provide detailed insights into the statistical properties of small-scale density fluctuations, such as the running spectrum and non-Gaussianity [188]–[190]. Additionally, it has been proposed that 21-cm observations can serve as an indirect method for constraining the abundance of primordial black holes [191], [192].

Currently, several observation projects are underway to detect 21-cm fluctuations around and prior to the EoR, such as the Low Frequency Array [193], the Giant Meterwave Radio Telescope [194], the Murchison Widefield Array [195], [196], and the Precision Array for probing the EoR [197]. Despite the challenges associated with measuring 21-cm fluctuations, these projects have only yielded upper limits thus far [198]–[202]. However, it is anticipated that the high sensitivity of the future instrument, the Square Kilometre Array (SKA), will allow for the detection of 21-cm fluctuations up to a redshift of $z \sim 28$ [203].

In the following sections, we will explore the potential for the SKA to detect 21-cm fluctuations originating from UCMHs. By constructing a baryon gas model within UCMHs and evaluating the resulting 21-cm fluctuations, we will assess the detectability of these fluctuations by the SKA and discuss the potential for constraints on both UCMH abundance and small-scale primordial curvature perturbations.

The paper is organized as follows: In Section 5.2, we provide a brief overview of UCMHs. In Section 5.3, we construct a baryon gas model within UCMHs and evaluate the 21-cm signal from an individual UCMH. In Section 5.4, we calculate the 21-cm fluctuations resulting from the distribution of UCMHs, and we also consider the detectability of these fluctuations by the SKA. Based on this analysis, we discuss the potential constraints on UCMHs and primordial curvature perturbations in Section 5.5. Finally, we provide a conclusion in Section 5.5.

5.2 UCMHs with the spiked matter spectrum

Small-scale matter density fluctuations with larger amplitude can be seeds of UCMHs. In this section, we begin with the brief review of UCMHs with the spiky shape power spectrum, according to Delos, Erickcek, Bailey, *et al.* [72], [73].

In addition to the nearly scale-invariant spectrum, we consider the spike shape of the primordial curvature power spectrum on a small scale, which enters the horizon during the radiation-dominated (RD) era. This can be represented by the equation:

$$\mathcal{P}\zeta(k) = \mathcal{A}\zeta k_{\mathrm{s}}\delta(k - k_{\mathrm{s}}), \tag{5.1}$$

where $\mathcal{A}\zeta$ is the amplitude of the spike shape and ks is the wave number of the spike. During the RD era, DM fluctuations can grow logarithmically. Here, for simplicity, we adopt the Dirac delta function to represent the additional spike-shaped spectrum. Then, after the radiation-matter equality, they evolve proportionally to the scale factor. When the density amplitude in an overdensity region reaches the critical value for collapse, the overdensity region can collapse into a DM halo, as per the standard hierarchical structure formation.

However, when the amplitude of the spike in the primordial curvature power spectrum is significantly larger than that of the standard scale-invariant spectrum, the properties of the resulting DM halos differ from those of typical DM halos. Numerical simulations by Delos, Erickcek, Bailey, *et al.* [73] have demonstrated that a spike spectrum can lead to the formation of isolated, compact DM halos known as UCMHs. The resultant DM density profile in a UCMH is represented by a self-similar form as

$$\rho_{\mathrm{dm}}(r) = \rho_{\mathrm{s}} y_{\mathrm{dm}}\left(\frac{r}{r_{\mathrm{s}}}\right), \tag{5.2}$$

where r is the radial distance from the centre, ρ_{s} is the scale density and r_s are the scale radius. The non-dimensional density profile y_{dm} is given by

$$y_{\mathrm{dm}}(x) = \frac{1}{x^{\alpha}(1+x)^{3-\alpha}}, \tag{5.3}$$

with defining $x \equiv r/r_{\mathrm{s}}$. The simulations demonstrated that the index α for UCMHs is $\alpha = 1.5$, that is the Moore profile [134]. It is known that the hierarchical structure formation yields the NFW profile [135] whose index corresponds to $\alpha = 1$. Therefore, UCMHs have a steeper DM profile in the inner region.

Delos, Erickcek, Bailey, *et al.* [73] also showed that ρ_s and r_s are related to the UCMH forming redshift z_{c} and the wave number of the spike as

$$\rho_{\mathrm{s}} = 30(1+z_{\mathrm{c}})^3 \Omega_{\mathrm{m},0}\rho_{\mathrm{crit},0} \tag{5.4}$$

$$r_{\mathrm{s}} = 0.7[(1+z_{\mathrm{c}})k_{\mathrm{s}}]^{-1}, \tag{5.5}$$

where $\rho_{\mathrm{crit},0}$ is the critical density at present.

For the UCMH (virial) mass, M_{vir}, we adopt the mass enclosed within r_{200},

$$M_{\mathrm{vir}} = 4\pi\rho_{\mathrm{s}} r_{\mathrm{s}}^3 m(u_v), \tag{5.6}$$

$$m(x) \equiv \int_0^x u^2 y_{\mathrm{dm}}(u) du. \tag{5.7}$$

where u_{v} is $u_{\mathrm{v}} \equiv r_{200}/r_{\mathrm{s}}$ and the scale r_{200} is defined as the scale inside which the averaged DM density is 200 times the mean DM density of the Universe. We found that the UCMH mass is related to $z_{\rm c}$ and $k_{\rm s}$ as in

$$M_{\rm vir} \sim 4 \times 10^3 \, {\rm M}_\odot \times \left(\frac{k_{\rm s}}{10^3 \, {\rm Mpc}^{-1}} \right)^{-3} \ln \left(\frac{1+z_{\rm c}}{1+z} \right). \tag{5.8}$$

Therefore, the virial mass of a UCMH continues to grow logarithmically even after its formation. This growth corresponds to the late-time accretion on the outer region as suggested by simulations [73]. The number density of UCMHs can be evaluated using the peak theory [87], as UCMHs form at the peak locations of the density fluctuations following the spike-shaped spectrum. As seen in Eq. (2.170), the differential UCMH number density can be expressed by

$$\frac{dn_{\rm UCMH}}{dz_{\rm c}} = \frac{k_{\rm s}^3}{1+z_{\rm c}} h \left[\frac{\delta_{\rm c}}{\mathcal{S}_{\rm mat,0}^{1/2} D(z_{\rm c})} \right], \tag{5.9}$$

where $\delta_{\rm c} = 1.686$ is the critical density contrast for collapse, and $\mathcal{S}_{\rm mat,0}$ is the variance of matter density contrast at present. As we explained in Sec. 3.4.1, we can estimate this variance and the growth rate through $\mathcal{S}_{\rm mat,0}^{1/2} D(z) = \mathcal{A}_{\rm mat,0}^{1/2}/(1+z_{\rm c})$ using $\mathcal{A}_{\rm mat,0}$ defined in Eq. (3.49) during MD epoch. In Eq. (5.9), $h(\nu)$ is the function defined in Eq. (2.171),

$$h(\nu) = \frac{3^{3/2}\nu}{(2\pi)^2} e^{-\nu^2/2} f(\nu). \tag{5.10}$$

with the function $f(\nu)$ defined in Eq. (2.161). The abundance of UCMHs, as expressed through Eq.(5.9), is contingent upon the properties of the spike shape, $\mathcal{A}\zeta$ and ks. Consequently, by obtaining a constraint on the abundance of UCMHs, we can infer limits on the peak-shape spectrum through Eq. (5.9).

5.3 21-cm signal from a single UCMH

In this section, we evaluate the 21-cm signal emitted by a single UCMH. The 21-cm signal is sensitive to the gas density profile within a UCMH. Therefore, we begin by deriving the profile of a UCMH under the assumption of hydrostatic equilibrium with the gravitational potential of the DM profile presented in the previous section.

5.3.1 Baryon gas mass in UCMHs

Unlike DM, baryonic density fluctuations cannot grow prior to the decoupling of photons. Following the decoupling, baryonic density fluctuations start to evolve, tracking the evolution of dark matter density fluctuations. However, due to the resistance of baryonic gas to gravitational collapse, there is a critical scale for collapse known as the Jeans scale. Therefore, in order to evaluate the baryonic gas mass within UCMHs, we consider two scenarios based on the spike scale, $k_{\rm s}$.

When $k_{\rm s}$ is smaller than the Jeans wave number, $k_{\rm J}$, baryonic density fluctuations with $k_{\rm s}$ can grow and collapse, tracking the evolution of dark matter density. Therefore, for simplicity, we assume that UCMHs can possess baryonic gas in proportion to the ratio of the cosmological background,

$$M_{\rm gas}(z) = \frac{\Omega_{\rm b,0}}{\Omega_{\rm dm,0}} M_{\rm vir}(z) \quad ({\rm for}\ k_{\rm s} < k_{\rm J}), \tag{5.11}$$

where $\Omega_{\mathrm{dm},0}$ is the density parameter of CDM.

On the contrary, if k_s exceeds k_J, then the baryon density fluctuations associated with k_s are hindered by their own pressure. Nevertheless, UCMHs can still possess a substantial amount of baryonic matter through the accretion of baryonic gas. We calculate the mass of accreted baryonic gas at the redshift z using

$$M_\mathrm{gas}(z) = \int_z^{z_\mathrm{acc}} dz' \frac{\dot{M}_\mathrm{gas}(z')}{(1+z')H(z')} \quad (\text{for } k_\mathrm{s} > k_\mathrm{J}), \tag{5.12}$$

where z_acc is the starting redshift of the gas accretion. We set z_acc to $z_\mathrm{acc} = \min[z_\mathrm{c}, z_\mathrm{dec}]$ where z_dec is the redshift for the decoupling of photons. For the accretion rate, $\dot{M}_\mathrm{gas}(z)$, we adopt the Bondi-Hoyle-Lyttleton accretion [204],

$$\dot{M}_\mathrm{gas}(z) = 4\pi G^2 \Omega_\mathrm{b} \rho_\mathrm{crit}(z) M_\mathrm{vir}^2(z) v_\mathrm{r}^{-3}(z). \tag{5.13}$$

Here v_r is the relative velocity between baryon and DM, $v_\mathrm{r}(z) = 30\ \mathrm{kms}^{-1}[(1+z)/1000]$ [205][1]. Note that, to avoid the over-accretion to UCMHs, we set the upper limit of the accretion gas mass, $M_\mathrm{gas} < M_\mathrm{vir}\Omega_{\mathrm{b},0}/\Omega_{\mathrm{dm},0}$.

In Figure 5.1, we plot the ratio of baryonic gas mass to DM mass in UCMHs, $f_\mathrm{mass} = M_\mathrm{gas}/M_\mathrm{vir}$, at a redshift of $z = 20$ as a function of the spike-wave number, k_s. The black solid, dashed, and dotted lines represent f_mass for UCMHs that collapsed at $z_\mathrm{c} = 50$, 100, and 1000, respectively. For reference, we also plot the Jeans wave number at $z = 20$ as a thin blue vertical line. In this work, we adopt the Jeans wave number as presented in Barkana and Loeb [206].

When the spike-wave number is smaller than k_J, we assume that the baryonic matter can collapse in tandem with the dark matter. As a result, the gas mass ratio is $f_\mathrm{mass} = \Omega_\mathrm{b}/\Omega_\mathrm{dm}$, as shown in Equation (5.11). Conversely, when $k_\mathrm{s} > k_\mathrm{J}$, UCMHs obtain baryonic gas through accretion, with the accretion rate given by Eq. (5.13). Since the accretion rate is proportional to $M_\mathrm{vir}^2 \propto k_\mathrm{s}^{-6}$, the baryonic gas mass steeply declines with increasing k_s. Figure 5.1 also demonstrates that a UCMH with a large z_c has a higher gas mass ratio. As UCMH formation occurs at earlier redshifts, the UCMH undergoes a longer period of accretion, resulting in a larger accreted gas mass within the UCMH.

5.3.2 Baryon gas density and temperature in UCMHs

Now we evaluate the density and temperature profiles of the baryon gas following the method of [207], which is based on the hydrostatic equilibrium assumption.

Since the DM profile is expressed in the self-similar form, the gas density profile of UCMHs, ρ_gas, would also be the self-similar form as

$$\rho_\mathrm{gas}(r) = \rho_\mathrm{gas}(0) y_\mathrm{gas}\left(\frac{r}{r_\mathrm{s}}\right), \tag{5.14}$$

where $y_\mathrm{gas}(x)$ is the non-dimensional gas profile normalised as $y_\mathrm{gas}(0) = 1$. Applying the polytropic gas model with the polytropic index γ, we can write the gas

---

[1] Here, we disregard the impact of the thermal velocity of baryons, as it is known to be smaller than the relative velocity between baryons and DM [205]. The peak spectrum also results in an additional relative velocity. Nevertheless, this velocity is dampened by the wave number k. Therefore, we also choose to omit this contribution.

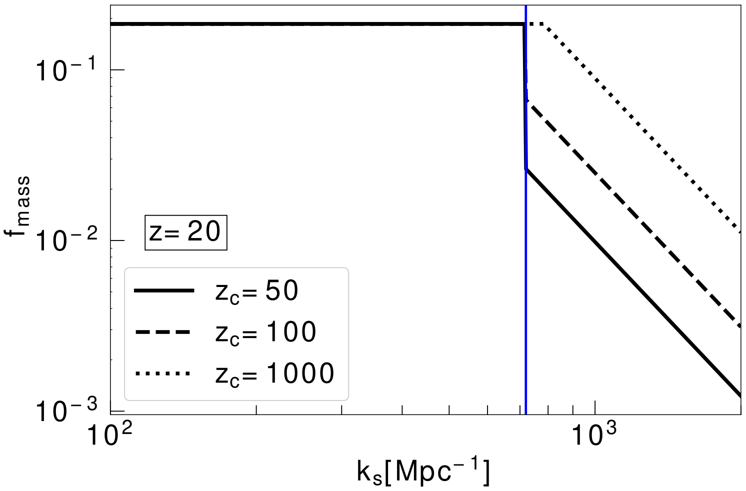

FIGURE 5.1: Baryon gas mass ratio to the DM mass, $f_{\rm mass} = M_{\rm gas}/M_{\rm vir}$, at the redshift $z = 20$. The solid, dashed and dotted black lines show the baryon gas mass fraction of the UCMH formed at $z_{\rm c} = 50$, 100 and 1000, respectively. We also provide the Jeans wave number at $z = 20$ in a vertical blue line.

temperature profile in

$$T_{\rm gas}(r) = T_{\rm gas}(0) y_{\rm gas}^{\gamma-1}\left(\frac{r}{r_{\rm s}}\right). \tag{5.15}$$

The assumption of the hydrostatic equilibrium allows us to relate the gas pressure profile to the DM density profile,

$$\rho_{\rm gas}^{-1}\frac{dP_{\rm gas}}{dr} = -\frac{GM(r)}{r^2}. \tag{5.16}$$

Here we assume that the gas component does not contribute to the gravitational potential. To derive the pressure profile, we adopt the equation of the state of an ideal gas,

$$P_{\rm gas} = \frac{k_{\rm B}T_{\rm gas}}{\mu m_{\rm p}}\rho_{\rm gas}, \tag{5.17}$$

where $k_{\rm B}$ is the Boltzmann constant, $m_{\rm p}$ is the proton mass and μ is the mean molecular weight of the gas. Using Eqs. (5.15) and (5.16), $y_{\rm gas}$ can be derived as [208]

$$y_{\rm gas}^{\gamma-1}(x) = 1 - 3\eta_0^{-1}\frac{\gamma-1}{\gamma}\frac{u_{\rm v}}{m(u_{\rm v})}\int_0^x du\frac{m(u)}{u^2}, \tag{5.18}$$

where the mass-temperature normalisation factor η_0 is expressed as

$$\eta_0 = \frac{3k_{\rm B}r_{200}T_{\rm gas}(0)}{G\mu m_{\rm p}M_{\rm vir}}. \tag{5.19}$$

To obtain the gas profile, it is required to fix η_0 and γ. For the determination of these parameters, we take the assumption that the gas profile traces the DM profile outside halo core. This condition is satisfied by imposing the slopes of these two profiles to match,

$$s_* \equiv \left.\frac{d\ln\rho_{\rm dm}(x)}{d\ln x}\right|_{x=x_*} = \left.\frac{d\ln\rho_{\rm gas}(x)}{d\ln x}\right|_{x=x_*}, \tag{5.20}$$

where x_* is the location outside the core region. As a result, we obtain

$$\gamma = 1 - \frac{1}{s_*} + \frac{\partial\ln[m(x_*)/s_*]}{s_*\partial\ln x_*}, \tag{5.21}$$

$$\eta_0 = 3\gamma^{-1}\left[\left(\frac{-1}{s_*}\right)\left[\frac{x_*^{-1}m(x_*)}{u_{\rm v}^{-1}m(u_{\rm v})}\right] + (\gamma-1)\frac{u_{\rm v}}{m(u_{\rm v})}\int_0^{x_*} du\frac{m(u)}{u^2}\right], \tag{5.22}$$

where s_* is provided from the DM distribution,

$$s_* = -\left[\alpha + (3-\alpha)\frac{x_*}{1+x_*}\right]. \tag{5.23}$$

One can see that η_0 is a function of x_* and γ. It is preferable that η_0 does not depend on the location x_*. To satisfy this condition, we impose the following condition, according to [209],

$$\frac{\partial\eta_0}{\partial x_*} = 0, \tag{5.24}$$

with setting $x_* = u_{\rm v}$. This equation yields

$$\gamma = \frac{16u_{\rm v}^2 + 20u_{\rm v} + 5}{3(1+2u_{\rm v})^2} - \frac{2u_{\rm v}}{3(1+2u_{\rm v})m(u_{\rm v})}\left(\frac{u_{\rm v}}{1+u_{\rm v}}\right)^{1/2}, \tag{5.25}$$

where $m(x)$ is given by

$$m(x) = 2\ln\left(\sqrt{x} + \sqrt{1+x}\right) - 2\sqrt{\frac{x}{1+x}}. \tag{5.26}$$

The final parameter to determine the gas profile is $\rho_{\rm gas}(0)$, which we obtain through

$$\rho_{\rm gas}(0) = M_{\rm gas}\left[4\pi r_{\rm s}^3\int_0^{u_{\rm v}} y_{\rm gas}(u)u^2du\right]^{-1}, \tag{5.27}$$

where $M_{\rm gas}$ is given in Eqs. (5.11) and (5.12).

5.3.3 Brightness temperature

Let us evaluate the 21-cm signal of a single UCMH at a given redshift. We first consider a line of sight that intersects the UCMH at an impact parameter $\alpha_{\rm R}$, measured in units of r_{200}, from its center. The brightness temperature along this line of sight is given by the following equation,

$$T_{\rm b}(\alpha_{\rm R}) = T_{\rm CMB}(z)e^{-\tau(\alpha_{\rm R})} + \int_{-R_{\rm max}}^{R_{\rm max}} T_{\rm s}(l)e^{-\tau(\alpha_{\rm R},R)}\frac{d\tau}{dR}dR, \tag{5.28}$$

where $T_{\rm CMB}(z) = T_{\rm CMB,0}(1+z)$ with $T_{\rm CMB,0} = 2.725\,{\rm K}$, R is the coordinate along the line of sight, whose origin is set to the center of the UCMH, $T_{\rm s}$ is the radial profile of the spin temperature in the UCMH, as we will discuss later, l represents the radial distance satisfying $l^2 = R^2 + (\alpha_\mathrm{R} r_{200})^2$ and R_max is defined as $R_\mathrm{max}^2 \equiv r_{200}^2(1-\alpha_\mathrm{R}^2)$.

The optical depth, $\tau(R)$, for the frequency at the rest frame of the UCMH, ν, is calculated from

$$\tau(\alpha_\mathrm{R}, R) = \frac{3c^2 A_{10} T_*}{32\pi\nu_*^2} \int_{-R_\mathrm{max}}^{\mathrm{R}} \frac{n_\mathrm{HI}(l)\phi(\nu, l)}{T_\mathrm{s}(l)} dR, \tag{5.29}$$

where $T_* = 0.0681$ K, $\nu_* = 1440$ MHz is the frequency of the 21-cm line in the rest frame, c is the speed of light, $A_{10} = 2.85 \times 10^{-15}\mathrm{s}^{-1}$ represents the Einstein A coefficient for the 21-cm transition, and $n_\mathrm{HI}(r)$ provides the radial profile of neutral hydrogen which we obtain through $n_\mathrm{HI}(r) = (1-Y_\mathrm{p})\rho_\mathrm{gas}/m_\mathrm{p}$ with the helium fraction Y_p. Here $\phi(\nu, r)$ is the line profile at the radial distance r for the rest-frame frequency ν, which suffers the Doppler broadening due to the thermal velocity of the gas,

$$\phi(\nu, r) = \frac{1}{\Delta\nu\sqrt{\pi}} \exp\left(-\frac{(\nu-\nu_*)^2}{\Delta\nu^2}\right), \tag{5.30}$$

where the Doppler width $\Delta\nu$ is given by

$$\Delta\nu = \frac{\nu_*}{c}\sqrt{\frac{2k_\mathrm{B}T_\mathrm{gas}(r)}{m_\mathrm{H}}}. \tag{5.31}$$

In Eq. (5.28), $\tau(\alpha_R)$ is obtained by $\tau(\alpha_R) = \tau(\alpha_R, R_\mathrm{max})$. Hereafter, we set the frequency, ν, to the reference frequency, ν_*, such that the observed frequency is $(1+z)\nu_*$. The reasoning behind this choice is discussed in Section 5.4.

It is necessary to determine the spin temperature, which is a function of the ratio of the number densities of the two hyperfine structure levels to calculate the brightness temperature of the 21-cm signal along a line of sight intersecting the UCMH, as given in Eq.(5.28) using Eq.(5.29). The spin temperature can be calculated using the expression provided by [210],

$$T_\mathrm{s}^{-1} = \frac{T_\mathrm{CMB}^{-1}(z) + x_\mathrm{c} T_\mathrm{gas}^{-1} + x_\alpha T_\alpha^{-1}}{1 + x_\mathrm{c} + x_\alpha}, \tag{5.32}$$

where T_α is the colour temperature of Lyα photons, and x_c and x_α represent the coupling coefficients for the gas collisions and the Lyα pumping, respectively. In this work, we set $x_\alpha = 0$, because we assume that there exist no UV and X-ray external sources. The coupling coefficient for gas collisions is expressed in

$$x_\mathrm{c} = \frac{T_*}{A_{10} T_\mathrm{CMB}} C_\mathrm{HI}, \tag{5.33}$$

where C_HI is the collisional coefficient between HI atoms and we adopt the value in [211]. In this context, we assume that the gas within UCMHs is entirely neutral, and thus, we neglect the contribution from the collisions of HI with protons and electrons. By utilizing Eq. (5.32) in conjunction with the gas radial profile derived in Section5.3.2, we can compute the radial profile of the spin temperature within UCMHs for Eqs. (5.28) and (5.29).

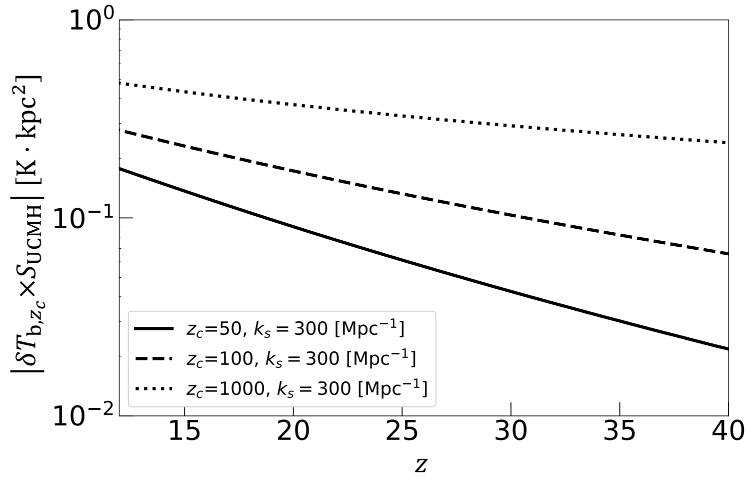

FIGURE 5.2: The 21-cm signal from a single UCMH, which is given a product of the differential brightness temperature and a geometrical cross section of UCMH, as a function of redshift. We show the 21-cm signal from a single UCMH at the formation redshift $z_\mathrm{c} = 50, 100, 1000$ as the solid, dashed and dotted black lines, respectively.

The effective brightness temperature, averaged over the cross-sectional area of a single UCMH, $S_{\mathrm{UCMH}} = \pi r_{200}^2$, is given by

$$T_{\mathrm{b},z_\mathrm{c}} = \frac{\int T_\mathrm{b} dS_{\mathrm{UCMH}}}{S_{\mathrm{UCMH}}} = 2\int_0^1 T_\mathrm{b}(\alpha_\mathrm{R})\alpha_\mathrm{R} d\alpha_\mathrm{R}. \tag{5.34}$$

We measure the 21-cm signals as the difference between the brightness and the CMB temperature, called the differential brightness temperature. The differential brightness temperature for the single UCMH at the redshift z can be calculated from

$$\delta T_{\mathrm{b},z_\mathrm{c}}(z) = \frac{T_{\mathrm{b},z_\mathrm{c}}}{1+z} - T_{\mathrm{CMB}}(0). \tag{5.35}$$

In Figure 5.2, we illustrate the evolution of the 21-cm signal emanating from a single UCMH. The y-axis of the figure represents the product of the differential brightness temperature and the UCMH cross-section, which corresponds to the total 21-cm flux emitted by the UCMH. Here, we set $k_\mathrm{s} = 300\ \mathrm{Mpc}^{-1}$, which is smaller than k_J at $z = 10$. In this scenario, the signal is observed as an emission on the CMB frequency spectrum. The strength of the signal is dependent on the baryon gas mass and temperature within the UCMH. As the redshift decreases, the signal monotonically increases due to the logarithmic growth of the UCMH's virial mass as a result of accretion, as per Eq. (5.8), even with a fixed value of k_s. The figure also demonstrates the dependence of the signal on the collapse redshift, z_c, with UCMHs collapsed at higher redshifts having larger virial masses and, thus, producing stronger signals in comparison to those collapsed at lower redshifts.

In Figure 5.3, we plot the signal as a function of k_s. The black lines represent the emission signals, while the red ones denote the absorption signal. As k_s becomes larger, UCMHs have smaller gas mass and lower baryon gas temperatures. As a result, the spin temperature decreases, and the signal shifts from emission to absorption because the average spin temperature cannot exceed the CMB temperature in such a low UCMH mass. The figure also illustrates that the signal drastically decreases when k_s exceeds k_J. This is because the baryons with such k_s cannot collapse

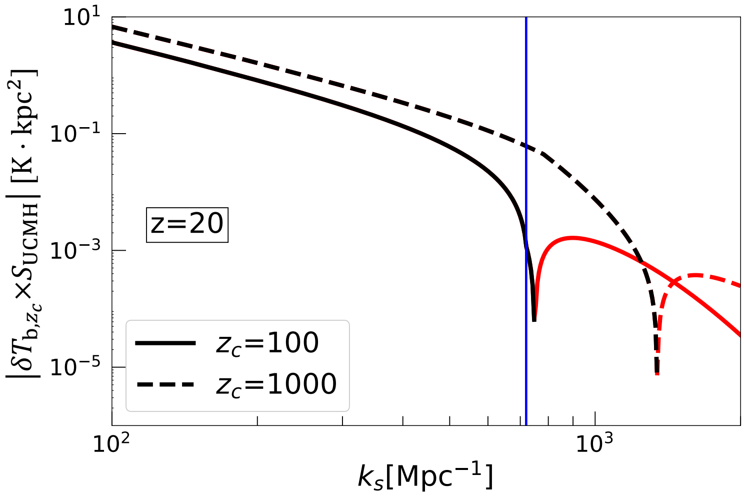

FIGURE 5.3: Dependence of the 21-cm signal from a single UCMH on the spike scale k_s. The solid and dashed lines correspond to the 21-cm signal from a single UCMH at $z_c = 100, 1000$, respectively. The vertical line shows the Jeans wave number at $z = 20$.

into the UCMH, and the baryon gas mass fraction decreases, as shown in Figure 5.1.

5.4 21-cm fluctuations due to the UCMH clustering

In this section, we evaluate the RMS fluctuations of the differential brightness temperature as the 21-cm signal of UCMHs, as the angular scale of an individual UCMH in the sky is too small to be resolved by forthcoming 21-cm observations, such as the SKA. The key observable for UCMHs is the differential brightness temperature fluctuations due to the number density fluctuation of UCMHs in the observational beam.

Now we consider the ensemble of UCMHs formed in the redshift from $z_{\mathrm{c,max}}$ to $z_{\mathrm{c,min}}$. Following Iliev, Shapiro, Ferrara, *et al.* [151], the mean 21-cm differential brightness temperature from this ensemble at the redshift z is given by

$$\overline{\delta T_{\mathrm{b}}}(z) = \frac{c(1+z)^4}{\nu_* H(z)} \int_{z_{\mathrm{c,min}}}^{z_{\mathrm{c,max}}} \Delta\nu_{\mathrm{eff}}(z)\delta T_{\mathrm{b},z_{\mathrm{c}}}(z) S_{\mathrm{UCMH}} \frac{dn_{\mathrm{UCMH}}}{dz_{\mathrm{c}}} dz_{\mathrm{c}}. \tag{5.36}$$

Here we set $z_{\mathrm{c,max}} = 4000$ and $z_{\mathrm{c,max}} = 50$, and $\Delta\nu_{\mathrm{eff}}$ is the effective linewidth, which is provided by

$$\Delta\nu_{\mathrm{eff}}(z) = [\phi(\nu_*)(1+z)]^{-1} \approx \frac{\nu_*}{c(1+z)} \sqrt{\frac{2\pi k_{\mathrm{B}} \overline{T}_{\mathrm{gas}}(z)}{m_{\mathrm{H}}}}, \tag{5.37}$$

where $\overline{T}_{\mathrm{gas}}(z)$ is the volume averaged temperature within an individual UCMH. In order to determine the mean differential brightness temperature of the 21-cm signal, we must calculate the total flux integrated over the line profile. To simplify this calculation, we utilize a rectangular approximation, which has a height obtained by setting $\nu = \nu_*$ in Eq. (5.29) and a width of $\Delta\nu_{\mathrm{eff}}$ (for further information, we refer readers to read Sec. 2 inIliev, Shapiro, Ferrara, *et al.* [151]).

On large scales, the distribution of UCMHs is homogeneous with a number density of $n_{\mathrm{UCMH}} = \int dz_{\mathrm{c}} dn_{\mathrm{UCMH}}/dz_{\mathrm{c}}$. However, as the scale-invariant fluctuations on large scales evolve, the distribution of UCMHs can gravitationally trace these fluctuations, resulting in fluctuations in the number of UCMHs within an observational beam volume that depend on the matter density fluctuations in the beam. The RMS fluctuations due to UCMHs can be evaluated by

$$\langle \delta T_{\mathrm{b}}^2 \rangle^{1/2}(z) = \beta_{\text{UCMH}}(z)\sigma_p(z)\overline{\delta T_b}(z), \tag{5.38}$$

where σ_p is the RMS fluctuation of the matter density averaged in the observation beam volume. We adopt the cylinder-shape beam: the diameter and height of the cylinder-shape beam respectively correspond to the angular resolution, $\Delta\theta$, and the frequency resolution, $\Delta\nu$, of the observations. In this configuration, σ_p is given by

$$\sigma_p(z) = \int_0^\infty \frac{dk}{k}\mathcal{P}_\delta(k,z)W_{\text{cy}}(k,z), \tag{5.39}$$

where $\mathcal{P}_\delta(k,z)$ is the non-dimensional matter power spectrum at the redshift z. For the matter power spectrum, we use the amplitude $\sigma_8 = 0.81$ and the spectral index $n_{\mathrm{s}} = 0.965$. The cylinder-shape beam window function is expressed in

$$W_{\text{cy}}(k,z) = \frac{16}{R^2L^2}\int_0^1 dx \frac{\sin^2(kLx/2)J_1^2(kR(1-x^2)^{1/2})}{k^4x^2(1-x^2)}, \tag{5.40}$$

where R and L are the comoving radius and height of the cylinder, $R = \Delta\theta(1+z)D_{\mathrm{A}}(z)/2$ and $L \approx (1+z)^2c(\Delta\nu/\nu_*)/H(z)$.

In Eq. (5.39), $\beta_{\text{UCMH}}(z)$ is the bias factor for the UCMH clustering to the matter density fields. We assume that β_{UCMH} can be obtained by the flux-weighted average of the linear bias over the different collapse redshifts,

$$\beta_{\text{UCMH}}(z) = \frac{\int_{z_{\text{c,min}}}^{z_{\text{c,max}}} b_{\text{UCMH}}\Delta\nu_{\text{eff}}(z)\delta T_{\mathrm{b},z_{\mathrm{c}}}(z)S_{\text{UCMH}}\frac{dn_{\text{UCMH}}}{dz_{\mathrm{c}}}dz_{\mathrm{c}}}{\int_{z_{\text{c,min}}}^{z_{\text{c,max}}} \Delta\nu_{\text{eff}}(z)\delta T_{\mathrm{b},z_{\mathrm{c}}}(z)S_{\text{UCMH}}\frac{dn_{\text{UCMH}}}{dz_{\mathrm{c}}}dz_{\mathrm{c}}}, \tag{5.41}$$

where b_{UCMH} is the linear bias in the peak theory as shown in Eq. (2.172). With the redshift decreasing, b_{UCMH} is monotonically becomes small.

In the top panel of Fig. 5.4, we illustrate the evolution of the 21-cm fluctuations of UCMHs as a function of redshift. As the redshift decreases, the fluctuations also become more pronounced, similar to the single UCMH signal in Fig. 5.2. It is important to note that we have not taken into account the impact of the cosmic reionization process on the fluctuations. During the EoR, the abundance of ionizing photons can photoevaporate the neutral gas in UCMHs, similar to the case of minihalos [212], and this can suppress the amplitude of the fluctuations near the EoR ($z \lesssim 10$).

In the top panel of Fig. 5.4, we also demonstrate the dependence of the fluctuations on the amplitude $\mathcal{A}\zeta$. An increase in $\mathcal{A}\zeta$ enhances the fluctuations through two effects. Firstly, it increases the number density of UCMHs. However, at the scales and redshifts of interest, the number density is saturated when $A_\zeta > 10^{-7}$. Thus the enhancement through the number density is weak. Secondly, an increase in $\mathcal{A}_\zeta$ results in the early-time formation of UCMHs. As shown in Fig.5.2, UCMHs that form at high redshifts provide large signals, which gives the dependency on $\mathcal{A}_\zeta$ as shown in the top panel of Fig. 5.4.

The bottom panel in Fig. 5.4 shows the dependence on k_{s} for two different $\mathcal{A}_\zeta$ at $z = 20$. As the value of ks increases, the signal emitted by individual UCMHs decreases, and as a result, the RMS fluctuations also decrease. As anticipated, when

k_s exceeds the Jeans wave number, the signal rapidly diminishes, as can be observed from Figure 5.3.

5.4.1 Detectability with SKA

Several ongoing observations are attempting to detect the 21-cm fluctuation signal coming from $z \gtrsim 10$, e.g., LOFAR, GMRT, MWA, and Paper. Although there has been no report of the signal detection yet, some observations have provided upper limits on the 21-cm fluctuations, e.g., $\delta T_\mathrm{b}^2(k) < (49.0\ \mathrm{mK})^2$ at $k \approx 0.59h\mathrm{Mpc}^{-1}$ at $z = 6.5$ by MWA [202] and $\delta T_\mathrm{b}^2(k) < (79.6\ \mathrm{mK})^2$ at $k \approx 0.053h\mathrm{Mpc}^{-1}$ at $z \sim 10$ by LOFAR [198].

However, the maximum fluctuations produced by UCMHs in our model, $\delta T_\mathrm{b}^2 \lesssim (5\ \mathrm{mK})^2$ at $z = 20$, are considerably smaller than the sensitivities of current 21-cm observation instruments. Thus, we are unable to constrain the UCMH abundance and the spike-shaped power spectrum using current 21-cm fluctuation observations.

The upcoming 21-cm observation, the SKA, is expected to detect and measure the 21-cm fluctuations at $z \gtrsim 10$. In this work, we estimate the detectability of 21-cm signals from UCMHs using the SKA by taking into account the 21-cm fluctuations from the IGM and minihalos (MHs), as well as the observational noise of the SKA.

In Fig.5.4, we plot the expected fluctuations due to the IGM + MHs and the noise of SKA in the blue lines. For more detailed calculations, we refer readers to AppendixD. We assume that the primary source of noise is the foreground emission of the sky. Since the foreground has a strong frequency dependence, the noise rapidly increases as the redshift increases (the observation frequency decreases). In the frequency and angular resolutions of our interest, the noise becomes larger than the IGM + MH fluctuations above $z \sim 20$. It is important to note that we do not take into account the effects of cosmic reionization, which might enhance the 21-cm fluctuations of the IGM below $z \sim 10$ based on the Planck constraint on Thomson scattering optical depth.

Our analysis involves two free parameters, k_s and $\mathcal{A}\zeta$ that pertain to the spike-shape spectrum and affect the amplitude of fluctuations. By surveying a range of (ks, $\mathcal{A}_\zeta$) parameter sets, we have identified the region in which the 21-cm fluctuations from UCMHs surpass those from the IGM and minihalos (MHs), as well as the observational noise of the upcoming SKA telescope, at a redshift of $z = 20$. This region is depicted in red in Fig. 5.5. In instances where the spike-shape spectrum generates fluctuations within this red region, the SKA will be able to detect an excess of 21-cm signals from UCMHs over the expected IGM and MH signals. Conversely, if the SKA fails to detect such an excess, the delta-shape spectrum within this red region can be ruled out.

At $k_\mathrm{s} \sim 700\ \mathrm{Mpc}^{-1}$, one can see the sharp cutoff in Figure 5.5. The cutoff scale corresponds to the Jeans scale at the observation redshift $z = 20$. When $k_\mathrm{s} > k_\mathrm{J}$, the baryon mass fraction drastically decreases in UCMHs, particularly those that form late. These UCMHs do not host enough baryonic gas to produce strong 21-cm signals for detection. Consequently, 21-cm observations cannot provide a constraint below the Jeans scale.

It is worth noting the dependence of this constraint on the observed redshift. As shown in the top panel of Figure 5.4, the fluctuation amplitude increases as the redshift decreases, with k_s fixed. Therefore, when a lower redshift is considered, the constraint becomes slightly tighter. Furthermore, as the redshift decreases, the Jeans scale becomes smaller. Accordingly, the sharp cutoff of the allowed region on the high-k side shifts towards larger k. When 21-cm observations are performed at

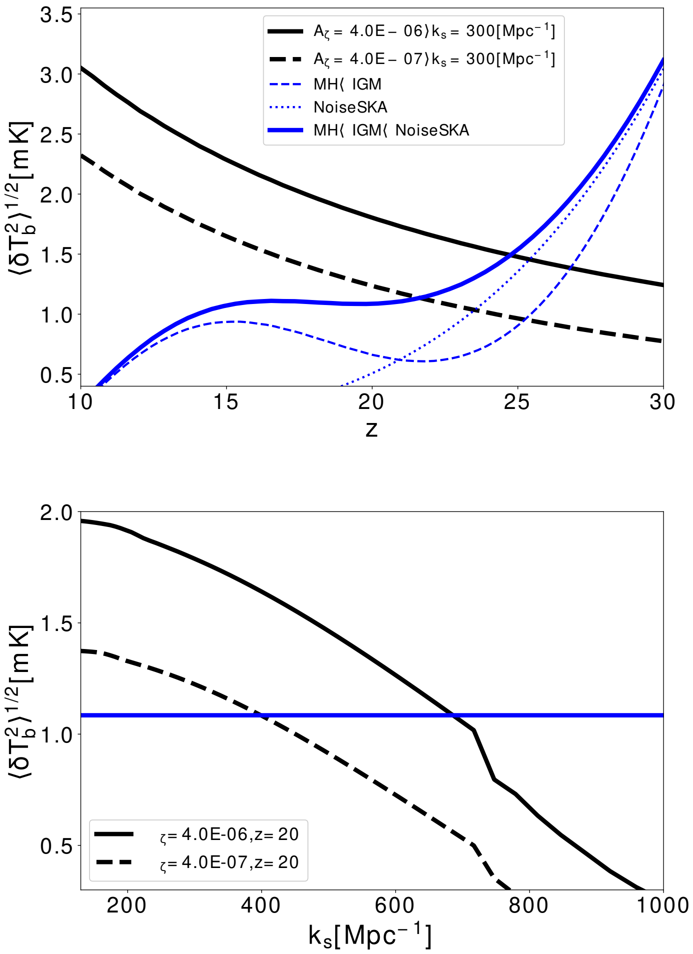

FIGURE 5.4: (*Top*) Redshift dependence of the 21-cm fluctuations from UCMHs. The black solid line and the dashed lines are the 21-cm fluctuations from UCMH for $A_\zeta = 4.0 \times 10^{-6}$ and 4.0×10^{-7}, respectively. In both lines, we set $k_s = 300$ Mpc^{-1}. We also plot the fluctuation from the IGM + MHs in the blue dotted line, the SKA noise level in the blue dot-dashed line and the sum of them in the blue solid line. (*Bottom*) Dependence of the 21-cm fluctuations on the spike wave number k_s at $z = 20$. The solid line is for $A_\zeta = 4.0 \times 10^{-6}$ while the dashed line is for 4.0×10^{-7}. The blue solid line represents the fluctuation from the IGM + MHs with the SKA noise level.

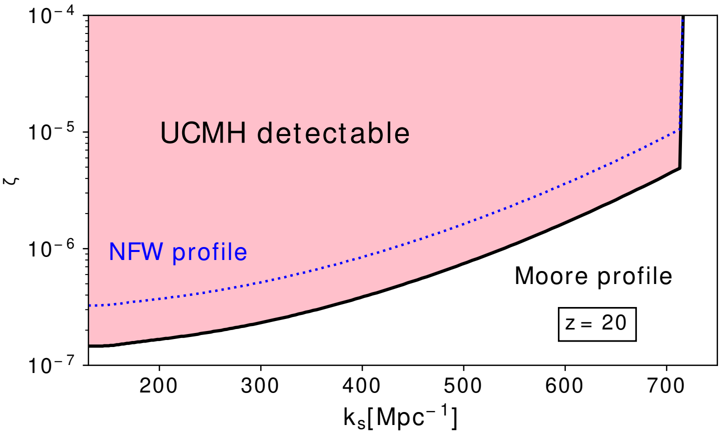

FIGURE 5.5: Detectability of the signal from UCMHs with observation by SKA. The parameter set within the red region of Fig. 5.5 can yield 21-cm fluctuations resulting from UCMHs that can be detected by the SKA at a redshift of $z = 20$. The leftmost boundary of the red region corresponds to the Jeans scale, k_J, and the dotted line represents the threshold for detection when the DM density distribution of UCMHs is modeled using the NFW profile.

$z = 10$, the red region can be extended to $k_s \approx 1000\ \mathrm{Mpc}^{-1}$ which corresponds to the Jeans scale at $z = 10$. In lower redshifts, the cosmological reionization process generates additional 21-cm fluctuations, which are dependent on the model of the reionization process. As a result, it is challenging to accurately evaluate the potential constraint on the primordial curvature amplitude while taking into account the impact of reionization.

Lastly in this section, we also examine the impact of the density profile on 21-cm signals. In our calculations, we utilize the Moore profile and determine the gas density and temperature profiles based on hydrostatic equilibrium. However, according to numerical simulations by Gosenca, Adamek, Byrnes, *et al.* [133], if UCMH formation occurs in non-isolated situations, the profile of the resultant UCMHs can be well-approximated by the NFW profile. To investigate the impact of the profile on the 21-cm signal, we adopt the NFW profile as the DM density distribution, using Eqs.(5.4)and(5.5), and evaluate the signal using the procedures outlined in sections 5.3and5.4. Since the NFW profile has a shallower slope in the inner region than the Moore profile, the signal from the NFW halo is weaker than that from the Moore halo. We depict the critical amplitude for detection in the blue dotted line in Fig.5.5. In summary, when a UCMH has a shallower profile, the constraint on the spike-shape amplitude becomes less stringent.

5.5 Conclusion

UCMHs are believed to be formed from density fluctuations with a spike-shape spectrum on small scales. As a result, the observational limit on the abundance of UCMHs serves as an upper bound on the small-scale power spectrum of primordial fluctuations. In this study, we evaluated the 21-cm signals emitted by UCMHs and demonstrated that the SKA could provide an upper limit on the abundance of UCMHs as well as the small-scale primordial fluctuations.

To construct a theoretical model of the baryon gas density and temperature within UCMHs, we adopted the Moore profile as the DM density distribution. We then calculated the 21-cm signal from an individual UCMH and found that the signal increases with the UCMH mass.

Our observable is the 21-cm fluctuations caused by the number density fluctuations of UCMHs. We investigated the relationship between these fluctuations and the spike-shape spectrum of primordial fluctuations. We found that the 21-cm fluctuations produced by UCMHs become larger as the spike amplitude increases or as the peak shifts to smaller scales. Additionally, we found that the 21-cm fluctuations due to UCMHs are on the order of millikelvin in the redshift range between $z = 10$ and 30. However, if the wave number of the spike-shape spectrum becomes smaller than the Jeans scale, the baryon gas mass within a UCMH drastically decreases, leading to a significant decrease in the signal.

Although the 21-cm fluctuations produced by UCMHs do not currently fall within the detection capabilities of current observational instruments, the SKA may be able to detect these signals if a spike-shaped spectrum on the primordial power spectrum is present. Conversely, if the SKA fails to detect the signal, an upper limit on the amplitude of the curvature perturbations can be placed at $\mathcal{A}_\zeta \lesssim 10^{-6}$ for $100\ \mathrm{Mpc}^{-1} \lesssim k \lesssim 1000\ \mathrm{Mpc}^{-1}$. Constraints on the abundance of UCMHs and the spike-shaped spectrum of primordial fluctuations have also been provided through gamma-ray observations, assuming the self-annihilation of DM particles within UCMHs. It is important to note that these constraints are highly dependent on the specific model of DM, such as its annihilation mechanism and mass. In contrast, 21-cm emission is independent of these properties of DM, making it a more robust method for surveying small-scale primordial fluctuations.

Chapter 6

Population III stars in UCMHs

In this chapter, we investigate the impact of first-generation stars, also known as Population III (Pop. III) stars, on the cosmic ionization history within ultracompact minihalos (UCMHs) by utilizing Planck observation data. Despite the current lack of understanding of high-redshift astrophysics, UCMH has the potential to host Pop III stars, similar to halos formed in the standard structure formation scenario. These stars would emit ionizing photons during their main sequence, potentially fostering cosmic reionization at higher redshifts, thus providing a powerful means for constraining primordial perturbations. To study their effect on global ionization, we model the cosmic reionization evolution based on the "tanh"-type reionization model, which is characterized by $z_{\rm reio}$ and two additional parameters representing the initial mass of UCMHs and their number density. We employ Monte Carlo Markov Chain analysis and the latest Planck observation data in our reionization model. Our results indicate that if the UCMH initial mass is larger than $10^{8.4}M_{\odot}$, the number density of UCMHs is strictly limited. This, in turn, leads to a constraint on the amplitude of the primordial power spectrum, specifically $\mathcal{A}_{\zeta} \lesssim 10^{-8}$ in the scales $k \lesssim 50\mathrm{Mpc}^{-1}$, assuming that standard "tanh" type reionization occurs by $z = 3$, and $zreio > 3$ is set.

6.1 Introduction

Ultracompact minihalo (UCMH) is gravitationally bound object formed by denser region of matter induced by excess power in primordial scalar perturbations on small scales [71]. Although there is currently no observational evidence to confirm the existence of UCMHs, they have been proposed as a powerful cosmological probe of primordial scalar perturbations, particularly on small scales, $k \gtrsim 1\mathrm{Mpc}^{-1}$. The basic formation process of UCMHs is thought to occur during the radiation-dominated epoch, in which dark matter density fluctuations can grow after entering the horizon, as long as the initial density perturbation is large enough at the time of horizon entry. Reference [71] suggests that UCMHs have a more compact profile with a larger central density than typical dark matter halos, known as NFW profiles [135], as a result of radial infall in high redshift. Subsequent studies, such as Refs.[72], [73], have performed cosmological simulations of UCMH formation for spike-type power spectra on small scales, demonstrating that the excess power in small-scale primordial scalar perturbations can lead to early structure formation, with UCMHs possessing a Moore-type matter density profile, $\rho \propto r^{-3/2}$ at the inner cusp region [134], which is steeper than the NFW profile.

In this context, previous works have studied the possibility that UCMHs emit energetic emissions through weakly-interacting massive particle (WIMP) annihilation, which is enhanced by the dense profile of UCMHs. Especially some previous works [72]–[78] have investigated the gamma-ray emission signal and provided constraints on the UCMH abundance. These studies also provided constraints on small-scale primordial scalar perturbation, with an amplitude $\mathcal{A}_\zeta$ less than 10^{-7} for wavenumbers between 10 Mpc^{-1} and 10^8 Mpc^{-1}, through the non-detection of such energetic signals in gamma-ray observations, such as those made by Fermi-LAT [140]. Additionally, UCMHs have been investigated through their gravitational lensing effect [77], [141] and their contribution to cosmic reionization [142]–[145].

The primary focus of the author is on the baryonic gas contained within UCMHs. When the mass of a UCMH exceeds the Jeans mass, it is capable of hosting baryonic gas. By studying the cosmological signals emitted by this baryonic gas within UCMHs, we can place constraints on both the abundance of UCMHs and the small-scale primordial perturbations without making any assumptions about the nature of dark matter. In previous research (referenced in [213]), we examined the anisotropy of 21cm line emission induced by UCMHs and established a constraint on primordial scalar perturbations on small scales, $\mathcal{A}_\zeta \lesssim 10^{-6}$ on $100\,\mathrm{Mpc}^{-1} \lesssim k \lesssim 1000\,\mathrm{Mpc}^{-1}$. Additionally, in reference [174], we studied the free-free emission from UCMHs and, utilizing measurements of free-free emission by Planck, established a constraint on primordial scalar perturbations of $\mathcal{A}\zeta \lesssim 10^{-7}$ for $1\,\mathrm{Mpc}^{-1} \lesssim k \lesssim 100\,\mathrm{Mpc}^{-1}$.

This paper presents another observable that has the potential to be more constraining than previous works. Our focus is on the astrophysical effects that occur within UCMHs. Given that UCMHs can form in the early Universe and possess a dense matter profile, such as the Moore profile, they may facilitate the formation of stars at significantly higher redshifts than what is predicted by standard cosmology. As a result, zero metallicity stars, commonly referred to as Population III (Pop. III) stars, would be formed from the primordial baryon gas, primarily composed of hydrogen, within UCMHs. According to theoretical and numerical studies [214], [215], Pop. III stars are known to emit ionizing photons effectively. As such, Pop. III stars hosted by UCMHs would proceed to globally ionize high redshifts and alter the standard cosmic reionization history. Our work builds upon a similar study of astrophysical effects in axion clusters formed by isocurvature fluctuations, presented in Ref. [216]. Although our focus is on the effects that occur within UCMHs formed by spike-type power spectra as opposed to isocurvature-type, we refer to this work in our calculations.

In the standard cosmology, after the cosmic recombination epoch at $z \sim 1000$, the kinematic decoupling of the baryons from radiation occurs [217], [218], the Universe enters the next epoch, referred to as the "dark age," where the global ionization fraction is very low, $x_\mathrm{e} \sim 10^{-4}$. This epoch culminates with the formation of stars, galaxies, etc., and their emission of ionizing photons; this is the standard cosmic dawn and reionization scenario. It is believed that the cosmic reionization has been primarily proceeded by Population II (Pop. II) stars and first galaxies [219], and was almost completed by $z \sim 6$, as indicated by observations of Lyman-α(Lyα) absorption lines imprinted on quasar spectra [220]. The luminosity of Lyα is highly sensitive to the amount of neutral hydrogen. Thus the observation of the redshift evolution of the Lyα luminosity can provide significant information on the evolution of neutral hydrogen fractions during the epoch of reionization. Current observations of Lyα emitters suggest that the number density of Lyα emitters decreases as the redshift increases, and the neutral hydrogen fraction increases from $z \sim 6-7$ [221]–[226].

One of the observables for the reionization history is cosmic microwave background (CMB) anisotropies. Specifically, the CMB E-mode polarization anisotropy is sensitive to the high redshift reionization expected by the UCMH Pop. III stars model through the Compton scattering. In this work, we investigate this model characterized by the mass and the number density of UCMHs using Markov Chain Monte Carlo (MCMC) methods with the Planck 2018 observation likelihoods [1].

The organization of this chapter is as follows: In Section II, we describe the properties of UCMHs formed by the spike-type curvature power spectrum. In Section III, we introduce the effect of Pop. III stars formed in UCMHs on the global ionization fraction. In Section IV, we explain our cosmic reionization model considered here and demonstrate the relationship between the reionization models and the anisotropies of the CMB temperature and E-mode polarization. In Section V, we explain the MCMC methods used in this work and present the results. We also discuss the constraint on the amplitude of the primordial power spectrum suggested by the MCMC results. Finally, we summarize in Section VI. Throughout this chapter, we adopt the flat ΛCDM model with the Planck best-fit parameters obtained from TT, TE, EE, and low-ℓ + lensing observation data[1].

6.2 The properties of UCMHs

The larger amplitude of the small-scale matter density fluctuation would provide the UCMH formation. In this work, we assume the existence of an UCMH population formed through a spike in the small-scale matter density fluctuation spectrum, characterized by a specific wavenumber k_{s} in addition to the nearly scale-invariant spectrum with an amplitude of $\mathcal{A}_\zeta^{\mathrm{CMB}} \sim 2.1 \times 10^{-9}$, as inferred from Planck CMB observations. Here, for simplicity, we adopt the Dirac delta function to represent the additional spike-type power spectrum as,

$$\mathcal{P}_\zeta(k) = \mathcal{A}_\zeta k_{\mathrm{s}} \delta(k - k_{\mathrm{s}}), \tag{6.1}$$

where $\mathcal{A}_\zeta$ is the amplitude of the additional power spectrum, and k_{s} is the wave number corresponding to the spike center. We begin with a brief summary of the features of UCMHs with the spike-type power spectrum (see Refs. [72], [73] for details.)

In the spike-type power spectrum case, the initial mass of UCMHs M_{i} are related to the spike-wave number k_{s} like

$$M_{\mathrm{i}} \sim 4 \times 10^4\ \mathrm{M}_\odot \times \left(\frac{k_{\mathrm{s}}}{10^3\ \mathrm{Mpc}^{-1}} \right)^{-3}. \tag{6.2}$$

The mass can increase after their formation at redshift z_{f} through late-time accretions from their outer region, e.g. intergalactic medium (IGM), as [73], [213]

$$M(z, z_{\mathrm{f}}) = M_{\mathrm{i}} \left(1 + \ln \left(\frac{1 + z_{\mathrm{f}}}{1 + z} \right) \right). \tag{6.3}$$

In this work, we assume that the accretion of matter onto UCMHs does not cease during the calculated duration, despite suggestions from reference [73] that the logarithmic mass increment may not continue beyond a certain point. Additionally, it is worth noting that previous literature, such as reference [127] and [76], have assumed that the mass of UCMHs increases proportionally to the scale factor a under the radial infall theory of mass accretion. However, since this theory relies on the presence of an overdense region within an otherwise unperturbed background, which may not be representative of the actual Universe, we utilize the mass increase specified in equation (6.3). In the subsequent calculations, we estimate the number density of UCMHs using the equations outlined in section 3.4.1 to derive an expression for the abundance of UCMHs.

In the following calculation, we estimate the number density of UCMHs by using equations explained in Sec. 3.4.1. Then one will obtain the expression for the abundance of UCMHs,

$$n_{\text{UCMH}}(M_{\text{i}}, z) = \frac{k_{\text{s}}^3}{(2\pi)^2 3^{3/2}} \int_{\delta_c / \mathcal{S}^{1/2}_{\text{mat},0}(M_{\text{i}}) D(z)}^{\infty} e^{-\nu^2/2} f(\nu) \mathrm{d}\nu. \tag{6.4}$$

Here we stress the following two points. First, we hereafter use $\mathcal{A}_{\text{mat},0}$ as a parameter about the present mass variance instead of $\mathcal{S}_{\text{mat},0}$. Secondly, we adopt the transfer function of Ref.[89] as already shown in Eq. (2.139),

$$T_\delta(k) = \frac{45}{2} \frac{\Omega_{\text{m},0}^2 H_0^2}{\Omega_{\text{r},0} k^2} \left(-\frac{7}{2} + \gamma_{\text{E}} + \ln \left(\frac{4\sqrt{\Omega_{\text{r},0}}k}{\sqrt{3}\Omega_{\text{m},0} H_0} \right) \right) , \tag{6.5}$$

when calculating $\mathcal{S}_{\text{mat},0}$ in this work. This transfer function is valid only for the scale, $k \gg 10^{-2}\text{Mpc}^{-1}$. These scales correspond to the range, $M_{\text{i}} < 10^{15} M_\odot$ in terms of the UCMH initial mass. Since we are interested in the mass range which is much smaller than $M_{\text{i}} = 10^{15} M_\odot$ as we will mention in Sec. 6.5, this function is valid throughout this work.

We also focus on the baryonic gas within UCMHs. To form stars within UCMHs, they must enclose baryonic gas. As long as the spike-wave number k_{s} is smaller than the Jeans wave number, k_{J}, at their formation redshift z_{f}, the baryonic gas can collapse towards the dark matter gravitational potential, overcoming its own gas pressure. In such a scenario, we assume that UCMHs would enclose enough baryonic gas to form stars with the same mass ratio to dark matter as in the cosmological background, $\Omega_{\text{b},0}/\Omega_{\text{m},0}$, where $\Omega_{\text{b},0}$ is the baryon density parameter at present, although there are other conditions that must be satisfied to host stars. We will discuss these conditions in the next section. Additionally, we postulate that the mass ratio between baryonic gas and dark matter in UCMHs remains constant throughout their mass evolution as represented by Eq. (6.3).

In addition, we mention the scenario in which the spike-wave number k_{s} is greater than the Jeans wave number, k_{J}, at their formation redshift z_{f}. In this scenario, although the baryon density fluctuations with k_{s} cannot collapse due to their own pressure, UCMHs may still host dense baryon gas through the accretion of baryonic matter, such as the Bondi accretion mechanism [227]. However, as previous studies [213] have shown, the amount of accreted baryonic matter would be small. Furthermore, as other conditions would impose stronger constraints on the mass of UCMHs, we neglect this accretion effect.

6.3 Pop. III stars formation in UCMHs

In high redshifts, $z \gtrsim 10$, the Universe is primarily composed of hydrogen and helium. In that case, the formation of zero-metallicity stars, known as Pop. III stars are possible. UCMHs, being minihalos formed at a higher redshift than the standard halo formation scenario, may also host Pop. III stars if certain conditions are met. In this section, we focus on the impact of ionizing photons emitted by Pop. III stars within UCMHs on the global ionization fraction.

These photons would create and evolve ionized bubbles, and the time evolution of the global ionization fraction induced by these bubbles is given by [228]

$$\frac{dx_\mathrm{e}}{dt} = \frac{d\left(\zeta f_\mathrm{coll}\right)}{dt} - \bar{n}_H(t)\alpha_\mathrm{B}\left(T_\mathrm{e}\right)C_\mathrm{HII}x_\mathrm{e} \tag{6.6}$$

where $\bar{n}$H, αB, T_e, C_HII, and f_coll represent the mean number density of hydrogen nuclei in the IGM, the case B recombination rate as detailed in Reference [229], the electron temperature, the clumping factor, and the collapsed fraction, respectively. In this work, we set the electron temperature as $T_\mathrm{e} = 10^4$K, and the clumping factor as $C_\mathrm{HII} \approx 3$. The star ionizing efficiency, ζ, is represented by $\zeta \equiv A_\mathrm{He}N_\gamma f_\mathrm{esc}f_\star$, where $A_{H_\mathrm{e}} \approx 1.22$ is the correction factor for singly ionized helium, N_γ represents the average number of ionizing photons produced per stellar baryon, f_esc represents the escape fraction of ionizing photons, and $f_\star$ represents the star formation efficiency. Due to the current uncertainty in understanding the contributions of Pop. III stars to the ionization history [230], we adopt a simplified model to mimic the approach used for Pop. II stars in previous work [216]. We assume an average number of ionizing photons produced per stellar baryon, N_γ, of 4×10^4, which is expected for the hotter photospheres of metal-free stars [231]. We postulate that all ionizing photons escape, as is typical for star formation in small halos, and set the escape fraction, f_esc, to 1. We also set the star formation efficiency, $f_\star$, to 5×10^{-4}, which is on the lower end of the values typically used in prior work [232], [233], with the most commonly used value being around 10^{-3}. It is worth noting that the value of the escape fraction can be considered one of the star formation efficiency parameters.

With the common assumption that the star formation rate in a halo is proportional to the baryon gas accretion rate $\dot{M}_\mathrm{acc}$ with $f_\star$ as the proportional coefficient, the first term in right-hand side of Eq. (6.6) can be written

$$\begin{aligned}\frac{\mathrm{d}\left(\zeta f_\mathrm{coll}\right)}{\mathrm{d}t} &= A_\mathrm{He}N_\gamma f_\mathrm{esc}\int_{M_\mathrm{min}}\mathrm{d}M'\, f_\star\dot{M}_\mathrm{acc}\frac{dn_\mathrm{UCMH}(M',z)}{dM}\frac{1}{\bar{\rho}_b(z)} \\ &= A_\mathrm{He}N_\gamma f_\mathrm{esc}\frac{\dot{\rho}_\mathrm{SFR}(z)}{\bar{\rho}_\mathrm{b}(z)},\end{aligned} \tag{6.7}$$

where $\dot{\rho}_\mathrm{SFR}$ is the star formation rate density, $\bar{\rho}_\mathrm{b}$ is the mean baryon density, $\dot{M}_\mathrm{acc}$ can be estimated from Eq. (6.3) as

$$\dot{M}_\mathrm{acc}(M,z) = M_\mathrm{i}H(z)\frac{\Omega_\mathrm{b,0}}{\Omega_\mathrm{m,0}}, \tag{6.8}$$

and dn_UCMH/dM is the UCMH mass function associated with Eq. (6.4). In Eq. (6.7), M_min represents the criteria of the halo mass to form the Pop. III stars including the Lyman-Werner negative feedback [234], [235],

$$M_\mathrm{min} = M_\mathrm{halo}\left(T_\mathrm{vir} = 500\ \mathrm{K}\right)\left[1 + 6.96F_\mathrm{LW,21}^{0.47}\right], \tag{6.9}$$

with $M_\mathrm{halo}(T_\mathrm{vir})$ which is the typical halo mass with a given virial temperature T_vir, and the Lyman-Werner intensity integrated over a solid angle, $F_\mathrm{LW,21}$ which is in units of $10^{-21}\mathrm{ergs}^{-1}\mathrm{Hz}^{-1}\mathrm{cm}^{-2}$.

To estimate $M_{\mathrm{halo}}(T_{\mathrm{vir}} = 500\ \mathrm{K})$, we use the relation,

$$M_{\mathrm{halo}}(T_{\mathrm{vir}}, z_{\mathrm{f}}) \approx 4 \times 10^5\ \mathrm{M}_\odot \left(\frac{T_{\mathrm{vir}}}{500\mathrm{K}} \frac{1+z_{\mathrm{f}}}{10}\right)^{\frac{3}{2}} \left(\frac{\Omega_{\mathrm{m},0}}{\Omega_{\mathrm{m}}(z_{\mathrm{f}})}\right)^{-\frac{1}{2}}, \tag{6.10}$$

where $\Omega_{\mathrm{m}}(z)$ is the matter density parameter at a redshift z after the matter-dominant era,

$$\Omega_{\mathrm{m}}(z) = \frac{\Omega_{\mathrm{m},0}(1+z)^3}{\Omega_{\mathrm{m},0}(1+z)^3 + \Omega_{\Lambda,0}}, \tag{6.11}$$

with $\Omega_{\Lambda,0}$, which is the present density parameter of the cosmological constant.

We also employ the relation between the Lyman-Werner intensity and $\dot{\rho}_{\mathrm{SFR}}$ [236], [237] and estimate $F_{\mathrm{LW},21}$ as

$$F_{\mathrm{LW},21} = 7.22 \frac{(1+z)^3}{H(z)} e^{-\tau_{LW}} N_{\mathrm{LW}} \frac{\dot{\rho}_{\mathrm{SFR}}}{\bar{\rho}_{\mathrm{b}}}, \tag{6.12}$$

where $H(z)$ is the Hubble parameter, τ_{LW} is the intergalactic opacity for the Lyman-Werner photons, and N_{LW} is the number of Lyman-Werner photons produced per baryon in stars. In our analysis, we adopt the value of $e^{-\tau_{\mathrm{LW}}} = 0.5$ as reported in previous studies [215], [238], acknowledging that the Lyman-Werner background optical depth, τ_{LW}, may be increased by the presence of UCMHs that obscure the background. Additionally, we adopt a value of $N_{\mathrm{LW}} = 10^5$ for Pop. III stars as suggested in[237].

In Eq. (6.9), we posit that a virial temperature of $T_{\mathrm{vir}} = 500\mathrm{K}$ is sufficient to excite rotational transitions of molecular hydrogen, which can serve as an efficient cooling mechanism for the formation of Pop. III stars. We further assume that UCMHs can host Pop. III stars as long as their mass exceeds the minimum mass, M_{min}, required for such cooling, as well as the Jeans mass. It is worth noting that in the parameter ranges of interest, M_{min} exceeds the Jeans mass.

UCMHs would have the mass variety even in the case of delta function type power spectrum of Eq. (6.1) because there is a variety of their formation redshifts z_{f} following the number density formed in the duration of $[z_{\mathrm{f}}, z_{\mathrm{f}} + \Delta z_{\mathrm{f}}]$,

$$\frac{dn_{\mathrm{UCMH}}}{dz_{\mathrm{f}}} = \frac{k_{\mathrm{s}}^3}{1+z_{\mathrm{f}}} h\left(\nu = \frac{\delta_{\mathrm{c}}(1+z_{\mathrm{f}})}{\mathcal{A}_{\mathrm{mat},0}^{1/2}}\right). \tag{6.13}$$

In Eq. (6.13), $h(\nu)$ is given by

$$h(\nu) = \frac{3^{3/2}\nu}{(2\pi)^2} e^{-\nu^2/2} f(\nu), \tag{6.14}$$

with the function $f(\nu)$ defined in Eq. (2.161). The earlier-formed UCMHs are heavier than the later-formed ones due to matter accretion. However, in peak theory, most UCMHs are formed around the specific redshift $z_{\mathrm{eff}} \approx 2.1936\mathcal{A}_{\mathrm{mat},0}^{1/2}/\delta_c - 1$ which can be estimated by the derivative of the differential number density of Eq. (6.13) unlike the Press Schechter halo formation formalism [91]. Then we assume that the mass of all UCMHs is given by

$$M_{\rm eff}(z) \equiv M(z, z_{\rm eff}) = M_{\rm i}\ {\rm Max}\left(1, 1 + \ln\left(\frac{1+z_{\rm eff}}{1+z}\right)\right), \tag{6.15}$$

and the mass function of UCMHs is given by

$$\frac{dn_{\rm UCMH}(M,z)}{dM} \approx n_{\rm UCMH}(M,z)\delta(M - M_{\rm eff}). \tag{6.16}$$

Therefore, we approximately calculate Eq. (6.7) as

$$\frac{{\rm d}\left(\zeta f_{\rm coll}\right)}{{\rm d}t} \approx \begin{cases} A_{\rm He} f_\gamma f_{\rm esc} f_\star \dot{M}_{\rm acc} n_{\rm UCMH}(M_{\rm eff}, z) & M_{\rm eff} > M_{\rm min} \\ 0 & otherwise, \end{cases} \tag{6.17}$$

Figure 6.1 illustrates the evolution of $M_{\rm eff}$ and $M_{\rm min}$ as a function of redshift. It is important to note that the minimum mass, $M_{\rm min}$, and $\dot{\rho}$SFR in Eq. (6.9) are independent of the UCMH initial mass. This is because the dependencies on UCMH mass for both $\dot{M}_{\rm acc}$ and dn/dM in Eq. (6.7) cancel each other out. Additionally, the dependency on $\mathcal{A}_{\rm mat,0}$ is also relatively weak because the redshift dependence of the bracket term in Eq. (6.9) and the other term, $M_{\rm h}(T_{\rm vir} = 500)$ almost cancel out.

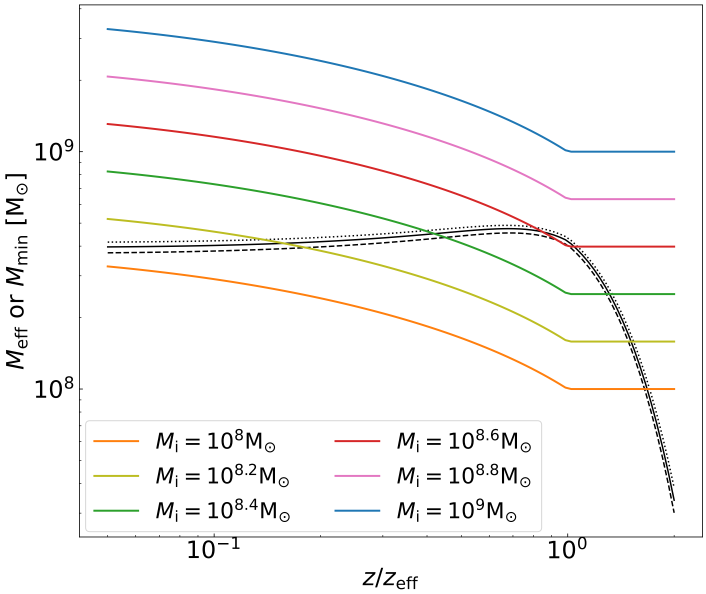

FIGURE 6.1: The minimum mass of UCMHs to host Pop. III stars in Eq. (6.9) (black line) and the UCMH effective mass represented in Eq. (6.15). The horizontal axis shows the redshift normalized by the $z_{\rm eff}$ with $\mathcal{A}_{\rm mat,0}$. The vertical axis shows the minimum and the effective mass of UCMHs in a unit of the solar mass. The black dotted, solid and dashed lines represent the minimum masses with $\mathcal{A}_{\rm mat,0} = 100, 200, 500$, respectively. The colorful solid lines show the effective masses with the different initial mass models.

6.4 Reionization model including UCMH Pop. III stars

The UCMH Pop. III stars might impact on the traditional ionization scenario, which predicts that the universe will be reionized a long time after the recombination epoch. Here we consider the global ionization history adding this effect of Pop. III stars formed in UCMH. In our model, Pop. II stars and first galaxies would take over as the primary ionizing photon sources after high redshifts, $z \gtrsim 10$, where impacts of UCMH Pop. III stars on cosmic reionization would become dominating. Therefore, we postulate that the evolution of the global ionization fraction can be split into three parts while accounting for the ionizing photons from the UCMH Pop. III stars for the cosmic reionization as

$$\begin{aligned} x_{\mathrm{e}}(z) =& (x_{\mathrm{e}}^{\mathrm{rec}}(z) + x_{\mathrm{e}}^{\mathrm{reio}}(z)) \\ &+ x_{\mathrm{e}}^{\mathrm{add}}(z)(1 - x_{\mathrm{e}}^{\mathrm{rec}}(z) - x_{\mathrm{e}}^{\mathrm{reio}}(z)), \end{aligned} \tag{6.18}$$

where $x_{\mathrm{e}}^{\mathrm{rec}}$ is the global ionization fraction in the recombination epoch, and $x_{\mathrm{e}}^{\mathrm{reio}}$ represents the contribution from the main reionization source including Pop II stars and galaxies. For obtaining $x_{\mathrm{e}}^{\mathrm{rec}}$, we employ the recombination code `RECFAST` [239]–[242], whereas for $x_{\mathrm{e}}^{\mathrm{reio}}$, we adopt the widely used “tanh" model as [243]

$$\begin{aligned} x_{\mathrm{e}}^{\mathrm{reio}}(z) &= x_{\mathrm{e}}^{\mathrm{before}} + \frac{1}{2}\left(x_{\mathrm{e}}^{\mathrm{after}} - x_{\mathrm{e}}^{\mathrm{before}}\right) \\ &\quad \times \left[1 + \tanh\left(\frac{y^{\mathrm{reio}} - y(z)}{\Delta y}\right)\right], \end{aligned} \tag{6.19}$$

$$y(z) = (1+z)^{3/2}, \tag{6.20}$$

where $y^{\mathrm{reio}} = y(z^{\mathrm{reio}})$, $\Delta y = 1.5\sqrt{1+z^{\mathrm{reio}}}\Delta z$ with the duration of reionizaiton, and we set $\Delta z = 0.5$. Note that $x_{\mathrm{e}}^{\mathrm{reio}}(z^{\mathrm{reio}}) = 0.5$. In Eq. (6.19), $x_{\mathrm{e}}^{\mathrm{after}} = 1$ is the ionization fraction after finishing reionization, and $x_{\mathrm{e}}^{\mathrm{before}}$ is the leftover ionization fraction well after the recombination epoch adopted as $x_{\mathrm{e}}^{\mathrm{before}} \sim 10^{-4}$. The evolution of $x_{\mathrm{e}}^{\mathrm{reio}}$(z) is characterized only by the value of z_{reio}. We deal with z_{reio} as a free parameter in the following analysis.

For the additional ionization fraction $x_{\mathrm{e}}^{\mathrm{add}}$, we estimate its value by solving Eq. (6.6). It is generally inadvisable to add ionization fractions from multiple sources. To accurately calculate the time evolution of the global ionization fraction, it is necessary to sum the photoionization rates and solve the equilibrium between recombination and ionization. However, in Eq. (6.6), we calculate the contribution of ionized bubbles surrounding Pop. III stars to the global ionization fraction, while terms $x_{\mathrm{e}}^{\mathrm{rec}}$ and $x_{\mathrm{e}}^{\mathrm{reio}}$ pertain to the global ionization fraction in the IGM. Therefore, in our model, we assume that the global ionization fraction can be estimated by Eq. (6.18). Although Eq. (6.18) is written with respect to redshift, Eq. (6.6) is written with respect to cosmic time. In order to estimate the three types of ionization fractions in Eq. (6.18) consistently, it is essential to exercise caution when calculating Eqs. (6.6) and (6.18) with respect to the time (redshift) step. We impose a lower limit on the redshift, z_{cut}, when calculating $x_{\mathrm{e}}^{\mathrm{add}}$, as we wish to focus on the contribution from halos created by the additional spike-type power spectrum, rather than standard halos originating from the almost scale-invariant spectrum. Therefore, we set z_{cut} to the redshift at which the standard halos are formed effectively, such that $z_{\mathrm{cut}} = \mathcal{A}_{\mathrm{mat},0}^{\mathrm{CMB}}/\delta_c - 1$.

Figure 6.2 illustrates examples of the evolution of the ionization fraction obtained from Eq. (6.18). The color differences in the figure correspond to variations in the initial mass of UCMHs, while different line styles indicate variations in the value of $\mathcal{A}_{\rm mat,0}$. The solid black line depicts the evolution of the global ionization fraction in the absence of any additional contributions from Pop. III stars hosted by UCMHs. In the figure, we set $zreio = 6$. Our analysis suggests that broadly speaking, the initial mass of UCMHs, $M_{\rm i}$, controls the extent of the ionizing effect, while the mass variance on the scale of $k_{\rm s}$, $\mathcal{A}_{\rm mat,0}$, determines the redshift at which the effect becomes significant. The non-monotonic behavior in the ionization fraction evolution depicted in Fig. 6.2 is a result of the varying duration of Pop. III star formation within UCMHs. As demonstrated in Fig.6.1, UCMHs with initial masses in the range of $10^8 M_\odot \lesssim M_i \lesssim 10^{8.6} M_\odot$ experience Pop. III star formation in two distinct periods. This results in the global ionization evolution progressing through three distinct phases: (1) an increase in the ionization fraction, x_e, due to ionizing photons emitted by Pop. III stars within UCMHs during the first period, (2) a decrease in x_e due to recombination in the absence of Pop. III stars within UCMHs, and (3) a subsequent increase in x_e resulting from the second period of Pop. III star formation within UCMHs. It is worth noting that the extent of the contributions from UCMHs with initial masses larger than $M_i = 10^{8.6} M_\odot$ saturates, as evidenced by the overlap of lines in Fig. 6.2. We also mention the contributions from UCMHs with a smaller initial mass than $10^8 M_\odot$, in that case, the contributions are too small to change the global ionization evolution.

The CMB anisotropy would be one of the helpful observables to test these models. Figures. 6.3 and 6.4 depict the temperature and the E-mode polarization anisotropies for different UCMH initial mass models. A meaningful indicator to explain these modifications in Figs. 6.3 and 6.4 is the Thomson scattering optical depth for CMB photons which is defined by,

$$\tau = \int \frac{dz}{H(z)} \sigma_{\rm T} x_{\rm e}(z) \bar{n}_H(z), \tag{6.21}$$

where $\sigma_{\rm T}$ is the Thomson cross section. As one can see in Fig. 6.3, the amplitude of the temperature anisotropy is suppressed as the optical depth increase. The theoretical dependency is $\propto \exp(-\tau)$, and the suppression is slight in these models. For the E-mode polarization anisotropy, one can find a significant difference among these models in Fig. 6.4, especially with the behavior at $\ell \lesssim 20$ mode. This behavior is called the “reionization bump," whose amplitude is proportional to τ^2.

6.5 MCMC analysis with Planck 2018

6.5.1 Setup

In order to investigate the impact of ionizing photons emitted from Pop III stars within UCMHs on the CMB using our proposed model (Eq. (6.18)), we employ the MCMC analysis utilizing Planck 2018 data. We generate chains of MCMC samples using the publicly available code `MontePython` [244], which incorporates the `CLASS` [245] code for calculating the theoretical CMB angular power spectrum. We have modified the `CLASS` code to include the global ionizing effect of Pop III stars within UCMHs represented by Eq. (6.18). In our calculations, we treat the following two parameters as free variables: (1) the mass variance on the scale $k_{\rm s}$, represented by $\mathcal{A}_{\rm mat,0}$, which relates to the amplitude of the spike power spectrum, and (2) the standard reionization parameter $zreio$ in Eq. (6.19). For the initial mass of UCMHs $M_{\rm i}$, which corresponds to the spike scale k_s, we fix it to a value within the range of $M_{\rm i} = 10^{8-9} M_\odot$ for each calculation. To ensure the validity of the approximation

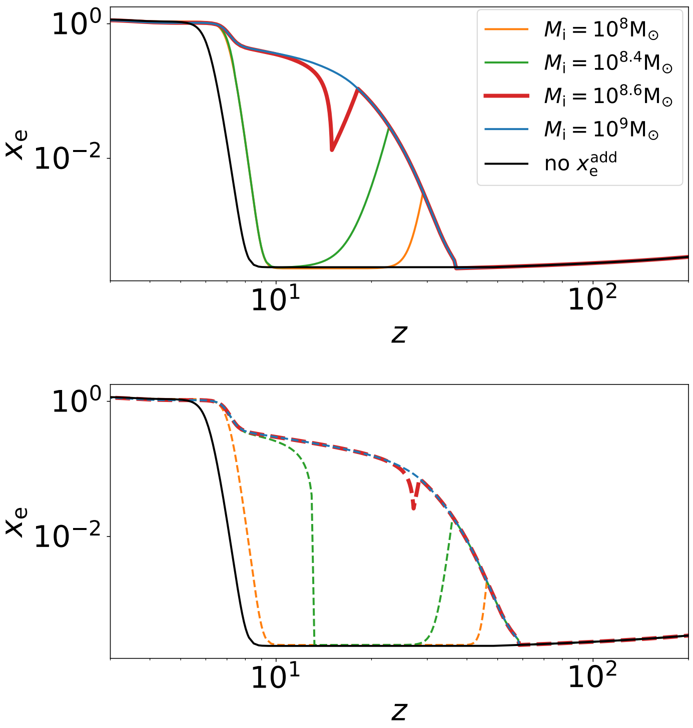

FIGURE 6.2: The cosmological evolution of the global ionization fraction estimated by Eq. (6.18). The color difference shows the difference of the initial mass of UCMHs, and the different line style shows the different value of $\mathcal{A}_{\mathrm{mat},0}$: $\mathcal{A}_{\mathrm{mat},0} = 200$ (solid) and $\mathcal{A}_{\mathrm{mat},0} = 500$ (dashed). The black solid line shows the global ionization fraction evolution without any additional contribution from Pop. III stars in UCMHs so that $x_e^{\mathrm{add}} = 0$. In this figure, we set $z_{\mathrm{reio}} = 6$. The extent of the contributions from UCMHs with a larger initial mass than $M_{\mathrm{i}} = 10^{8.6} M_\odot$ would saturate. Thus, the lines for $M_{\mathrm{i}} = 10^{8.6} M_\odot$ and $M_{\mathrm{i}} = 10^9 M_\odot$ mostly overlap.

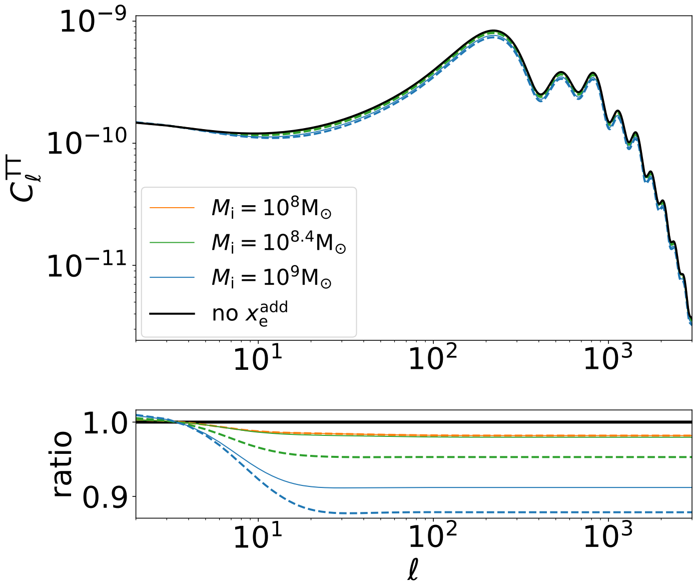

FIGURE 6.3: (*Top*): Angular power spectrum of the CMB temperature. The colorful lines shows CMB temperature anisotropies with the three different initial mass of UCMHs, and the different line style shows the different value of $\mathcal{A}_{\rm mat,0}$: $\mathcal{A}_{\rm mat,0} = 200$ (solid) and $\mathcal{A}_{\rm mat,0} = 500$ (dashed). The black solid line shows the standard CMB temperature anisotropy without any additional effects from Pop. III stars in UCMHs, $x_e^{\rm add} = 0$. (*Bottom*): Ratio between the standard CMB temperature anisotropy (black solid line) and one of each UCMH initial mass model.

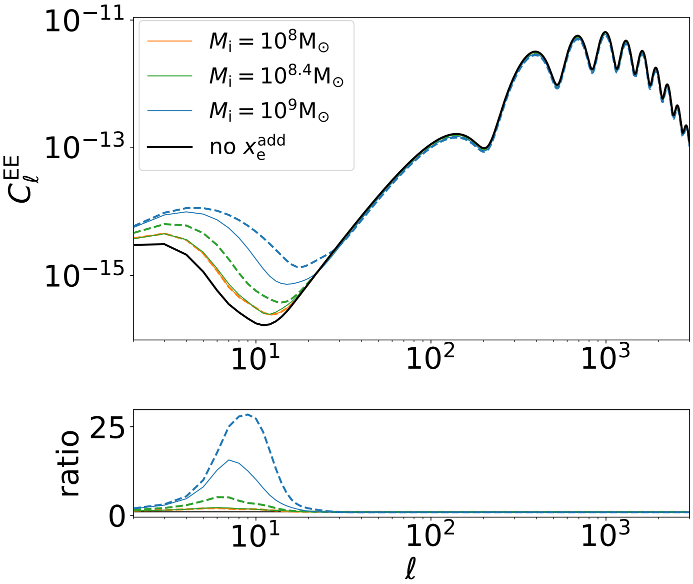

FIGURE 6.4: (*Top*): Angular power spectrum of the CMB E-mode polarization. The colorful lines shows CMB E-mode polarization anisotropies with the three different initial mass of UCMHs, and the different line style shows the different value of $\mathcal{A}_{\mathrm{mat},0}$: $\mathcal{A}_{\mathrm{mat},0} = 200$ (solid) and $\mathcal{A}_{\mathrm{mat},0} = 500$ (dashed). The black solid line shows the standard CMB E-mode polarization anisotropy without any additional effects from Pop. III stars in UCMHs, $x_\mathrm{e}^\mathrm{add} = 0$. (*Bottom*): Ratio between the standard CMB E-mode polarization anisotropy (black solid line) and one of each UCMH initial mass model.

represented in Eq. (3.50), we set a lower limit for $\mathcal{A}_{\rm mat,0}$, and impose hard priors for $\mathcal{A}_{\rm mat,0}$ such that the condition $\mathcal{A}_{\rm mat,0}(M_i) > \mathcal{A}^{\rm CMB}_{\rm mat,0}(M_i)$ shown in Fig. 3.4 is satisfied for each $M_{\rm i}$. For example, we set $\mathcal{A}_{\rm mat,0}(10^8 M\odot) > 79.2$ and $\mathcal{A}_{\rm mat,0}(10^9 M\odot) > 64.7$. We also assume that standard "tanh" type reionization occurs by $z = 3$, and thus set $z_{\rm reio} > 3$.

It is important to note the other cosmological parameters that are fixed in this analysis. Our primary focus is on the global ionization fraction evolution as represented in equation (6.6) and the resultant optical depth that appears in the reionization bump. The three parameters ($M_{\rm i}$, $\mathcal{A}_{\rm mat,0}$, $z$reio) primarily control these factors, and as such, we fix other cosmological parameters to the Planck best-fit values obtained from the TT, TE, EE, low-ℓ + lensing measurement, specifically $\Omega_{\rm b,0} = 0.02237$, $\Omega_{\rm cdm,0} = 0.1200$, $100\theta_{\rm s} = 1.04092$, $\ln 10^{10}\mathcal{A}^{\rm CMB}_{\zeta} = 3.044$, and $n_s = 0.9649$. These parameters do not significantly affect the reionization bump.

It is also worth noting the accuracy of the MCMC analysis. It is essential to ensure that the MCMC chains contain enough samples that are independent of each other and cover a sufficient volume of parameter space for confirmation of the accuracy of results from MCMC methods. Otherwise, the density of the samples will not converge to the actual posterior probability distribution. To address this, we employ the Gelman and Rubin convergence statistic R, which represents the ratio of the variance of parameters between chains to the variance within each chain, and only consider chains that satisfy the condition, $R - 1 < 0.05$ [246], [247].

6.5.2 MCMC results and discussion

We have conducted an MCMC analysis with UCMH initial masses ranging from $10^8 M_\odot$ to $10^9 M_\odot$. We have presented the results of our ionization history model represented by Eq. (6.18) for four UCMH initial mass values, namely $M_{\rm i} = 10^8 M_\odot$, $10^{8.2} M_\odot$, $10^{8.4} M_\odot$, and $10^9 M_\odot$ in Fig. 6.5. In this analysis, $\mathcal{A}_{\rm mat,0}$ and $z_{\rm reio}$ were treated as free parameters, while the optical depth τ was derived from Eq. (6.21) using the sampled data of the aforementioned parameters. The thick-colored region in the figure represents the 1σ region, while the thin-colored region denotes the 2σ region. As outlined in Sec. 6.4, the CMB polarization anisotropy is sensitive to the optical depth τ both during and after cosmic reionization, and the Planck measurement provides a constraint on τ. We have found that, even in our ionization history model, that accounts for the effects of UCMH Pop. III stars, the Planck observation data (TT, TE, EE, low-ℓ + lensing) prefer a similar best-fit value for the optical depth, $\tau^{\rm CMB} = 0.0544$. Thus, as the additional ionization fraction $x_{\rm e}^{\rm add}$ increases the optical depth to some extent, the value of $z_{\rm reio}$ is shifted to a lower value than the Planck result, $z^{\rm CMB}_{\rm reio} = 7.67$. If the mass of UCMHs is smaller than the lower mass criteria estimated by Eq. (6.9), the effect from UCMH Pop. III stars will not be observed, regardless of the value of $\mathcal{A}_{\rm mat,0}$.

In contrast, when the initial mass of UCMHs exceeds $10^8 M_\odot$, the ionizing photons emitted by Pop. III stars within these UCMHs can produce a non-insignificant optical depth. To compensate for this increase in optical depth, the reionization redshift, $z_{\rm reio}$, must be lower, as depicted in Figs. 6.1 and 6.2. If the UCMH initial mass exceeds $10^{8.2} M_\odot$, Pop. III stars can persist within UCMHs for prolonged periods, resulting in a significant increase in their contribution to the optical depth. If the initial mass exceeds $10^{8.6} M_\odot$, the contribution reaches its maximum. In such cases, decreasing $z_{\rm reio}$ cannot fully offset the increase in optical depth resulting from high values of $\mathcal{A}_{\rm mat,0}$, and the constraint on $\mathcal{A}_{\rm mat,0}$ becomes more stringent. In this study, we have considered UCMH initial mass ranges up to $10^9 M_\odot$. However, this constraint would also apply to UCMHs with initial masses exceeding $10^9 M_\odot$.

Although this work includes several uncertainties in astrophysics, it may be useful to convert the constraint on $\mathcal{A}_{\mathrm{mat},0}$ to one on $\mathcal{A}_\zeta$, which quantitatively demonstrates the amplitude of the additional spike-type power spectrum. By considering the relation between $\mathcal{A}_{\mathrm{mat},0}$ and $\mathcal{A}_\zeta$ represented by Eq. (3.50), one can infer

$$\mathcal{A}_\zeta \approx 0.94 \times 10^{-9} \mathcal{A}_{\mathrm{mat},0} \left(8.67 - \frac{1}{3} \ln \left(\frac{M_{\mathrm{i}}}{10^6 \mathrm{M}_\odot}\right)\right)^{-2}, \tag{6.22}$$

where ln represent natural logarithm.

The Fig. 6.6 illustrates the upper limit of the amplitude of the additional spike-type power spectrum, $\mathcal{A}_\zeta$, as constrained by the Planck 2018 data. This limit is calculated via Eq. (6.22), utilizing the 2-σ constraint of $\mathcal{A}_{\mathrm{mat},0}$ obtained through the MCMC analysis. It should be noted that in this figure, we have assumed $z_{\mathrm{reio}} > 3$, although current observations of Lyα emitters suggest that the epoch when the neutral hydrogen fraction increases, so that z_{reio} is about $z \sim 6 - 7$ [221]–[226]. As UCMHs with initial masses greater than $10^{8.4} M_\odot$ are powerful in globally ionizing in our model, the large excess in the primordial power spectrum on scales $k_{\mathrm{s}} \lesssim 40 \mathrm{Mpc}^{-1}$ is constrained. Conversely, this work is unable to put a constraint on the power spectrum on smaller scales, $k_{\mathrm{s}} \gtrsim 60 \mathrm{Mpc}^{-1}$, as such diminutive UCMHs lack the power to significantly alter the global ionization evolution.

We also test the case where UCMH will be formed from $z = z_{\mathrm{eff}}$. In this scenario, the non-monotonic behavior in the ionization fraction evolution depicted in Fig. 6.2 does not appear. Although the ionization fraction during the first of the three phases outlined in Sec. 6.4 is relatively low ($x_{\mathrm{e}} \ll 1$), this initial phase occurs in the high-redshift era and has the potential to significantly increase the optical depth by up to $\mathcal{O}(10)\%$. We conducted the MCMC analysis with this scenario and found that the final result shown in Fig. 6.6 is relaxed by $\mathcal{O}(10)\%$. It is worth noting that the formation of UCMHs prior to $z = z_{\mathrm{eff}}$ is not taken into account in this scenario. Thus this test is useful in assessing the impact of non-monotonic behavior on the conclusions of this study.

6.6 Conclusion

In this study, we examined the impact of Pop. III stars in UCMHs on the cosmic ionization history using data from the Planck observation. The formation of UCMHs could occur at an earlier epoch than the standard halo formation scenario, depending on the scale or amplitude of the additional spike-type power spectrum. While high-redshift astrophysics is not yet fully understood, it is believed that UCMHs may host Pop. III stars, similar to standard halos. These stars would emit ionizing photons during their main sequence and thus facilitate reionization at high redshifts.

To assess the effect of UCMH Pop. III stars on the cosmic reionization history, we employed the conventional "tanh" reionization model, which represents the contribution of the first galaxies and Pop. II stars as the main sources of ionizing photons. We also implemented the MCMC analysis with the latest Planck observation data to investigate the effect of UCMH Pop. III stars on the CMB anisotropies. We examined three parameters that compose our reionization model: (1) the mass variance on the scale k_{s}, represented by $\mathcal{A}_{\mathrm{mat},0}$, which relates to the amplitude of the additional power spectrum, (2) the standard reionization parameter zreio, which controls the conventional "tanh" reionization, and (3) initial mass models of UCMHs in the range

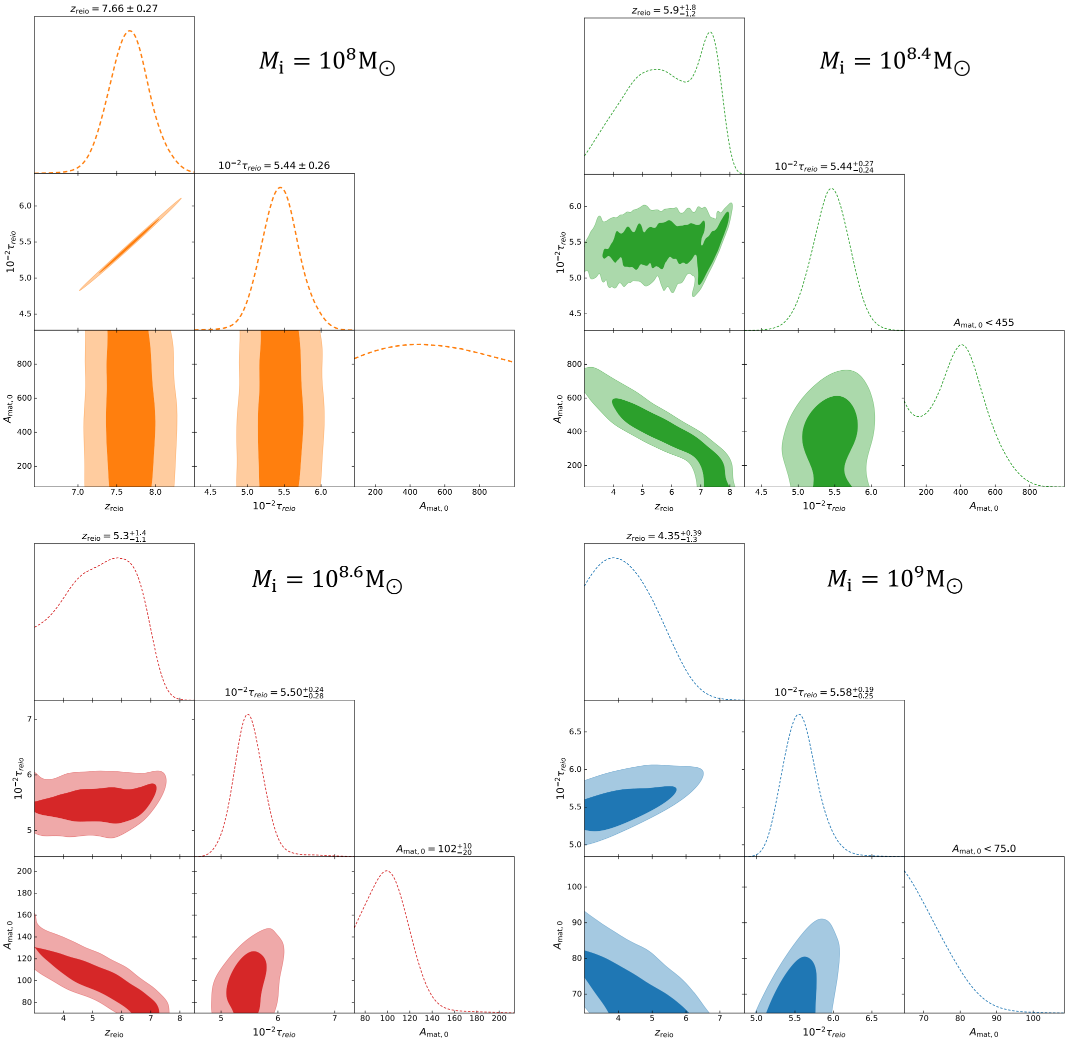

FIGURE 6.5: MCMC results for several models of the UCMH initial mass, $M = 10^8 M_\odot$ (top left), $M = 10^{8.2} M_\odot$ (top right), $M = 10^{8.4} M_\odot$ (bottom left), $M = 10^9 M_\odot$ (bottom right). $z_{\rm reio}$ and $\mathcal{A}_{\rm mat,0}$ are free paramters, and τ is the derived paramter. The thick shaded region shows the 1σ region, and the thin shaded region shows the 2σ region.

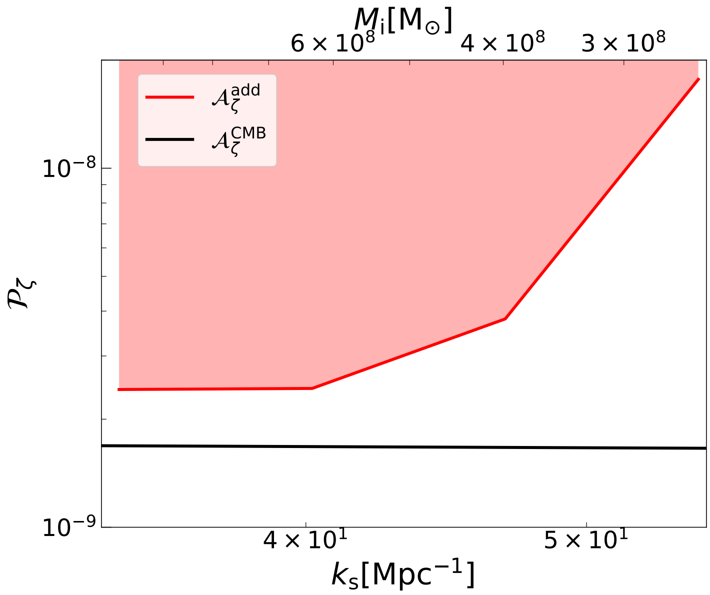

FIGURE 6.6: Upper limit on the amplitude of the additional spike-type power spectrum, $\mathcal{A}_\zeta$, corresponding to the 2-σ constraint of the $\mathcal{A}_{\mathrm{mat},0}$ through the MCMC analysis with Planck 2018 data. It is noted that we assume $z_\mathrm{reio} > 3$ in this figure. The red-shaded region shows the limited parameter region through this work.
The solid black line shows the almost scale-invariant power spectrum with amplitude $\mathcal{A}_\zeta^\mathrm{CMB} \simeq 2 \times 10^{-9}$ with the spectral index, $n_\mathrm{s} = 0.9649$.

of $10^8 M_\odot < M_\mathrm{i} < 10^9 M_\odot$ corresponding to the spike scale k_s of the additional power spectrum. We conducted separate MCMCs for several UCMH initial mass models to explore the other parameters of $\mathcal{A}_{\mathrm{mat},0}$ and z_reio.

We discovered that, while UCMH Pop. III stars have minimal effect on the cosmic reionization when the initial mass is less than $10^8 M_\odot$, their contribution increases as the initial mass becomes greater than $10^8 M_\odot$. Then UCMH Pop. III stars gradually affect the reionization history and thus the CMB Thomson scattering optical depth, whose value is well determined by the CMB observation. In order to compensate for the early reionization due to the UCMH Pop. III stars, the “tanh"-type reionization would be delayed. Once the UCMHs mass becomes larger than the minimum mass to host Pop. III stars, their contribution significantly increases. In such case, the decrement of z_reio cannot cancel out the increase of the Thomson scattering optical depth of the CMB, resulting in a stringent constraint on the value of $\mathcal{A}_{\mathrm{mat},0}$. This constraint can be translated into a constraint on the amplitude of the additional spike-type power spectrum, $\mathcal{A}_\zeta$, of $\mathcal{A}_\zeta \lesssim 10^{-8}$ in the scales $k \lesssim 50\mathrm{Mpc}^{-1}$ when assuming that the standard "tanh" type reionization occurs by $z = 3$.

In conclusion, it is worth noting several limitations of this study. Firstly, we have adopted a fixed set of assumptions regarding the unknown astrophysical properties of Pop. III stars and UCMHs, as previously established in the literature [216]. However, it would be necessary to conduct further simulations to validate these assumptions. This is a subject for future research.

Additionally, we have not considered the formation of Pop. II stars and the connection between the formation of Pop. III stars and Pop. II stars. This would require taking into account the lifetimes of Pop. III stars, their fate to produce heavier elements, the increment of cosmic metalicity, and the subsequent formation of Pop. II stars. These are also topics for future research.

Chapter 7

Summary of this thesis

In this thesis, we studied the DM halos and UCMHs to explore primordial small-scale perturbations. Our universe has a wealth of hierarchical structures spanning many orders of magnitude, from asteroids to galaxy clusters. The seeds of such hierarchical structures are called primordial scalar perturbations. Despite the great success of recent measurements for large-scale perturbations, primordial small-scale perturbations have yet to be observationally revealed well. Throughout this thesis, we discussed the current status of the investigation on primordial small-scale perturbations and proposed new methods to probe them.

First, we introduced the primordial perturbations generated by quantum fluctuations during inflation, especially slow-roll single-field inflation in Chapter 2. To do that, we discussed how inflation converts microscopic quantum fluctuations into macroscopic seeds for cosmological structure formation, i.e., primordial perturbations. For the discussion, we demonstrated cosmological linear perturbation theory. The perturbation theory is based on the Einstein equation. Thus we reviewed the perturbed Einstein equation in the Conformal Newtonian gauge during the inflationary epoch. After that, we discussed the connection between the quantum fluctuation during inflation and primordial perturbations through quantization of the scalar field. We also linked the primordial perturbations and the observables regarding CMB and LSS. We derived the theoretical prediction for the number density and the bias of DM halos in the case where the primordial power spectrum is monochromatic.

Second, we reviewed the current status of exploring small-scale perturbations in Chapter 3. The most robust limit would come from measurements of CMB spectral distortion. So far, the COBE/FIRAS had measured the μ- and y-distortion in the CMB spectrum and put a limit on the primordial power spectrum like $\mathcal{A}_\zeta \lesssim 10^{-5}$ for the scales, $k \approx 1 - 10^4$ Mpc^{-1} [16]. The next-generation project like PIXIE would allow us to achieve a deeper investigation at the level of $\mathcal{A}_\zeta \lesssim 10^{-8}$. There are also other projects to measure the CMB distortion at a similar level. However, any projects have not been selected yet. Measurements of PBHs also provide information on the primordial power spectrum on small scales. However, the obtained limits from the nondetection of PBHs are very weak. Investigations of small-scale structures like galaxies would be usable for probing small-scale perturbations. Recently, Ref. [69] proposed a new measurement using high-redshift UV galaxy LF data from the HST. This measurement is powerful, and the authors succeeded in constraining the perturbations until $k \lesssim 10\text{Mpc}^{-1}$. Besides, measurements of UCMHs could explore small-scale perturbations. So far, Refs. [72]–[78] have investigated the gamma-ray emission signal from the DM annihilation inside UCMHs and provided the tight constraint on the primordial power spectrum, $\mathcal{A}_\zeta < 10^{-7}$ for $10\ \text{Mpc}^{-1} < k < 10^8\ \text{Mpc}^{-1}$, through the nondetection of such energetic signals in a gamma-ray observation like Fermi-LAT [140]. However, this constraint highly depends on the nature of DM. Based on the above, new measurements which can more deeply explore the primordial power spectrum have been anticipated.

Third, we studied the diffuse background free-free emission induced by DM halos as the new measurement in Chapter 4. Investigations of small-mass DM halos would be useful for probing the small-scale perturbations in the same way as galaxies. We found that the free-free emission signal is dominantly contributed by small-mass DM halos rather than massive DM halos. We also found that the signal is significantly sensitive to the spectral index and the running. For example, the signal would be modified by $\sim 20\%$ even in the parameter sets consistent with the recent Planck result. Therefore, we suggested that the measurement of the cosmological free-free signals has the potential to provide more stringent constraints on the abundance of small-mass DM halos and the primordial perturbations while carefully removing the Galactic free-free emission is required. The multifrequency radio observation or the cross-correlation study with the galaxy surveys or 21-cm intensity map would help reduce the contamination.

Fourth, we studied the 21-cm fluctuations induced by UCMHs, which can allow us to explore primordial small-scale perturbations by using the SKA observation in Chapter 5. We calculated the 21-cm signal from UCMHs and showed that UCMHs enhance the 21-cm fluctuations. We also investigated the constraint on the UCMH abundance and small-scale curvature perturbations, which indicates that the upcoming SKA observation can provide the constraint on amplitude of primordial power spectrum as $\mathcal{A}_\zeta \lesssim 10^{-6}$ on $100\ \mathrm{Mpc}^{-1} \lesssim k \lesssim 1000\ \mathrm{Mpc}^{-1}$. Although it is not stronger than the one from the nondetection of gamma rays induced by DM annihilation in UCMHs, this constraint by the SKA would be important as a new DM model-independent method to explore the primordial perturbations.

Fifth, we also investigated the effect of Pop. III stars in UCMHs on the cosmic ionization history. Although high-redshift astrophysics is not well-understood yet, UCMHs could host the Pop. III stars like the standard DM halos. Such Pop. III stars would emit ionizing photons and foster cosmic reionization in higher redshifts, which could be potent probes to cut into constraining the primordial perturbations. We have implemented the MCMC analysis with the latest Planck observation data to test our reionization model, including the effects of the Pop. III stars. As a result, if the UCMH initial mass is larger than $10^{8.4} M_\odot$, the number density of UCMHs is strictly limited. Then we obtained the constraint on the amplitude of the primordial power spectrum through the constraint on the UCMH number density like $\mathcal{A}_\zeta \lesssim 10^{-8}$ on $k \lesssim 50\mathrm{Mpc}^{-1}$ with the assumption that the standard reionization by Pop. II stars and first galaxies occurs by $z = 3$.

Here we mention the summary of our works described in Chapters. 4, 5, and 6. Figure. 7.1 shows the constraint on the primordial power spectrum on wide scales with this works described in Chapters 4, 5, and 6. The regions and lines colored except for red illustrate the current and future constraints on the primordial power spectrum as depicted in Fig. 1.1. The red box indicates the parameter space that will be explored through free-free emission measurements from DM halos, as discussed in Chapter 4. The red dashed line and red-shaded area depict the constraints that will be obtained from SKA observations (Chapter 5) and is obtained by CMB observations (Chapter 6), respectively. In conclusion, we have made significant advancements in the constraints on small scales and proposed novel methods for further exploration.

Finally, in closing this thesis, We also mention the future direction of study about DM halos and primordial perturbations. There are a lot of ongoing/upcoming projects in cosmology, such as JWST, the Prime Focus Spectrograph, SKA, and so on. These

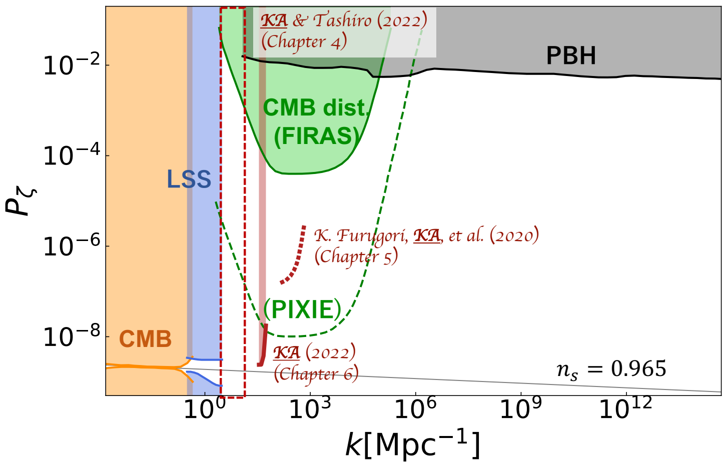

FIGURE 7.1: Constraint on the primordial power spectrum on wide scales with this works described in Chapters 4, 5, and 6. The regions and lines colored except for red illustrate the current and future constraints on the primordial power spectrum as depicted in Fig.1.1. The red box indicates the parameter space that will be explored through free-free emission measurements from DM halos, as discussed in Chapter 4. The red dashed line and red-shaded area depict the constraints that will be obtained from SKA observations (Chapter 5) and is obtained by CMB observations (Chapter 6), respectively.

observations would give us new insight into small-scale structures such as small-mass DM halos and UCMHs. As discussed in this thesis, their abundance and distribution will provide new insight into primordial small-scale perturbations and the inflationary mechanism. Also, such information would provide clues on the problems in cosmology, e.g., the nature of DM and dark energy. We hope the day will come when we solve such cosmological problems by studying them.

Appendix A

Stress-Energy Tensor

Here we introduce the stress-energy tensor which is defined by

$$T_{\mu\nu} = (\rho + p)u_\mu u_\nu + p g_{\mu\nu} + \sigma_{\mu\nu}, \tag{A.1}$$

where ρ, p, and $\sigma_{\mu\nu}$ are the matter energy density, the isotropic pressure, and the anisotropic stress tensor, respectively. $\sigma_{\mu\nu}$ satisfies,

$$\sigma^{\mu}_{\ \mu} = 0, \quad \sigma^{\mu\nu}u_\nu = 0, \quad \sigma^{\mu\nu} = \sigma^{\nu\mu}. \tag{A.2}$$

In Eq. (A.1), u_μ is the 4-vector,

$$u^\mu \equiv \frac{dx^\mu}{d\tau} \tag{A.3}$$

which satisfies $u^\mu u_\nu = -1$. Introducing the metric of the 3-dimensional spatial sections orthogonal to u_μ as $\gamma_{\mu\nu} = g_{\mu\nu} + u_\mu u_\nu$, the Eq. (A.1) can be rewritten by

$$T_{\mu\nu} = \rho u_\mu u_\nu + p\gamma_{\mu\nu} + \sigma_{\mu\nu}. \tag{A.4}$$

We can use this metric $\gamma_{\mu\nu}$ to project physical quantities orthogonal to 4-velocity into the instantaneous rest frame of the observers. Then one can obtain the following relations;

$$\begin{aligned} \rho = T_{\mu\nu}u^\mu u^\nu, \qquad p = \frac{1}{3}T_{\mu\nu}\gamma^{\mu\nu}, \\ \sigma_{\mu\nu} = \left(\frac{1}{2}(\gamma_\mu^{\ \alpha}\gamma_\nu^{\ \beta} + \gamma_\nu^{\ \alpha}\gamma_\mu^{\ \beta})\gamma_\alpha^{\ \lambda}\gamma_\beta^{\ \rho} - \frac{1}{3}\gamma^{\alpha\beta}\gamma_\alpha^{\ \lambda}\gamma_\beta^{\ \rho}\gamma_{\mu\nu}\right) T_{\lambda\rho}. \end{aligned} \tag{A.5}$$

In a case of the perfect fluid, the stress-energy tensor would become

$$T^\mu_{\ \nu} = g^{\mu\alpha}T_{\alpha\nu} = (\rho + p)u^\mu u_\nu - p\delta^\mu_{\ \nu}. \tag{A.6}$$

In the comoving frame where the observer is comoving with the fluid, one may choose the simple 4-velocity as $u^\mu = (1.0, 0, 0)$. Then the stress-energy tensor can be written by

$$T^\mu_{\ \nu} = \begin{pmatrix} \rho & 0 & 0 & 0 \\ 0 & -p & 0 & 0 \\ 0 & 0 & -p & 0 \\ 0 & 0 & 0 & -p \end{pmatrix}. \tag{A.7}$$

Let us consider the stress-energy tensor in the case of perturbative metric (Eq. (2.45)) until the linear order. From the normalization condition, $u^\mu u_\mu = -1$, one can get

$$\begin{aligned} u^\mu &= a^{-1}\left(1 - A, v^i\right) \\ u_\mu &= a\left(-1 - A, v_i - B_i\right). \end{aligned} \tag{A.8}$$

Assuming that q_μ and $\sigma_{\mu\nu}$ in Eq. (A.1) are perturbative quantities, one can also obtain

$$\sigma^{00} = \sigma^{0i} = \sigma^{i0} = 0, \quad \gamma_{ij}\sigma^{ij} = 0, \quad \sigma^{ij} = \sigma^{ji}, \tag{A.9}$$

and

$$\sigma^0_{\ 0} = \sigma^0_{\ i} = \sigma^i_{\ 0} = 0, \quad \sigma^i_{\ i} = 0, \quad \sigma^i_{\ j} = \sigma^i_{\ j}. \tag{A.10}$$

Defining perturbations as $\delta\rho \equiv \rho - \bar{\rho}$ and $\delta p \equiv p - \bar{p}$, one may obtain

$$\begin{aligned} T^0_{\ 0} &= -\bar{\rho} - \delta\rho, \\ T^0_{\ i} &= \left(\bar{\rho} + \bar{p}\right)\left(v_i - B_i\right), \\ T^i_{\ 0} &= -(\bar{\rho} + \bar{p})v^i, \\ T^i_{\ j} &= \bar{p}\delta^i_{\ j} + \delta p \delta^i_{\ j} + \sigma^i_{\ j}. \end{aligned} \tag{A.11}$$

Appendix B

Relation between ζ and $\mathcal{R}$ on superhorizon scales

As we discussed in Sec. 2.4.6, ζ and $\mathcal{R}$ are commonly used gauge-invariant quantities representing curvature perturbations on uniform-density hypersurface and comoving curvature perturbations respectively. Here we show the relation between them; they would match on superhorizon scales from linearized Einstein equations.

From the expressions in Eqs. (2.61) and (2.66), the difference between ζ and $\mathcal{R}$ is given by

$$\zeta - \mathcal{R} = \mathcal{H}\left(\frac{\delta\rho}{\rho'} - \frac{\delta\phi}{\phi'}\right). \tag{B.1}$$

Using the (00) and $(0i)$ components of linearized Einstein equations represented in Eq. (2.71) and Eq. (2.72), one can obtain following two equations,

$$-2M_{\rm pl}^2 a^{-2}\left(\frac{1}{\bar{\rho}_\phi + \bar{p}_\phi}(\mathcal{H}\Phi - \Psi') + \frac{\Delta\Psi}{3\mathcal{H}(\bar{\rho}_\phi + \bar{p}_\phi)}\right) = \frac{\delta\rho_\phi}{\bar{\rho}'_\phi} + B + E', \tag{B.2}$$

and

$$\mathcal{H}\Phi - \Psi' = 4\pi G a^2(\bar{\rho}_\phi + \bar{p}_\phi)\frac{\delta\phi - \phi'(B+E')}{\bar{\phi}'}. \tag{B.3}$$

Combining these two equations reads the relation between $\delta\rho_\phi/\bar{\rho}'_\phi$ and $\delta\phi/\bar{\phi}'$ like

$$\frac{\delta\rho_\phi}{\bar{\rho}'_\phi} - \frac{\delta\phi}{\bar{\phi}'} = -\frac{\Delta\Psi}{12\pi G a^2\mathcal{H}(\bar{\rho}_\phi + \bar{p}_\phi)}, \tag{B.4}$$

where we use $\rho_\phi = 3M_{\rm pl}^2 a^{-2}\mathcal{H}^2$. Inserting this equation to Eq. (B.1) and transforming to the Fourier space, one can obtain

$$\zeta - \mathcal{R} = \frac{k^2}{\mathcal{H}^2}\frac{2\bar{\rho}_\phi}{3(\bar{\rho}_\phi + \bar{p}_\phi)}\Psi. \tag{B.5}$$

In the superhorizon limit ($k/\mathcal{H} \to 0$), Eq. (B.5) shows their matching. That is important result. (Remind that ζ and $\mathcal{R}$ are also equal during slow-roll inflation as mentioned in Sec. 2.4.6.) The correlation functions of ζ and $\mathcal{R}$ are therefore equal at horizon crossing.

Appendix C

Jeans mass

In this appendix, we introduce the typical mass scale of gravitationally collapsing against the baryonic gas pressure, the Jeans mass. The basic equations related to the evolution of density perturbation through gravity are

- Continuity Eq.:

$$\frac{\partial \rho}{\partial t} + \nabla \cdot (\rho \boldsymbol{v}) = 0, \tag{C.1}$$

- Euler Eq.:

$$\frac{\partial \boldsymbol{v}}{\partial t} + (\boldsymbol{v} \cdot \nabla)\boldsymbol{v} = -\frac{\nabla P}{\rho} - \nabla \phi, \tag{C.2}$$

- Poisson Eq.:

$$\Delta \phi = 4\pi G \rho. \tag{C.3}$$

These equations are represented in the rest frame, $\boldsymbol{x}$. In order to take into account the expansion of our universe, let us transform the variables defined in the rest frame to the new ones in the comoving frame with the Hubble expansion as $\boldsymbol{x} = \boldsymbol{r}/a$, where $\mathbf{r}$ is the comoving spatial coordinate, and a is the scale factor.

First, we transform the velocity field in Eqs. (C.1) and (C.2). Considering the time derivative of $\boldsymbol{r}$, one can obtain

$$\dot{\boldsymbol{r}} = \dot{a}\boldsymbol{x} + a\dot{\boldsymbol{x}}. \tag{C.4}$$

The first term on the right-hand side of Eq. (C.4) represents the Hubble expansion. Therefore, in the comoving frame, we need not count it as a velocity of "matter," so that we replace the velocity in Eqs. (C.1) and (C.2) like

$$v \to v + \dot{a}\boldsymbol{x}. \tag{C.5}$$

In addition, considering the coordinate transformation, $(t, \boldsymbol{r}) \to (t, \boldsymbol{x})$, the partial derivatives in the above three equations should be replaced like

$$\frac{\partial}{\partial t} \to \frac{\partial}{\partial t} - \frac{\dot{a}}{a}\boldsymbol{x} \cdot \boldsymbol{\nabla}, \qquad \boldsymbol{\nabla} \to \frac{1}{a}\boldsymbol{\nabla}, \tag{C.6}$$

where $\boldsymbol{\nabla} = \partial/\partial \boldsymbol{x}$. Combining these transforms with Eqs. (C.1) and (C.2) reads

$$\frac{\partial \rho}{\partial t} + 3\frac{\dot{a}}{a}\rho + \frac{1}{a}\nabla \cdot (\rho \boldsymbol{v}) = 0, \tag{C.7}$$

$$\frac{\partial \boldsymbol{v}}{\partial t} + 2\frac{\dot{a}}{a}\boldsymbol{v} + \frac{1}{a}(\boldsymbol{v} \cdot \nabla)\boldsymbol{v} = -\frac{\nabla P}{a\rho} - \nabla \Phi, \tag{C.8}$$

where we define Φ as

$$\Phi \equiv \phi + \frac{1}{2}a\ddot{a}|\boldsymbol{x}|^2. \tag{C.9}$$

We next consider the ϕ in Eq. (C.9). Let us assume that the dominant component in the Universe is *matter* whose energy density is represented by $\rho_{\rm tot}$. Then the gravitational potensial ϕ is determinded by the Poisson equation in Eq. (C.3) as

$$\Delta\phi = 4\pi G\rho_{\rm tot}, \tag{C.10}$$

where Δ is the Laplacian in the rest frame.

From Eqs. (2.20) and (2.22), one can obtain

$$\frac{\ddot{a}}{a} = -\frac{4\pi G}{3}\bar{\rho}_{\rm tot}. \tag{C.11}$$

Inserting Eqs. (C.9) and (C.10) to Eq. (C.11), one can obtain the Poisson equation in the comoving frame,

$$\Delta\Phi = 4\pi Ga^2(\rho_{\rm tot} - \bar{\rho}_{\rm tot}). \tag{C.12}$$

Here we put perturbations for the density and pressure as

$$\rho = \bar{\rho}(1+\delta), \tag{C.13}$$

$$P = \bar{P} + \delta P, \tag{C.14}$$

in Eqs. (C.7), (C.8) and (C.12). The background terms in Eq. (C.7) read

$$\frac{d}{dt}(a^3\bar{\rho}) = 0. \tag{C.15}$$

Then the linear terms in Eqs. (C.7), (C.8) and (C.12) read

$$\frac{\partial}{\partial t}\bar{\rho}\delta + \frac{1}{a}\nabla\cdot(\bar{\rho}v) = 0, \tag{C.16}$$

$$\frac{\partial}{\partial t}v + 2\frac{\dot{a}}{a}v = -\frac{\nabla\delta P}{a\bar{\rho}} - \frac{1}{a}\nabla\Phi, \tag{C.17}$$

$$\Delta\Phi = 4\pi a^2 G\bar{\rho}_{\rm tot}\delta_{\rm tot}, \tag{C.18}$$

where $\delta_{\rm tot}$ is the density perturbation with respect to $\rho_{\rm tot}$.

Combining Eqs. (C.16) to (C.18) reads

$$\frac{\partial^2\delta}{\partial t^2} + 2\frac{\dot{a}}{a}\frac{\partial\delta}{\partial t} - c_{\rm s}^2\frac{\Delta\delta}{a^2} = 4\pi G\bar{\rho}_{\rm tot}\delta_{\rm tot}, \tag{C.19}$$

where we assume $\delta P = \left(\frac{\partial P}{\partial\rho}\right)\bar{\rho}\delta = c_{\rm s}^2\bar{\rho}\delta$ with the sound speed of this fluid, $c_{\rm s}$. Here let us neglect the component apart from the matter. Then in the Fourier space, Eq. (C.19) can be written by

$$\frac{\partial^2\tilde{\delta}}{\partial t^2} + 2\frac{\dot{a}}{a}\frac{\partial\tilde{\delta}}{\partial t} - \left(4\pi G\bar{\rho} - \frac{c_{\rm s}^2k^2}{a^2}\right)\tilde{\delta} = 0. \tag{C.20}$$

Eq. (C.20) suggest that the perturbation would evolve if $4\pi G\bar{\rho} - c_{\rm s}^2k^2/a^2 > 0$, which corresponds that the perturbation would gravitationally collapse in the case that the gravity overcomes the matter(gas) pressure. On the contrary, the perturbations would be suppressed by the pressure when $4\pi G\bar{\rho} - c_{\rm s}^2 k^2/a^2 < 0$. The critical wavenumber is called the Jeans wavenumber, which is defined by

$$k_{\rm J} = \frac{a\sqrt{4\pi G\bar{\rho}}}{c_{\rm s}}. \tag{C.21}$$

The corresponding mass scale is called Jeans mass, which is defined by

$$M_{\rm J} \equiv \frac{4\pi\bar{\rho}}{3}\left(\frac{\pi a}{k_{\rm J}}\right)^3 = \frac{\pi^{5/2}}{6}\frac{c_{\rm s}^3}{\sqrt{G^3\bar{\rho}}}. \tag{C.22}$$

Appendix D

21-cm signals from IGM and Minihalos

In this appendix, we give descriptions for construction of 21-cm signals from IGM and MHs. Here, we assume $x_\alpha = 0$ in Eq. (5.32) because we assume that no UV and X-ray sources exist in the Universe above $z = 20$.

D.1 IGM fluctuations

The mean differential brightness temperature of the IGM is given by [248]

$$\overline{\delta T_{\mathrm{b}}} = 9.1\,(1+z)^{1/2}\left(1-\frac{T_{\mathrm{CMB}}}{T_{\mathrm{S}}}\right)\left(\frac{\Omega_{\mathrm{b}}h}{0.33}\right)\left(\frac{\Omega_{\mathrm{m}}}{0.27}\right)^{-1/2}\ \mathrm{m}K, \tag{D.1}$$

where we assume that the IGM is fully neutral. The IGM spin temperature is assumed to evolve solely through Compton heating.

The spatial fluctuations of 21-cm signals are contingent upon variations in baryonic density. It is postulated that the distribution of baryons mirrors fluctuations in matter density, thus enabling the computation of the observed rms 21-cm fluctuations resulting from the IGM in

$$\langle \delta T_{\mathrm{b,IGM}}^2 \rangle^{1/2} = \sigma_p(z)\overline{\delta T_{\mathrm{b}}}, \tag{D.2}$$

where $\sigma_p(z)$ is given in Eq. (5.39). In our assessment, we neglect the effect of ionization fluctuations on the IGM. However, as cosmological reionization advances, this contribution to 21-cm fluctuations becomes more substantial. Consequently, our evaluation of IGM fluctuations is likely to be underestimated at around $z \sim 10$.

D.2 Minihalo fluctuations

Minihalos (MHs) are virialized structures with virial temperatures less than 10^4 K. In the standard hierarchical structure formation paradigm, they are formed in copious quantities at high redshifts, and are composed primarily of neutral hydrogen atoms. Therefore, MHs are considered to be potential sources of 21-cm signals at high redshifts [151], [187].

As depicted in Fig. 5.4, we estimate the 21-cm fluctuations arising from MHs in a similar fashion to ultracompact minihalos (UCMHs), with the exception of the dark matter profile. It is predicted that the dark matter distribution within MHs can be characterized by the NFW profile. For the concentration parameter, $p_{con} \equiv r_{\mathrm{vir}}/r_{\mathrm{s}}$ in the NFW profile, we set [249]

$$p_{con} = \frac{10}{1+z_c}\left[\frac{M}{M_*(z=0)}\right]^{-0.2}, \tag{D.3}$$

In this instance, $M_*(z)$ is defined such that $\sigma(M_*, z) = \delta_c$, where $\sigma(M, z)$ represents the dispersion of density fluctuations smoothed using a top-hat filter with a radius corresponding to the mass M at redshift z. In our calculation, we posit that the mass range of MHs extends from the Jeans mass M_J to the virial mass, with a virial temperature of 10^4 K.

D.3 Noise level of SKA

The noise level of an interferometer such as SKA is given with the observation wave length λ by Furlanetto, Oh, and Briggs [155]

$$\delta T_N(\lambda) = \frac{\lambda^2}{A_{\rm eff}\Delta\theta^2}\frac{T_{\rm sys}}{\sqrt{\Delta\nu t_{\rm obs}}}, \tag{D.4}$$

where $A_{\rm eff}$, $t_{\rm obs}$ and $T_{\rm sys}$ are the effective collecting area, the observational time, and the system temperature, respectively.

We are interested in low-frequency observations, specifically in the range of $\nu <$ 150 MHz. In this low-frequency regime, the sky temperature is the primary component of $T_{\rm sys}$. Consequently, we consider sky temperature at high Galactic latitudes, where the foreground is minimal as

$$T_{\rm sys} \sim 180\left(\frac{180\ {\rm MHz}}{\nu}\right)^{2.6} {\rm K}. \tag{D.5}$$

Therefore, the noise level is given in

$$\begin{aligned}\delta T_N(\nu) = 0.507{\rm mK}\left(\frac{8\times10^5{\rm m}^2}{A_{\rm eff}}\right)\left(\frac{20'}{\Delta\theta}\right)^2\left(\frac{3{\rm MHz}}{\Delta\nu}\right)^{1/2} \\ \times\left(\frac{1000{\rm h}}{t_{\rm obs}}\right)^{1/2}\left(\frac{1+z}{21}\right)^{4.6}.\end{aligned} \tag{D.6}$$

For SKA, we set $A_{\rm eff} = 8\times10^5$ m^2, $\Delta\theta = 20$ arcmin, $\Delta\nu = 3$ MHz and $t_{\rm obs} = 1000$ h.

Bibliography

[1] Planck Collaboration and N. e. a. Aghanim, “Planck 2018 results. VI. Cosmological parameters,” *ArXiv e-prints*, Jul. 2018. arXiv: `1807.06209`.

[2] E. Hubble, “A Relation between Distance and Radial Velocity among Extra-Galactic Nebulae,” *Proceedings of the National Academy of Science*, vol. 15, no. 3, pp. 168–173, Mar. 1929. DOI: `10.1073/pnas.15.3.168`.

[3] A. A. Penzias and R. W. Wilson, “A Measurement of Excess Antenna Temperature at 4080 Mc/s.,” *ApJ*, vol. 142, pp. 419–421, Jul. 1965. DOI: `10.1086/148307`.

[4] G. F. Smoot, C. L. Bennett, A. Kogut, *et al.*, “Structure in the COBE Differential Microwave Radiometer First-Year Maps,” *ApJ*, vol. 396, p. L1, Sep. 1992. DOI: `10.1086/186504`.

[5] R. K. Sachs and A. M. Wolfe, “Perturbations of a Cosmological Model and Angular Variations of the Microwave Background,” *ApJ*, vol. 147, p. 73, Jan. 1967. DOI: `10.1086/148982`.

[6] J. Silk, “Cosmic Black-Body Radiation and Galaxy Formation,” *ApJ*, vol. 151, p. 459, Feb. 1968. DOI: `10.1086/149449`.

[7] W. Hu and N. Sugiyama, “Anisotropies in the Cosmic Microwave Background: an Analytic Approach,” *ApJ*, vol. 444, p. 489, May 1995. DOI: `10.1086/175624`. arXiv: `astro-ph/9407093 [astro-ph]`.

[8] Liddle, Andrew R. and Lyth, David H., *Cosmological Inflation and Large-Scale Structure*. 2000.

[9] J. Martin, “The Observational Status of Cosmic Inflation After Planck,” in *The Cosmic Microwave Background*, ser. Astrophysics and Space Science Proceedings, vol. 45, Jan. 2016, p. 41. DOI: `K35-72415`. arXiv: `1502.05733 [astro-ph.CO]`.

[10] J. Chluba and R. A. Sunyaev, “The evolution of CMB spectral distortions in the early Universe,” *MNRAS*, vol. 419, no. 2, pp. 1294–1314, Jan. 2012. DOI: `10.1111/j.1365-2966.2011.19786.x`. arXiv: `1109.6552 [astro-ph.CO]`.

[11] H. Tashiro, “CMB spectral distortions and energy release in the early universe,” *Progress of Theoretical and Experimental Physics*, vol. 2014, no. 6, 06B107, 06B107, Jun. 2014. DOI: `10.1093/ptep/ptu066`.

[12] J. Chluba and D. Jeong, “Teasing bits of information out of the CMB energy spectrum,” *MNRAS*, vol. 438, no. 3, pp. 2065–2082, Mar. 2014. DOI: `10.1093/mnras/stt2327`. arXiv: `1306.5751 [astro-ph.CO]`.

[13] R. A. Daly, “Spectral Distortions of the Microwave Background Radiation Resulting from the Damping of Pressure Waves,” *ApJ*, vol. 371, p. 14, Apr. 1991. DOI: `10.1086/169866`.

[14] W. Hu, D. Scott, and J. Silk, “Power Spectrum Constraints from Spectral Distortions in the Cosmic Microwave Background,” *ApJ*, vol. 430, p. L5, Jul. 1994. DOI: `10.1086/187424`. arXiv: `astro-ph/9402045 [astro-ph]`.

[15] J. Chluba, R. Khatri, and R. A. Sunyaev, "CMB at 2 × 2 order: the dissipation of primordial acoustic waves and the observable part of the associated energy release," *MNRAS*, vol. 425, no. 2, pp. 1129–1169, Sep. 2012. DOI: `10.1111/j.1365-2966.2012.21474.x`. arXiv: `1202.0057 [astro-ph.CO]`.

[16] J. Chluba, A. L. Erickcek, and I. Ben-Dayan, "Probing the Inflaton: Small-scale Power Spectrum Constraints from Measurements of the Cosmic Microwave Background Energy Spectrum," *ApJ*, vol. 758, no. 2, 76, p. 76, Oct. 2012. DOI: `10.1088/0004-637X/758/2/76`. arXiv: `1203.2681 [astro-ph.CO]`.

[17] E. Pajer and M. Zaldarriaga, "New Window on Primordial Non-Gaussianity," *Phys. Rev. Lett.*, vol. 109, no. 2, 021302, p. 021 302, Jul. 2012. DOI: `10.1103/PhysRevLett.109.021302`. arXiv: `1201.5375 [astro-ph.CO]`.

[18] J. B. Dent, D. A. Easson, and H. Tashiro, "Cosmological constraints from CMB distortion," *Phys. Rev. D*, vol. 86, no. 2, 023514, p. 023 514, Jul. 2012. DOI: `10.1103/PhysRevD.86.023514`. arXiv: `1202.6066 [astro-ph.CO]`.

[19] J. Chluba and D. Grin, "CMB spectral distortions from small-scale isocurvature fluctuations," *MNRAS*, vol. 434, no. 2, pp. 1619–1635, Sep. 2013. DOI: `10.1093/mnras/stt1129`. arXiv: `1304.4596 [astro-ph.CO]`.

[20] D. J. Fixsen, E. S. Cheng, J. M. Gales, J. C. Mather, R. A. ShaFer, and E. L. Wright, "The cosmic microwave background spectrum from the full cobe firas data set," *The Astrophysical Journal*, vol. 473, no. 2, p. 576, 1996. [Online]. Available: `http://stacks.iop.org/0004-637X/473/i=2/a=576`.

[21] M. Sathyanarayana Rao, R. Subrahmanyan, N. Udaya Shankar, and J. Chluba, "On the Detection of Spectral Ripples from the Recombination Epoch," *ApJ*, vol. 810, no. 1, 3, p. 3, Sep. 2015. DOI: `10.1088/0004-637X/810/1/3`. arXiv: `1501.07191 [astro-ph.IM]`.

[22] A. Schillaci, G. D'Alessandro, P. de Bernardis, *et al.*, "Efficient differential Fourier-transform spectrometer for precision Sunyaev-Zel'dovich effect measurements," *A&A*, vol. 565, A125, A125, May 2014. DOI: `10.1051/0004-6361/201423631`. arXiv: `1402.4091 [astro-ph.IM]`.

[23] S. Masi, P. Ade, P. de Bernardis, *et al.*, "OLIMPO: A few arcmin resolution survey of the sky at mm and sub-mm wavelengths," *Memorie della Società Astronomica Italiana*, vol. 74, p. 96, Jan. 2003.

[24] B. Maffei *et al.*, "BISOU: a balloon project to measure the CMB spectral distortions," in *16th Marcel Grossmann Meeting on Recent Developments in Theoretical and Experimental General Relativity, Astrophysics and Relativistic Field Theories*, Oct. 2021. arXiv: `2111.00246 [astro-ph.IM]`.

[25] P. André, C. Baccigalupi, A. Banday, *et al.*, "PRISM (Polarized Radiation Imaging and Spectroscopy Mission): an extended white paper," *J. Cosmology Astropart. Phys.*, vol. 2014, no. 2, 006, p. 006, Feb. 2014. DOI: `10.1088/1475-7516/2014/02/006`. arXiv: `1310.1554 [astro-ph.CO]`.

[26] *PRISTINE*, `https://www.ias.u-psud.fr/en/content/pristine`.

[27] A. Kogut, M. H. Abitbol, J. Chluba, *et al.*, "CMB Spectral Distortions: Status and Prospects," in *Bulletin of the American Astronomical Society*, vol. 51, Sep. 2019, 113, p. 113. arXiv: `1907.13195 [astro-ph.CO]`.

[28] J. Chluba, M. H. Abitbol, N. Aghanim, *et al.*, “New Horizons in Cosmology with Spectral Distortions of the Cosmic Microwave Background,” *arXiv e-prints*, arXiv:1909.01593, arXiv:1909.01593, Sep. 2019. arXiv: `1909.01593 [astro-ph.CO]`.

[29] A. Kogut, D. J. Fixsen, D. T. Chuss, *et al.*, “The Primordial Inflation Explorer (PIXIE): a nulling polarimeter for cosmic microwave background observations,” *J. Cosmology Astropart. Phys.*, vol. 2011, no. 7, 025, p. 025, Jul. 2011. DOI: `10.1088/1475-7516/2011/07/025`. arXiv: `1105.2044 [astro-ph.CO]`.

[30] A. Kogut, J. Chluba, D. J. Fixsen, S. Meyer, and D. Spergel, “The primordial inflation explorer (pixie),” in *Space telescopes and instrumentation 2016: optical, infrared, and millimeter wave*, SPIE, vol. 9904, 2016, pp. 331–353.

[31] C. T. Byrnes, P. S. Cole, and S. P. Patil, “Steepest growth of the power spectrum and primordial black holes,” *J. Cosmology Astropart. Phys.*, vol. 2019, no. 6, 028, p. 028, Jun. 2019. DOI: `10.1088/1475-7516/2019/06/028`. arXiv: `1811.11158 [astro-ph.CO]`.

[32] J. Chluba *et al.*, “Spectral Distortions of the CMB as a Probe of Inflation, Recombination, Structure Formation and Particle Physics: Astro2020 Science White Paper,” *Bull. Am. Astron. Soc.*, vol. 51, no. 3, p. 184, 2019. arXiv: `1903.04218 [astro-ph.CO]`.

[33] B. J. Carr and S. W. Hawking, “Black holes in the early Universe,” *Mon. Not. Roy. Astron. Soc.*, vol. 168, pp. 399–415, 1974.

[34] B. J. Carr, “The Primordial black hole mass spectrum,” *Astrophys. J.*, vol. 201, pp. 1–19, 1975. DOI: `10.1086/153853`.

[35] S. W. Hawking, “Particle creation by black holes,” *Communications in Mathematical Physics*, vol. 43, pp. 199–220, Aug. 1975. DOI: `10.1007/BF02345020`.

[36] B. J. Carr, K. Kohri, Y. Sendouda, and J. Yokoyama, “New cosmological constraints on primordial black holes,” *Phys. Rev. D*, vol. 81, no. 10, 104019, p. 104 019, May 2010. DOI: `10.1103/PhysRevD.81.104019`. arXiv: `0912.5297 [astro-ph.CO]`.

[37] H. Tashiro and N. Sugiyama, “Constraints on primordial black holes by distortions of the cosmic microwave background,” *Phys. Rev. D*, vol. 78, no. 2, 023004, p. 023 004, Jul. 2008. DOI: `10.1103/PhysRevD.78.023004`. arXiv: `0801.3172`.

[38] S. J. Clark, B. Dutta, Y. Gao, L. E. Strigari, and S. Watson, “Planck constraint on relic primordial black holes,” *Phys. Rev. D*, vol. 95, no. 8, 083006, p. 083 006, Apr. 2017. DOI: `10.1103/PhysRevD.95.083006`. arXiv: `1612.07738`.

[39] S. J. Clark, B. Dutta, Y. Gao, Y.-Z. Ma, and L. E. Strigari, “21 cm limits on decaying dark matter and primordial black holes,” *Phys. Rev. D*, vol. 98, no. 4, 043006, p. 043 006, Aug. 2018. DOI: `10.1103/PhysRevD.98.043006`. arXiv: `1803.09390 [astro-ph.HE]`.

[40] D. N. Page and S. W. Hawking, “Gamma rays from primordial black holes,” *ApJ*, vol. 206, pp. 1–7, May 1976. DOI: `10.1086/154350`.

[41] B. J. Carr, “Some cosmological consequences of primordial black-hole evaporations,” *ApJ*, vol. 206, pp. 8–25, May 1976. DOI: `10.1086/154351`.

[42] J. H. MacGibbon and B. J. Carr, “Cosmic rays from primordial black holes,” *ApJ*, vol. 371, pp. 447–469, Apr. 1991. DOI: `10.1086/169909`.

[43] P. Tisserand, L. Le Guillou, C. Afonso, *et al.*, "Limits on the Macho content of the Galactic Halo from the EROS-2 Survey of the Magellanic Clouds," *A&A*, vol. 469, pp. 387–404, Jul. 2007. DOI: `10.1051/0004-6361:20066017`. eprint: `astro-ph/0607207`.

[44] H. Niikura, M. Takada, N. Yasuda, *et al.*, "Microlensing constraints on primordial black holes with the Subaru/HSC Andromeda observation," *arXiv e-prints*, Jan. 2017. arXiv: `1701.02151`.

[45] M. Zumalacárregui and U. Seljak, "Limits on Stellar-Mass Compact Objects as Dark Matter from Gravitational Lensing of Type Ia Supernovae," *Physical Review Letters*, vol. 121, no. 14, 141101, p. 141 101, Oct. 2018. DOI: `10.1103/PhysRevLett.121.141101`. arXiv: `1712.02240`.

[46] M. Sasaki, T. Suyama, T. Tanaka, and S. Yokoyama, "Primordial Black Hole Scenario for the Gravitational-Wave Event GW150914," *Physical Review Letters*, vol. 117, no. 6, 061101, p. 061 101, Aug. 2016. DOI: `10.1103/PhysRevLett.117.061101`. arXiv: `1603.08338`.

[47] S. Clesse and J. García-Bellido, "The clustering of massive Primordial Black Holes as Dark Matter: Measuring their mass distribution with advanced LIGO," *Physics of the Dark Universe*, vol. 15, pp. 142–147, Mar. 2017. DOI: `10.1016/j.dark.2016.10.002`. arXiv: `1603.05234`.

[48] M. Ricotti, J. Ostriker, and K. Mack, "Effect of Primordial Black Holes on the Cosmic Microwave Background and Cosmological Parameter Estimates," U5.004, U5.004, Jan. 2017.

[49] Y. Ali-Haïmoud and M. Kamionkowski, "Cosmic microwave background limits on accreting primordial black holes," *Phys. Rev. D*, vol. 95, no. 4, 043534, p. 043 534, Feb. 2017. DOI: `10.1103/PhysRevD.95.043534`. arXiv: `1612.05644`.

[50] V. Poulin, P. D. Serpico, F. Calore, S. Clesse, and K. Kohri, "CMB bounds on disk-accreting massive primordial black holes," *Phys. Rev.*, vol. D96, no. 8, p. 083 524, 2017. DOI: `10.1103/PhysRevD.96.083524`. arXiv: `1707.04206 [astro-ph.CO]`.

[51] J. L. Bernal, N. Bellomo, A. Raccanelli, and L. Verde, "Cosmological implications of primordial black holes," *J. Cosmology Astropart. Phys.*, vol. 10, 052, p. 052, Oct. 2017. DOI: `10.1088/1475-7516/2017/10/052`. arXiv: `1709.07465`.

[52] H. Tashiro and N. Sugiyama, "The effect of primordial black holes on 21-cm fluctuations," *MNRAS*, vol. 435, pp. 3001–3008, Nov. 2013. DOI: `10.1093/mnras/stt1493`. arXiv: `1207.6405`.

[53] J.-O. Gong and N. Kitajima, "Small-scale structure and 21cm fluctuations by primordial black holes," *J. Cosmology Astropart. Phys.*, vol. 8, 017, p. 017, Aug. 2017. DOI: `10.1088/1475-7516/2017/08/017`. arXiv: `1704.04132`.

[54] C. Alcock, R. A. Allsman, D. R. Alves, *et al.*, "MACHO Project Limits on Black Hole Dark Matter in the 1-30 M_{solar} Range," *ApJ*, vol. 550, pp. L169–L172, Apr. 2001. DOI: `10.1086/319636`. eprint: `astro-ph/0011506`.

[55] K. Griest, A. M. Cieplak, and M. J. Lehner, "Experimental limits on primordial black hole dark matter from the first 2 yr ofkeplerdata," *The Astrophysical Journal*, vol. 786, no. 2, p. 158, Apr. 2014, ISSN: 1538-4357. DOI: `10.1088/0004-637x/786/2/158`. [Online]. Available: `http://dx.doi.org/10.1088/0004-637X/786/2/158`.

[56] M. Oguri, J. M. Diego, N. Kaiser, P. L. Kelly, and T. Broadhurst, "Understanding caustic crossings in giant arcs: Characteristic scales, event rates, and constraints on compact dark matter," *Physical Review D*, vol. 97, no. 2, Jan. 2018, ISSN: 2470-0029. DOI: 10.1103/physrevd.97.023518. [Online]. Available: http://dx.doi.org/10.1103/PhysRevD.97.023518.

[57] H. Niikura, M. Takada, S. Yokoyama, T. Sumi, and S. Masaki, "Constraints on Earth-mass primordial black holes from OGLE 5-year microlensing events," *Phys. Rev. D*, vol. 99, no. 8, 083503, p. 083 503, Apr. 2019. DOI: 10.1103/PhysRevD.99.083503. arXiv: 1901.07120 [astro-ph.CO].

[58] D. Croon, D. McKeen, N. Raj, and Z. Wang, "Subaru-HSC through a different lens: microlensing by extended dark matter structures," *Phys. Rev. D*, vol. 102, no. 8, p. 083 021, 2020. DOI: 10.1103/PhysRevD.102.083021. arXiv: 2007.12697 [astro-ph.CO].

[59] P. D. Serpico, V. Poulin, D. Inman, and K. Kohri, "Cosmic microwave background bounds on primordial black holes including dark matter halo accretion," *Physical Review Research*, vol. 2, no. 2, 023204, p. 023 204, May 2020. DOI: 10.1103/PhysRevResearch.2.023204. arXiv: 2002.10771 [astro-ph.CO].

[60] M. A. Monroy-Rodríguez and C. Allen, "The end of the MACHO era revisited: new limits on MACHO masses from halo wide binaries," *ApJ*, vol. 790, no. 2, 159, p. 159, Aug. 2014. DOI: 10.1088/0004-637X/790/2/159. arXiv: 1406.5169 [astro-ph.GA].

[61] T. D. Brandt, "Constraints on MACHO Dark Matter from Compact Stellar Systems in Ultra-faint Dwarf Galaxies," *ApJ*, vol. 824, L31, p. L31, Jun. 2016. DOI: 10.3847/2041-8205/824/2/L31. arXiv: 1605.03665 [astro-ph.GA].

[62] R. Murgia, G. Scelfo, M. Viel, and A. Raccanelli, "Lyman-α forest constraints on primordial black holes as dark matter," *Phys. Rev. Lett.*, vol. 123, no. 7, 071102, p. 071 102, Aug. 2019. DOI: 10.1103/PhysRevLett.123.071102. arXiv: 1903.10509 [astro-ph.CO].

[63] B. J. Kavanagh, D. Gaggero, and G. Bertone, "Merger rate of a subdominant population of primordial black holes," *Phys. Rev. D*, vol. 98, no. 2, 023536, p. 023 536, Jul. 2018. DOI: 10.1103/PhysRevD.98.023536. arXiv: 1805.09034 [astro-ph.CO].

[64] B. P. Abbott *et al.*, "Search for subsolar mass ultracompact binaries in advanced LIGO's second observing run," *Phys. Rev. Lett.*, vol. 123, no. 16, p. 161 102, 2019. DOI: 10.1103/PhysRevLett.123.161102. arXiv: 1904.08976 [astro-ph.CO].

[65] Z.-C. Chen and Q.-G. Huang, "Distinguishing primordial black holes from astrophysical black holes by Einstein Telescope and Cosmic Explorer," *J. Cosmology Astropart. Phys.*, vol. 2020, no. 8, 039, p. 039, Aug. 2020. DOI: 10.1088/1475-7516/2020/08/039. arXiv: 1904.02396 [astro-ph.CO].

[66] O. Mena, S. Palomares-Ruiz, P. Villanueva-Domingo, and S. J. Witte, "Constraining the primordial black hole abundance with 21-cm cosmology," *Phys. Rev.*, vol. D100, no. 4, p. 043 540, 2019. DOI: 10.1103/PhysRevD.100.043540. arXiv: 1906.07735 [astro-ph.CO].

[67] P. Villanueva-Domingo and K. Ichiki, "21 cm forest constraints on primordial black holes," *PASJ*, Feb. 2022. DOI: 10.1093/pasj/psab119. arXiv: 2104.10695 [astro-ph.CO].

[68] P. Villanueva-Domingo, O. Mena, and S. Palomares-Ruiz, "A brief review on primordial black holes as dark matter," *Frontiers in Astronomy and Space Sciences*, vol. 8, 87, p. 87, May 2021. DOI: `10.3389/fspas.2021.681084`. arXiv: `2103.12087 [astro-ph.CO]`.

[69] N. Sabti, J. B. Muñoz, and D. Blas, "Galaxy luminosity function pipeline for cosmology and astrophysics," *Phys. Rev. D*, vol. 105, no. 4, 043518, p. 043 518, Feb. 2022. DOI: `10.1103/PhysRevD.105.043518`. arXiv: `2110.13168 [astro-ph.CO]`.

[70] K. T. Abe and H. Tashiro, "Cosmological free-free emission from dark matter halos in the Λ CDM model," *Phys. Rev. D*, vol. 106, no. 6, 063523, p. 063 523, Sep. 2022. DOI: `10.1103/PhysRevD.106.063523`. arXiv: `2206.11261 [astro-ph.CO]`.

[71] M. Ricotti and A. Gould, "A New Probe of Dark Matter and High-Energy Universe Using Microlensing," *ApJ*, vol. 707, no. 2, pp. 979–987, Dec. 2009. DOI: `10.1088/0004-637X/707/2/979`. arXiv: `0908.0735 [astro-ph.CO]`.

[72] M. S. Delos, A. L. Erickcek, A. P. Bailey, and M. A. Alvarez, "Are ultracompact minihalos really ultracompact?" *Phys. Rev. D*, vol. 97, no. 4, 041303, p. 041 303, Feb. 2018. DOI: `10.1103/PhysRevD.97.041303`. arXiv: `1712.05421 [astro-ph.CO]`.

[73] M. S. Delos, A. L. Erickcek, A. P. Bailey, and M. A. Alvarez, "Density profiles of ultracompact minihalos: Implications for constraining the primordial power spectrum," *Phys. Rev. D*, vol. 98, no. 6, 063527, p. 063 527, Sep. 2018. DOI: `10.1103/PhysRevD.98.063527`. arXiv: `1806.07389 [astro-ph.CO]`.

[74] A. S. Josan and A. M. Green, "Gamma rays from ultracompact minihalos: Potential constraints on the primordial curvature perturbation," *Phys. Rev. D*, vol. 82, no. 8, 083527, p. 083 527, Oct. 2010. DOI: `10.1103/PhysRevD.82.083527`. arXiv: `1006.4970 [astro-ph.CO]`.

[75] P. Scott and S. Sivertsson, "Gamma Rays from Ultracompact Primordial Dark Matter Minihalos," *Phys. Rev. Lett.*, vol. 103, no. 21, 211301, p. 211 301, Nov. 2009. DOI: `10.1103/PhysRevLett.103.211301`. arXiv: `0908.4082 [astro-ph.CO]`.

[76] T. Bringmann, P. Scott, and Y. Akrami, "Improved constraints on the primordial power spectrum at small scales from ultracompact minihalos," *Phys. Rev. D*, vol. 85, no. 12, 125027, p. 125 027, Jun. 2012. DOI: `10.1103/PhysRevD.85.125027`. arXiv: `1110.2484 [astro-ph.CO]`.

[77] H. A. Clark, G. F. Lewis, and P. Scott, "Investigating dark matter substructure with pulsar timing - I. Constraints on ultracompact minihaloes," *MNRAS*, vol. 456, no. 2, pp. 1394–1401, Feb. 2016. DOI: `10.1093/mnras/stv2743`. arXiv: `1509.02938 [astro-ph.CO]`.

[78] T. Nakama, T. Suyama, K. Kohri, and N. Hiroshima, "Constraints on small-scale primordial power by annihilation signals from extragalactic dark matter minihalos," *Phys. Rev. D*, vol. 97, no. 2, 023539, p. 023 539, Jan. 2018. DOI: `10.1103/PhysRevD.97.023539`. arXiv: `1712.08820 [astro-ph.CO]`.

[79] K. Tomikawa and T. Kobayashi, "Gauge dependence of gravitational waves generated at second order from scalar perturbations," *Phys. Rev. D*, vol. 101, no. 8, p. 083 529, 2020. DOI: `10.1103/PhysRevD.101.083529`. arXiv: `1910.01880 [gr-qc]`.

[80] V. De Luca, G. Franciolini, A. Kehagias, and A. Riotto, "On the Gauge Invariance of Cosmological Gravitational Waves," *JCAP*, vol. 03, p. 014, 2020. DOI: `10.1088/1475-7516/2020/03/014`. arXiv: `1911.09689 [gr-qc]`.

[81] P. A. R. Ade, Z. Ahmed, M. Amiri, *et al.*, "Improved Constraints on Primordial Gravitational Waves using Planck, WMAP, and BICEP/Keck Observations through the 2018 Observing Season," *Phys. Rev. Lett.*, vol. 127, no. 15, 151301, p. 151 301, Oct. 2021. DOI: `10.1103/PhysRevLett.127.151301`. arXiv: `2110.00483 [astro-ph.CO]`.

[82] K. Freese, J. A. Frieman, and A. V. Olinto, "Natural inflation with pseudo nambu-goldstone bosons," *Phys. Rev. Lett.*, vol. 65, pp. 3233–3236, 26 Dec. 1990. DOI: `10.1103/PhysRevLett.65.3233`. [Online]. Available: `https://link.aps.org/doi/10.1103/PhysRevLett.65.3233`.

[83] F. C. Adams, J. R. Bond, K. Freese, J. A. Frieman, and A. V. Olinto, "Natural inflation: Particle physics models, power-law spectra for large-scale structure, and constraints from the Cosmic Background Explorer," *Phys. Rev. D*, vol. 47, no. 2, pp. 426–455, Jan. 1993. DOI: `10.1103/PhysRevD.47.426`. arXiv: `hep-ph/9207245 [hep-ph]`.

[84] S. Dodelson, *Modern cosmology*. 2003.

[85] U. Seljak and M. Zaldarriaga, "A Line-of-Sight Integration Approach to Cosmic Microwave Background Anisotropies," *ApJ*, vol. 469, p. 437, Oct. 1996. DOI: `10.1086/177793`. arXiv: `astro-ph/9603033 [astro-ph]`.

[86] A. Lewis, A. Challinor, and A. Lasenby, "Efficient computation of CMB anisotropies in closed FRW models," *ApJ*, vol. 538, pp. 473–476, 2000. DOI: `10.1086/309179`. arXiv: `astro-ph/9911177 [astro-ph]`.

[87] J. M. Bardeen, J. R. Bond, N. Kaiser, and A. S. Szalay, "The Statistics of Peaks of Gaussian Random Fields," *ApJ*, vol. 304, p. 15, May 1986. DOI: `10.1086/164143`.

[88] N. Sugiyama, "Cosmic Background Anisotropies in Cold Dark Matter Cosmology," *ApJS*, vol. 100, p. 281, Oct. 1995. DOI: `10.1086/192220`. arXiv: `astro-ph/9412025 [astro-ph]`.

[89] S. Weinberg, *Cosmology*. 2008.

[90] D. J. Eisenstein and W. Hu, "Baryonic Features in the Matter Transfer Function," *ApJ*, vol. 496, no. 2, pp. 605–614, Mar. 1998. DOI: `10.1086/305424`. arXiv: `astro-ph/9709112 [astro-ph]`.

[91] W. H. Press and P. Schechter, "Formation of Galaxies and Clusters of Galaxies by Self-Similar Gravitational Condensation," *ApJ*, vol. 187, pp. 425–438, Feb. 1974. DOI: `10.1086/152650`.

[92] R. G. Bower, "The evolution of groups of galaxies in the Press – Schechter formalism," *Monthly Notices of the Royal Astronomical Society*, vol. 248, no. 2, pp. 332–352, Jan. 1991, ISSN: 0035-8711. DOI: `10.1093/mnras/248.2.332`. eprint: `https://academic.oup.com/mnras/article-pdf/248/2/332/3437756/mnras248-0332.pdf`. [Online]. Available: `https://doi.org/10.1093/mnras/248.2.332`.

[93] J. R. Bond, S. Cole, G. Efstathiou, and N. Kaiser, "Excursion Set Mass Functions for Hierarchical Gaussian Fluctuations," *ApJ*, vol. 379, p. 440, Oct. 1991. DOI: `10.1086/170520`.

[94] H. J. Mo and S. D. M. White, "An analytic model for the spatial clustering of dark matter haloes," *MNRAS*, vol. 282, no. 2, pp. 347–361, Sep. 1996. DOI: `10.1093/mnras/282.2.347`. arXiv: `astro-ph/9512127 [astro-ph]`.

[95] H. J. Mo, Y. P. Jing, and S. D. M. White, "High-order correlations of peaks and haloes: a step towards understanding galaxy biasing," *MNRAS*, vol. 284, pp. 189–201, Jan. 1997. DOI: `10.1093/mnras/284.1.189`. eprint: `astro-ph/9603039`.

[96] W. Hu and J. Silk, "Thermalization and spectral distortions of the cosmic background radiation," *Phys. Rev. D*, vol. 48, pp. 485–502, 2 Jul. 1993. DOI: `10.1103/PhysRevD.48.485`. [Online]. Available: `https://link.aps.org/doi/10.1103/PhysRevD.48.485`.

[97] R. A. Sunyaev and Y. B. Zeldovich, "Small-Scale Fluctuations of Relic Radiation," *Ap&SS*, vol. 7, no. 1, pp. 3–19, Apr. 1970. DOI: `10.1007/BF00653471`.

[98] A. Kosowsky and M. S. Turner, "Cbr anisotropy and the running of the scalar spectral index," *Phys. Rev. D*, vol. 52, R1739–R1743, 4 Aug. 1995. DOI: `10.1103/PhysRevD.52.R1739`. [Online]. Available: `https://link.aps.org/doi/10.1103/PhysRevD.52.R1739`.

[99] Y. B. Zel'dovich and I. D. Novikov, "The Hypothesis of Cores Retarded during Expansion and the Hot Cosmological Model," *Soviet Ast.*, vol. 10, p. 602, Feb. 1967.

[100] S. Hawking, "Gravitationally collapsed objects of very low mass," *MNRAS*, vol. 152, p. 75, 1971. DOI: `10.1093/mnras/152.1.75`.

[101] Y. Ali-Haïmoud, E. D. Kovetz, and M. Kamionkowski, "Merger rate of primordial black-hole binaries," *Phys. Rev. D*, vol. 96, p. 123 523, 12 Dec. 2017. DOI: `10.1103/PhysRevD.96.123523`. [Online]. Available: `https://link.aps.org/doi/10.1103/PhysRevD.96.123523`.

[102] B. Carr, K. Kohri, Y. Sendouda, and J. Yokoyama, "Constraints on primordial black holes," *Reports on Progress in Physics*, vol. 84, no. 11, 116902, p. 116 902, Nov. 2021. DOI: `10.1088/1361-6633/ac1e31`. arXiv: `2002.12778 [astro-ph.CO]`.

[103] N. Kitajima, Y. Tada, S. Yokoyama, and C.-M. Yoo, "Primordial black holes in peak theory with a non-Gaussian tail," *JCAP*, vol. 10, p. 053, 2021. DOI: `10.1088/1475-7516/2021/10/053`. arXiv: `2109.00791 [astro-ph.CO]`.

[104] T. Nakama, T. Harada, A. G. Polnarev, and J. Yokoyama, "Identifying the most crucial parameters of the initial curvature profile for primordial black hole formation," *J. Cosmology Astropart. Phys.*, vol. 2014, no. 1, 037, p. 037, Jan. 2014. DOI: `10.1088/1475-7516/2014/01/037`. arXiv: `1310.3007 [gr-qc]`.

[105] A. Escrivà, "Simulation of primordial black hole formation using pseudo-spectral methods," *Physics of the Dark Universe*, vol. 27, 100466, p. 100 466, Jan. 2020. DOI: `10.1016/j.dark.2020.100466`. arXiv: `1907.13065 [gr-qc]`.

[106] V. Atal, J. Cid, A. Escrivà, and J. Garriga, "PBH in single field inflation: the effect of shape dispersion and non-Gaussianities," *J. Cosmology Astropart. Phys.*, vol. 2020, no. 5, 022, p. 022, May 2020. DOI: `10.1088/1475-7516/2020/05/022`. arXiv: `1908.11357 [astro-ph.CO]`.

[107] T. Harada, C.-M. Yoo, T. Nakama, and Y. Koga, "Cosmological long-wavelength solutions and primordial black hole formation," *Phys. Rev. D*, vol. 91, p. 084 057, 8 Apr. 2015. DOI: `10.1103/PhysRevD.91.084057`. [Online]. Available: `https://link.aps.org/doi/10.1103/PhysRevD.91.084057`.

[108] M. Shibata and M. Sasaki, "Black hole formation in the friedmann universe: Formulation and computation in numerical relativity," *Phys. Rev. D*, vol. 60, p. 084 002, 8 Sep. 1999. DOI: `10.1103/PhysRevD.60.084002`. [Online]. Available: `https://link.aps.org/doi/10.1103/PhysRevD.60.084002`.

[109] A. Escrivà, C. Germani, and R. K. Sheth, "Universal threshold for primordial black hole formation," *Phys. Rev. D*, vol. 101, no. 4, 044022, p. 044 022, Feb. 2020. DOI: `10.1103/PhysRevD.101.044022`. arXiv: `1907.13311 [gr-qc]`.

[110] G. Sato-Polito, E. D. Kovetz, and M. Kamionkowski, "Constraints on the primordial curvature power spectrum from primordial black holes," *Phys. Rev. D*, vol. 100, no. 6, 063521, p. 063 521, Sep. 2019. DOI: `10.1103/PhysRevD.100.063521`. arXiv: `1904.10971 [astro-ph.CO]`.

[111] J. B. Muñoz, E. D. Kovetz, L. Dai, and M. Kamionkowski, "Lensing of fast radio bursts as a probe of compact dark matter," *Phys. Rev. Lett.*, vol. 117, p. 091 301, 9 Aug. 2016. DOI: `10.1103/PhysRevLett.117.091301`. [Online]. Available: `https://link.aps.org/doi/10.1103/PhysRevLett.117.091301`.

[112] T. Venumadhav, L. Dai, and J. Miralda-Escudé, "Microlensing of Extremely Magnified Stars near Caustics of Galaxy Clusters," *ApJ*, vol. 850, no. 1, 49, p. 49, Nov. 2017. DOI: `10.3847/1538-4357/aa9575`. arXiv: `1707.00003 [astro-ph.CO]`.

[113] K. Schutz and A. Liu, "Pulsar timing can constrain primordial black holes in the ligo mass window," *Phys. Rev. D*, vol. 95, p. 023 002, 2 Jan. 2017. DOI: `10.1103/PhysRevD.95.023002`. [Online]. Available: `https://link.aps.org/doi/10.1103/PhysRevD.95.023002`.

[114] M. Raidal, V. Vaskonen, and H. Veermäe, "Gravitational waves from primordial black hole mergers," *J. Cosmology Astropart. Phys.*, vol. 2017, no. 9, 037, p. 037, Sep. 2017. DOI: `10.1088/1475-7516/2017/09/037`. arXiv: `1707.01480 [astro-ph.CO]`.

[115] P. Madau, L. Pozzetti, and M. Dickinson, "The Star Formation History of Field Galaxies," *ApJ*, vol. 498, no. 1, pp. 106–116, May 1998. DOI: `10.1086/305523`. arXiv: `astro-ph/9708220 [astro-ph]`.

[116] J. Kennicutt Robert C., "Star Formation in Galaxies Along the Hubble Sequence," *Ann. Rev. Astron. Astrophys.*, vol. 36, pp. 189–232, Jan. 1998. DOI: `10.1146/annurev.astro.36.1.189`. arXiv: `astro-ph/9807187 [astro-ph]`.

[117] P. Madau and M. Dickinson, "Cosmic Star-Formation History," *Ann. Rev. Astron. Astrophys.*, vol. 52, pp. 415–486, Aug. 2014. DOI: `10.1146/annurev-astro-081811-125615`. arXiv: `1403.0007 [astro-ph.CO]`.

[118] J. B. Oke and J. E. Gunn, "Secondary standard stars for absolute spectrophotometry.," *ApJ*, vol. 266, pp. 713–717, Mar. 1983. DOI: `10.1086/160817`.

[119] P. A. Oesch, R. J. Bouwens, G. D. Illingworth, I. Labbé, and M. Stefanon, "The Dearth of z $\sim$ 10 Galaxies in All HST Legacy Fields—The Rapid Evolution of the Galaxy Population in the First 500 Myr," *ApJ*, vol. 855, no. 2, 105, p. 105, Mar. 2018. DOI: `10.3847/1538-4357/aab03f`. arXiv: `1710.11131 [astro-ph.GA]`.

[120] R. J. Bouwens, P. A. Oesch, M. Stefanon, *et al.*, "New Determinations of the UV Luminosity Functions from z 9 to 2 Show a Remarkable Consistency with Halo Growth and a Constant Star Formation Efficiency," *AJ*, vol. 162, no. 2, 47, p. 47, Aug. 2021. DOI: `10.3847/1538-3881/abf83e`. arXiv: `2102.07775 [astro-ph.GA]`.

[121] N. Sabti, J. B. Muñoz, and D. Blas, "New Roads to the Small-scale Universe: Measurements of the Clustering of Matter with the High-redshift UV Galaxy Luminosity Function," *ApJ*, vol. 928, no. 2, L20, p. L20, Apr. 2022. DOI: `10.3847/2041-8213/ac5e9c`. arXiv: `2110.13161 [astro-ph.CO]`.

[122] M. A. Troxel, N. MacCrann, J. Zuntz, *et al.*, "Dark energy survey year 1 results: Cosmological constraints from cosmic shear," *Phys. Rev. D*, vol. 98, p. 043 528, 4 Aug. 2018. DOI: `10.1103/PhysRevD.98.043528`. [Online]. Available: `https://link.aps.org/doi/10.1103/PhysRevD.98.043528`.

[123] B. A. Reid, W. J. Percival, D. J. Eisenstein, and et al., "Cosmological constraints from the clustering of the Sloan Digital Sky Survey DR7 luminous red galaxies," *Monthly Notices of the Royal Astronomical Society*, vol. 404, no. 1, pp. 60–85, Apr. 2010, ISSN: 0035-8711. DOI: `10.1111/j.1365-2966.2010.16276.x`. eprint: `https://academic.oup.com/mnras/article-pdf/404/1/60/11177257/mnras0404-0060.pdf`. [Online]. Available: `https://doi.org/10.1111/j.1365-2966.2010.16276.x`.

[124] B. Abolfathi, D. S. Aguado, G. Aguilar, and et al., "The Fourteenth Data Release of the Sloan Digital Sky Survey: First Spectroscopic Data from the Extended Baryon Oscillation Spectroscopic Survey and from the Second Phase of the Apache Point Observatory Galactic Evolution Experiment," *ApJS*, vol. 235, no. 2, 42, p. 42, Apr. 2018. DOI: `10.3847/1538-4365/aa9e8a`. arXiv: `1707.09322 [astro-ph.GA]`.

[125] P. Meszaros, "The behaviour of point masses in an expanding cosmological substratum.," *A&A*, vol. 37, no. 2, pp. 225–228, Dec. 1974.

[126] W. Hu and N. Sugiyama, "Small-Scale Cosmological Perturbations: an Analytic Approach," *ApJ*, vol. 471, p. 542, Nov. 1996. DOI: `10.1086/177989`. arXiv: `astro-ph/9510117 [astro-ph]`.

[127] E. Bertschinger, "Self-similar secondary infall and accretion in an Einstein-de Sitter universe," *ApJS*, vol. 58, pp. 39–65, May 1985. DOI: `10.1086/191028`.

[128] A. Huss, B. Jain, and M. Steinmetz, "How Universal Are the Density Profiles of Dark Halos?" *ApJ*, vol. 517, no. 1, pp. 64–69, May 1999. DOI: `10.1086/307161`. arXiv: `astro-ph/9803117 [astro-ph]`.

[129] J. D. MacMillan, L. M. Widrow, and R. N. Henriksen, "On Universal Halos and the Radial Orbit Instability," *ApJ*, vol. 653, no. 1, pp. 43–52, Dec. 2006. DOI: `10.1086/508602`. arXiv: `astro-ph/0604418 [astro-ph]`.

[130] J. M. Bellovary, J. J. Dalcanton, A. Babul, *et al.*, "The Role of the Radial Orbit Instability in Dark Matter Halo Formation and Structure," *ApJ*, vol. 685, no. 2, pp. 739–751, Oct. 2008. DOI: `10.1086/591120`. arXiv: `0806.3434 [astro-ph]`.

[131] M. Vogelsberger, S. D. M. White, R. Mohayaee, and V. Springel, "Caustics in growing cold dark matter haloes," *MNRAS*, vol. 400, no. 4, pp. 2174–2184, Dec. 2009. DOI: `10.1111/j.1365-2966.2009.15615.x`. arXiv: `0906.4341 [astro-ph.CO]`.

[132] M. Vogelsberger, R. Mohayaee, and S. D. M. White, "Non-spherical similarity solutions for dark halo formation," *MNRAS*, vol. 414, no. 4, pp. 3044–3051, Jul. 2011. DOI: `10.1111/j.1365-2966.2011.18605.x`. arXiv: `1007.4195 [astro-ph.CO]`.

[133] M. Gosenca, J. Adamek, C. T. Byrnes, and S. Hotchkiss, "3D simulations with boosted primordial power spectra and ultracompact minihalos," *Phys. Rev. D*, vol. 96, no. 12, 123519, p. 123 519, Dec. 2017. DOI: `10.1103/PhysRevD.96.123519`. arXiv: `1710.02055 [astro-ph.CO]`.

[134] B. Moore, T. Quinn, F. Governato, J. Stadel, and G. Lake, "Cold collapse and the core catastrophe," *MNRAS*, vol. 310, no. 4, pp. 1147–1152, Dec. 1999. DOI: `10.1046/j.1365-8711.1999.03039.x`. arXiv: `astro-ph/9903164 [astro-ph]`.

[135] J. F. Navarro, C. S. Frenk, and S. D. M. White, "Simulations of X-ray clusters," *Monthly Notices of the Royal Astronomical Society*, vol. 275, no. 3, pp. 720–740, Aug. 1995, ISSN: 0035-8711. DOI: `10.1093/mnras/275.3.720`. eprint: `http://oup.prod.sis.lan/mnras/article-pdf/275/3/720/2805863/mnras275-0720.pdf`. [Online]. Available: `https://doi.org/10.1093/mnras/275.3.720`.

[136] P. J. E. Peebles, *Principles of Physical Cosmology*. Princeton University Press, 1993.

[137] G. Steigman and M. S. Turner, "Cosmological constraints on the properties of weakly interacting massive particles," *Nuclear Physics B*, vol. 253, pp. 375–386, Jan. 1985. DOI: `10.1016/0550-3213(85)90537-1`.

[138] G. Jungman, M. Kamionkowski, and K. Griest, "Supersymmetric dark matter," *Phys. Rep.*, vol. 267, pp. 195–373, Mar. 1996. DOI: `10.1016/0370-1573(95)00058-5`. arXiv: `hep-ph/9506380 [hep-ph]`.

[139] E. W. Kolb, D. J. H. Chung, and A. Riotto, "WIMPZILLAS!" In *Dark matter in Astrophysics and Particle Physics*, H. V. Klapdor-Kleingrothaus and L. Baudis, Eds., Jan. 1999, p. 592. arXiv: `hep-ph/9810361 [hep-ph]`.

[140] W. B. Atwood, A. A. Abdo, M. Ackermann, *et al.*, "The Large Area Telescope on the Fermi Gamma-Ray Space Telescope Mission," *ApJ*, vol. 697, no. 2, pp. 1071–1102, Jun. 2009. DOI: `10.1088/0004-637X/697/2/1071`. arXiv: `0902.1089 [astro-ph.IM]`.

[141] F. Li, A. L. Erickcek, and N. M. Law, "A new probe of the small-scale primordial power spectrum: Astrometric microlensing by ultracompact minihalos," *Phys. Rev. D*, vol. 86, no. 4, 043519, p. 043 519, Aug. 2012. DOI: `10.1103/PhysRevD.86.043519`. arXiv: `1202.1284 [astro-ph.CO]`.

[142] D. Zhang, "Impact of primordial ultracompact minihaloes on the intergalactic medium and first structure formation," *MNRAS*, vol. 418, no. 3, pp. 1850–1872, Dec. 2011. DOI: `10.1111/j.1365-2966.2011.19602.x`. arXiv: `1011.1935 [astro-ph.CO]`.

[143] Y. Yang, L. Feng, X. Huang, X. Chen, T. Lu, and H. Zong, "Constraints on ultracompact minihalos from extragalactic γ-ray background," *J. Cosmology Astropart. Phys.*, vol. 2011, no. 12, 020, p. 020, Dec. 2011. DOI: `10.1088/1475-7516/2011/12/020`. arXiv: `1112.6229 [astro-ph.CO]`.

[144] Y. Yang, “Contributions of dark matter annihilation within ultracompact minihalos to the 21 cm background signal,” *European Physical Journal Plus*, vol. 131, no. 12, 432, p. 432, Dec. 2016. DOI: `10.1140/epjp/i2016-16432-8`. arXiv: `1612.06559 [astro-ph.CO]`.

[145] H. A. Clark, N. Iwanus, P. J. Elahi, G. F. Lewis, and P. Scott, “Heating of galactic gas by dark matter annihilation in ultracompact minihalos,” *J. Cosmology Astropart. Phys.*, vol. 2017, no. 5, 048, p. 048, May 2017. DOI: `10.1088/1475-7516/2017/05/048`. arXiv: `1611.08619 [astro-ph.CO]`.

[146] G. Nicholson and C. R. Contaldi, “Reconstruction of the primordial power spectrum using temperature and polarisation data from multiple experiments,” *J. Cosmology Astropart. Phys.*, vol. 2009, no. 7, 011, p. 011, Jul. 2009. DOI: `10.1088/1475-7516/2009/07/011`. arXiv: `0903.1106 [astro-ph.CO]`.

[147] G. Nicholson, C. R. Contaldi, and P. Paykari, “Reconstruction of the primordial power spectrum by direct inversion,” *J. Cosmology Astropart. Phys.*, vol. 2010, no. 1, 016, p. 016, Jan. 2010. DOI: `10.1088/1475-7516/2010/01/016`. arXiv: `0909.5092 [astro-ph.CO]`.

[148] S. Bird, H. V. Peiris, M. Viel, and L. Verde, “Minimally parametric power spectrum reconstruction from the Lyman α forest,” *MNRAS*, vol. 413, no. 3, pp. 1717–1728, May 2011. DOI: `10.1111/j.1365-2966.2011.18245.x`. arXiv: `1010.1519 [astro-ph.CO]`.

[149] T. Bringmann, “Particle models and the small-scale structure of dark matter,” *New Journal of Physics*, vol. 11, no. 10, 105027, p. 105 027, Oct. 2009. DOI: `10.1088/1367-2630/11/10/105027`. arXiv: `0903.0189 [astro-ph.CO]`.

[150] E. Aprile, J. Aalbers, F. Agostini, *et al.*, “Constraining the Spin-Dependent WIMP-Nucleon Cross Sections with XENON1T,” *Phys. Rev. Lett.*, vol. 122, no. 14, 141301, p. 141 301, Apr. 2019. DOI: `10.1103/PhysRevLett.122.141301`. arXiv: `1902.03234 [astro-ph.CO]`.

[151] I. T. Iliev, P. R. Shapiro, A. Ferrara, and H. Martel, “On the Direct Detectability of the Cosmic Dark Ages: 21 Centimeter Emission from Minihalos,” *ApJ*, vol. 572, no. 2, pp. L123–L126, Jun. 2002. DOI: `10.1086/341869`. arXiv: `astro-ph/0202410 [astro-ph]`.

[152] B. A. Reid, W. J. Percival, D. J. Eisenstein, *et al.*, “Cosmological constraints from the clustering of the Sloan Digital Sky Survey DR7 luminous red galaxies,” *MNRAS*, vol. 404, no. 1, pp. 60–85, May 2010. DOI: `10.1111/j.1365-2966.2010.16276.x`. arXiv: `0907.1659 [astro-ph.CO]`.

[153] S. Chabanier, N. Palanque-Delabrouille, C. Yèche, *et al.*, “The one-dimensional power spectrum from the SDSS DR14 Lyα forests,” *J. Cosmology Astropart. Phys.*, vol. 2019, no. 7, 017, p. 017, Jul. 2019. DOI: `10.1088/1475-7516/2019/07/017`. arXiv: `1812.03554 [astro-ph.CO]`.

[154] S. Chabanier, M. Millea, and N. Palanque-Delabrouille, “Matter power spectrum: from Ly α forest to CMB scales,” *MNRAS*, vol. 489, no. 2, pp. 2247–2253, Oct. 2019. DOI: `10.1093/mnras/stz2310`. arXiv: `1905.08103 [astro-ph.CO]`.

[155] S. R. Furlanetto, S. P. Oh, and F. H. Briggs, “Cosmology at low frequencies: The 21 cm transition and the high-redshift Universe,” *Phys. Rep.*, vol. 433, no. 4-6, pp. 181–301, Oct. 2006. DOI: `10.1016/j.physrep.2006.08.002`. arXiv: `astro-ph/0608032 [astro-ph]`.

[156] A. Loeb and M. Zaldarriaga, "Measuring the Small-Scale Power Spectrum of Cosmic Density Fluctuations through 21cm Tomography Prior to the Epoch of Structure Formation," *Phys. Rev. Lett.*, vol. 92, no. 21, 211301, p. 211 301, May 2004. DOI: `10.1103/PhysRevLett.92.211301`. arXiv: `astro-ph/0312134 [astro-ph]`.

[157] A. Cooray and S. R. Furlanetto, "Free-Free Emission at Low Radio Frequencies," *ApJ*, vol. 606, no. 1, pp. L5–L8, May 2004. DOI: `10.1086/421241`. arXiv: `astro-ph/0402239 [astro-ph]`.

[158] P. P. Ponente, J. M. Diego, R. K. Sheth, C. Burigana, S. R. Knollmann, and Y. Ascasibar, "The cosmological free-free signal from galaxy groups and clusters," *MNRAS*, vol. 410, no. 4, pp. 2353–2362, Feb. 2011. DOI: `10.1111/j.1365-2966.2010.17611.x`. arXiv: `1006.2243 [astro-ph.CO]`.

[159] B. Liu, J. Jaacks, S. L. Finkelstein, and V. Bromm, "Global radiation signature from early structure formation," *MNRAS*, vol. 486, no. 3, pp. 3617–3635, Jul. 2019. DOI: `10.1093/mnras/stz910`. arXiv: `1901.08994 [astro-ph.GA]`.

[160] L. Gleser, A. Nusser, and A. J. Benson, "Decontamination of cosmological 21-cm maps," *MNRAS*, vol. 391, no. 1, pp. 383–398, Nov. 2008. DOI: `10.1111/j.1365-2966.2008.13897.x`. arXiv: `0712.0497 [astro-ph]`.

[161] S. Murray, C. Power, and A. Robotham, *Hmfcalc: An online tool for calculating dark matter halo mass functions*, 2013. arXiv: `1306.6721 [astro-ph.CO]`.

[162] Rybicki, George B. and Lightman, Alan P., *Radiative Processes in Astrophysics*. 1986.

[163] B. T. Draine, *Physics of the Interstellar and Intergalactic Medium*. 2011.

[164] E. Komatsu and U. Seljak, "Universal gas density and temperature profile," *Monthly Notices of the Royal Astronomical Society*, vol. 327, no. 4, pp. 1353 – 1366, Nov. 2001, ISSN: 1365-2966. DOI: `10.1046/j.1365-8711.2001.04838.x`. [Online]. Available: `http://dx.doi.org/10.1046/j.1365-8711.2001.04838.x`.

[165] E. Komatsu and U. Seljak, "The Sunyaev-Zel'dovich angular power spectrum as a probe of cosmological parameters," *MNRAS*, vol. 336, no. 4, pp. 1256–1270, Nov. 2002. DOI: `10.1046/j.1365-8711.2002.05889.x`. arXiv: `astro-ph/0205468 [astro-ph]`.

[166] J. F. Navarro, C. S. Frenk, and S. D. M. White, "A Universal Density Profile from Hierarchical Clustering," *ApJ*, vol. 490, no. 2, pp. 493–508, Dec. 1997. DOI: `10.1086/304888`. arXiv: `astro-ph/9611107 [astro-ph]`.

[167] P. Salucci, "The distribution of dark matter in galaxies," *Astron. Astrophys. Rev.*, vol. 27, no. 1, p. 2, 2019. DOI: `10.1007/s00159-018-0113-1`. arXiv: `1811.08843 [astro-ph.GA]`.

[168] T. Ishiyama, F. Prada, A. A. Klypin, *et al.*, "The Uchuu Simulations: Data Release 1 and Dark Matter Halo Concentrations," *arXiv e-prints*, arXiv:2007.14720, arXiv:2007.14720, Jul. 2020. arXiv: `2007.14720 [astro-ph.CO]`.

[169] J. Schaye, T. Theuns, M. Rauch, G. Efstathiou, and W. L. W. Sargent, "The thermal history of the intergalactic medium*," *MNRAS*, vol. 318, no. 3, pp. 817–826, Nov. 2000. DOI: `10.1046/j.1365-8711.2000.03815.x`. arXiv: `astro-ph/9912432 [astro-ph]`.

[170] G. D. Becker, J. S. Bolton, M. G. Haehnelt, and W. L. W. Sargent, “Detection of extended He II reionization in the temperature evolution of the intergalactic medium,” *MNRAS*, vol. 410, no. 2, pp. 1096–1112, Jan. 2011. DOI: `10.1111/j.1365-2966.2010.17507.x`. arXiv: `1008.2622 [astro-ph.CO]`.

[171] A. Garzilli, J. S. Bolton, T. S. Kim, S. Leach, and M. Viel, “The intergalactic medium thermal history at redshift z = 1.7-3.2 from the Lyα forest: a comparison of measurements using wavelets and the flux distribution,” *MNRAS*, vol. 424, no. 3, pp. 1723–1736, Aug. 2012. DOI: `10.1111/j.1365-2966.2012.21223.x`. arXiv: `1202.3577 [astro-ph.CO]`.

[172] J. S. Bolton, G. D. Becker, M. G. Haehnelt, and M. Viel, “A consistent determination of the temperature of the intergalactic medium at redshift z = 2.4,” *MNRAS*, vol. 438, no. 3, pp. 2499–2507, Mar. 2014. DOI: `10.1093/mnras/stt2374`. arXiv: `1308.4411 [astro-ph.CO]`.

[173] E. Boera, M. T. Murphy, G. D. Becker, and J. S. Bolton, “The thermal history of the intergalactic medium down to redshift z = 1.5: a new curvature measurement,” *MNRAS*, vol. 441, no. 3, pp. 1916–1933, Jul. 2014. DOI: `10.1093/mnras/stu660`. arXiv: `1404.1083 [astro-ph.CO]`.

[174] K. T. Abe, T. Minoda, and H. Tashiro, “Constraint on the early-formed dark matter halos using the free-free emission in the Planck foreground analysis,” *Phys. Rev. D*, vol. 105, no. 6, 063531, p. 063 531, Mar. 2022. DOI: `10.1103/PhysRevD.105.063531`. arXiv: `2108.00621 [astro-ph.CO]`.

[175] A. Cooray and R. Sheth, “Halo models of large scale structure,” *Phys. Rep.*, vol. 372, no. 1, pp. 1–129, Dec. 2002. DOI: `10.1016/S0370-1573(02)00276-4`. arXiv: `astro-ph/0206508 [astro-ph]`.

[176] P. J. E. Peebles, *The large-scale structure of the universe*. 1980.

[177] S. Cole and N. Kaiser, “Sunyaev-Zel’dovich fluctuations in the cold dark matter scenario,” *MNRAS*, vol. 233, pp. 637–648, Aug. 1988. DOI: `10.1093/mnras/233.3.637`.

[178] T. Horii, S. Asaba, K. Hasegawa, and H. Tashiro, “Can HI 21-cm lines trace the missing baryons in the filamentary structures?” *Publications of the Astronomical Society of Japan*, vol. 69, no. 4, Jul. 2017, 73, ISSN: 0004-6264. DOI: `10.1093/pasj/psx056`. eprint: `https://academic.oup.com/pasj/article-pdf/69/4/73/19489306/psx056.pdf`. [Online]. Available: `https://doi.org/10.1093/pasj/psx056`.

[179] Planck Collaboration, Y. Akrami, F. Arroja, *et al.*, “Planck 2018 results. X. Constraints on inflation,” *arXiv e-prints*, arXiv:1807.06211, arXiv:1807.06211, Jul. 2018. arXiv: `1807.06211 [astro-ph.CO]`.

[180] A. H. Guth and S. Y. Pi, “Fluctuations in the New Inflationary Universe,” *Phys. Rev. Lett.*, vol. 49, no. 15, pp. 1110–1113, Oct. 1982. DOI: `10.1103/PhysRevLett.49.1110`.

[181] J. M. Bardeen, P. J. Steinhardt, and M. S. Turner, “Spontaneous creation of almost scale-free density perturbations in an inflationary universe,” *Phys. Rev. D*, vol. 28, no. 4, pp. 679–693, Aug. 1983. DOI: `10.1103/PhysRevD.28.679`.

[182] P. McDonald, U. Seljak, S. Burles, *et al.*, “The Lyα Forest Power Spectrum from the Sloan Digital Sky Survey,” *ApJS*, vol. 163, no. 1, pp. 80–109, Mar. 2006. DOI: `10.1086/444361`. arXiv: `astro-ph/0405013 [astro-ph]`.

[183] A. S. Josan, A. M. Green, and K. A. Malik, “Generalized constraints on the curvature perturbation from primordial black holes,” *Phys. Rev. D*, vol. 79, no. 10, 103520, p. 103 520, May 2009. DOI: `10.1103/PhysRevD.79.103520`. arXiv: `0903.3184 [astro-ph.CO]`.

[184] R. Emami and G. F. Smoot, “Observational constraints on the primordial curvature power spectrum,” *J. Cosmology Astropart. Phys.*, vol. 2018, no. 1, 007, p. 007, Jan. 2018. DOI: `10.1088/1475-7516/2018/01/007`. arXiv: `1705.09924 [astro-ph.CO]`.

[185] P. Scott and S. Sivertsson, “Erratum: Gamma Rays from Ultracompact Primordial Dark Matter Minihalos [Phys. Rev. Lett. 103, 211301 (2009)],” *Phys. Rev. Lett.*, vol. 105, no. 11, 119902, p. 119 902, Sep. 2010. DOI: `10.1103/PhysRevLett.105.119902`.

[186] Y. Yang, G. Yang, and H. Zong, “Neutrino signals from ultracompact minihalos and constraints on the primordial curvature perturbation,” *Phys. Rev. D*, vol. 87, no. 10, 103525, p. 103 525, May 2013. DOI: `10.1103/PhysRevD.87.103525`. arXiv: `1305.4213 [astro-ph.CO]`.

[187] S. R. Furlanetto and S. P. Oh, “Redshifted 21 cm Emission from Minihalos before Reionization,” *ApJ*, vol. 652, no. 2, pp. 849–856, Dec. 2006. DOI: `10.1086/508448`. arXiv: `astro-ph/0604080 [astro-ph]`.

[188] S. Chongchitnan and J. Silk, “The 21-cm radiation from minihaloes as a probe of small primordial non-Gaussianity,” *MNRAS*, vol. 426, no. 1, pp. L21–L25, Oct. 2012. DOI: `10.1111/j.1745-3933.2012.01315.x`. arXiv: `1205.6799 [astro-ph.CO]`.

[189] T. Sekiguchi, T. Takahashi, H. Tashiro, and S. Yokoyama, “21 cm angular power spectrum from minihalos as a probe of primordial spectral runnings,” *J. Cosmology Astropart. Phys.*, vol. 2018, no. 2, 053, p. 053, Feb. 2018. DOI: `10.1088/1475-7516/2018/02/053`. arXiv: `1705.00405 [astro-ph.CO]`.

[190] T. Sekiguchi, T. Takahashi, H. Tashiro, and S. Yokoyama, “Probing primordial non-Gaussianity with 21 cm fluctuations from minihalos,” *J. Cosmology Astropart. Phys.*, vol. 2019, no. 2, 033, p. 033, Feb. 2019. DOI: `10.1088/1475-7516/2019/02/033`. arXiv: `1807.02008 [astro-ph.CO]`.

[191] K. J. Mack and D. H. Wesley, “Primordial black holes in the Dark Ages: Observational prospects for future 21cm surveys,” *arXiv e-prints*, May 2008. arXiv: `0805.1531`.

[192] H. Tashiro and N. Sugiyama, “The effect of primordial black holes on 21-cm fluctuations,” *MNRAS*, vol. 435, no. 4, pp. 3001–3008, Nov. 2013. DOI: `10.1093/mnras/stt1493`. arXiv: `1207.6405 [astro-ph.CO]`.

[193] M. P. van Haarlem, M. W. Wise, A. W. Gunst, *et al.*, “LOFAR: The LOw-Frequency ARray,” *A&A*, vol. 556, A2, A2, Aug. 2013. DOI: `10.1051/0004-6361/201220873`. arXiv: `1305.3550 [astro-ph.IM]`.

[194] G. Paciga, T.-C. Chang, Y. Gupta, *et al.*, “The GMRT Epoch of Reionization experiment: a new upper limit on the neutral hydrogen power spectrum at z$\approx$ 8.6,” *MNRAS*, vol. 413, no. 2, pp. 1174–1183, May 2011. DOI: `10.1111/j.1365-2966.2011.18208.x`. arXiv: `1006.1351 [astro-ph.CO]`.

[195] S. J. Tingay, R. Goeke, J. D. Bowman, *et al.*, “The Murchison Widefield Array: The Square Kilometre Array Precursor at Low Radio Frequencies,” *Publ. Astron. Soc. Australia*, vol. 30, e007, e007, Jan. 2013. DOI: `10.1017/pasa.2012.007`. arXiv: `1206.6945 [astro-ph.IM]`.

[196] J. D. Bowman, I. Cairns, D. L. Kaplan, *et al.*, "Science with the Murchison Widefield Array," *Publ. Astron. Soc. Australia*, vol. 30, e031, e031, Apr. 2013. DOI: 10.1017/pas.2013.009. arXiv: 1212.5151 [astro-ph.IM].

[197] A. R. Parsons, D. C. Backer, G. S. Foster, *et al.*, "The Precision Array for Probing the Epoch of Re-ionization: Eight Station Results," *AJ*, vol. 139, no. 4, pp. 1468–1480, Apr. 2010. DOI: 10.1088/0004-6256/139/4/1468. arXiv: 0904.2334 [astro-ph.CO].

[198] A. H. Patil, S. Yatawatta, L. V. E. Koopmans, *et al.*, "Upper Limits on the 21 cm Epoch of Reionization Power Spectrum from One Night with LOFAR," *ApJ*, vol. 838, no. 1, 65, p. 65, Mar. 2017. DOI: 10.3847/1538-4357/aa63e7. arXiv: 1702.08679 [astro-ph.CO].

[199] G. Paciga, J. G. Albert, K. Bandura, *et al.*, "A simulation-calibrated limit on the H I power spectrum from the GMRT Epoch of Reionization experiment," *MNRAS*, vol. 433, no. 1, pp. 639–647, Jul. 2013. DOI: 10.1093/mnras/stt753. arXiv: 1301.5906 [astro-ph.CO].

[200] Z. S. Ali, A. R. Parsons, H. Zheng, *et al.*, "PAPER-64 Constraints on Reionization: The 21 cm Power Spectrum at z = 8.4," *ApJ*, vol. 809, no. 1, 61, p. 61, Aug. 2015. DOI: 10.1088/0004-637X/809/1/61. arXiv: 1502.06016 [astro-ph.CO].

[201] A. P. Beardsley, B. J. Hazelton, I. S. Sullivan, *et al.*, "First Season MWA EoR Power spectrum Results at Redshift 7," *ApJ*, vol. 833, no. 1, 102, p. 102, Dec. 2016. DOI: 10.3847/1538-4357/833/1/102. arXiv: 1608.06281 [astro-ph.IM].

[202] W. Li, J. C. Pober, N. Barry, *et al.*, "First Season MWA Phase II Epoch of Reionization Power Spectrum Results at Redshift 7," *ApJ*, vol. 887, no. 2, 141, p. 141, Dec. 2019. DOI: 10.3847/1538-4357/ab55e4. arXiv: 1911.10216 [astro-ph.CO].

[203] L. Koopmans, J. Pritchard, G. Mellema, *et al.*, "The Cosmic Dawn and Epoch of Reionisation with SKA," in *Advancing Astrophysics with the Square Kilometre Array (AASKA14)*, Apr. 2015, 1, p. 1. arXiv: 1505.07568 [astro-ph.CO].

[204] H. Bondi and F. Hoyle, "On the mechanism of accretion by stars," *MNRAS*, vol. 104, p. 273, Jan. 1944. DOI: 10.1093/mnras/104.5.273.

[205] D. Tseliakhovich and C. Hirata, "Relative velocity of dark matter and Baryonic fluids and the formation of the first structures," *Phys. Rev. D*, vol. 82, no. 8, 083520, p. 083 520, Oct. 2010. DOI: 10.1103/PhysRevD.82.083520. arXiv: 1005.2416 [astro-ph.CO].

[206] R. Barkana and A. Loeb, "In the beginning: the first sources of light and the reionization of the universe," *Phys. Rep.*, vol. 349, no. 2, pp. 125–238, Jul. 2001. DOI: 10.1016/S0370-1573(01)00019-9. arXiv: astro-ph/0010468 [astro-ph].

[207] E. Komatsu and U. Seljak, "Universal gas density and temperature profile," *MNRAS*, vol. 327, no. 4, pp. 1353–1366, Nov. 2001. DOI: 10.1046/j.1365-8711.2001.04838.x. arXiv: astro-ph/0106151 [astro-ph].

[208] Y. Suto, S. Sasaki, and N. Makino, "Gas Density and X-Ray Surface Brightness Profiles of Clusters of Galaxies from Dark Matter Halo Potentials: Beyond the Isothermal β-Model," *ApJ*, vol. 509, no. 2, pp. 544–550, Dec. 1998. DOI: 10.1086/306520. arXiv: astro-ph/9807112 [astro-ph].

[209] E. Komatsu and U. Seljak, “The Sunyaev-Zel’dovich angular power spectrum as a probe of cosmological parameters,” *MNRAS*, vol. 336, no. 4, pp. 1256–1270, Nov. 2002. DOI: `10.1046/j.1365-8711.2002.05889.x`. arXiv: `astro-ph/0205468 [astro-ph]`.

[210] G. B. Field, “The Spin Temperature of Intergalactic Neutral Hydrogen.,” *ApJ*, vol. 129, p. 536, May 1959. DOI: `10.1086/146653`.

[211] M. Kuhlen, P. Madau, and R. Montgomery, “The Spin Temperature and 21 cm Brightness of the Intergalactic Medium in the Pre-Reionization era,” *ApJ*, vol. 637, no. 1, pp. L1–L4, Jan. 2006. DOI: `10.1086/500548`. arXiv: `astro-ph/0510814 [astro-ph]`.

[212] I. T. Iliev, P. R. Shapiro, and A. C. Raga, “Minihalo photoevaporation during cosmic reionization: evaporation times and photon consumption rates,” *MNRAS*, vol. 361, no. 2, pp. 405–414, Aug. 2005. DOI: `10.1111/j.1365-2966.2005.09155.x`. arXiv: `astro-ph/0408408 [astro-ph]`.

[213] K. Furugori, K. T. Abe, T. Tanaka, D. Hashimoto, H. Tashiro, and K. Hasegawa, “The 21-cm signals from ultracompact minihaloes as a probe of primordial small-scale fluctuations,” *MNRAS*, vol. 494, no. 3, pp. 4334–4342, May 2020. DOI: `10.1093/mnras/staa1033`. arXiv: `2002.04817 [astro-ph.CO]`.

[214] M. A. Alvarez, V. Bromm, and P. R. Shapiro, “The H II Region of the First Star,” *ApJ*, vol. 639, no. 2, pp. 621–632, Mar. 2006. DOI: `10.1086/499578`. arXiv: `astro-ph/0507684 [astro-ph]`.

[215] J. L. Johnson, T. H. Greif, and V. Bromm, “Local Radiative Feedback in the Formation of the First Protogalaxies,” *ApJ*, vol. 665, no. 1, pp. 85–95, Aug. 2007. DOI: `10.1086/519212`. arXiv: `astro-ph/0612254 [astro-ph]`.

[216] V. Iršič, H. Xiao, and M. McQuinn, “Early structure formation constraints on the ultralight axion in the postinflation scenario,” *Phys. Rev. D*, vol. 101, no. 12, 123518, p. 123 518, Jun. 2020. DOI: `10.1103/PhysRevD.101.123518`. arXiv: `1911.11150 [astro-ph.CO]`.

[217] P. J. E. Peebles, “Recombination of the Primeval Plasma,” *ApJ*, vol. 153, p. 1, Jul. 1968. DOI: `10.1086/149628`.

[218] Y. B. Zeldovich, V. G. Kurt, and R. A. Syunyaev, “Recombination of Hydrogen in the Hot Model of the Universe,” *Zhurnal Eksperimentalnoi i Teoreticheskoi Fiziki*, vol. 55, pp. 278–286, Jul. 1968.

[219] J. B. Muñoz, Y. Qin, A. Mesinger, S. G. Murray, B. Greig, and C. Mason, “The impact of the first galaxies on cosmic dawn and reionization,” *MNRAS*, vol. 511, no. 3, pp. 3657–3681, Apr. 2022. DOI: `10.1093/mnras/stac185`. arXiv: `2110.13919 [astro-ph.CO]`.

[220] X. Fan, M. A. Strauss, R. H. Becker, *et al.*, “Constraining the Evolution of the Ionizing Background and the Epoch of Reionization with z~6 Quasars. II. A Sample of 19 Quasars,” *The Astronomical Journal*, vol. 132, no. 1, pp. 117–136, Jul. 2006. DOI: `10.1086/504836`. arXiv: `astro-ph/0512082 [astro-ph]`.

[221] E. M. Hu, L. L. Cowie, A. J. Barger, P. Capak, Y. Kakazu, and L. Trouille, “An Atlas of z = 5.7 and z = 6.5 Lyα Emitters,” *ApJ*, vol. 725, no. 1, pp. 394–423, Dec. 2010. DOI: `10.1088/0004-637X/725/1/394`. arXiv: `1009.1144 [astro-ph.CO]`.

[222] K. Ota, M. Iye, N. Kashikawa, *et al.*, "Lyα Emitters at z = 7 in the Subaru/XMM-Newton Deep Survey Field: Photometric Candidates and Luminosity Functions," *ApJ*, vol. 722, no. 1, pp. 803–811, Oct. 2010. DOI: `10.1088/0004-637X/722/1/803`. arXiv: `1008.4842 [astro-ph.CO]`.

[223] M. Ouchi, K. Shimasaku, H. Furusawa, *et al.*, "Statistics of 207 Lyα Emitters at a Redshift Near 7: Constraints on Reionization and Galaxy Formation Models," *ApJ*, vol. 723, no. 1, pp. 869–894, Nov. 2010. DOI: `10.1088/0004-637X/723/1/869`. arXiv: `1007.2961 [astro-ph.CO]`.

[224] N. Kashikawa, K. Shimasaku, Y. Matsuda, *et al.*, "Completing the Census of Lyα Emitters at the Reionization Epoch," *ApJ*, vol. 734, no. 2, 119, p. 119, Jun. 2011. DOI: `10.1088/0004-637X/734/2/119`. arXiv: `1104.2330 [astro-ph.CO]`.

[225] A. Konno, M. Ouchi, Y. Ono, *et al.*, "Accelerated Evolution of the Lyα Luminosity Function at z $\gtrsim$7 Revealed by the Subaru Ultra-deep Survey for Lyα Emitters at z = 7.3," *ApJ*, vol. 797, no. 1, 16, p. 16, Dec. 2014. DOI: `10.1088/0004-637X/797/1/16`. arXiv: `1404.6066 [astro-ph.CO]`.

[226] S. Santos, D. Sobral, and J. Matthee, "The Lyα luminosity function at z = 5.7 - 6.6 and the steep drop of the faint end: implications for reionization," *MNRAS*, vol. 463, no. 2, pp. 1678–1691, Dec. 2016. DOI: `10.1093/mnras/stw2076`. arXiv: `1606.07435 [astro-ph.GA]`.

[227] H. Bondi, "On spherically symmetrical accretion," *MNRAS*, vol. 112, p. 195, Jan. 1952. DOI: `10.1093/mnras/112.2.195`.

[228] G. Sun and S. R. Furlanetto, "Constraints on the star formation efficiency of galaxies during the epoch of reionization," *MNRAS*, vol. 460, no. 1, pp. 417–433, Jul. 2016. DOI: `10.1093/mnras/stw980`. arXiv: `1512.06219 [astro-ph.GA]`.

[229] M. Fukugita and M. Kawasaki, "Reionization during Hierarchical Clustering in a Universe Dominated by Cold Dark Matter," *MNRAS*, vol. 269, p. 563, Aug. 1994. DOI: `10.1093/mnras/269.3.563`. eprint: `astro-ph/9309036`.

[230] R. J. Bouwens, P. A. Oesch, G. D. Illingworth, R. S. Ellis, and M. Stefanon, "The z $\sim$ 6 Luminosity Function Fainter than -15 mag from the Hubble Frontier Fields: The Impact of Magnification Uncertainties," *ApJ*, vol. 843, no. 2, 129, p. 129, Jul. 2017. DOI: `10.3847/1538-4357/aa70a4`. arXiv: `1610.00283 [astro-ph.GA]`.

[231] V. Bromm, R. P. Kudritzki, and A. Loeb, "Generic Spectrum and Ionization Efficiency of a Heavy Initial Mass Function for the First Stars," *ApJ*, vol. 552, no. 2, pp. 464–472, May 2001. DOI: `10.1086/320549`. arXiv: `astro-ph/0007248 [astro-ph]`.

[232] M. Trenti and M. Stiavelli, "Formation Rates of Population III Stars and Chemical Enrichment of Halos during the Reionization Era," *ApJ*, vol. 694, no. 2, pp. 879–892, Apr. 2009. DOI: `10.1088/0004-637X/694/2/879`. arXiv: `0901.0711 [astro-ph.CO]`.

[233] E. Visbal, Z. Haiman, and G. L. Bryan, "Self-consistent semi-analytic models of the first stars," *MNRAS*, vol. 475, no. 4, pp. 5246–5256, Apr. 2018. DOI: `10.1093/mnras/sty142`. arXiv: `1705.09005 [astro-ph.GA]`.

[234] M. E. Machacek, G. L. Bryan, and T. Abel, "Simulations of Pregalactic Structure Formation with Radiative Feedback," *ApJ*, vol. 548, no. 2, pp. 509–521, Feb. 2001. DOI: `10.1086/319014`. arXiv: `astro-ph/0007198 [astro-ph]`.

[235] J. H. Wise and T. Abel, "Suppression of H_2 Cooling in the Ultraviolet Background," *ApJ*, vol. 671, no. 2, pp. 1559–1567, Dec. 2007. DOI: `10.1086/522876`. arXiv: `0707.2059 [astro-ph]`.

[236] E. Visbal, Z. Haiman, and G. L. Bryan, "Limits on Population III star formation in minihaloes implied by Planck," *MNRAS*, vol. 453, no. 4, pp. 4456–4466, Nov. 2015. DOI: `10.1093/mnras/stv1941`. arXiv: `1505.06359 [astro-ph.CO]`.

[237] R. H. Mebane, J. Mirocha, and S. R. Furlanetto, "The Persistence of Population III Star Formation," *MNRAS*, vol. 479, no. 4, pp. 4544–4559, Oct. 2018. DOI: `10.1093/mnras/sty1833`. arXiv: `1710.02528 [astro-ph.GA]`.

[238] M. Ricotti, N. Y. Gnedin, and J. M. Shull, "Feedback from Galaxy Formation: Production and Photodissociation of Primordial H_2," *ApJ*, vol. 560, no. 2, pp. 580–591, Oct. 2001. DOI: `10.1086/323051`. arXiv: `astro-ph/0012335 [astro-ph]`.

[239] S. Seager, D. D. Sasselov, and D. Scott, "A New Calculation of the Recombination Epoch," *ApJ*, vol. 523, no. 1, pp. L1–L5, Sep. 1999. DOI: `10.1086/312250`. arXiv: `astro-ph/9909275 [astro-ph]`.

[240] S. Seager, D. D. Sasselov, and D. Scott, "How Exactly Did the Universe Become Neutral?" *ApJS*, vol. 128, no. 2, pp. 407–430, Jun. 2000. DOI: `10.1086/313388`. arXiv: `astro-ph/9912182 [astro-ph]`.

[241] W. Y. Wong, A. Moss, and D. Scott, "How well do we understand cosmological recombination?" *MNRAS*, vol. 386, no. 2, pp. 1023–1028, May 2008. DOI: `10.1111/j.1365-2966.2008.13092.x`. arXiv: `0711.1357 [astro-ph]`.

[242] D. Scott and A. Moss, "Matter temperature during cosmological recombination," *MNRAS*, vol. 397, no. 1, pp. 445–446, Jul. 2009. DOI: `10.1111/j.1365-2966.2009.14939.x`. arXiv: `0902.3438 [astro-ph.CO]`.

[243] A. Lewis, "Cosmological parameters from WMAP 5-year temperature maps," *Phys. Rev. D*, vol. 78, no. 2, 023002, p. 023002, Jul. 2008. DOI: `10.1103/PhysRevD.78.023002`. arXiv: `0804.3865 [astro-ph]`.

[244] B. Audren, J. Lesgourgues, K. Benabed, and S. Prunet, "Conservative Constraints on Early Cosmology: an illustration of the Monte Python cosmological parameter inference code," *JCAP*, vol. 1302, p. 001, 2013. DOI: `10.1088/1475-7516/2013/02/001`. arXiv: `1210.7183 [astro-ph.CO]`.

[245] D. Blas, J. Lesgourgues, and T. Tram, "The cosmic linear anisotropy solving system (class). part ii: Approximation schemes," *Journal of Cosmology and Astroparticle Physics*, vol. 2011, no. 07, pp. 034 – 034, Jul. 2011, ISSN: 1475-7516. DOI: `10.1088/1475-7516/2011/07/034`. [Online]. Available: `http://dx.doi.org/10.1088/1475-7516/2011/07/034`.

[246] A. Gelman and D. B. Rubin, "Inference from Iterative Simulation Using Multiple Sequences," *Statistical Science*, vol. 7, pp. 457–472, Jan. 1992. DOI: `10.1214/ss/1177011136`.

[247] S. P. Brooks and A. Gelman, "General methods for monitoring convergence of iterative simulations," *Journal of Computational and Graphical Statistics*, vol. 7, no. 4, pp. 434–455, 1998. DOI: `10.1080/10618600.1998.10474787`.

[248] P. Madau, A. Meiksin, and M. J. Rees, "21 Centimeter Tomography of the Intergalactic Medium at High Redshift," *ApJ*, vol. 475, no. 2, pp. 429–444, Feb. 1997. DOI: `10.1086/303549`. arXiv: `astro-ph/9608010 [astro-ph]`.

[249] U. Seljak, “Analytic model for galaxy and dark matter clustering,” *MNRAS*, vol. 318, no. 1, pp. 203–213, Oct. 2000. DOI: `10.1046/j.1365-8711.2000.03715.x`. arXiv: `astro-ph/0001493 [astro-ph]`.